Production, Characterization and Reflectivity Measurements of Diamond-like Carbon and other Ultracold Neutron Guide Materials

---

Dissertation

zur

Erlangung der naturwissenschaftlichen Doktorwürde
(Dr. sc. nat.)

vorgelegt der

Mathematisch-naturwissenschaftlichen Fakultät

der

Universität Zürich

von

Stefan Heule

von Zürich und Widnau SG

Promotionskomitee:

Prof. Dr. Ulrich Straumann (Vorsitz, Leitung der Dissertation)
Dr. Manfred Daum
Dr. Reinhold Henneck
Dr. Thomas Lippert

Zürich, 2008

Abstract / Zusammenfassung

This thesis presents the results of investigations of the reflection of ultracold neutrons (UCN) by various material surfaces, particularly diamond-like carbon (DLC), on various substrates.

In the first part, the build-up of a facility for coating the inner walls of tubes with DLC is described; this was based on pulsed laser deposition with an irradiation wavelength of 193 nm. A standard procedure for the structural characterization of DLC coatings was developed, that included use of Raman spectroscopy, X-ray photoelectron spectroscopy and cold neutron reflectometry. Test samples produced with the coating facility and from other sources were found to have a Fermi potential above 200 neV but had insufficient adhesion to smooth substrates such as glass. Also, the deposition rates ($\lesssim$30 pm/s over 10 cm^2 at a repetition rate of 10 Hz) are too low for the coating of long tubes within realistic time scales.

The second part of the thesis describes and gives results from an experiment, which was performed to systematically study the reflection from sample surfaces commonly used for UCN guides. A collimated beam of UCN directed at about 50° to the surface normal of two plates makes many reflections during its passage through the gap. As new feature, converging configurations of the two plates were also used, allowing a direct measurement of the non-specularly reflected fraction. The results were compared with two theoretical models, Lambert's model of diffuse reflection, which is widely used in optics and the microroughness model developed by Steyerl.

Monte Carlo simulations with GEANT4UCNwere used to obtain values for the two parameters of the microroughness model, the RMS roughness b and the correlation length w and the single parameter of the Lambert model, the fraction of diffuse reflection d: 0.91 ± 0.06 nm $\leq b \leq 3.13\pm0.12$ nm, 11.8 ± 1.4 nm $\leq w \leq 125.9\pm5.5$ nm and $0.11\pm0.03\% \leq d \leq 3.35\pm0.13\%$ was found. Significantly better agreement with the experimental results was obtained with the microroughness model. For the first time, the model parameters were compared to corresponding values measured for the same samples using atomic force microscopy; moderately good agreement was found. Floatglass substrates coated with either NiV or DLC yielded the best transmission and are best suited as neutron guides for the UCN source being built at the Paul Scherrer Institut.

Im Rahmen dieser Arbeit wurde das Reflektionsverhalten von ultrakalten Neutronen (UCN) an verschiedenen Materialoberflächen, speziell an diamantähnlichem Kohlenstoff (DLC), auf verschiedenen Substraten untersucht.

Im ersten Teil wird der Aufbau einer Anlage zur Beschichtung von Rohrinnenwänden mit DLC beschrieben, welche auf Laserstrahlverdampfen mit einer Bestrahlungswellenlänge von 193 nm basiert. Ein Standardverfahren zur strukturellen Charakterisierung von DLC Beschichtungen wurde entwickelt, welches Raman Spektroskopie, Röntgen-Photoelektron-Spektroskopie (XPS) und Reflektometrie mit kalten Neutronen beinhaltet. Für Testbeschichtungen, welche mit der Beschichtungsanlage produziert wurden, konnte ein Fermi Potential oberhalb von 200 neV festgestellt werden; allerdings war die Haftung auf glatten Substraten wie Glas ungenügend. Weiter sind die Beschichtungsraten ($\lesssim$30 pm/s über 10 cm^2 bei einer Repetitionsrate von 10 Hz) zu tief für die Beschichtung langer Rohre innerhalb realistischer Zeiten.

Der zweite Teil der Arbeit beschreibt den Aufbau und die Resultate eines Experiments, das zum Zweck der systematischen Untersuchung des Reflektionsverhaltens an Testoberflächen, wie sie typischerweise in UCN Leitern eingesetzt werden, durchgeführt wurde. Ein kollimierter UCN Strahl mit 50° Neigung zur Plattennormalen unterläuft viele Reflektionen auf seinem Weg durch den Spalt zwischen den Platten. Erstmals wurden konvergente Konfigurationen der Platten benutzt, welche eine direkte Messung des nicht-spekular reflektierten Anteils erlauben. Die Resultate wurden mit zwei theoretischen Modellen verglichen, einerseits mit dem Lambert-Modell der diffusen Reflektion, welches in der Optik eingesetzt wird, und andererseits dem Mikrorauheits-Modell, entwickelt von Steyerl.

Monte Carlo Simulationen mit GEANT4UCN wurden durchgeführt um die zwei Parameter des Mikrorauheits-Modells, die quadratische Rauheit b und die Korrelationslänge w, sowie für den einzigen Parameter des Lambert-Modells, den Anteil diffuser Reflektion d, zu bestimmen: 0.91 ± 0.06 nm $\leq b \leq 3.13\pm0.12$ nm, 11.8 ± 1.4 nm $\leq w \leq 125.9\pm5.5$ nm und $0.11\pm0.03\% \leq d \leq 3.35\pm0.13\%$ konnte gefunden werden. Eine signifikant bessere Übereinstimmung mit den Resultaten des Experiments wurde für das Mikrorauheits-Modell beobachtet. Ein erstmals durchgeführter Vergleich mit mit Werten, welche für die gleichen Oberflächen mittels Raster-Kraft-Mikroskopie (AFM) bestimmt wurden, zeigte eine einigermassen gute Übereinstimmung. Die beste Transmission ergab sich für NiV oder DLC beschichtete Flachglas-Substrate; diese sind am besten als Neutronenleiter für die UCN Quelle geeignet, welche am Paul Scherrer Institut entsteht.

Contents

Chapter 1

Introduction

The goal of this work was to understand the mechanisms of ultracold neutron wall scattering in terms of surface properties such as roughness, and their influence on the specular or diffuse behavior of the reflection. Within this context, a coating facility for the production of inner wall coatings of ultracold neutron guides was built up. Materials used for wall coatings have to fulfill the following conditions: 1) high Fermi potential, 2) low loss probability per wall collision and 3) highly specular reflection behavior. The third criterium only applies to wall coatings of neutron guides. The structural characterization of a specific wall coating material, diamond-like carbon, is discussed; the coating facility is described and the results from a guide surface test experiment, the double plate experiment, are reported and discussed.

1.1 Short history

The neutron was discovered experimentally 1932 by Chadwick [1], twelve years after the existence of a neutral particle within the atomic nucleus was considered by Rutherford [2]. The neutron has a mass of 939.56536±0.00008 MeV/c^2 and consists of an up-quark and two down-quarks [4].

It was Fermi who realized first that the coherent scattering of slow neutrons would result in an effective interaction potential for neutrons traveling through matter, which would be positive for most materials [3]. The consequence of such a potential would be the total reflection of neutrons slow enough and incident on a surface at a glancing angle. This effect was experimentally demonstrated by Fermi and Zinn [5] and Fermi and Marshall [6]. The storage of neutrons with very low kinetic energies was predicted by Zeldovich [7] and experimentally realized simultanously by groups at Dubna [8] and Munich [9].

1.1.1 Ultracold Neutrons

Free neutrons with kinetic energies below the Fermi potential of a good wall material, e.g. beryllium, with ∼250 neV, are totally reflected under any angle of incidence on such a material and are usually referred to as ultracold neutrons (UCN). Their kinetic energy corresponds to a temperature below 3 mK and a velocity of 6.9 m/s. Thus, UCN are strongly affected by the Earth's gravitational field, leading to a change of the potential energy of ∼102 neV/m. The magnetic moment of the neutron, caused by the spin $\frac{1}{2}\hbar$, interacts with an external magnetic field; the corresponding energy is ∼60 neV/T. Like any free neutrons, UCN are also affected by the weak interaction, resulting in the neutron β-decay.

Neutrons and protons consist of three elementary particles (quarks) each, which are tightly bound together by the strong interaction. In atomic nuclei, the residual of the strong interaction binds neutrons and protons together. Due to their long wavelengths UCN also interact strongly with atomic nuclei. This interaction can be represented by an effective potential usually referred

to as the Fermi potential. Ultracold neutrons can be stored in traps due to total reflection on materials with high Fermi potential and the interaction with magnetic field gradients. This allows for the observation of UCN for times comparable to the lifetime of the free neutron. A more detailed discussion based on the common literature in the field of UCN, is given in Section 1.2.

1.1.2 Experiments with UCN

The production, transportation and storage of UCN is currently motivated by their usefulness as a tool to determine properties of the neutron and to study fundamental physical interactions. Storage experiments have improved the accuracy or the upper limit of some neutron related physical values.

Neutron β-decay, $n \rightarrow p + e^- + \overline{\nu_e}$, is the prototype semi-leptonic weak decay and is described by the interaction of two left-handed lepton currents with two hadron currents. The neutron lifetime τ_n is used for the determination of the V_{ud} element of the CKM quark-mixing matrix [10, 11],

$$|V_{ud}|^2 = \frac{4908.7(1.9)\text{sec}}{\tau_n(1+3g_A^2)} \tag{1.1}$$

with the ratio of axial-vector/vector couplings, $g_A = G_A/G_V$, where $G_V = G_F$ is the Fermi coupling constant. Today's world average value for the neutron lifetime is 885.7 ± 0.8 s [12], to which the experiment of Arzumanov et al. [13] contributes strongest. Ref. [13] measured $\tau_n[\text{sec}] = 885.4 \pm 0.9_{\text{stat}} \pm 0.4_{\text{syst}}$ by storage of UCN in a material bottle covered with Fomblin oil. Using traps with different surface to volume ratios allowed them to separate storage decay time and neutron life time from each other. There is another result, obtained by Serebrov et al. [14], who found $878.5 \ \pm 0.7_{\text{stat}} \pm 0.4_{\text{syst}}$. Thus, the two most presicely measured values deviate by 5.6σ.

Until today, no evidence was found that any interaction exists which violates the combination of the charge (C), parity (P) and time reversal (T) symmetry operations [4]. However, a violation of the combined CP symmetry was first found in the K^0 system [15]. Thus, T violation should also exist if CPT is conserved. The existence of an electric dipole moment (EDM) of a fundamental particle like the neutron would directly prove T (and P) violation, as the energy of an electric dipole $\vec{d} \sim \vec{s}$ contains a term of the form

$$\vec{s}\vec{E} \underbrace{\rightarrow}_{P \text{ or } T} -\vec{s}\vec{E} \tag{1.2}$$

and is not invariant under P or T.

The best value for the upper limit of the neutron EDM, $|d_n| < 2.9 \cdot 10^{-26} e\text{cm}$ (90% C.L.), has been obtained in an experiment performed by the Rutherford-Sussex-ILL nEDM collaboration [16]. This experiment applied the Ramsey-resonance technique [17] to stored UCN. This technique is based on a spin precession measurement, where the rotation frequency in magnetic field is given by the Larmor frequency $\omega_L = \mu B/\hbar$. The (simplified) Hamiltonian of a system with both electric and magnetic field is

$$H = \hbar\omega_L = \pm\vec{\mu} \cdot \vec{B} - \vec{d} \cdot \vec{E}, \tag{1.3}$$

where $\vec{\mu}$ is the magnetic dipole moment of the neutron. Thus, a neutron EDM would change the Larmor frequency. During a typical storage time of ∼100 s a phase is accumulated. The same measurement is performed with reversed electric field, resulting in a phase difference $\delta\omega = -4d_nE/\hbar$. Excellent stability and homogeneity of the fields is required, which is an experimental challenge. A neutron EDM is predicted in the range of 10^{-25} to 10^{-28} e·cm by the Minimal Supersymmetric Standard Model (MSSM) or around 10^{-31} e·cm by the Standard Model of Particle Physics (see e.g. [18], p. 111ff).

The measurements of other fundamental neutron properties with UCN have also been performed, e.g. the observation of gravitational interactions of the neutron [19] or the determination

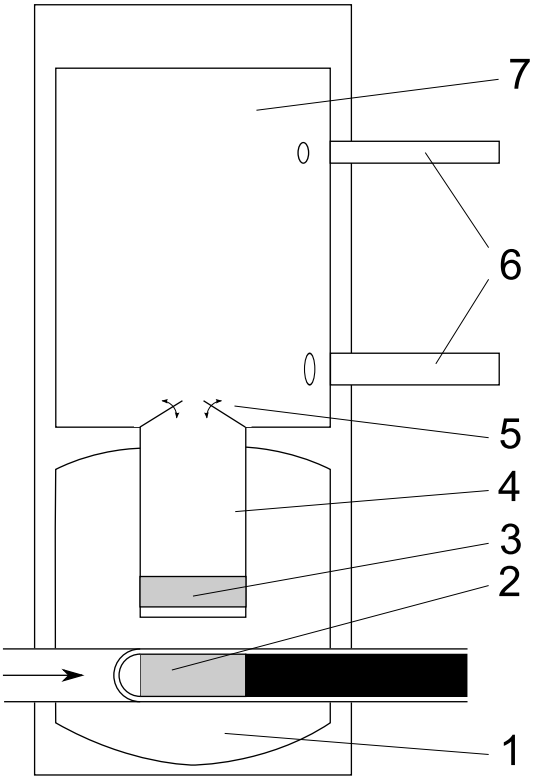

Figure 1.1: The Spallation UCN source at PSI. The total height of the source is about 6 m. The arrow denotes the proton beam. [1] heavy water moderator, [2] lead Spallation target, [3] solid deuterium UCN converter at 6 K, [4] vertical neutron guide, [5] UCN shutter, open during production, closed during storage, [6] neutron guides to experiments, [7] Ni/DLC coated storage volume (2 m^3).

of a lower limit for the neutron-mirror neutron oscillation time [20]. Further experiments are ongoing, as e.g. the UCNA experiment for the measurement of the A-coefficient of the neutron beta decay correlation at Los Alamos [21], or suggested, e.g. the measurement of the electric charge of the free neutron [22].

1.1.3 The UCN source at PSI

The UCN source at PSI (see Figure 1.1.3) is based on the spallation principle and an UCN-converter made of solid deuterium (sD_2). The source parameters are described in detail in Ref. [23]. Fast neutrons are produced by the pulsed proton beam at PSI (kinetic energy of the protons 590 MeV, beam intensity $I_p \geq 2$ mA) at a low duty cycle of 1% with a spallation target (lead filled zircaloy tubes, see Ref. [24]) and are moderated to thermal energies by about 3.3 m^3 of heavy water at room temperature. The production of UCN is done in a sD_2 converter with a volume of 30 liters kept at low temperature (6 K). The source is operated in pulsed mode (4-8 s production and 400-800 s storage time) in order to keep the sD_2 at low temperature although the power deposition during a pulse is large ($\sim$0.2 W/g [25]). The number of neutrons produced in the spallation target per incoming proton is expected to be $\sim$10.

In an ideal moderator of infinite size and without neutron absorbing materials neutron energies would be distributed according to a Maxwellian. Although real systems differ from the ideal case, the consideration of the spectrum to be Maxwellian is a good approximation. For a given very

low temperature T one finds the density of UCN in an energy range E≤V to be [26]

$$\rho_{\mathrm{UCN}} = \frac{2}{3}\frac{\Phi_0}{\alpha}\left(\frac{V}{k_{\mathrm{B}}T}\right)^{3/2}, \tag{1.4}$$

where Φ_0 is the incoming thermal neutron flux and $\alpha = \sqrt{2k_{\mathrm{B}}T_n/m}$ with the neutron temperature T_n. For thermal neutrons (T_n=300 K) with an energy limit after conversion of V=250 neV (Fermi potential of nickel or beryllium) and an incident neutron flux of 10^{15} $\mathrm{s^{-1}cm^{-2}}$ (order of the largest steady thermal neutron fluxes presently available) the maximum UCN density becomes 10^2 $\mathrm{cm^{-3}}$.

In order to further increase the UCN density, one can use the concept of a super-thermal neutron source. It is based on thermal non-equilibrium which allows further down-scattering while the reversed process, thermal up-scattering, is suppressed. In a simplified model, the moderator is considered to have two energy levels, separated by an excitation energy Δ. In the case of sD_2 at low temperature (∼6 K), rotational states are excited. By cooling the converter, less excited states are occupied, leading to a decreased up-scattering cross section

$$\sigma_{\mathrm{up}} = \frac{E_{\mathrm{UCN}} + \Delta}{E_{\mathrm{UCN}}} \cdot e^{-\frac{\Delta}{k_{\mathrm{B}}T}} \cdot \sigma_{\mathrm{down}}. \tag{1.5}$$

Test experiments for a super-thermal sD_2 source were carried out at a reactor [27] and at spallation sources [28–30]. Further experiments on the performance of sD_2 as converter were carried out at PSI, from which the design and operation parameters can be extracted [31, 32].

After extraction from the sD_2 source, UCN are stored in a volume of about 2 $\mathrm{m^3}$. The surfaces of this storage volume and of the guides between the sD_2 moderator and the storage volume as well as of the guides from the storage volume to UCN experiments are a crucial issue for the performance of the source. In order to optimize this, reflective interaction of UCN with material surfaces and fields have to be studied.

1.2 Interactions of UCN

Ultracold neutrons, like any free neutrons, are affected by all fundamental interactions as described subsequently (see also e.g. Ref. [26]). Their kinetic energy is so low that these interactions make them a unique tool for fundamental and applied physics.

1.2.1 The strong interaction

Scattering from a single nucleus

Ultracold neutron scattering on a single scattering center can be described by an incident plane wave and a scattered spherical wave

$$\psi = e^{i\vec{k}\cdot\vec{r}} + f(\theta)\frac{e^{ikr}}{r}, \tag{1.6}$$

where f is the scattering amplitude. The current density, $\vec{j}$, associated with ψ is

$$\vec{j} = \frac{\hbar}{2im_n}(\psi^*\nabla\psi - \psi\nabla\psi^*) = \vec{v}, \tag{1.7}$$

where m_n is the neutron mass and $\vec{v}$ the neutron velocity. Thus, the probability of scattering, dP, into a solid angle element $d\Omega$ is

$$dP = (\vec{j}\cdot\vec{e_r})r^2 d\Omega = v|f(\theta)|^2 d\Omega, \tag{1.8}$$

where $\vec{e_r}$ is the unit vector in direction of $\vec{r}$. The fact that the wavelength of a UCN, λ_n, is much larger than the range of the strong interaction potential responsible for scattering leads to

$$f(\theta) = \text{constant} = -a, \tag{1.9}$$

where a is called the scattering length, which only describes the interaction without spin.

As the strength of the interaction potential $V(\vec{r}-\vec{r_n})$, where $\vec{r_n}$ is the position of the scattering center (nucleus), is much larger than the neutron energy, the neutron wave function is largely different in the presence of the interaction from that in the absence of the interaction. Thus, perturbation theory cannot be used for the description of the scattering within the interaction range and consequently, $f(\theta)$ cannot be calculated by using the Born approximation. However, as the changes in the wave function outside the interaction range are small, it is possible to calculate the wave function by perturbation theory and the introduction of an equivalent potential, as first done by Fermi [3]. The resulting effective potential is usually referred to as the material optical or Fermi (pseudo) potential,

$$V_F(\vec{r} - \vec{r_n}) = \frac{2\pi\hbar^2 a}{\mu}\delta^{(3)}(\vec{r} - \vec{r_n}) \tag{1.10}$$

and can only be used in the first Born approximation. The scattering of an UCN from a single nucleus can therefore be described by the Schrödinger equation

$$-\frac{\hbar^2}{2\mu}\nabla_r^2\psi + [E - V_F(\vec{r} - \vec{r_n})]\psi = 0. \tag{1.11}$$

Neutron scattering from many scattering centers

In a material with the scattering centers assumed to be uniformly distributed, the scattering center density n replaces the δ function in Eq. 1.11. Using the reduced mass in the description of the neutron-nucleus interaction the recoil of the nucleus is accommodated. Assuming the nucleus to be rigidly bound, i.e. having an infinite mass, one has to replace the reduced mass μ by the mass of the neutron m_n. Thus, the bound nucleus scattering length

$$a_B = \frac{m_n}{\mu}a \tag{1.12}$$

is introduced.

Coherent effects appear when multiple scattering centers are involved. Two definitions of coherence can be made (see Ref. [33]): (i) absolute coherence, which describes the wave interference with itself while it undergoes a reflection and which is therefore also elastic; (ii) relative coherence for the interference of waves scattered from different nuclei. Here, the second will be used as definition of coherence. If the neutron interacts with a single scattering center, the phase correlation between incident and scattered wave is lost and the interaction is called incoherent. The differential scattering cross section can be split into two parts,

$$\frac{\mathrm{d}\sigma}{\mathrm{d}\Omega} = a_{\mathrm{coh}}^2 |\sum_j e^{i(\vec{k_i}-\vec{k_f})\vec{R}_j}|^2 + N a_{\mathrm{inc}}^2, \tag{1.13}$$

with the total numbers of nuclei in the scatterer N and the coherent and incoherent scattering lengths a_{coh} and a_{inc}. There is a value for $\vec{k_i} - \vec{k_f}$ for which $(\vec{k_i} - \vec{k_f}) \cdot \vec{R}_j = 2\pi n$ for all j. In this case the sum in Eq. 1.13 is equal to N and the first term is proportional to N^2.

Loss effects can be included into the Fermi potential, extending it to a complex potential

$$U = V - iW = \frac{2\pi\hbar^2}{m}N(\Re(a_B) - i\Im(a_B)) = \frac{2\pi\hbar^2}{m}\frac{\rho N_A}{M_M}(\Re(a_B) - i\Im(a_B)), \tag{1.14}$$

where a_B is the bound coherent scattering length, ρ the mass density, N_A Avogadro's constant and M_M the molecular mass. It is a consequence of probability conservation and the optical theorem

$$\Im(a_B) = \frac{\sigma_l k}{4\pi}, \tag{1.15}$$

where $\sigma_l \sim 1/v$ is the loss probability. Nevertheless, the imaginary part W is velocity independent, as absorption and inelastic scattering cross sections are both proportional to $1/v$ and therefore $W \sim \sigma_l v$=const. The loss coefficient, η, is defined as

$$\eta = \frac{W}{V} = \frac{\sigma_l k}{4\pi a_B} = \frac{\sigma_l}{2a_B\lambda}, \tag{1.16}$$

where λ is the neutron wave length. However, experimentally found values for η, of the order 10^{-5} to 10^{-4} for good wall materials, are up to 2 orders of magnitude higher than the theoretical values computed by Eq. 1.16. The discrepancy is often referred to as anomalous losses. Major contributions from different origins could be identified in the case of beryllium [34] and carbon [35]. For an ideal surface, i.e. a surface without roughness, with Fermi potential V,

$$R = \frac{k - k'}{k + k'} = \frac{\sqrt{E_\perp} - \sqrt{E_\perp - V}}{\sqrt{E_\perp} + \sqrt{E_\perp - V}} \tag{1.17}$$

is the amplitude of the reflected wave, where $E_\perp = \frac{\hbar^2 k_\perp^2}{2m}$ is the energy corresponding to the velocity component of the incident neutron perpendicular to the reflecting surface and k and k' are the wavenumber of the incident and the reflected neutron, respectively. Using the complex potential U instead of V and expanding the square roots in (1.17), as usually $W \ll V$, leads to the reflection probability

$$|R|^2 = 1 - 2\eta\sqrt{\frac{E_\perp}{V - E_\perp}} \equiv 1 - \mu(E, \theta), \tag{1.18}$$

where μ is defined as the wall loss probability per bounce. Thus,

$$\mu(E, \theta) = 2\eta\sqrt{\frac{E\cos^2\theta}{V - E\cos^2\theta}} \tag{1.19}$$

with θ the angle of incidence with respect to the surface normal. As shown in Eq. (1.18), only the velocity (and the energy respectively) component normal to the reflecting surface decides if the neutron is reflected or not. This is not only true for the ideal case of a perfectly smooth surface as described above but also for real surfaces with roughness. Section 4.3 deals with the reflection of UCN at rough surfaces.

1.2.2 The weak interaction

Free neutrons are not stable and decay after ∼900 s according to the reaction

$$n \rightarrow p + e^- + \overline{\nu_e}, \tag{1.20}$$

as described in Section 1.1.2.

1.2.3 Gravity

As neutrons have a mass, they are affected by gravitation. Unlike as for particles in high energy physics, the contribution of the gravitational interaction,

$$V_g = mgh \tag{1.21}$$

is non-negligible for UCN due to their small velocities. It is equivalent to 102 neV/m, which allows an UCN in rest to drop by ∼2.5 m and still to be reflected afterward by e.g. a beryllium surface with a Fermi potential of 250 neV.

Table 1.1: Selected materials typically used in UCN experiments. Only the Fermi potential and the absorption cross section was used for the calculation of the loss coefficient.

Material	V_{Fermi} [neV]	v_C [m/s]	η [10^{-5}]
Be	250	6.92	0.027
^{58}Ni	335	8.01	8.85
Fe	209	6.32	7.51
Cu	170	5.70	13.60
Diamond	305	7.64	0.013
Al	54	3.22	1.86
Si	54	3.21	
Ti	-51	-	-

1.2.4 The magnetic interaction

As the neutron has a spin $\frac{1}{2}\hbar$, it also possesses a magnetic dipole moment $\vec{\mu}$. The potential energy of the interaction of $\vec{\mu}$ with an external magnetic field $\vec{B}(\vec{r})$ is given by

$$V_m = -\vec{\mu} \cdot \vec{B}(\vec{r}) = \pm 60\,\text{neV/T}. \tag{1.22}$$

Also internal magnetic fields produced by atomic electrons interact with the magnetic moment of a neutron. Material surface magnetism can therefore give an additional contribution to the total effective potential, i.e. $U = V + V_m - iW$, resulting in an increase or decrease of the Fermi potential depending on the spin orientation of the incident UCN.

1.3 Wall materials for UCN reflections

As mentioned above, first measurements of UCN storage were performed in 1969, ten years after its theoretical prediction by Zeldovich [7]. Subsequent experiments found loss probabilities significantly higher than those predicted. Table 1.1 shows the Fermi potential, the corresponding critical velocity and the loss coefficient for some selected materials. An ideal UCN wall material has a high Fermi potential and a low loss cross section. Most materials have either a high Fermi potential and also a significant loss probability, as e.g. natural nickel or its isotope ^{58}Ni, or only a moderate to low Fermi potential together with a low cross section as e.g. aluminium or silicon. Only very few materials really combine both advantages; the one of them used most widely is beryllium. Unfortunately, beryllium is highly toxic and not easy to machine. Diamond and diamond-like materials have been investigated recently [36–39] and show similar properties as beryllium in terms of a high Fermi potential and a low loss probability.

In most cases the wall material is applied as a coating on top of another material used as substrate. The thickness of the coating is an important issue as too thin a coating has a significant UCN transmission, caused by the penetration of the coating by UCN, which leads to additional losses. The coating has to be of a minimal thickness for which this additional loss rate is not exceeding the loss probability μ. The penetration depth of UCN, i.e. the depth for which the UCN transmission is $1/e$, is typically of the order of $\sim$10 nm. A coating thickness of the order of 300 nm for a high Fermi potential material as beryllium limits the UCN transmission to below 10^{-7}.

1.4 Carbon surfaces

Pure diamond is a much more favorable material as its Fermi potential (306 neV) exceeds the one of beryllium and the loss cross section is expected to be roughly on the same level. Diamond consists of sp^3 hybridized carbon atoms which are covalently bond in a face centered cubic (fcc) structure. As its elementary unit cell builds a tetrahedron, it bond structure is often referred to as tetragonal.

A second form of pure carbon, graphite, consists of sp^2 hybridized atoms. It is structured in layers where the bonds within the layers are strong and those between layers weak. Due to the decreased density (≤ 2.25 g/cm^3) compared to diamond (3.52 g/cm^3), the Fermi potential of graphite (196 neV) is significantly lower and not of major interest for UCN applications.

Other allotropes of carbon are Fullerenes, amorphous carbon (see Section 1.4.2), carbon nanofoam or carbon nanotubes.

1.4.1 Hybridization

Naively, the electron configuration of carbon would be expected to be $(1s)^2(2s)^2(2p)^2$. This would allow carbon atoms to form two (relatively weak) bonds with other atoms. However, it is well known that carbon atoms form four bonds with their neighbors. This is due to the true electron configuration $(1s)^2(2s)^1(2p)^3$ and the hybridization of (2s) and (2p) orbitals. One distinguishes three cases (see e.g. Ref. [40]):

sp^3 hybridization: The (2s) electron is hybridized with all three (2p) electrons and four sp^3 electrons on an energy level somewhere between the (2s) and the (2p) level are formed. The overlap of sp^3 orbitals of two carbon atoms leads to strong covalent bonds, usually referred to as σ-bonds.

sp^2 hybridization: Only two of three (2p) electrons are hybridized with the (2s) electron; three sp^2 orbitals are formed which can be used for σ-bonds. One (2p) electron remains in its original orbital state and can only form weak bonds, usually referred to as π-bonds.

sp^1 hybridization: The (2s) orbital is hybridized with only one (2p) orbital. Carbon atoms which are sp^1 hybridized can form threefold bonds with each other.

The binding energy of σ-bonds is in the range of 284-285 eV while the π-bonds, formed by Van-der-Waals forces, are much weaker.

1.4.2 Diamond-like carbon

A detailed review of diamond-like carbon can be found in e.g. Ref. [41]: parts of the following sections have been taken from this reference. There are many forms of amorphous carbon, some of them include other elements while others are very pure. Two main groups are usually distinguished: hydrogenated amorphous carbon, denoted by a-C:H, and hydrogen-free amorphous carbon, denoted by a-C. Amorphous carbon forms which include a significant fraction of sp^3 bonds are referred to as diamond-like carbon (DLC) independent of the amount of hydrogen they include. In this work DLC refers to the hydrogen-free forms. If the sp^3 fraction is high, the material is denoted as tetragonal amorphous carbon, ta-C, and has a density of about 3 g/cm^3 or higher.

Diamond-like carbon is widely used in industry as protective and non-abrasive coating for many applications due to its high mechanical hardness. Its high chemical inertness leads to an excellent bio compatibility and it is therefore used for medical implants and in food processing industry.

1.5 DLC Production Methods

Diamond-like carbon, hydrogenated or hydrogen-free, can be produced by various deposition methods. This section gives an overview of these methods including the individual advantages and disadvantages when used for the production of DLC films as UCN wall coatings.

The methods can be split into two groups: chemical vapor deposition (CVD) and physical vapor deposition (PVD).

1.5.1 CVD Methods

For most industrial applications of DLC, CVD methods are used as they are easy to scale-up. Their so-called precursor, i.e. the material to start with, is a gas which contains carbon atoms. The gases commonly used are acetylene (C_2H_2) and methane (CH_4). As for most application maximum hardness is desired, the amount of hydrogen, which lowers the hardness, should be minimized. Thus, acetylene is the most widely used precursor gas.

Plasma enhanced chemical vapor deposition

The most popular method is RF-plasma enhanced chemical vapor deposition (PECVD, see e.g. [42]). A PECVD setup consists mainly of two electrodes of different area. The bigger electrode, often including the walls of the deposition chamber, is usually set to ground potential while the smaller electrode, on which the substrate is mounted is capacitively coupled to the RF power. A plasma is produced between the two electrodes by the RF power. Sheaths with positive space charge are built close to the electrodes due to the higher mobility of electrons compared to the ions. This leads to an additional DC voltage between the sheaths and the electrodes which is inversely proportional to the area of the electrodes. Thus, a higher voltage is obtained at the smaller electrode which is why the smaller electrode is used as substrate electrode. The sheath voltage accelerates positive carbon ions to the substrate, providing them with enough energy to create the sp^3 bonding.

A major drawback of PECVD is the relatively large amount of hydrogen which is incorporated into the DLC film. Due to the similar mass of a hydrogen nucleus and a UCN, the latter gains easily energy by interaction with the hydrogen nucleus which is kept at a significantly higher temperature than the UCN temperature which is in the range of a few millikelvin. Thus, incorporated hydrogen leads to an increase of loss by thermal up scattering. The effect can be reduced by using deuterized gases as the energy transfer is reduced by the doubling of the mass of the nucleus. Van der Grinten et al. [43] worked with methane and deuterated methane as precursor gases and found about 20% hydrogen resp. deuterium within their films. In addition, they measured 153 neV and 221 neV for the Fermi potential when using the hydrogenated and deuterated precursor gas, respectively. The low values for the Fermi potential were explained by a decreased density of the material.

1.5.2 PVD Methods

As seen above, the incorporation of hydrogen into the DLC films leads to an increased loss probability per wall collision. Thus, the amount of hydrogen within the films should be minimized. The best approach is to use a hydrogen-free precursor, which can be realized with PVD methods.

The first DLC deposition was done by Aisenberg and Chabot [44] using ion beam deposition. The common feature of all PVD methods is that the DLC film is produced by the condensation of medium energy ($\sim$100 eV) carbon ions on a substrate. The ideal deposition process is a carbon ion flux provided at this energy with a narrow energy distribution and a minimum number of non-energetic, generally neutral, species [45].

Mass selected ion beam deposition

Carbon ions are produced in an ion source from a graphite target with a small spread of the ion energy, i.e. in the range 1-10 eV. The ions are then accelerated to 5-40 keV and pass through a magnetic filter, e.g. a magnetic field perpendicular to the flight direction of the ions. This filters out nearly all neutrals and selects ions with an e/m ratio of the C^+ ion. Due to the Coulomb repulsion of the ions, the ion beam diverges. The deceleration of the ions to the desired energy is done subsequently by an electrostatic lens and the beam is focused onto the substrate in a vacuum of the order 10^{-6} Pa to produce a ta-C film.

Major disadvantages of this method are the low deposition rate (of the order of 10^{-4} nm/s) and the high costs and size of the setup.

Sputtering

Sputtering is very often used in industry for the production of DLC coatings. Most frequently dc or RF sputtering of a graphite electrode by an argon plasma is utilized. As the sputter yield of graphite is quite low, magnetron sputtering is often used to increase the deposition rate. There, magnets, which are placed at the back of the target, make the electrons moving on spirals which increases their path length. This leads to an increase of the degree of ionization of the plasma. If the magnetic field is extended to the substrate, Ar ions can enhance the formation of sp^3 bonds. The energy of the carbon ions can be varied by applying a dc bias voltage to the substrate.

Another form of sputtering is ion beam assisted deposition (IBAD). A beam of argon ions is used to sputter a graphite target and to form the carbon particle flux. A second Ar beam is used to bombard the growing film and therefore enhance the formation of sp^3 bonds.

As usually no filtering is applied, sputter processes produce plasma with a high fraction of neutral and therefore low-energetic species which results in a low sp^3 fraction.

Cathodic arc deposition

Different kinds of setups exist for cathodic arc deposition. They all have in common that an arc is initiated in vacuum. For most of them this is done by touching a graphite cathode with a small carbon striker electrode and subsequent withdrawal of the striker. An energetic plasma with a high ion density of up to 10^{13} cm^{-3} is produced. A low voltage, high current power supply is used. A very high current density of $10^6 - 10^8$ A/cm^2 is carried by the small (1-10 μm) cathode spot, which is formed by an explosive emission process producing not only the desired plasma but a big amount of particulates, e.g. small pieces of graphite.

Filtered cathodic vacuum arc (FCVA) uses a toroidal magnetic filter duct to get rid of neutral species and therefore achieves a grade of ionization close to 1. The toroidal currents produce a magnetic field similar to the one created by a solenoid, but with a curvature of either 90 degree or even a S-shape. The electrons within the plasma follow the magnetic field lines on a helix around the filter axis. Attracted by Coulomb forces, the positive ions follow the electrons around the filter. The neutral particulates cannot follow the plasma and hit the walls and baffles on the walls. The method produces high growth rates of the order of 1 nm/s. However, without the quite spacious filtering system, only medium quality DLC can be produced.

Furthermore the cathode spot is unstable, resulting in an inhomogeneous ablation of the graphite target. For carbon the spot has a lower resistivity than the surrounding material causing the arc spot to stay at the same position. Countermeasures are re-striking of the arc, using a magnetic field in the cathode region to steer the cathode spot around the cathode surface (see e.g. [46]) and repetitive initiation of the arc by a laser [47].

Pulsed laser deposition

A pulsed laser beam ablates a graphite or glassy carbon target. This method is described in detail in Section 3.1.

Chapter 2

Characterization of DLC films[1]

As shown in Eq. (1.14), the Fermi potential depends on the coherent scattering length of the material in question and on its mass density ρ. Thus, the development of improved DLC coatings has to go in the direction of high sp^3 fractions: the Fermi potential rises from 176 neV for zero porosity graphite (ρ=2.25 g/cm^3) to 305 neV for pure diamond (ρ=3.52 g/cm^3). The sp^3 fraction is referred to as the number of sp^3 hybridized carbon atoms divided by the total number of carbon atoms.

Characterization techniques for DLC are Electron Energy Loss Spectroscopy (EELS, see e.g. [49, 50]), X-ray Photoelectron Spectroscopy (XPS, see e.g. [49, 51]), Auger Electron Spectroscopy (AES, see e.g. [49]), X-ray Absorption Near-Edge Spectroscopy (XANES, see e.g. [52]), Raman Spectroscopy (see e.g. [53, 54]), hardness measurements (see e.g. [55]) and Optical Ellipsometry (see e.g. [56]). Some of these methods are based on opto-electrical or mechanical properties while other methods exploit fundamental properties of the atomic structure like scattering of particles on the lattice. Therefore, it is of principle interest to compare the results of some of them (Visible Raman Spectroscopy (Raman), XANES, XPS, Laser induced surface acoustic wave (LISAW), Optical Ellipsometry) with each other and with those of cold neutron reflectometry, which is closely related to UCN applications.

On a more practical level there is the demand for a well-tested technique which allows reliable measurement of the sp^3 fraction. Many studies, in particular those involving Raman Spectroscopy and XANES have been used to establish a qualitative characterization of the sp^3 fraction, in order to decide whether one DLC film is more 'diamond-like' than another. Conducting a systematic comparison with different methods will allow to (a) derive calibration curves for methods, which do not deliver absolute sp^3 fractions when used individually and (b) find a standard characterization procedure for DLC coatings used in UCN applications. The main objective of the characterization procedure is a quick and precise determination of the Fermi potential of the DLC films.

2.1 Test Samples

A series of eight DLC films with systematically varied sp^3 fraction was produced by physical vapor deposition (PVD) at the Fraunhofer Institut für Werkstoff- und Strahltechnik in Dresden (Germany), using two slightly different deposition methods. The main part of the samples (films 1-6) was coated by unfiltered, laser controlled vacuum arc discharge [47]. Additional samples (films 7 and 8) were produced by magnetically filtered High Current Arc deposition [57]. These methods were described in section 1.5.2. In order to get different film densities, argon was added at different pressure levels: this affects the kinetic energy of the carbon species at deposition and thus the sp^3 fraction [58]. In order to test for effects which depend on the film thickness, films 5 and 6 were produced under identical conditions as films 1 and 2, but are much thinner. Different film

[1] The work in this chapter was previously published; see Ref. [48].

Table 2.1: Deposition method and background pressure used for the production of the different samples and the corresponding film thickness measured by ellipsometry.

Sample	Deposition method	Argon background press. [Pa]	film thickness [nm]
1	LaserArc	0	105.0±0.1
2	LaserArc	0.06	117.6±0.2
3	LaserArc	0.17	118.7±0.2
4	LaserArc	0.33	105.3±0.2
5	LaserArc	0	12.0±0.1
6	LaserArc	0.06	11.3±0.1
7	High-Current Arc	-	45.0±0.8
8	High-Current Arc	-	17.0±0.4

thicknesses were achieved by using different deposition times. The film thickness was measured by ellipsometry (WVASE32 from Woollam Co.), see also [59]. Table 2.1 gives an overview of the process parameters and sample properties.

For all samples spectroscopically pure graphite (total impurity level lower than 5 ppm) was used as target material. The films were deposited on standard silicon wafers, which, because of their smooth surfaces, allow production of thin films that still cover the whole surface. Since the different characterization methods required different sample sizes, the wafers were cut into pieces after deposition. The size of the pieces varied from a few mm^2 to about 4 cm^2. The typical pressure before the addition of argon was less than $3 \cdot 10^{-3}$ Pa. The pulse length of the vacuum arc was about 100 μs, the current was 1300 A. The degree of ionization was close to 100 % and ions had energies up to 50 eV.

The aim was to produce hydrogen-free DLC films with a thickness in the range of 100-300 nm, i.e. like samples 1 to 4. The thinner samples 5 to 8 were produced to crosscheck the results from the thicker samples and to check the depth sensitivity of the different characterization methods.

2.2 Characterization Methods

The characterization methods used determine either the sp^2 fraction (XPS, XANES), the sp^3 fraction (XPS) or the density ρ (neutron reflectometry, LISAW) of the film. The relationship between the sp^3 fraction and the density of (t)a-C films was determined by Ferrari et al. with a linear fit of measured data and found to be [60]:

$$\rho\,(g/cm^3) \;=\; 1.92 \;+\; 1.37 \;\cdot\; k, \tag{2.1}$$

where k is the sp^3 fraction. Assuming the amorphous structure to contain only sp^2 and sp^3 bonds, this equation can be derived from

$$\rho = (1-k)\cdot\rho_2 + k\cdot\rho_3 = \rho_2 + (\rho_3-\rho_2)\cdot k \tag{2.2}$$

where ρ_3 and ρ_2 are the density of a totally sp^3 and a totally sp^2 bonded (t)a-C film, respectively. The corresponding values for the densities are ρ_3=3.29 g/cm^3 and ρ_2=1.92 g/cm^3. Both values for an amorphous structure are well below those for the ordered structure (graphite up to 2.25 g/cm^3, diamond 3.52 g/cm^3).

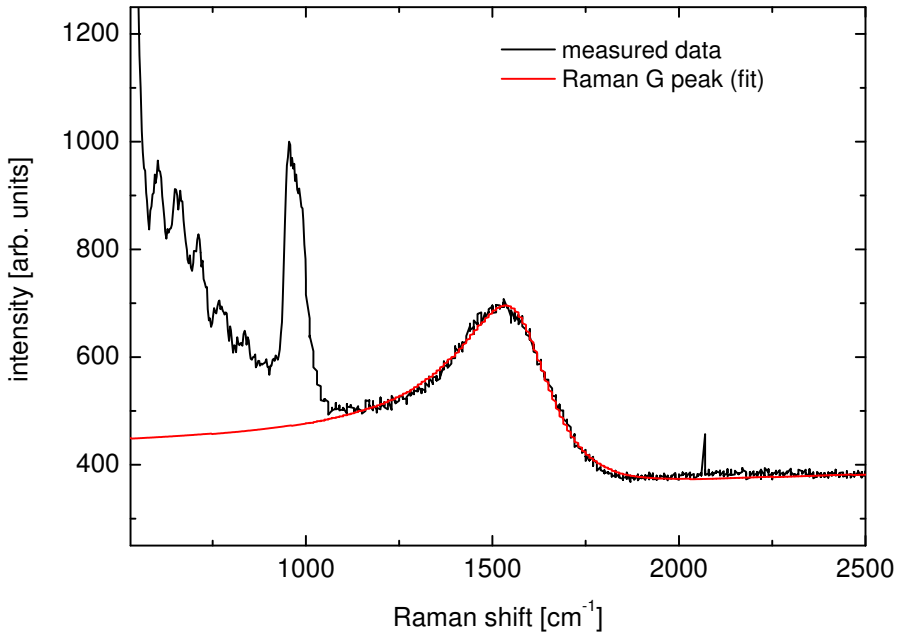

Figure 2.1: The measured Raman data for the DLC sample 3 (measured with the 600 lines/mm grating) including the Breit-Wigner-Fano fit for the G band. No significant D band contribution was found. A linear background was included in the fit. The prominent feature around 1000 cm^{-1} originates from the Si substrate.

Since the Fermi potential (which is the relevant quantity for UCN applications) is calculated from the density ρ, the sp^2 and sp^3 fraction is converted into density for the final comparison using equations 2.1 and 2.2, respectively.

2.2.1 Raman Spectroscopy

Raman spectroscopy can probe the structure of diamond-like carbon films. Depending on the excitation wavelength, the sp^2 or sp^3 bonds may be examined (sp^3 bonds only with UV-Raman). A detailed study of the Raman spectra of various types of amorphous carbon films taken at different excitation wavelengths can be found in [61]. For Raman studies with excitation light in the visible range, the contributions due to sp^2 sites dominate over those of sp^3 bonds, as e.g. investigated in [62].

The Raman spectrum of DLC shows a distinctive broad band with a maximum at ∼1580 cm^{-1}, as shown in Figure 2.1 for sample 3. Standard deconvolution techniques resolve this into two bands, the Raman G band, which is centered around 1500-1600 cm^{-1} and the Raman D band, which is centered around 1350-1400 cm^{-1}. For (t)a-C, the peak intensity (amplitude) ratio $I(D)/I(G)$ is found to be below 20% [53, 61]. It has also been shown that the center position of the G band depends on the sp^3 fraction of the a-C film at short excitation wavelengths [61]. Internal stress in the a-C film may (also) cause a shift of the G band [63, 64]. At excitation wavelengths in the visible range such as 632.8 nm, there is no dependence of the G band position on the sp^3 fraction.

Raman spectroscopy at 632.8 nm excitation wavelength probes the whole bulk of a thin, optically transparent DLC film (up to some micrometers) and also the substrate. Figure 2.1 also shows a contribution from silicon around 1000 cm^{-1}, see also Ref. [65].

The Raman measurements were performed on a Dilor LabRam spectrometer. The excitation light source was a HeNe laser at 632.8 nm with a power of 25 mW. The spectrometer is equipped with two different gratings (600 lines/mm and 1800 lines/mm) and selectable magnification. For this work the 1800 lines/mm grating with magnification of 50 was used for the analysis, as for this

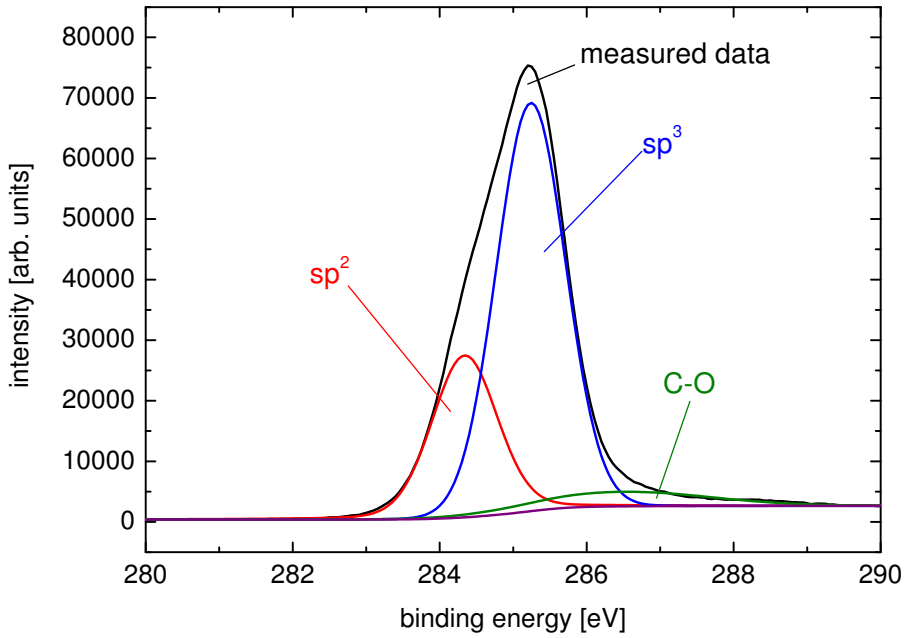

Figure 2.2: The XPS spectrum of DLC sample 3 including its decomposition into a Shirley background and the sp^2 (at 284.4 eV), sp^3 (at 285.2 eV) and C-O (at 286.5 eV) peaks.

configuration the investigated area is comparable to the sensitive area of the other characterization methods ($\lesssim$1 mm^2) at the highest possible wavenumber resolution.

The spectra were fitted with a Breit-Wigner-Fano (BWF) curve to represent the G band, and a Lorentzian (as recommended in, e.g., Ref. [66]), to represent the D band. The BWF curve is given as

$$I(\omega) = I_0 \cdot \frac{(1 + 2(\omega - \omega_0)/Q\Gamma)^2}{1 + (2(\omega - \omega_0)/\Gamma)^2}, \tag{2.3}$$

where ω is the Raman shift, ω_0 the center position, Γ the width parameter and I_0 an amplitude scaling factor. The tilting factor Q is responsible for the typical asymmetric shape of a BWF curve. A linear background was also included in the fit. The BWF curve was found to be centered in the range of 1565-1580 cm^{-1} for all samples. The amplitude of the fitted Lorentzian was found to be very small compared to the amplitude of the G band; $I(D)/I(G)$ was below one percent for all measured samples. All measured samples can therefore be considered to be of good quality in terms of a high sp^3 fraction [61].

The signal-to-background ratio was too low for the samples with film thicknesses below 40 nm, therefore, no Raman results can be given for the samples 5, 6 and 8. The lack of a sufficient Raman signal can be used as a first quality control feature. Films with very small or no Raman signal may be too thin for the use as wall coating material in UCN applications. As mentioned in the introduction, wall coatings should be at least 100 nm thick to prevent additional UCN losses due to an insufficiently thick DLC layer.

2.2.2 X-ray Photoelectron Spectroscopy

X-ray Photoelectron Spectroscopy (XPS) is one of the standard methods for the determination of the sp^2 and the sp^3 fractions in (t)a-C films on an absolute level. The chemical bonds of the carbon atoms show up as a composition of slightly different atomic energy levels. The resulting, broadened C1s peak of DLC films thus contains the sp^2 peak at 284.4 eV and the sp^3 peak at 285.2 eV, which can be deconvolved with good resolution [51], as shown in Figure 2.2. Typically,

there is also a small contribution around 286.5 eV, attributed mainly to C-O bonds at the very surface due to contamination by air exposure, which are potentially also related to some minor contributions from various hydrocarbons. As mentioned above, hydrogen is to be kept at a low level in UCN applications. A larger contribution of the 286.5 eV peak can therefore indicate a contamination of the DLC film that would result in an increased loss probability upon collisions of UCN with the wall material.

The bond fractions are represented by the peak areas. In contrast to other methods, the spectra display only very low background. The determination of the sp^3 fraction is independent of contaminants in the film, to which XPS is very sensitive, as long as their binding energy is not in the range of the C1s peak. In order to find such contamination a XPS survey measurement covering the full energy range up to 1100 eV was performed. No significant contamination was found. Another advantage, particularly for UCN applications, is the fact that the film is probed only to a depth of approximately 3 nm, which is close to the UCN penetration depth upon reflection of about 10 nm. Therefore XPS and UCN probe a similar depth range.

The measurements have been performed on an ESCALAB 220i XL spectrometer using an Al $K\alpha$ monochromatic X-ray source. All samples have been measured as produced, without any special cleaning; only dry air has been used to remove macroscopic dust particles. The pressure in the XPS chamber was below $5 \cdot 10^{-7}$ Pa. The data analysis has been performed with XPSPeak, which is a freely available software package [67]. The peak evaluation followed closely the procedure given in Ref. [51]. After the subtraction of a Shirley background [68], the peaks corresponding to the sp^2, sp^3 and C-O fraction were fitted with symmetric Gaussian-Lorentzian sum functions [69]. It has to be pointed out that although the fit routine computes a normalized minimum of χ^2, its value can be much larger than 1 (up to one order of magnitude). This is caused by the boundary conditions applied, as described below, introducing systematic errors. In addition the χ^2 distribution has not the shape of a parabola as the parameters are not statistically independent of each other. Thus, no information about the fit quality can be derived from the value of χ^2_{min}. The fit parameters from Ref. [51] were refined by using the spectra from all samples simultaneously: The sp^2 peak is constrained to (284.4 ± 0.1) eV (FWHM = (1.0 ± 0.1) eV), the sp^3 peak to (285.2 ± 0.1) eV (FWHM =(1.1 ± 0.1) eV) and the C-O peak to (286.5 ± 0.2) eV (FWHM = (1.5 ± 1.4) eV). The C-O fraction was found to be proportional to the sp^2 fraction for all measured samples. Therefore the carbon atom in the C-O compound is considered to be sp^2 hybridized. For computing the film density the small C-O fraction was therefore assumed to have the same density as the purely sp^2 hybridized sections. Then equation (2.2) extends to

$$\rho = a \cdot \rho_3 + (b + c) \cdot \rho_2, \quad a + b + c = 1 \tag{2.4}$$

where a, b and c are the relative contributions of the sp^3, sp^2 and C-O peak areas. The results including statistical errors are summarized in Table 2.2. There is a general decrease in the sp^3 fraction from samples 1 to 4, clearly related to the decreasing sp^3 fraction, as expected from the production process parameters. The sp^2 fraction in contrast is increasing. The relative number of C-O bonds stays on a low level, in between three and seven percent of the total number of carbon bonds. This is in agreement with the findings of other investigations [70] and can be explained by surface contamination, as mentioned above. Subsequent tests have shown that the C-O peak is significantly increased, up to a fraction of 20%, if the DLC is cleaned with e.g. methanol. Based on the process parameters, sample 5 is expected to have about the same film density as sample 1, and sample 6 the same as sample 2, assuming that the film density of the surface layer is independent of the film thickness. Within uncertainties, the XPS results support this. Samples 7 and 8, however, are of low quality in terms of the film density and are therefore not candidates for a high-quality UCN wall coating.

Table 2.2: Results of the XPS measurements. The density was calculated by using equation (2.1).

Sample	sp^2 fraction [%]	sp^3 fraction [%]	C-O fraction [%]	film density [g/cm^3]
1	21.0±0.4	74.0±0.1	4.9±0.5	2.93±0.01
2	28.4±1.0	66.3±0.8	5.3±0.3	2.83±0.01
3	30.5±0.8	64.2±0.8	5.3±0.1	2.80±0.01
4	34.2±1.5	59.6±1.0	6.3±0.6	2.74±0.01
5	22.8±1.7	73.1±1.4	4.2±0.3	2.92±0.02
6	31.7±1.6	62.5±1.3	5.8±1.1	2.78±0.02
7	43.0±1.6	50.4±1.5	6.8±0.2	2.61±0.02
8	40.4±1.6	51.7±1.4	8.0±0.2	2.63±0.02

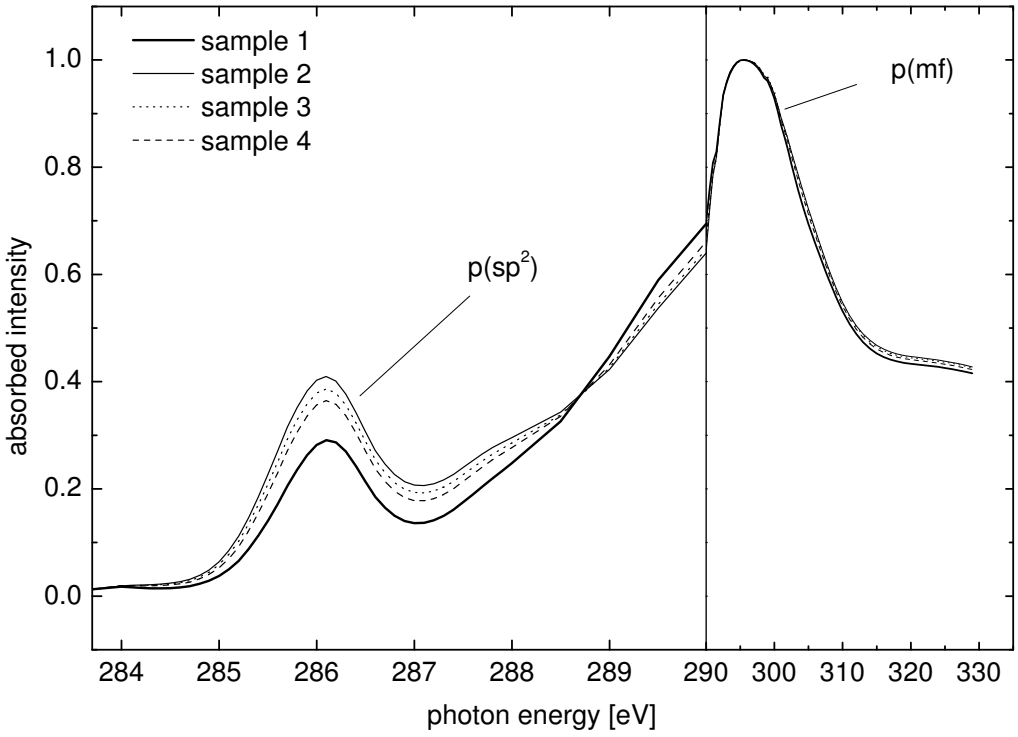

Figure 2.3: The XANES spectra of the DLC samples 1-4. The spectra are normalized to a maximum absorbed intensity (at 295 eV) of 1. Please note the change in energy scale at photon energy of 290 eV.

2.2.3 X-ray Absorption Near-Edge Spectroscopy

X-ray Absorption Near-Edge Spectroscopy (XANES), sometimes also called Near-Edge X-ray Absorption Fine-structure Spectroscopy (NEXAFS), is another method that has been widely used for amorphous carbon film characterization for over a decade [71].

The XANES spectrum of DLC consists of a broad feature around 295 eV and a "pre-edge" peak at 285.5 eV, subsequently denoted by $p(\mathrm{sp}^2)$, as can be seen in Figure 2.3. This first peak in the rising edge of the main feature was identified as a $1s \rightarrow \pi$ transition whereas the main peak

Table 2.3: Results of the XANES measurements. The sp^2 fraction and the corresponding density were calculated using the values for $A(p(sp^2))/A(p(mf))$ of graphite and diamond.

Sample	$A(p(sp^2))/A(p(mf))$	sp^2 fraction [%]	film density [g/cm^3]
1	0.224±0.017	$26.2^{+8.3}_{-2.0}$	$2.93^{+0.03}_{-0.11}$
2	0.271±0.023	$31.7^{+8.4}_{-2.7}$	$2.86^{+0.04}_{-0.12}$
3	0.301±0.024	$35.1^{+8.5}_{-2.8}$	$2.81^{+0.04}_{-0.12}$
4	0.320±0.025	$37.4^{+8.5}_{-2.9}$	$2.78^{+0.04}_{-0.12}$
5	0.227±0.022	$26.5^{+8.4}_{-2.5}$	$2.93^{+0.04}_{-0.11}$
6	0.271±0.022	$31.7^{+8.4}_{-2.6}$	$2.86^{+0.04}_{-0.12}$
7	0.312±0.020	$36.5^{+8.3}_{-2.4}$	$2.79^{+0.04}_{-0.11}$
8	0.311±0.025	$36.3^{+8.5}_{-2.9}$	$2.79^{+0.04}_{-0.12}$

(denoted by $p(mf)$) is caused by both $1s \rightarrow \pi$ and $1s \rightarrow \sigma$ transitions [72]. As $p(sp^2)$ is caused by graphitic bonds only, it can be used as an indicator for sp^2 sites after proper normalization. This fact was used to derive a simple phenomenological analysis prescription, using the fact that the XANES spectra for pure graphite (100% sp^2) and pure diamond (0% sp^2) are known and can be used for absolute normalization. The peak amplitudes of $p(sp^2)$and $p(mf)$, $A(p(sp^2))$ and $A(p(mf))$, were extracted; the ratio $A(p(sp^2))/A(p(mf))$ was calculated and compared to the calculated curve obtained from the graphite and diamond reference spectra [73]. This curve was assumed to be a linear function defined by the graphite and diamond values for $A(p(sp^2))/A(p(mf))$ and was found to be

$$sp^2 = \frac{A(p(sp^2))}{A(p(mf))} \frac{1}{0.8555}. \tag{2.5}$$

While $A(p(mf))$ is simply the maximum value around 295 eV, the determination of $A(p(sp^2))$ requires to consideration of the background induced by the tail of $p(mf)$. For this, the spectrum was fitted by a sum of Gaussians, following the procedure given in Ref. [73]. In order to account for impurities, which are neither sp^2 nor sp^3 hybridized, but nevertheless contribute to $p(mf)$, the maximum C-O peak contribution determined by XPS was used to enlarge the uncertainties of the sp^3 fraction, calculated as sp^3= 1 - sp^2, to lower values. This leads to asymmetric errors for both the sp^3 fraction and the corresponding film density.

The XANES measurements were performed at the SIM beamline [74] of the Swiss Light Source (SLS) at PSI. The spectra were acquired in the total electron yield mode measuring the sample photo current with an electrometer. The depth sensitivity of XANES is limited by the electron escape depth and is typically around 5 nm. Therefore XANES is similarly sensitive to surface contamination as other X-ray methods like XPS. The results are given in Table 2.3. The full spectra of samples 1 to 4 are shown in Figure 2.3. The film density was calculated using Eq. (2.2) and sp^3=1-sp^2. Samples 1 to 4 show clearly a systematic decrease of the sp^3 fraction and of the film density, as expected from the process parameters. As the results for samples 1 and 5 as well as for samples 2 and 6 agree within statistics, it can again be concluded that the density in the surface layer of the film does not depend on how thick the total film is.

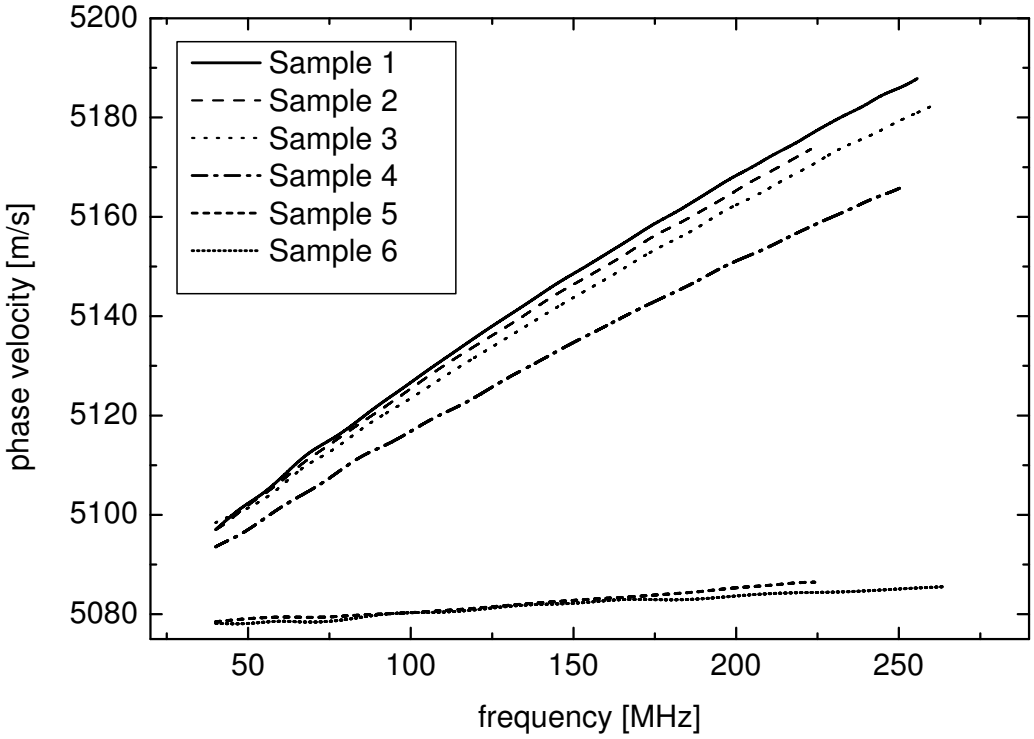

Figure 2.4: LISAW frequency spectra (dispersion curves) for the samples 1-6. See text for explanation.

2.2.4 Laser induced surface acoustic waves

Mechanical properties like hardness and Young's modulus are directly related to the density of DLC and their determination can therefore be used to measure the density [41]. Here, Young's modulus was determined by measuring the phase velocity of laser-induced surface acoustic waves (LISAW) as a function of the frequency (dispersion curve) [75, 76]. Fitting the dispersion curve yields Young's modulus of the film and of the substrate. For DLC, Young's modulus increases with the sp^3 fraction [41, 77, 78]. Details of this method and its application to (t)a-C films are given in Refs. [59, 76]. On this basis a commercially available device, called LAwave [79], has been developed which was used here. It is equipped with a N_2 Laser at a wavelength of 337.1 nm and a wide-band piezoelectric transducer fixed on the sample surface at a distance of several millimeters from the laser focus.

At film thicknesses below about 200 nm the dispersion curve is close to linear (for homogeneous film density) and allows determination of Young's modulus if the film thickness is known [76]. The latter was determined independently by ellipsometry (see [59]), as mentioned above. From Young's modulus the density of a thin DLC film can then be extracted using an empirical relationship [76]. Figure 2.4 shows the dispersion curves for the first six samples. The close-to-ideal linearity indicates that the condition of density homogeneity is nearly fulfilled. Table 2.4 shows the measured Young's moduli as well as the corresponding film densities and sp^3 fractions (calculated via Eq. 2.2). The uncertainties given include statistical errors as well as an estimate of the systematic uncertainties which originate mainly from the thickness measurement (see Table 2.1). The density and consequently the sp^3 fraction decrease with sample number. For the samples 1 to 4 this is as expected, i.e. caused by the argon background gas addition. For the thinner films, namely samples 5 and 6, lower densities have been determined. However, as samples 1 and 5 as well as 2 and 6 have been deposited with the same process parameters, the observed difference in the film density

Table 2.4: Results of the LAWave measurements. The film density was calculated using the calibration function published in Ref. [76]

Sample	Young's modulus (GPa)	film density [g/cm^3]	sp^3 fraction [%]
1	710±1	3.196±0.004	93.1±0.3
2	633±1	3.083±0.005	84.9±0.4
3	612±1	3.050±0.005	82.5±0.4
4	591±1	3.017±0.003	80.1±0.2
5	543±4	2.936±0.008	74.2±0.6
6	485±4	2.833±0.015	66.6±1.1
7	458±1	2.783±0.015	63.0±1.1
8	358±1	2.583±0.014	48.4±1.0

of about 0.25 g/cm^3 requires explanation (see section 2.3).

2.2.5 Cold Neutron Reflectometry

As described in the introduction, neutrons are reflected from certain materials if the velocity component normal to the surface is less than the critical velocity

$$v_c = \sqrt{\frac{2 \cdot V_F}{m_n}}, \tag{2.6}$$

V_F being the Fermi potential and m_n the neutron mass. Cold neutrons with typical velocities of about 500 m/s are thus reflected for angles below ∼1 degree and transmitted for larger angles (see Ref. [80]). The exact determination of the critical reflection angle allows to extract the Fermi potential and, as a consequence, the density. A distinct advantage of this method for characterization of DLC as wall coating material for UCN applications is that it makes use of neutrons which probe the proper depth range of the samples, around 10 nm. It is therefore a suitable characterization method for UCN wall coatings [80].

The measurements were performed at the AMOR instrument [81, 82] of the Swiss Spallation Neutron Source (SINQ) at PSI. The spectrometer was run in time-of-flight (TOF) mode. This means that the time distribution of the detected neutrons is measured and the velocity obtained from the distance between the TOF chopper and the detector. Figure 2.5 shows typical reflectivity spectra as a function of the velocity component normal to the reflection surface. It can be easily seen, e.g. for samples 1 and 7, that the reflectivity decreases rapidly for velocities above about 6.5 m/s, corresponding to a Fermi potential of 220 neV or a film density of 2.55 g/cm^3. At a more elaborate level, the reflectivity curve can be predicted by dispersion theory (as originally done for X-rays [83]) and fitted to the measured spectrum in order to extract the film density, thickness and roughness.

The reflectivity curves were fitted with the freely available software Parratt32 [84]. A single film layer model was used. The film thickness obtained from optical ellipsometry was used as fixed parameter. Fit parameters were the roughness of both substrate and film and, most importantly, the scattering length density (SLD) $N \cdot a$ of the film. It is the product of the scattering length a, which is 6.646 fm for carbon [85], and the particle density N (for which diamond has the highest value of all known materials). Therefore from the SLD and knowing the material composition one can derive the particle density and consequently the mass density and the sp^3 fraction, respectively.

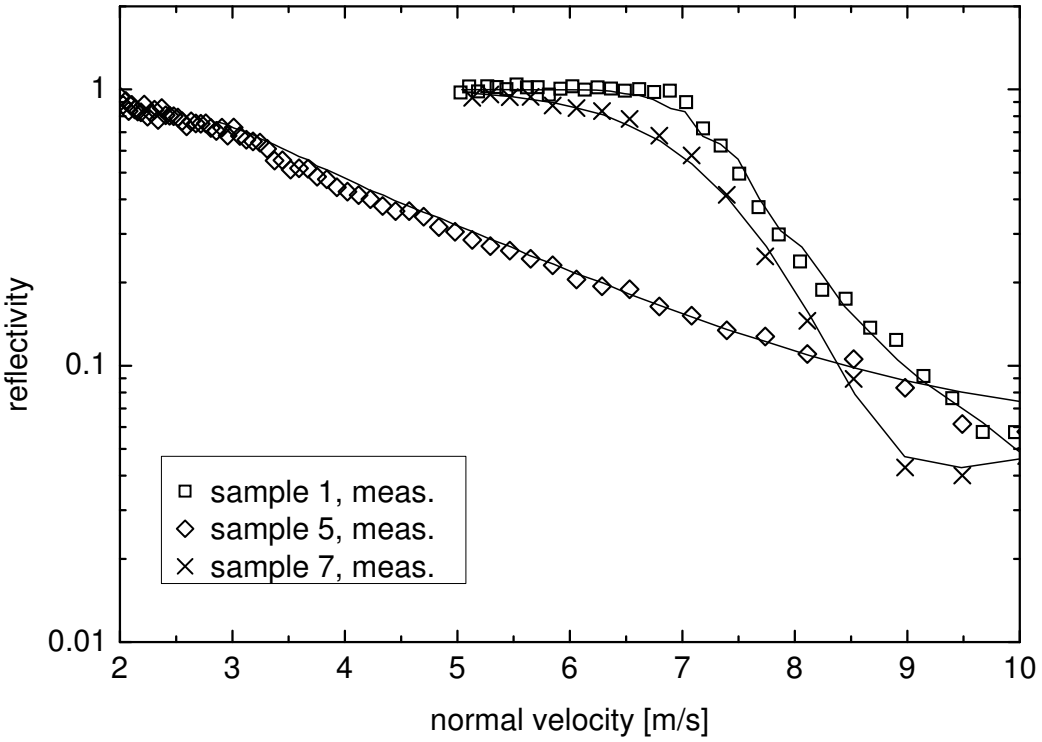

Figure 2.5: Cold neutron reflectivity of selected DLC samples as a function of the normal velocity component. The solid lines denote the corresponding reflectivities obtained by fitting various model parameters such as the SLD, layer thickness and layer roughness.

The scattering length values of air and of the silicon substrate were set to literature values [85]. Also the instrument resolution was taken into account. However, the uncertainties of the cold neutron reflectometry measurement depend on the flatness of the investigated samples. Although the silicon wafers used have a small roughness, this does not imply a correspondingly high flatness over the whole coated sample. The unevenness of the sample decreases the resolution of the neutron spectrometer. This leads to increased uncertainties in the fitting process and consequently to large uncertainties in the final results. The values for χ^2_{min}, normalized by the degrees of freedom (DOF), are on the level of 0.1 or slightly below. These low values are due to the modification of the χ^2 function. The modification, which is commonly used in the neutron reflectivity community, consists of the exchange of the error of the measured value in the χ^2 function by the measured value itself. It is done in order to get converging fits for reflectivity data, which decays over orders of magnitude. The measured reflectivity curves, as well as the corresponding fits, are shown in Figure 2.5, the results of the curve fitting are summarized in Table 2.5.

The results for the thicker samples (1 to 4) show a systematic decrease with sample number. The curves of the thinner samples (5, 6 and 8) display an almost exponential behavior over the entire range measured which can only be explained if one assumes that the substrate roughness is of the order of the film thickness. This is the case for the thin samples, as the averaged roughness, R_a, of the silicon substrates was determined independently (with a Perthometer S3P) as close to 10 nm. As the film thickness of sample 7 is somewhere in between that of the first four samples and the thin ones, this sample only shows an increased smoothing around the critical velocity.

Table 2.5: Results of the cold neutron reflectivity measurements. The film density and the corresponding sp^3 fraction were calculated from the particle density which was derived from the scattering length density.

Sample	Scattering length density [$Å^{-1}$]	film density [g/cm^3]	sp^3 fraction [%]
1	$(1.03 \pm 0.06) \cdot 10^{-5}$	3.10±0.17	86±12
2	$(1.03 \pm 0.06) \cdot 10^{-5}$	3.10±0.17	86±12
3	$(9.95 \pm 0.52) \cdot 10^{-6}$	2.99±0.15	78±11
4	$(9.56 \pm 0.52) \cdot 10^{-6}$	2.87±0.16	69±11
5	$(9.8 \pm 1.1) \cdot 10^{-6}$	2.93±0.34	73±25
6	$(9.21 \pm 0.53) \cdot 10^{-6}$	2.76±0.16	62±12
7	$(9.23 \pm 0.89) \cdot 10^{-6}$	2.77±0.27	62±19
8	$(8.17 \pm 0.86) \cdot 10^{-6}$	2.45±0.26	39±19

Table 2.6: Results of the optical ellipsometry measurements. The density was calculated by using equation (2.1).

Sample	sp^2 fraction [%]	sp^3 fraction [%]	film density [g/cm^3]
1	5.73±0.02	94.27±0.02	3.211±0.001
2	9.26±0.05	90.73±0.05	3.163±0.002
3	10.17±0.10	89.83±0.1	3.151±0.004
4	11.58±0.2	85.74±0.06	3.043±0.004

2.2.6 Optical Ellipsometry[2]

In addition to the previously described five methods, ellipsometric measurements were performed on samples 1-4 by Budai *et al.* This method measures the change in the polarization of light which is reflected from the sample under investigation. Measuring at different angles and/or different wave lengths allows to extract information about material properties as the refractive index or the thickness of a film. This extraction is done by using fitting models. Details about the method itself and the fitting models used can be found in Ref. [86]. Table 2.6 shows the results.

2.3 Comparison of the different methods

Based on the sub-implantation model for the DLC growth mechanism (see Refs. [87–89]), the results are best discussed by considering the films to have two layers: (i) a carbon bulk layer with homogeneous DLC structure and (ii) a surface layer with probably reduced density, which also contains some contamination (e.g. oxygen, hydrocarbons). From this picture one might expect differences when comparing the results of methods with different depth sensitivity (surface sensitive XPS and XANES versus bulk sensitive LISAW, Raman and Optical Ellipsometry) and samples with various film thicknesses.

[2]Not included in the original publication [48].

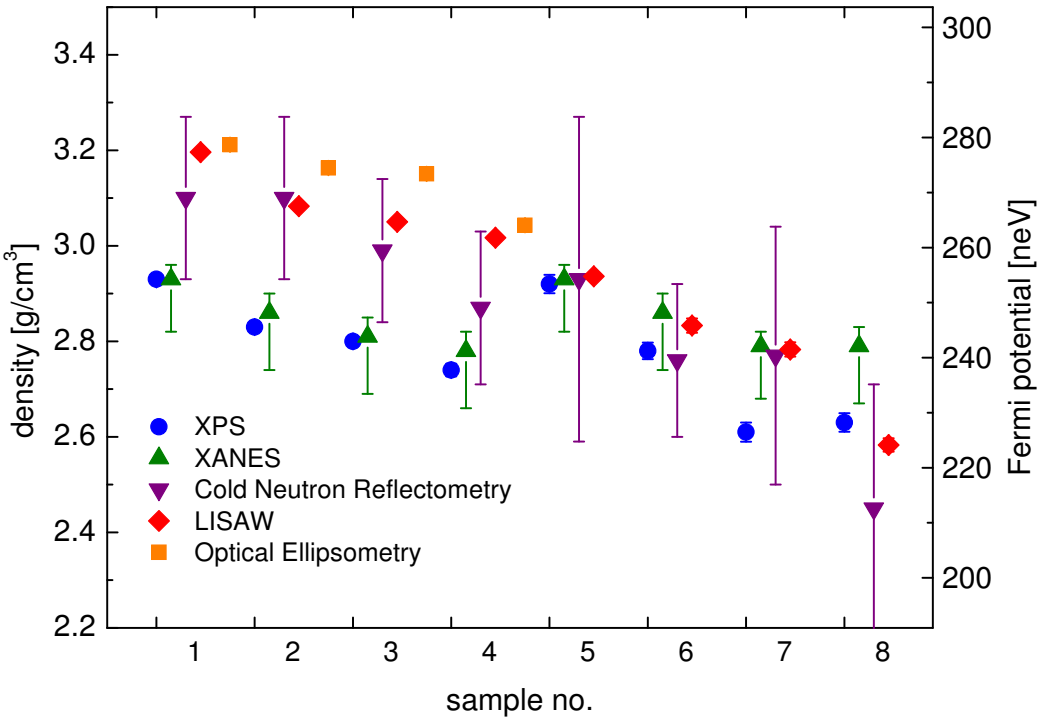

Figure 2.6: Summary of the results of all characterization methods for all samples.

The results from the previous section, expressed in terms of density and the corresponding Fermi potential, are summarized in Figure 2.6. For further discussion of the results and, particularly, their impact on the desired standard characterization procedure, the samples were split into three groups: (a) samples 1 to 4, with thickness of the order of 100 nm, samples 5, 6 and 8, with a thickness in the order of 10 nm, and sample 7 with an intermediate thickness of about 50 nm.

(a) The bulk sensitive methods LISAW and Optical Ellipsometry show sp^3 fractions which are up to 20% higher than those obtained by the surface sensitive methods XPS and XANES. This is to be expected from the sub-implantation model, although the difference is quite large. The results obtained by XPS and XANES are consistent within their uncertainties. The results from cold neutron reflectometry lie in between those of the surface sensitive methods and the bulk sensitive methods. Although the uncertainties in cold neutron reflectometry results are large, the method is useful for cross-checking and for obtaining more direct data about the Fermi potential of the DLC coating. From the results of the first four samples it is concluded that the ideal characterization procedure for DLC as wall-coating material for UCN application should include a surface sensitive method, in order to find the minimal density of the coating, i.e. the density of the surface layer. As both, XPS and XANES, probe about the same depth, the method, which determines the sp^3 fraction directly and which has the smaller uncertainties, is to be preferred. This method is XPS.

(b) The results for the thin samples are in reasonable agreement. There is no systematic difference between bulk-sensitive and surface-sensitive methods, also the results of the cold neutron reflectometry are consistent with those of the other methods. This can be easily understood if one considers that for thin coatings one cannot distinguish between surface layer and bulk as they are (nearly) identical. Such a thin coating has about the same density as that of the surface of a thicker coating would have, prepared with the same process parameters. Thus, the lower densities obtained by LISAW for samples 5 and 6 compared to samples 1 and 2, which were produced using the same process parameters, are due to the reduced film thickness. Using too thin coatings for

UCN applications would result in an increased transmission through the film and, consequently, to an increased loss probability.

(c) Sample 7 (about 50 nm thick) shows results that lie somewhere in between the 100 nm and the 10 nm thick films. There is a slight difference between surface sensitive methods and bulk sensitive methods, however, much smaller than for the thick samples. The difference for the sp^3 fraction is of the order of 10%. Thus, sample 7 does not reveal new information but supports the findings in categories (a) and (b).

Chapter 3

DLC Coating of Tubes

It was one objective of the project described in this work to build up a coating facility for the production of high-quality UCN guides. As described in the introduction, good UCN guides have a high Fermi potential and a low loss probability; two criteria which are well satisfied by DLC. But not only the loss probability per wall collision plays an important role. Another important parameter for the quality of UCN guides is the area of slits in the guides, where neutrons can escape, relative to the reflecting portion of the walls. The loss probability caused by slits must not be larger than the loss probability caused by the material, i.e. of the order of 10^{-4} for high-quality UCN wall coatings. The area of the slits is minimized for cylindrical tubes, as it is chosen for the setup described in this chapter. A conservative estimation for the average width of the slits between two guide sections is 0.1 mm. This leads to a length for each section of 1 m which the coatings facility should be able to process.

The deposition method used in the setup built at PSI is PLD, based on promising results obtained with a similar setup [91] as the one described in this work. Pulsed laser deposition at short wavelength is also the method of choice due to the fact that thin DLC films with a high sp^3 fraction and of uniform thickness can be produced [90].

As described in the introduction, UCN guides with high transmission need to have a high Fermi potential. For an amorphous material with fixed chemical composition, the highest possible Fermi potential can be achieved by maximizing the density. In terms of DLC this means a maximized sp^3 fraction. Pulsed laser deposition is known to produce higher sp^3 fractions at shorter wavelengths [92]. The shortest wavelength for which lasers with high power and optical components including mirrors are commercially available, 193 nm, was used.

3.1 Pulsed Laser Deposition (PLD)

Pulsed laser deposition (PLD) is nowadays a common method for the production of thin films. Many standard textbooks have been written about PLD, see e.g. Ref. [93].

3.1.1 Short history and overview

The first experimental studies on the interaction of intense laser beam with solid surfaces [94, 95], liquids [96] and gaseous materials [97] were performed in 1963. The first deposition of a thin film by intense laser radiation was accomplished in 1965 [98]. Within the following years only little progress was made until a major milestone was achieved in the middle of the 1970s, when electronic Q-switches, developed since the begin of the 1960's (see e.g. Ref. [99]), became reliable. It allows for short pulses with very high peak intensity. The final breakthrough for the method was the successful growth of high-temperature superconductors by PLD [100].

Pulsed laser deposition is conceptually very simple. The schematic overview in Figure 3.1

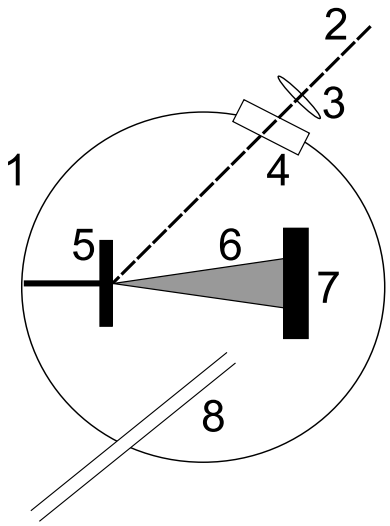

Figure 3.1: Principle of a general PLD setup: [1] vacuum chamber with pump, [2] pulsed laser beam, [3] focusing lens, [4] entrance window, [5] target on target holder, [6] target plume, [7] substrate on substrate holder, [8] gas pulser.

shows a general PLD setup. It consists mainly of a target (item 5 in Figure 3.1) and a substrate (item 7), usually each mounted onto a dedicated holder inside a vacuum chamber (item 1). A high-power pulsed laser beam (item 2) is used to evaporate the target material, forming a cloud of emitted particles which builds the so-called *plume*. Since the plume expands predominantly normal to the target surface, the substrate to be coated is typically mounted opposite to the target. In order to maximize the beam power, the beam is focused by a lens or a more complex optical system (item 3) and enters the vacuum chamber through an entrance window (item 4) of 1/8" thickness. Certain gases can enhance the plasma or the formation of the desired thin film on the substrate. Thus, they are added in pulsed mode by a gas pulser or as a constant background atmosphere.

Different types of lasers are used for PLD, depending on the application and the material to be ablated, respectively. Used wavelengths range from vacuum ultraviolet (157 nm, excimer laser) to infrared light (10.6 μm, CO_2 laser). Typical pulse lengths are 10-50 ns for ns-PLD at repetition rates up to 100 Hz and 30 fs-30 ps for the more recently developed fs-PLD at repetition rates of up to several kilohertz. For PLD of DLC, wavelengths between 193 nm and 1064 nm are commonly used (see e.g. Ref. [90]). Power densities of 10^8-10^{11} W/cm^2 are needed for the deposition of ta-C, depending on the wavelength used.

Pulsed laser deposition can be described as a three-step process: evaporation of the target material, transport of the vapor plume and film growth on the substrate. The following subsections describe the mechanisms during evaporation, with a special focus for graphite, during the transport of the evaporated material and during the deposition of DLC.

3.1.2 Ablation mechanisms

Sputtering of a material with different kinds of particles (photons, electrons, ions, etc.) leads to particle emission which is termed *ablation* or *desorption*. For PLD there are four *primary sputtering mechanisms*: thermal, electronic, exfoliational and hydrodynamic sputtering.

For sputtering with pulses of particles rather than with a single particle, the number of emitted particles from the target material may be sufficiently high to allow interaction between them. If the density of the ablated material is small enough, the individual particles expand in free flight. In this case the expansion is described by a formalism which is appropriate to the way the material

was ablated, i.e. to the *primary mechanism*. If interaction between the emitted particles is non-negligible due to a high density of the ablated material, the expansion of the emitted particles is dominated by these interactions which can be termed *secondary mechanisms*.

Primary mechanisms

In the following the primary mechanisms [101] appropriate to incident laser pulses are considered.

Thermal sputtering: The incident laser energy is (partially) absorbed and the target material is locally heated above the melting or boiling point. This leads to a transition of the solid material into liquid or gas phase. As there is no liquid phase for carbon (at least not at low pressure) only the direct transition from the solid to the gas phase is possible. The absorption of a material depends on the material-dependent absorption coefficient, the incident wavelength and the angle of incidence.

Electronic sputtering: It is a group of processes which have the common feature of involving some form of excitation or ionization. The target material can e.g. become locally ionized resulting in large Coulomb forces between the ions which lead to an explosion-like behavior of the ablation.

Exfoliational sputtering: A high power pulsed laser beam can induce thermal shock in the target material. This allows the formation of cracks which can lead to the detachment of flakes. It is a strong source of so-called *particulates* if the thermal stress, i.e. $\frac{E\Delta L}{L_0}$ with Young's modulus E and the relative thermal expansion $\Delta L/L_0$, is high. This is the case for carbon.

Hydrodynamic sputtering: It is an umbrella term for processes in which droplets, i.e. small quantities of molten target material, are formed and leave the target surface. Usually droplets are formed at spots where an elevation existed before the laser pulse arrived. As carbon has no liquid phase at low pressure no droplets are formed.

Secondary mechanisms

Four types of secondary mechanisms exist [102]: Outflow and effusion with either reflection or re-condensation. They have in common that evaporated material expands into the vacuum of the deposition chamber. Part of the various particles in this gas volume reach the target surface again. There, they are either reflected or they re-condensate. The transition of the target material from solid to gas phase by one of the primary mechanisms takes place during the time the laser pulse interacts with the target surface, i.e. during the pulse length. Outflow continues until the gas volume has fully expanded. Effusion stops after a certain time, which can be understood as that a wall, which became porous to allow effusion, is resealed.

Ablation threshold

For many materials the removal rates are found to be only significant above a certain energy level which can be referred to as the ablation threshold energy density, measured in $\mathrm{J/cm^2}$. If the target material is heated slow enough to allow normal phase transition, the ablation of the material depends on the vapor pressure described by the Clausius-Clapeyron equation

$$\frac{\mathrm{d}P}{\mathrm{d}T} = \frac{L}{T\Delta V}, \tag{3.1}$$

where P is the pressure, T the temperature in Kelvin, L the latent heat and ΔV the volume change of the phase transition. Rapid energy absorption, can lead to super-heating, i.e. to heating above

boiling temperature, and subsequent explosive phase transition (see e.g. [106]). This happens at a certain laser energy density, where the laser heating rate (about 10^{11} K/s) becomes higher than the thermal diffusion rate and radiation losses, and evaporation proceeds nonlinearly.

3.1.3 Plasma organization, transportation and characterization

During the initial expansion the plasma, produced by PLD and only partially ionized, has a temperature of up to 10'000 K. Inverse-Bremsstrahlung absorption of the laser light in a free-free transition of an electron-ion pair is thought to be the mechanism for heating the plasma to such high temperatures [93].

Different models exist for the expansion and transportation of the plasma, e.g. the space-charge acceleration model for the ions in the plume [103–105]. This model is based on the much higher mobility of the electrons compared to that of the ions and neutrals in the plume. This leads to a collective motion of the electrons away from the ions and creates a strong space-charge field. This field attracts the ions and accelerates them accordingly to their charge $n \cdot e$, where n is the ionization number. Consequently, a typical plasma shows multiple zones with different fractions of electrons, ions and neutrals. The existence of fast neutrals at the plume front can be explained by e.g. recombination of ions and electrons. Different diagnostic techniques exist for the observation of the plume conditions and for the plume characterization. In the following a description of some of them is compiled.

Quadrupole mass spectroscopy is able to select ions of a certain mass and to determine the kinetic energies of the selected ions by their time of flight. The mass spectrometer has to be mounted in the flight path of the ions, which makes simultaneous deposition and plume characterization impossible (see e.g. Ref. [107]).

Ion probes, especially electrostatic ones, are among the oldest plasma diagnostics. They are quite inexpensive and rugged and give the possibility of local characterization. Its simplest form is a wire tip with an electrostatic bias to select the kinetic energy range. The resulting current is displayed on an oscilloscope. Multiple ion probes can be used in time-of-flight mode. Although they do not provide information about which species are included in the plasma, they are the most versatile in-situ monitor for the overall plasma conditions. Due to their small cross section they can be used even during deposition (see e.g. Ref. [104]).

Optical emission spectroscopy yields information about the plume composition as different species show different optical transitions. In the simplest form a simple photo-diode records the entire visible plume emission for each laser shot. More complex instruments allow for a time and/or space resolved analysis of the plume. Details of optical emission spectroscopy during the ablation of graphite can be found in e.g. Ref. [108]. Optical emission spectroscopy was performed during some pretests for the Tube PLD setup (see Section 3.2).

Photography and imaging with high-speed cameras can provide two-dimensional snapshots of different stages of the plume transportation.

Ambient gases present during PLD can have many effects on the plume evolution, all of them achieved by scattering of the ablated species with background gas molecules. The most important effects are attenuation, thermalization and chemical reactions of the ablated species. The latter is usually referred to as plasma enhancement, which is an important concept for the deposition of certain materials but is not desired for the deposition of DLC. As it is described in the next section high-quality DLC is achieved by the deposition of particles with relatively high kinetic energies compared to the typical energy distribution achieved by the ablation of graphite with a laser. Thus, attenuation of the plume is not desired for the deposition of a high-quality DLC film. Consequently, the pressure inside the deposition chamber has to be as low as possible, but at least

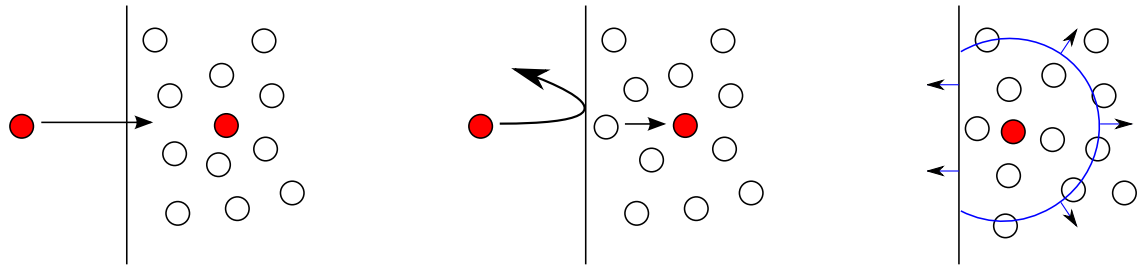

(a) direct penetration (b) knock-on penetration (c) relaxation

Figure 3.2: Deposition mechanism for DLC: Concepts of the subplantation model.

below 0.1 Pa, as the mean free path length, λ, of carbon ions in a thin argon atmosphere at 0.1 Pa is of the order of 30 cm. The mean free path length is given by $\lambda = \frac{1}{N\sigma}$, where N is the particle density of the gas and σ the cross section for collisions between carbon ions and argon atoms. The cross section can be estimated by treating the atoms as hard spheres [109] with the corresponding atomic radii e.g. taken from Ref. [110].

3.1.4 Deposition mechanisms for DLC

From the variety of the mechanisms for the deposition of different materials, the description in this section deals with ones relevant to DLC. The most important property of DLC is its high density, achieved by a large fraction of sp^3 bonds. Thus, a model of deposition mechanisms for DLC should explain how different fractions of sp^2 and sp^3 bonds are achieved for different deposition parameters. One of the most accepted models is the so-called subplantation model [41].

The basic idea of the low energy subsurface implantation model, subsequently denoted as *subplantation* model, is the partial sub-surface growth of the DLC film. Carbon ions and neutrals with kinetic energies high enough, around 100 eV, can penetrate the existing DLC surface and increase the local film density and lead to an increased sp^3 fraction. The penetration can be either direct or by a knock-on process, as shown in Figure 3.2a and b. At kinetic energies substantially higher than the optimal 100 eV, the ions lose their energy not only by penetrating the surface but also by energy dissipation as phonons (heat). A relaxation phase producing lower local density leads to an increase of the sp^2 fraction, as indicated in Figure 3.2c. Very low kinetic energies of the carbon ions lead to a simple sticking to the surface resulting in a low density and therefore preferred sp^2 hybridization.

Although the ideal kinetic energy of 100 eV is well below the binding energy of carbon, 284-285 eV, re-sputtering of deposited carbon may be significant if the kinetic energy distribution of the ions is broad and includes energies above the binding energy of surface atoms, i.e. above the sputtering threshold.

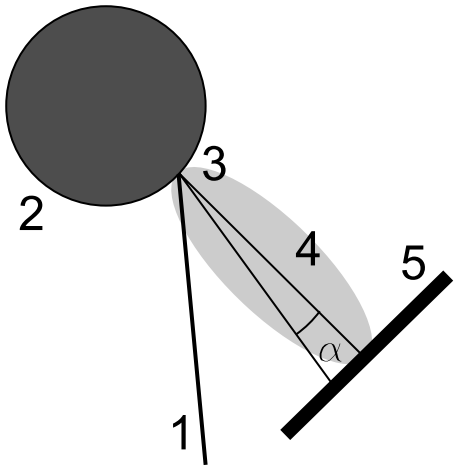

Figure 3.3: Schematic drawing (view from top) of the ablation situation during the pretests in the small PLD chamber: [1] incident laser beam, [2] cylindrical graphite target, [3] target spot, [4] plume, [5] substrate.

3.2 Pretests in a small PLD setup with incident wavelengths of 248 nm and 266 nm[1]

An existing PLD setup at PSI, which is described in Ref. [112], was used to produce flat test samples of 10 × 10 mm^2 and 20 × 20 mm^2 size. The DLC films were deposited onto silicon wafers and highly polished stainless steel plates. The substrate was mounted on a holder which was rotated during deposition. A spectroscopically pure graphite target from Minteq Int. Inc. (total impurities <10 ppm, 0.54 ppm Si, <5 ppm Ta, <0.5 ppm Hg, all other elements <0.1 ppm) with cylindrical shape and a density of 2.21 g/cm^3 was used. Figure 3.3 shows a scheme of the ablation situation. The laser beam (item 1) was aligned to hit the target (item 2) such that the resulting plume (item 4) was directed to the substrate. For the production of the samples, an excimer laser (Lambda Physik LPX105E, KrF, 248 nm) and a Nd:YAG-laser with frequency quadrupling (266 nm) at repetition rates of 5 Hz and 10 Hz were used. The samples were produced at pressures in the range of 10^{-5}-10^{-3} Pa. In order to study the ionic composition of the ablation plume, emission spectra of the plume were recorded with a spectrometer (ARC SpectraDrive). Figure 3.4 shows an emission spectrum recorded during DLC deposition at 266 nm wavelength. The lines at 391.2, 426.1 and 512.7 nm were identified to originate from C^+ ions and those at 406.5, 417.7, 451.5 and 464.4 nm from C^{2+} ions (see e.g. Ref. [113]). The small feature at ∼530 nm was identified as neutral carbon line. Following the characterization procedure described in Chapter 2, the DLC films were measured with Raman spectroscopy, XPS and cold neutron reflectometry (only the 20 × 20 mm^2 samples) using the experimental equipment described in Chapter 2.

Various process parameters were systematically varied and the sp^3 fraction of samples produced at different values of these parameters was determined. The values obtained by cold neutron reflectometry are consistent with those measured with XPS.

The dependence of the sp^3 fraction on the distance between target and substrate was investigated firstly. A constant but low film density (due to the settings of other process parameters in this series) was observed for distances in the range of 2.5 cm - 5.5 cm.

The second parameter studied was the laser power density on the target. Figure 3.5 shows the XPS spectra of four samples deposited at 248 nm wavelength with different laser power densities while all other process parameters were kept constant. The extracted sp^3 fractions range from 22% for $1.3 \cdot 10^8$ W/cm^2 to 34% for $2.7 \cdot 10^8$ W/cm^2. Theses power densities are close to the maximum

[1]The work in this section was previously published; see Ref. [111].

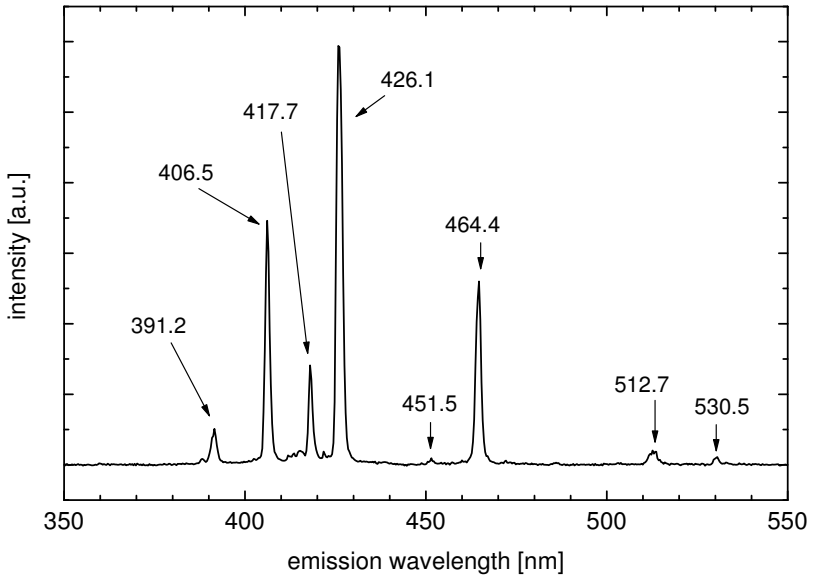

Figure 3.4: Emission spectrum for PLD of DLC at 266 nm wavelength. For details see text.

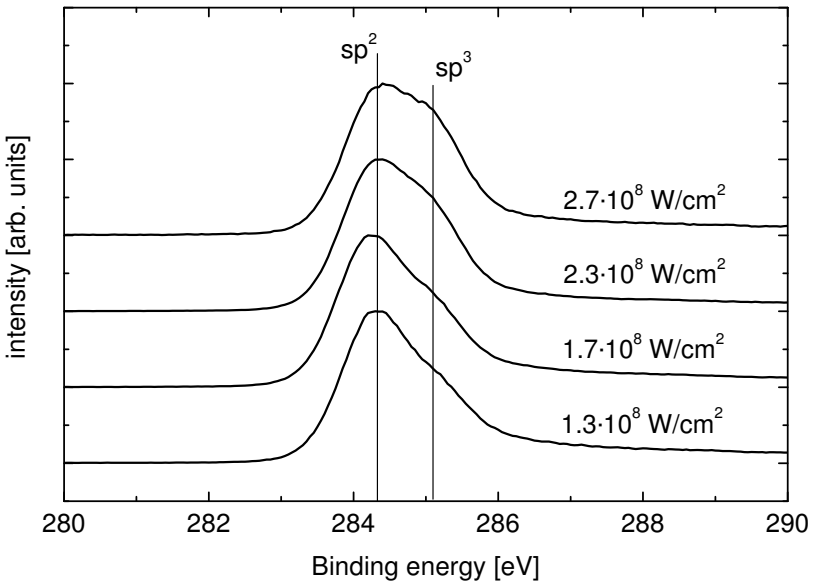

Figure 3.5: XPS spectra of four samples deposited with different laser power densities. An increase of the sp^3 fraction at increasing laser power density was found. The values for the sp^3 fraction range from 22% for the lowest laser power density to 34% for the highest laser power density. The sp^2 and sp^3 binding energies are indicated by the vertical lines at 284.4 eV and 285.2 eV. The increased sp^3 fraction for higher laser power density is indicated by the hump at binding energies around 285 eV.

laser power density which could be achieved with the used excimer laser. For the production of these samples a focal length of 50 cm was used. Using a significantly larger focal length would lead to a laser power density well below the ablation threshold for a highly diverging laser beam as the one of an excimer laser (up to a few mrads). However, the highest laser power possible in connection with an optimally focussed beam led to an undesired deposition of graphite particulates. Exchanging the graphite target with a target of the same shape but made out of glassy carbon

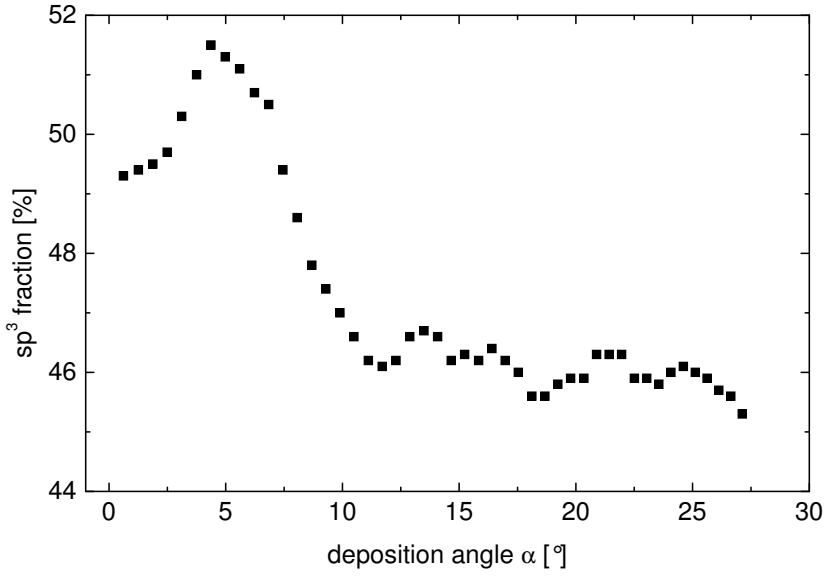

Figure 3.6: Diamond fraction as a function of the deposition angle α, measured with XPS.

did not improve the situation although other studies observed such an improvement [114].

The third process parameter studied was the pressure in the deposition chamber during the laser ablation process. Samples were deposited at pressures from $\sim 3 \cdot 10^{-5}$ Pa to $3 \cdot 10^{-3}$ Pa. The deposition rates were found to be similar for the different pressures used, e.g. about 0.2 nm/s for both $5 \cdot 10^{-}5$ Pa and $1.5 \cdot 10^{-}3$ Pa, where the target to substrate distance was 4 cm and the excimer laser was used. As shown in Section 3.1.3, collisions with residual gas molecules are not to be expected for pressures well below 0.1 Pa as the ones used.

Also investigated was the film density as a function of the deposition angle α, which is shown in Figure 3.3. The angular dependence was investigated by measuring a series of points on the diagonal from edge to the center of a sample with XPS. The target to substrate distance was about 25 mm in order to cover a large solid angle around the target spot. The obtained sp^3 fractions are plotted in Figure 3.6. The highest values for the sp^3 fraction were reached for positions slightly off center, indicating a non-optimal alignment of the target plume. For $\alpha \leq 5°$, the sp^3 fraction is up to 5% higher than for larger deposition angles. Thus, the highest value of the sp^3 fraction was found for deposition angles close to the normal of the target surface.

No significant difference in the sp^3 fraction was found for samples deposited with fixed process parameters on silicon and on stainless steel. The highest sp^3 fractions found were around 55% for depositions at 266 nm and around 45% for depositions performed at 248 nm laser wavelength. This result can be understood with the shorter pulse length of the Nd:YAG laser (∼10 ns) compared to the excimer laser (∼20-30 ns) leading to a higher laser power density.

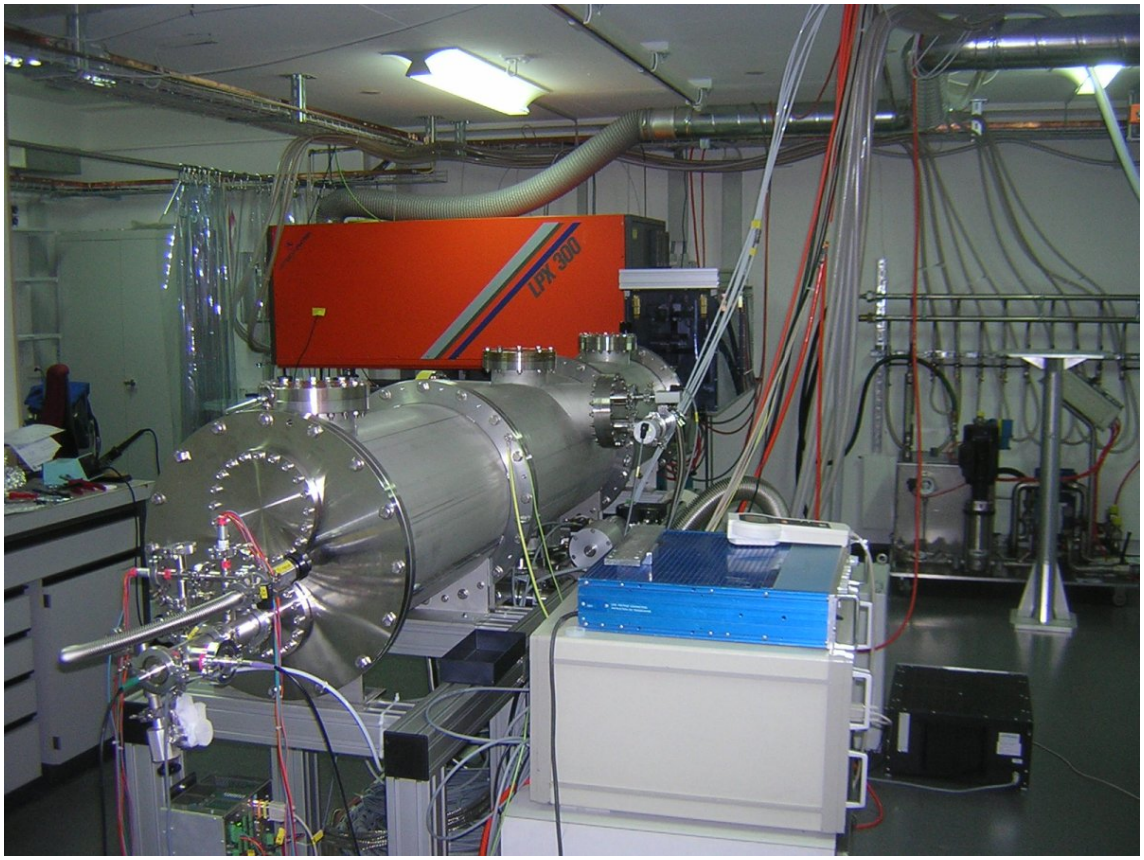

Figure 3.7: The Tube PLD setup at PSI. A pulsed laser beam at 193 nm wavelength produced by an excimer laser (the orange device in the background) is guided by various optical elements, which are all kept inside the nitrogen-flooded box (to the right of the laser), into the cylindrical deposition chamber (in front).

3.3 The Tube PLD setup

As mentioned at the beginning of this chapter, the Tube PLD setup was designed for coating the inner wall of UCN guide tubes with DLC. The maximum (minimum) dimensions of the tubes are 1 m (20 cm) length and ∼25 cm (∼6 cm) inner diameter. The setup is based on a pulsed laser with a wavelength of 193 nm and the corresponding optics which are described in Subsection 3.3.1. The deposition takes place inside a vacuum chamber the dimensions of which are about twice the maximum dimensions of the guides to be coated in order to move the whole guide along the fixed target. Details of the deposition chamber and the instrumentation within are given in Subsection 3.3.2.

Figure 3.7 shows a picture of the setup for the production of DLC inner wall coatings, subsequently referred to as Tube PLD setup.

3.3.1 Laser and optical components

For the deposition of high-quality DLC a powerful laser at short wavelength or an even more powerful laser at longer wavelength is needed. The term powerful refers to high power densities during laser pulses to exceed the ablation threshold of the target material, i.e. graphite. Only a few kinds of laser types fulfill this condition; most widely used are Nd:YAG lasers, excimer lasers and, more recently, femtosecond lasers, such as Ti:Sapphire lasers. The latter work with a fixed

Table 3.1: Incomplete list of gas mixtures and the corresponding wavelength for excimer lasers without additional inert and buffer gases [115]. Asterisks denote the commercially important wavelengths. Only configurations with narrow bandwidth are shown.

Rare Gas						
Gas molecule	Ar_2	Kr_2	Xe_2			
Wavelength [nm]	126	146	172			
Halogen						
Gas molecule	F_2					
Wavelength [nm]	157*					
Rare Gas - Halogen (diatomic)						
Gas molecule	ArF	KrCl	KrF	XeBr	XeCl	XeF
Wavelength [nm]	193*	222	248*	262	308*	351*

wavelength of ∼800 nm. Wavelength dividers for Nd:YAG lasers transfer the initial 1064 nm to lower values like 532, 355, 266 and 213 nm. The most versatile and also most powerful type of short wavelength lasers are excimer lasers. Their wavelength can be adjusted using different gas mixtures. Table 3.1 shows a list of gas mixtures and their corresponding wavelengths for excimer lasers. Additional buffer and inert gases are included in the gas mixture but are not mentioned here.

Excimer is a short term for *excited dimer* which denotes a class of molecules formed by the combination of two identical constituents in the excited state. By convention the name "excimer" laser is still used although the most common excimer lasers of today use excited complexes, commonly referred to as exciplexes, of rare-gas mono-halides (e.g. ArF) as active laser medium rather than excited dimers.

The main mechanism for the ArF excimer laser is the production of ArF^* molecules, where the asterisk denotes an excited state, and the subsequent decay of the ArF^* molecule to Ar and F under emission of a photon with 193 nm wavelength, i.e. $ArF^* \rightarrow Ar + F + h\nu$ [116].

The excimer laser used for the Tube setup is a Lambda Physik LPX-301. The specified maximum energy per pulse for this model is 800 mJ at 193 nm wavelength. This value can be obtained using the standard stable resonator optics, which leads to a divergence of 1×3 mrad^2. Calculations with a raytracing software [117] have shown that such a highly diverging laser beam cannot be focused to a spot of only a few squaremillimeters size when using a lens with large focal length (f $>$ 1 m). Thus, the divergence was reduced to about 0.5×0.5 mrad^2 by using unstable resonator optics. In general, the resonator optics of an excimer laser consists of two elements, the rear mirror which has always a plane surface and a high-reflectivity coating and the uncoated output coupler at the front. In the case of the unstable resonator optics, the output coupler is slightly convex. This leads to a different reflection position of the the laser beam on the output coupler for each time the beam is reflected inside the laser cavity during amplification. This is where the term *unstable* comes from. The laser beam produced with unstable resonator optics has only about half the power of a beam produced with stable resonator optics. However, the total divergence is reduced by up to one order of magnitude. The resulting laser beam is slightly converging.

The laser can be operated at repetition rates up to 50 Hz. The pulse length is 23 ns and the energy per pulse is up to 650 mJ if the laser is run at 10 Hz. The shape of a typical laser pulse is shown in Figure 3.8. Its multi-peak shape is typical for ArF excimer lasers [115]. Table 3.2 shows the laser characteristics measured during acceptance tests at PSI. The average energy per

Figure 3.8: Shape of a typical laser pulse, measured with a photo-diode.

Table 3.2: Laser characteristics measured with an external energy meter during acceptance tests at PSI.

Laser run at 29 kV				
Frequency	10 Hz	20 Hz	30 Hz	50 Hz
Maximum energy per pulse	570 mJ	554 mJ	544 mJ	526 mJ
Minimum energy per pulse	508 mJ	511 mJ	503 mJ	487 mJ
Average energy per pulse	538 mJ	531 mJ	523 mJ	507 mJ
RMS deviation	1.52%	1.27%	1.20%	1.28%
Average power	5.4 W	10.6 W	15.7 W	25.4 W

Laser run at 10 Hz						
High voltage	22 kV	23 kV	24 kV	26 kV	28 kV	29 kV
Energy per pulse	430 mJ	480 mJ	520 mJ	560 mJ	590 mJ	600 mJ

pulse is the same for repetition rates up to 30 Hz; at 50 Hz the energy per pulse is ∼6% lower than at 10 Hz, if the laser is run at 29 kV. With a reduced voltage of 27 kV, as it is used during deposition, the energy at 50 Hz is 15% lower than at 10 Hz.

The cross section of the beam at the exit of the laser has rectangular shape with dimensions of 23×5 mm^2. The laser cavity is filled with the following gas mixture: 140 mbar of 5% F_2 in He (purity 99.998%), 230 mbar of Ar (purity 99.999%), 1000 mbar of Ne (purity 99.999%) and 1730 mbar of He (purity 99.9999%). The static lifetime of the gas mixture, defined as the time after which the energy per pulse drops to half of the initial value if the laser is not run, is about two weeks. The dynamic lifetime, defined as the time after which the energy per pulse drops to half of the initial value if the laser is run continuously (at 10 Hz), is of the order 10-12 hours. The laser energy is not only a function of time but also depends on factors like the cleanliness of the output coupler or the flow rate and temperature of the cooling water of the laser.

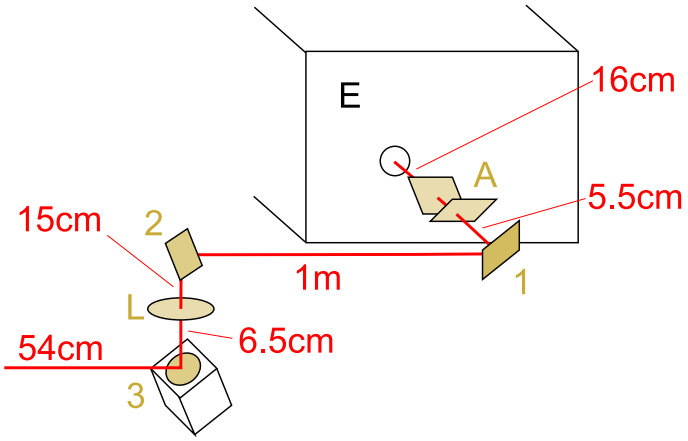

Figure 3.9: The optical path of the Tube PLD setup and the elements within: [E] excimer laser, [A] attenuator, [1] first fixed mirror, [2] second fixed mirror, [L] focusing lens, [3] fast steering mirror

Only few materials exist which have a high transmission (above 85%) for light at 193 nm; most widely used are MgF_2, CaF_2, LiF_2, quartz and ultra-violet graded fused silica (UVFS). For high power laser applications UVFS is commonly used and was also selected for optical elements in the Tube PLD setup. The laser beam passes five optical elements on the way from the output coupler of the laser to the entrance window of the deposition chamber. The optical path between laser and deposition chamber is shown in Figure 3.9.

As ultra-violet light of 193 nm wavelength is strongly absorbed by atmospheric oxygen producing ozone (O_3) with even higher absorption cross-section than O_2. The optical path between the laser and the deposition chamber has therefore to be kept in a nitrogen atmosphere. Thus, the optical elements were mounted inside a sealed PVC box which was flooded continuously with N_2 during deposition. The oxygen concentration was monitored by an oxygen probe. No deposition was performed as long as the oxygen concentration was above 0.3%.

The laser beam is reflected three times by two fixed mirrors and a fast steering mirror. The two fixed mirrors are necessary as the reflection on the fast steering mirror has to be in vertical direction due to the limited size of the fast steering mirror (see below). Reflecting the laser beam horizontally on this mirror would lead to a large cut of the laser beam (∼40%) due to the larger dimension of the leaser beam cross section in horizontal direction.

The first element in the optical path is an attenuator which allows the compensation of long-term decrease in laser energy due to the lifetime of the gas mixture in the laser cavity. It follows the principle of partial reflection and transmission of light at the surface of a material with an index of refraction larger than 1. Figure 3.10 shows a picture and a functional schematic of the attenuator. It mainly consists of two uncoated quartz plates (Suprasil 311, see Ref. [118]), which are embedded in support structures mounted onto the axis of a stepper motor each. One rotation of the motor axis consists of 500 steps per turn, corresponding to an angular resolution of 0.72°/step. They are operated in full step mode. The driver electronics of the two motors was located below the optical level. The transmission was selected by rotating both quartz plates in opposite directions to a certain angle. Both plates have to be rotated by the same angle in order to avoid a vertical shift of the laser beam. The value of the transmission can be calculated by using Snell's law of refraction, $n_1 \cdot \sin\alpha = n_2 \cdot \sin\beta$, where α is the angle of incidence and β the angle of the refracted beam, as indicated in Figure 3.10. The indices of refraction, n_1 and n_2, are the indices of refraction of air, $n_{N_2} = 1$, and quartz, $n_{quartz} = 1.561$ at 193 nm. As the maximum angle by which the plates can be rotated is 63°, possible values for the transmission are in the range of 63-82%. The attenuator

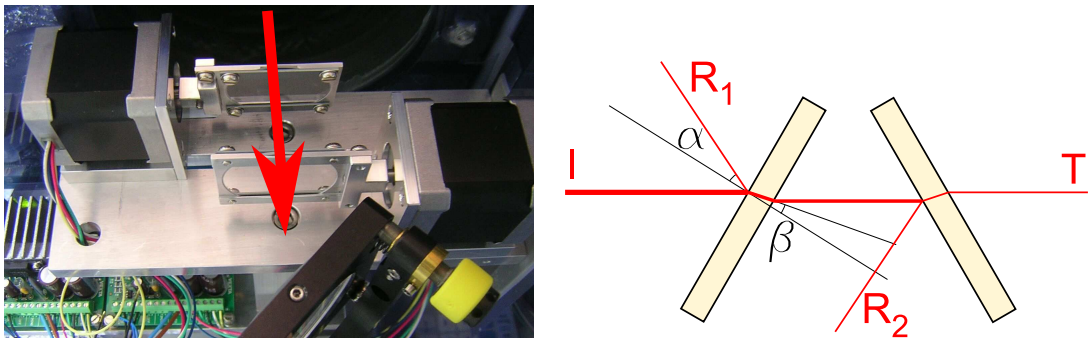

Figure 3.10: The Attenuator of the Tube PLD setup. In the photo, the laser beam enters the attenuator, which is set to maximum transmission, from top, denoted by the arrow. The first mirror - placed directly behind of the attenuator - is visible too. The functional schematic shows the determination of the transmission by selection of the tilt angle of the two quartz plates: [I] incident beam, [R_1] reflected intensity from first quartz plate, [R_2] reflected intensity from second plate, [T] transmitted intensity.

has to be switched off when starting the laser, since electromagnetic interference signals from the excimer laser influence the stepper motor electronics and induce artificial steps of the motors. No such behavior was observed during laser operation. The distance between the laser and the first rotation axis is 16 cm, the distance between the rotation axes 4 cm.

Directly behind the attenuator, at 26 cm from the laser, the first mirror is located. It consists of a plane UVFS substrate with 50 mm diameter and a high-reflectivity coating for 193 nm. The reflectivity specified (for fully polarized light) is $\geq$99% for an angle of incidence of 45°, but practically obtained values are in the range of 95%. This can be understood with the polarization of an excimer laser beam which is slightly below 100%. The first mirror is embedded in a support which allows for the transmitted fraction of the beam to be measured. This fixed fraction, commonly of the order of 1-2% of the incident beam, is monitored by a laser energy meter (Gentec SOLO with QE50-SP-H-MB measurement head). As the energies measured are on the level of a few milli-Joules per pulse, the signals have to be amplified (amplifier Gentec QEX).

After being deflected at the first mirror by 90°, the laser beam travels a distance of 1 m before it is again deflected by 90° at a second fixed mirror, identical to the first one, to the bottom. The large distance between the mirrors is necessary due to the fact that the part of the (converging) laser beam reflected at the entrance window of the deposition chamber should not have its focal point close to a mirror: A smaller distance between the mirrors can create such a situation and the first mirror can be damaged as the focused beam exceeds the ablation energy threshold of the high-reflectivity coating.

At a distance of 15 cm below the central reflection spot on the second mirror the beam passes a lens made out of UVFS with a anti-reflection coating for 193 nm. The lens has a focal length of 2 m. However, due to the non-negligible divergence of the excimer laser, the smallest cross section of the beam, called *waist*, is reached at a distance of 1925 mm from the lens. This length was determined by separate focal tests using the lens as the only optical element and shooting a single pulse onto a photo sensitive paper. During these tests a diffraction pattern was discovered in the waist which is shown in Figure 3.11. It must be pointed out that the photo-sensitive paper has an energy threshold for its color change which is significantly below the ablation threshold of graphite. Therefore the waist shape obtained in these tests is larger than what would be obtained for the ablated area on graphite with the same beam. However, ablation tests with perpendicular incidence on graphite showed that the vertical diffraction tails do not contain enough energy to

Figure 3.11: Diffraction pattern obtained at a distance of 106 cm from the lens during focal tests with the excimer laser. The lens had a nominal focal length of 1.5 m (at 1064 nm wavelength). The width of the pattern is ∼6 mm and its height ∼3 mm.

ablate significant quantities whereas the horizontal diffraction tails were clearly visible also in graphite after application of multiple pulses. The origin of the diffraction pattern are reflections on the surfaces of the electrodes in the laser cavity [119]. The effect only happens if unstable resonator optics are used with the LPX-301i excimer laser and is wavelength independent[2].

After having passed the lens the now converging laser beam is again deflected by 90° into the horizontal direction. This third reflection takes place on a mirror with one inch diameter made out of UVFS and coated with the same coating as the first two mirrors. The mirror is mounted on a fast steering system (Newport FSM-300-01). It allows for tilting of the mirror in two directions by up to ±3°. The appropriate electronics are located in a separate box and translate voltage signals in the range of -10 V to +10 V into the corresponding tilt of the mirror for each axis. The central reflection spot of the third mirror is located 6.5 cm below the lens. Unfortunately the beam diameter at this point exceeds the diameter of the mirror. Consequently only a part of the beam is reflected. However, the one inch fast steering mirror system had the largest diameter available at the time the Tube PLD setup was built up.

After the third mirror the beam travels horizontally for 54 cm until it reaches the entrance window of the deposition chamber. The relatively large distance between the fast steering mirror and the entrance window is determined by the focal length of the lens, its position and the position of the graphite target inside the deposition chamber.

3.3.2 The deposition chamber

The deposition chamber of the Tube PLD setup is a 2.5 m long vacuum tube with 40 cm inner diameter and a ISO-K flange of type DN400 at each end. This length allows for the translation of a 1 m long guide tube along the graphite target including a safety margin. The diameter of the chamber allows for the coating of tube with diameters of up to ∼25 cm. The main flange, which includes the entrance window and the associated elements (see below) facing the excimer laser, is subsequently denoted as the front end. The chamber itself is segmented into three sections which allowed pretests in the central segment. The three segments and the two main flanges are sealed by VITON™ gaskets. Smaller CF-flanges for the installation of feedthroughs, entrance window etc. are embedded in the main flanges. Two lateral CF-160 flanges are placed at each end of the vacuum tube and three of them in the middle. At the bottom, the central section of the vacuum tube has two flanges for connection of pumps. The vacuum tube is mounted onto a support structure made out of aluminum profiles. Figure 3.12 shows a picture of the vacuum chamber including pumps. Various installations and support structures are included in the vacuum chamber, see Figure 3.13. The two main structures inside the chamber are the support structure for the graphite target and

[2]It should be noted that Lambda Physik only became aware of this problem after they were informed by the users of the Tube PLD setup. The solution proposed by Lambda Physik, using an aperture close to the target, cannot be realized due to the moving focal point in the Tube PLD setup.

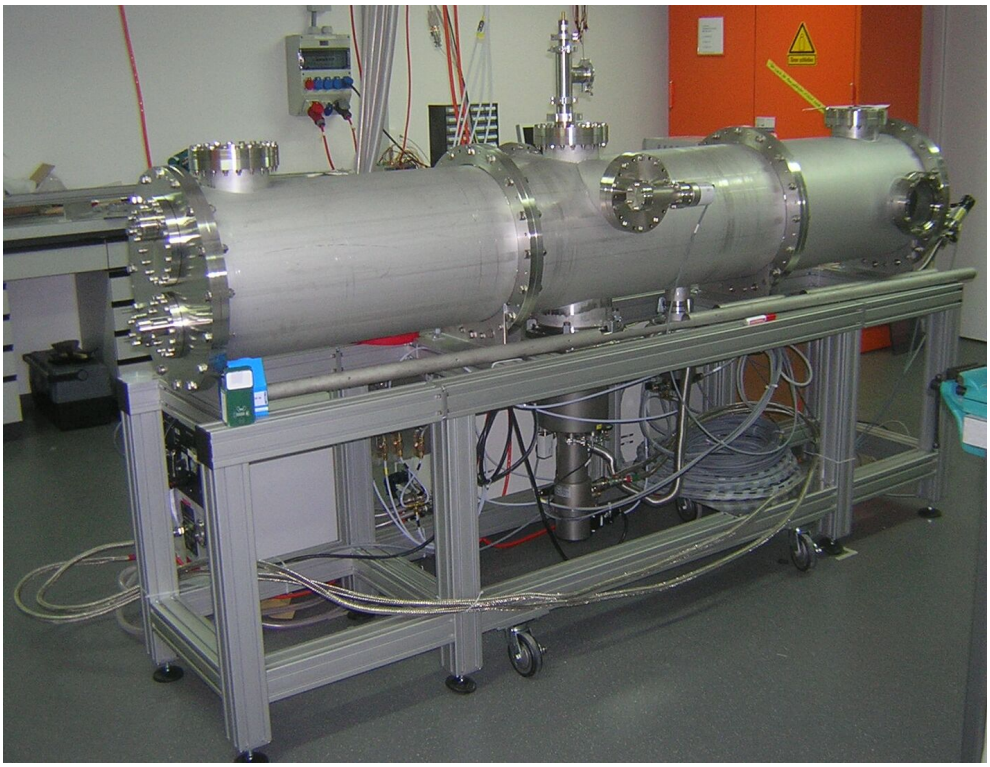

Figure 3.12: The vacuum chamber of the Tube PLD setup.

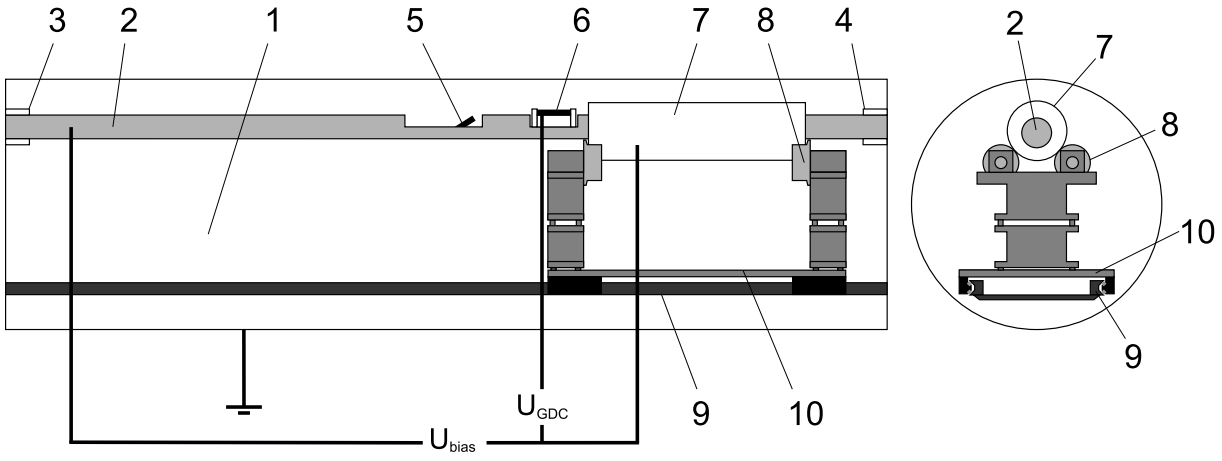

Figure 3.13: Length cut (left) and cross section (right) through the Tube PLD deposition chamber: [1] vacuum chamber, [2] target tube, [3] PTFE guide for target tube, [4] PTFE isolation for target tube, [5] pyrolytic graphite target, [6] GDC electrode, [7] substrate tube, [8] substrate wheels, [9] rail system, [10] substrate trolley. Bias voltage, U_{bias}, is applied between the target tube and the substrate tube; the voltage for GDC, U_{GDC}, is applied between the GDC electrode and the substrate tube.

the glow discharge cleaning unit, subsequently referred to as the target tube, and the rail system with the substrate trolley.

The vacuum system

A special pumping station was employed for the evacuation of the vacuum chamber. A combined system of a screw and a roots pump (Busch COBRA DS 700) reduces the pressure inside the chamber in a first stage down to 1 Pa via the so-called bypass valve which is mounted to the smaller of the two flanges at the bottom of the vacuum chamber. Usually 1 Pa is reached after about 45 minutes. A programmable logic controller (PLC) then closes the bypass valve and opens the so-called cryo valve which is a shutter valve with 20 cm diameter mounted on the bigger of the two flanges at the bottom of the vacuum chamber. Mounted on the bottom of the cryo valve is the cold head (Leybold COOLVAC 1500CL) of a cryo pump system. This cold head is cooled by a compressor unit (COOLPAK 4000) via a closed liquid helium loop. The pressure inside the chamber falls below 10^{-3} Pa after about another 30 minutes. After one night of continuous pumping the pressure is on the level of about $5 \cdot 10^{-5}$ Pa. The end pressure of the deposition chamber including the installations within which are described below is $\sim 2 \cdot 10^{-5}$ Pa. It is measured by a full range pressure gauge which is mounted on a lateral flange in the middle of the chamber.

The gas inlet system

The PLC also allows for controlled inlet of gases and keeping their pressure stable. This is done automatically by an inlet valve mounted to the rear end flange and by the monitoring of the pressure with a full range pressure gauge. The inlet valve is connected to a mixing tap which allows to select between air, nitrogen, argon, oxygen and helium.

The laser beam entrance system

The surface of the entrance window on the inside of the chamber faces the graphite target on a straight line. The cleaning of the window is a challenge as no solvent for graphite exists. Thus, it has to be protected from being coated; otherwise the transmission continuously decreases. A special mechanism is built around the entrance window which is shown in Figure 3.14 in a schematic drawing and a picture. The laser beam enters the deposition chamber through a quartz window embedded into a CF-40 flange (item 1 in Figure 3.14). A quartz disk of 40 mm diameter and 1 mm thickness, mounted in a support structure (item 2) directly behind the entrance window, prevents the coating of the window. This support structure also includes a vacuum bypass around the quartz protection disk and two lateral flanges (summarized as item 3) of which one can be connected to an additional pump. Monitoring the transmission during deposition tests showed that it is necessary to regularly exchange and/or clean the quartz protection disk during the deposition of a UCN guide tube. It has to be possible to do this exchange without breaking the vacuum in the chamber as this can lead to a substantial decrease of the DLC quality. Thus, entrance window and protection disk holder are mounted onto a shutter valve (item 4, continuous line shows open position, dashed line shows closed position). Due to practical reasons a distance piece (item 5) has to be mounted in between the shutter valve and the main flange of the deposition chamber (item 6).

Cleaning of the quartz disk is only possible with reactive ion etching using oxygen. Application of this method to the entrance window itself is disadvantageous as it may lead to leaking of the metal seals.

The entrance window and a clean quartz protection disk are found to have a total transmission of about 80-85%. When the transmission falls below about 70% the protection disk is exchanged. This is done by closing the shutter valve and ventilating the volume in front of the shutter valve

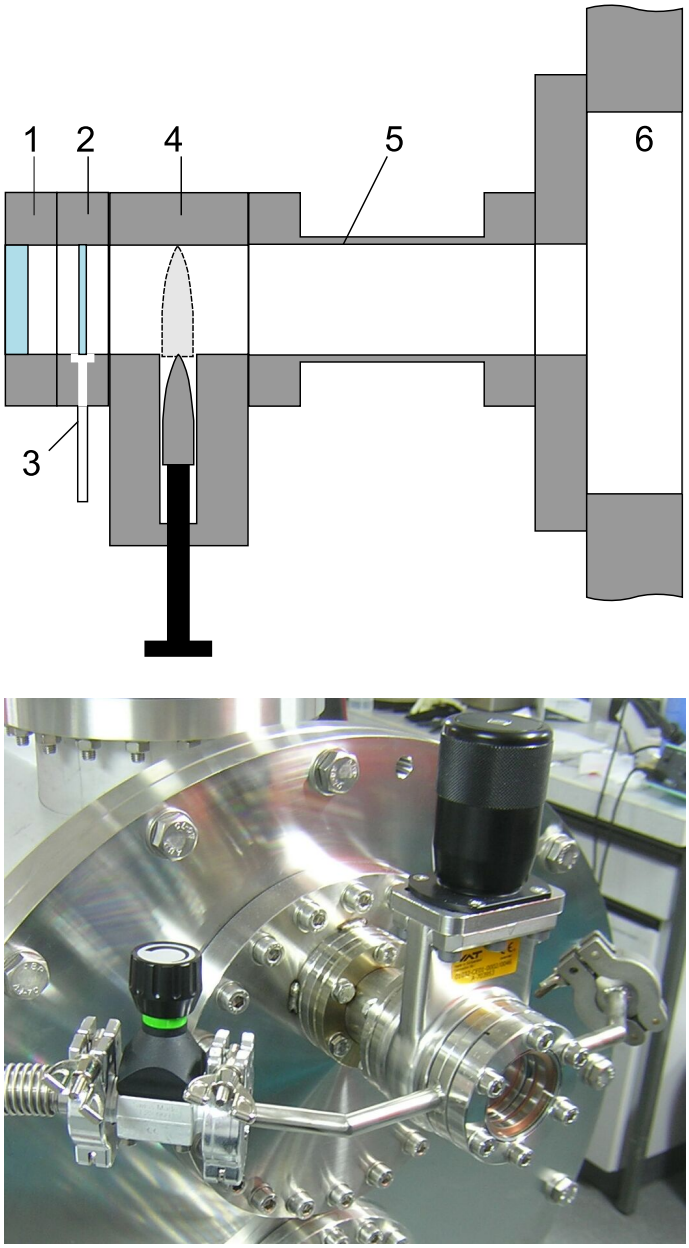

Figure 3.14: The beam entrance section of the Tube PLD setup: [1] quartz entrance window, [2] quartz protection disk mounted in a support with vacuum bypass, [3] vacuum flange to pump, [4] shutter valve, [5] distance piece, [6] main flange of the vacuum chamber.

by opening a valve mounted to one of the flanges of the protection disc holder. Afterwards, the entrance window and the protection disk holder are dismounted from the shutter valve, the protection disk, which is fixed by a circlip, is exchanged and both the window and the protection disk holder are remounted. A small pump is connected to the valve mounted at the disk holder and the volume in front of the shutter valve is evacuated again. The shutter valve is not opened until the pressure in front of the valve is lower than inside the deposition chamber in order to prevent a contamination of the substrate. This can be facilitated by adding an inert gas to the deposition chamber. The valve at the disk holder is then closed and the additional pump is switched off.

Figure 3.15: The pyrolytic graphite target is mounted under an angle of 35° on a stainless steel wedge which is embedded in the half-opened target tube. An additional feature is the second target, which is a plate of 2×1 cm^2 size clamped within the fixing of the graphite target. Also visible is the mask which prevents particulates from dropping into the substrate tube.

The target and its support structure

The target tube is a horizontal 2.5 m long stainless steel tube with 40 mm outer diameter and 1 mm wall thickness. The upper half of the central part is cut out, leaving the tube half-opened. Embedded into this central part of 30 cm length is a cylindrical wedge with an angle of 35°made out of stainless steel. This wedge is the support for the main target, which is a plate with dimensions 42×24×4 mm^3 made out of the same pyrolytic graphite as was used in the pretests (see Section 3.2). Figure 3.15 shows a picture of the graphite target mounted onto the target support inside the target tube. A secondary target, e.g. for the admixture of another material, can be mounted under an angle of 45° slightly above the main target by clamping a plate of 2×1 cm^2 size of the desired material within the fixing of the main target. The half-opened part of the target tube is partially closed by an aluminum mask which allows for the ablation of target material under angles up to 30° from the surface normal. It prevents particles ablated under large angles with low kinetic energy and especially particulates from reaching the surface of the substrate tube (see below). The target tube is electrically isolated from the vacuum vessel by polytetrafluorethylene (PTFE) at both end flanges. It is fixed to the rear end flange and is held by a guide at the front end flange. A wire connection to a high voltage feedthrough allows to set the target tube to an electric potential up to a maximum voltage of ∼1000 V with respect to the vacuum chamber.

The substrate holder for fixed test sample position

In a first stage, to produce flat, small samples fixed in space for optimization of the process parameters, a reduced setup was built up, using an alternative, fixed substrate holder. In order to be able to use glow discharge cleaning, the holder was isolated as it is described in the following and shown by Figure 3.16. It consists of three identical structures for mounting test samples of 10 × 10 mm^2 and 20 × 20 mm^2 size with a thickness of up to ∼2 mm. Each structure consists of a PTFE socket (item 2 in Figure 3.16) and a cap of the same material (item 3). Embedded in the socket is an aluminum cylinder (item 4) which allows an electric connection (item 6) of the substrate (item 5) from the back. The sockets are mounted rotationally symmetric to a cylindrical plate made out of PTFE (item 1). This plate is mounted at the end of a threaded rod (item 7) which is connected to a rotary feed-through (item 8) at its other end.

As all three substrate structures are exposed to the ablation plume, a deposition mask is used.

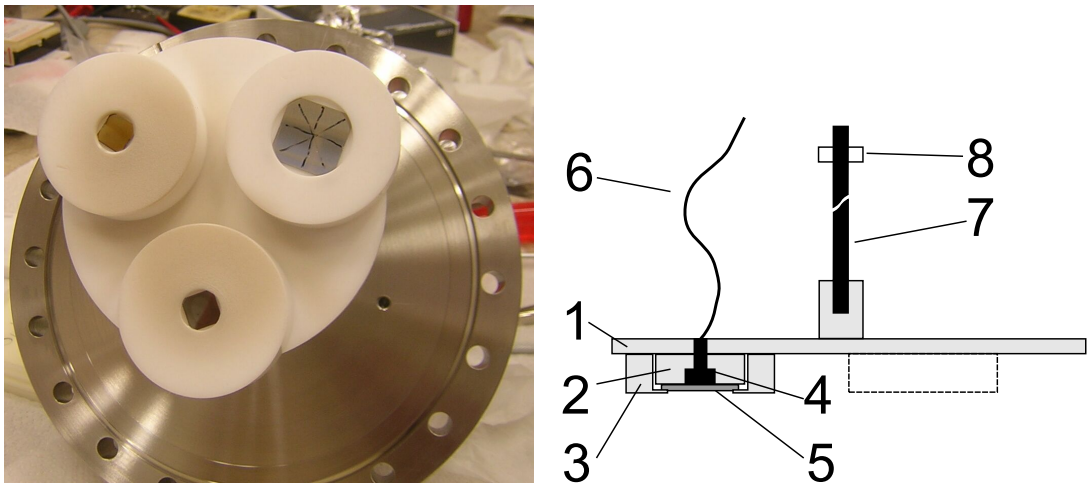

Figure 3.16: The substrate holder for fixed substrates. Left: view from bottom, right: schematic diagram: [1] PTFE base plate, [2] PTFE socket, [3] PTFE cap, [4] embedded aluminum cylinder, [5] substrate, [6] electric connection, [7] threaded rod, [8] rotary feedthrough. Only one substrate holding structure is drawn, the other two are indicated by the dashed line.

It consists of an aluminum sheet with a circular hole of 3 cm diameter. The mask can be inserted from lateral direction. The substrate holder and the mask were aligned in such a way that the central surface normal of the target crosses the circular hole and the substrate surface in the center.

An electrically isolated electrode for glow discharge cleaning was embedded in a PTFE plate mounted at the end of the deposition mask. During tests with different shapes of the electrode, significant cleaning could only be obtained if peak-like shapes were used. The final GDC electrode design was then based on this information.

The glow discharge cleaning (GDC) unit

Clean substrate surfaces are required for well adherent coatings and for a low level of contamination in the coating. Cleaning outside of the deposition chamber, e.g. in an ultrasonic bath filled with solvents such as different types of alcohols, can remove strong contaminations. Residues from evaporated solvents and contaminations due to exposure to air cannot be avoided and cannot be removed with external cleaning procedures. Only an in-situ cleaning inside the deposition chamber with subsequent deposition can minimize such deposits on the substrate surface. One possibility for in-situ cleaning is using glow discharge (see e.g. Ref. [120]). Any gas kept at low pressure contains a small fraction of ionized particles. In an electric field applied between two electrodes the positive ions and the negative electrons begin to drift toward the electrode with opposite charge sign. This leads to an acceleration of the particles and to further ionization by collisions. The surface to be cleaned has to be the electrode with negative polarity in order to accelerate the positively charged ions to kinetic energies high enough to remove atoms at the surface on collision. Typical pressures for GDC are of the order 0.1-100 Pa; typical voltages for DC glow discharge cleaning are of the order of a several hundred kilovolts.

A GDC unit was implemented in the Tube PLD setup. It consists mainly of the gas inlet system described above and an electrically isolated electrode which is shown in Figure 3.17. The aluminum electrode has a blade-like shape and is embedded in a piece of PTFE in order to electrically isolate it from the supporting target tube. No electric breakdown is observed up to 1200 V, which is the maximum voltage of the used power supply (Heinzinger PHN-1200-1). The second electrode of the GDC unit is the substrate tube. A resistor designed for maximum power of 11 W with a

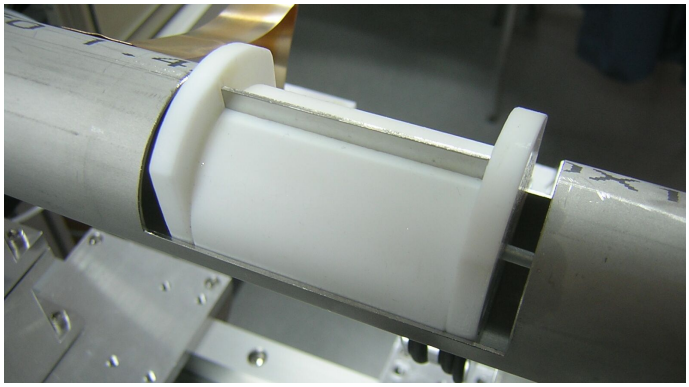

Figure 3.17: The blade-like GDC electrode, embedded in PTFE.

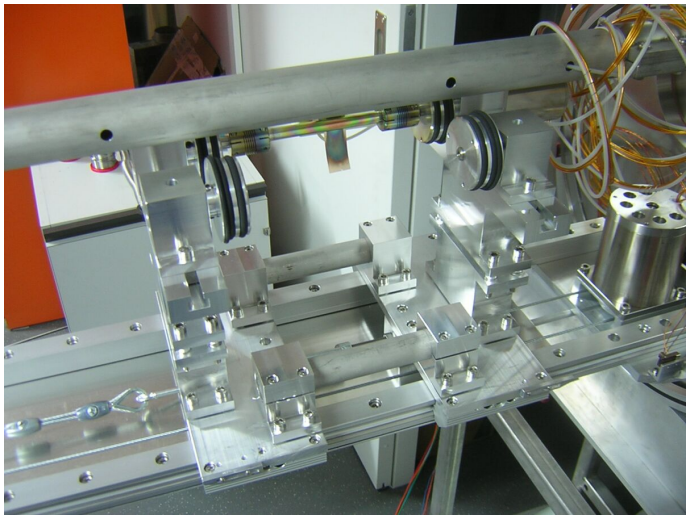

Figure 3.18: The substrate trolley on its rails, adjusted for a substrate tube of 7 cm diameter and 20 cm length.

resistance of 48.5 kΩ is connected in series with the glow discharge setup. No stable glow discharge is possible for lower resistance. Typical discharge currents are of the order of 10 mA for 10 Pa of argon.

The substrate trolley

The design is for a substrate tube of 0.2-1.0 m length and a diameter of ∼6-20 cm, see Figure 3.13. It is put over the target tube and sits on a trolley which moves along rails. The trolley and the rail system are shown in Figure 3.18. The rail system itself consists of two aluminum rails at a distance of 25 cm mounted on aluminum struts every 80 cm. Additional aluminum sheets are mounted in between the main struts in order to improve the parallelism of the two rails. Reels are mounted to the rail system and allow the whole system, which is connected to the rear end flange, to be moved in and out of the vacuum chamber easily. The substrate trolley runs with reels on the rail system and consists of two base plates which are connected by a strut of arbitrary length in order to adjust the trolley for the length of the substrate tube. Support structures with two wheels each on top are mounted on both base plates of the trolley. The substrate tube lies on top of these four wheels, subsequently referred to as substrate wheels. One of the wheels is directly connected to a in-vacuum motor which drives the rotation of the substrate tube. The translation of the trolley is done by a pulley which is driven by another in-vacuum motor. Both motors are two phase stepper

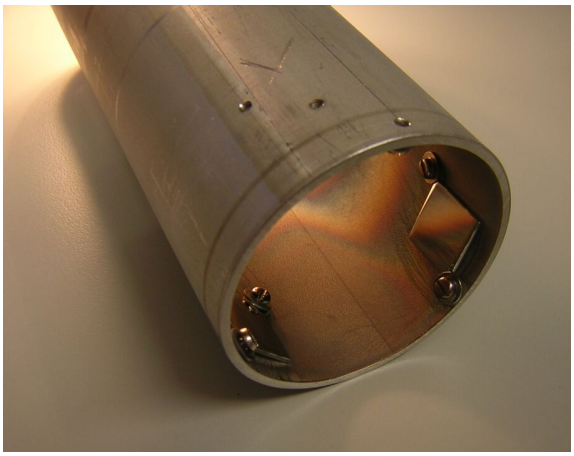

Figure 3.19: One end of the tube-shaped substrate holder with stainless steel substrates mounted.

motors and are connected via electric feedthroughs with a programmable stepper motor control (Phytron TMC-93-70 MINI) outside the vacuum chamber. At each end of the rail system an end switch is mounted which allows for the initialization of the translational position and prevents accidentally driving the trolley beyond limits.

The substrate wheels are made from aluminum but have two grooves each with VITON™ gaskets therein, see Figure 3.18. These totally eight rings isolate the substrate tube electrically from the trolley and its superstructure. Additional VITON™ rings fix the end of the substrate tube. At one end of the substrate tube, an extension made out of PTFE is mounted on the superstructure. At its end a BeCu sliding contact is mounted and allows a low-resistance connection of the substrate tube via feedthrough to any potential supplied outside the vacuum chamber.

The tube-shaped substrate holder

In the second stage, a tube-shaped substrate holder was used, made from a stainless steel tube with 70 mm diameter and 20 cm length. It allows for the coating of flat test substrates under tube-like coating conditions. Close to each end of the tube tapped bores exist in order to fix substrates of approximately 20×20 mm^2 size with two screws and washers at two corners opposite to each other, as shown in Figure 3.19. Additional tapped bores exist for mounting smaller substrates of approximately 10×10 mm^2 size. Metallic substrates and thicker glass substrates can be mounted directly, thin glass plates need an additional support plate underneath in order not to break it during tightening of the screws.

Control software and electronics for the Tube PLD setup

A central software, written in LabVIEW™ [121], controls all the subsystems used in the Tube PLD setup:

- Laser trigger
- Pressure monitoring and background pressure control
- Temperature monitoring
- Attenuator control
- Laser energy meter

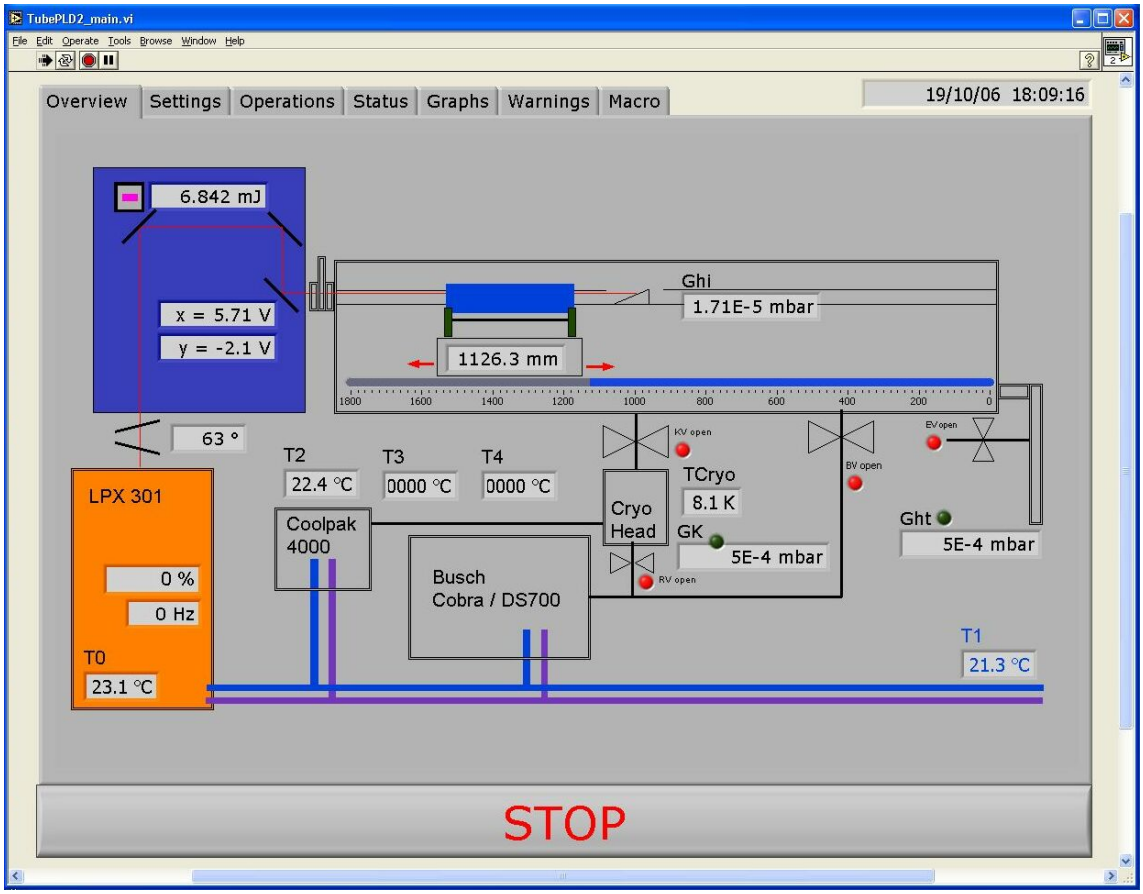

Figure 3.20: The main overview tab of the graphical user interface of the Tube PLD software.

- Fast steering mirror system
- Motion of the substrate trolley

Figure 3.20 shows the main overview tab of the graphical user interface of the Tube PLD software. The software runs on a standard Personal Computer which is equipped with an analog/digital I/O interface card (National Instruments NI-6229) and additional serial ports for the communication with the subsystems. The external contact of the NI-interface card is wired to a special connector block from which connections to coaxial sockets (type BNC for analog signals, type Lemo for digital lines) are made. These electronics are mounted in a separate box, subsequently referred to as the electronics box. The box also includes electronics for the conversion of the status voltage signal from the laser into logic signals which can be read by the NI interface card.

The temperature monitoring is based on the readout of thermo-sensitive resistors (PT-100). The electronic box includes the circuits which convert the resistance of up to five PT-100 to voltage signals which are read out by analog input channels. Temperature sensors are placed on top of the cavity inside the excimer laser, at the cooling water system and, during some depositions, at the back of the graphite target. The recorded signals are noisy and have to be averaged over times of the order of 1-10 s, which is done by the software.

As the actions of some of the subsystems, e.g. the laser trigger signal and the motion of the substrate trolley, have to be well synchronized a macro system was programmed.

Additional information about the Tube PLD software can be found in Appendix A.

Table 3.3: List of substrates used for test samples produced with the Tube PLD setup. The RMS roughness was derived from line scans performed by a profilometer.

Type	Material	RMS roughness	size	holder type used
A	Silicon	4 nm	20×20 mm^2	fixed
B	Aluminum	150 nm	20×20 mm^2	fixed & tube-shaped
C	Quartz	2 nm	10×10 mm^2	fixed & tube-shaped
D	Stainless steel (1)	54 nm	10×10 mm^2& 20×20 mm^2	fixed & tube-shaped
E	Stainless steel (2)	110 nm	20×20 mm^2	tube-shaped
F	Microscope slide (glass)	2 nm	20×20 mm^2	tube-shaped
G	Sand-blasted glass	54 nm	∼20×25 mm^2	tube-shaped
H	Al on glass	3 nm	20×20 mm^2	tube-shaped
I	Ti on glass	4 nm	∼20×25 mm^2	tube-shaped
J	Cr on glass	6 nm	20×20 mm^2	tube-shaped

3.4 Production and results of test samples

Various series of test samples were produced with the Tube PLD setup in order to find optimal process parameters. The deposition with these parameters should lead to DLC films with the following properties:

1. high density, i.e. high sp^3 fraction,
2. film thickness of 200-300 nm,
3. well adherent,
4. as smooth as possible.

Different substrate materials and surface qualities were tested. Table 3.3 shows a list of the used substrates. The RMS value of the surface roughness was measured with different profilometers (Dektak 8000, Ambios XP-1, Dektak 8). It has to be pointed out that the values below 10 nm are close to the sensitivity limit of a mechanical profilometer and represent height differences on a lateral scale of a few 100 nm. Stainless steel substrates were purchased from two different companies. The metallic layers of the last four substrate types in Table 3.3 were deposited by magnetron sputtering (with a Leybold Z600) and have a thickness of 30 nm.

All films were grown at room temperature as heating the substrate leads to a decrease of the sp^3 fraction (see e.g. [90]) and substrate cooling may result in unwanted contaminations by residual gas species.

3.4.1 Test samples produced with the fixed substrate holder[3]

A first series of test coatings was produced on stainless steel (type 1) substrates using the fixed substrate holder described above. This was done in order to find optimal process parameters for the Tube PLD setup and to investigate the sensitivity of the setup to changes of these parameters. The substrates were cleaned with methanol in an ultrasonic bath. The average distance between target and substrate was fixed to ∼6 cm, as the pretests (see Section 3.2) have shown no dependency of the sp^3 fraction on the target-to-substrate distance. Each film was grown by using 3000 laser pulses on the graphite target. The samples were characterized with Raman spectroscopy and XPS,

[3]Part of the work in this section was previously published; see Ref. [122].

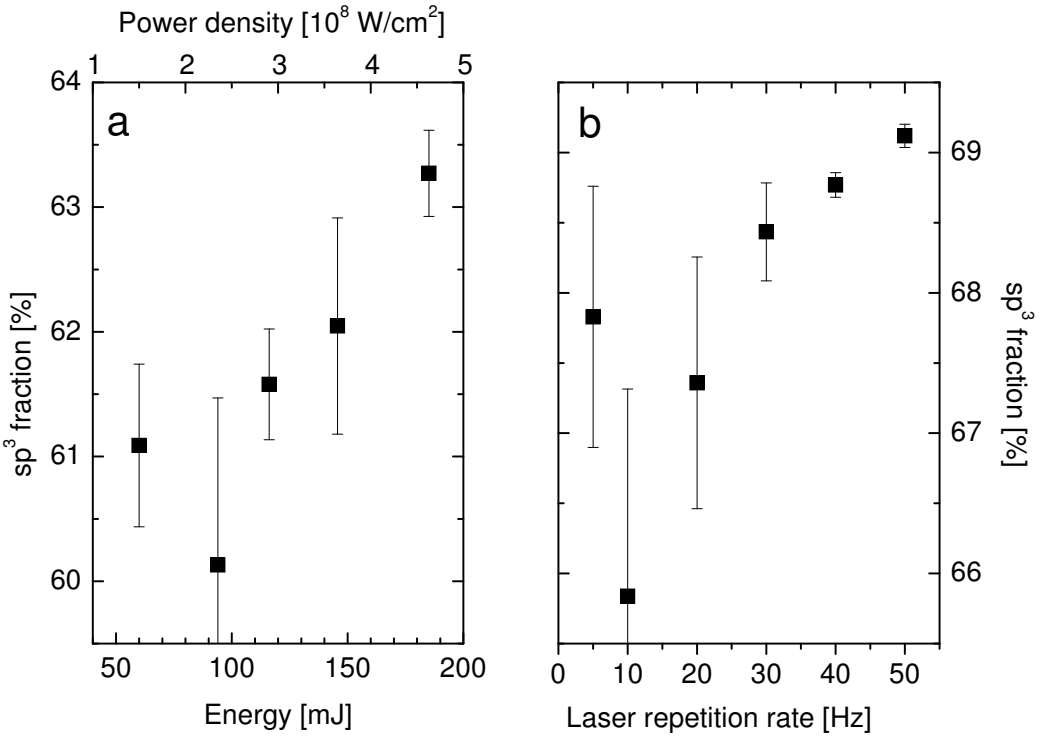

Figure 3.21: Results of XPS measurements for test samples as a function of (a) energy, deposited at 10 Hz, and (b) laser repetition rate, deposited with a laser energy of ∼80 mJ/pulse. An argon background pressure of 10^{-4} Pa was used for both series. The error bars result from the statistical uncertainties of the XPS measurements; the large variation in the uncertainty is due to the fact that for each data point two measurements at different locations on the sample were averaged. For (a) the resulting power density of the laser beam on the target is plotted on the top axis, although the values have to be considered as estimation due to the inhomogeneous laser spot (see text).

following the standard procedure described in Chapter 2, using the same equipment. The values for the sp^3 fraction range from 40% to 70% and are therefore significantly higher compared to the results in Section 3.2.

The values and (statistical) errors in Figure 3.21 constitute an average over two independent measurements performed at two different locations on the samples (one central and one peripheral). One process parameter studied was the laser energy on the graphite target per pulse. It was varied from 50 mJ to 200 mJ. The laser repetition rate was set to 10 Hz, the pressure was kept at $1 \cdot 10^{-4}$ Pa (stabilized by adding argon). The XPS results for the sp^3 fraction, which are shown in Figure 3.21a, show slightly higher values for higher energies. This can be understood with a higher kinetic energy of the ablated particles due to the higher energy input. As the major part of the ablated carbon ions and atoms have a kinetic energy below 100 eV, which are ideal for the growth of sp^3 rich DLC films (cf. Section 3.1.4), an increase of the kinetic energy favors sp^3 bonding. It is difficult to accurately determine the energy density on the target due to the diffraction effects described above which result in a focus spot with badly determined intensity distribution. The area of the central spot without the diffraction pattern is estimated to be about 1.7 mm^2. Assuming 80% of the total energy to be concentrated in this central spot, an energy density of ∼5 J/cm^2 and a power density of $\sim 2 \cdot 10^8$ W/cm^2 is calculated for the central spot using a total laser energy per pulse of 100 mJ. It is not known whether the energy in the central spot is linearly dependent on the total laser energy, i.e. if a factor of two higher total laser energy also results in doubling the energy density of the central spot. The sp^3 fraction may also be limited by the tails of the laser

beam with lower energy density producing ablated particles with lower kinetic energies. Caused by these tails, the target area illuminated with low energy density, just high enough to be above the ablation threshold of graphite, as described in Section 3.1.2, is expected to increase with increasing total laser energy. This results in a different ratio of high-energy density and low-energy density area for different laser energies.

Another process parameter studied was the laser repetition rate, which was varied from 5 to 50 Hz. The laser energy per pulse was kept around 80 mJ, the pressure inside the chamber at $1 \cdot 10^{-4}$ Pa. The XPS measurements show a small but systematic increase of the sp^3 fraction with increasing repetition rate, as shown in Figure 3.21b. However, within the systematic uncertainties of the XPS measurements the sp^3 fraction is found to be constant for repetition rates in the range of 5 to 50 Hz.

The profilometric measurements showed roughnesses of the same order for the uncoated substrates and for the coated samples, which agrees with findings from Ref. [90]. The film thickness, obtained by measuring the height of an artificial coating edge, could only be measured for a part of the samples due to the waviness of some of the substrates. The values obtained show film thicknesses in the range of 50-150 nm, which is about 25-50% of the necessary film thickness for a UCN wall coating. No adhesion tests were performed for the coatings produced with the fixed substrate holder. A test series with a positive bias voltage applied between target and substrate, where the substrate was set to ground potential, showed a significant drop of the sp^3 fraction from 60% without bias voltage to 40% with an applied voltage of 500 V. This can be understood with the large kinetic energies of the ablated carbon ions leading to energy dissipation within the DLC film with subsequent decreasing of the sp^3 fraction, as described in Section 3.1.4. A more detailed study was performed with bias voltages between 0 and 200 V. The values for the sp^3 fraction obtained with XPS were consistent within uncertainties and of the order 60-65%.

The highest sp^3 fractions were measured for coatings deposited at high repetition rates, although differences to the values obtained for coatings deposited at low repetition rates are small. As the optical components of the Tube PLD setup, especially the coatings on the mirrors and the lens, showed an increased wearing for repetition rates above 20 Hz, subsequent coatings were produced with repetition rates $\leq$20 Hz.

As mentioned above, the highest sp^3 fraction measured was close to 70%. The corresponding film density, calculated by Eq. 2.1, is 2.88 g/cm^3, the corresponding Fermi potential 250 neV, i.e. on the same level as for beryllium or nickel. As the power densities were on the same level for the pretests and the tests with the Tube PLD setup, the increase of the sp^3 fraction has to be caused by the shorter laser wavelength, 193 nm compared to the 248 nm and 266 nm applied in the pretests.

3.4.2 Glow discharge cleaning of substrates for test sample production

Various GDC tests were performed in order to determine the cleaning efficiency of different gases. The surface contamination used were lines drawn with an overhead marker onto stainless steel substrates. The substrate were mounted inside the tube-shaped substrate holder. Argon, nitrogen, oxygen and helium were tested. Figure 3.22 shows images of the glow discharge for the different gases. A first test with argon was performed at a terminal voltage of 600 V. Together with a measured voltage drop of 330 V at the 47 kΩ resistor, this results in a voltage between GDC electrode and the substrate tube, which are separated by about 1 cm, of about 270 V. The pressure inside the chamber was kept around 10-15 Pa while the chamber was pumped via an additional bypass valve with a cross section of a few square millimeters. The glow discharge had a violet-blueish color. Stable discharge could be observed down to $\sim$3 Pa. The glow discharge current was $\sim$7 mA. After 2 hours of continuous cleaning a clear reduction of the artificial contamination could be observed. The lines in the range close to the GDC electrode were significantly weaker after cleaning. The test was repeated at a higher terminal voltage (1000 V) leading to a discharge

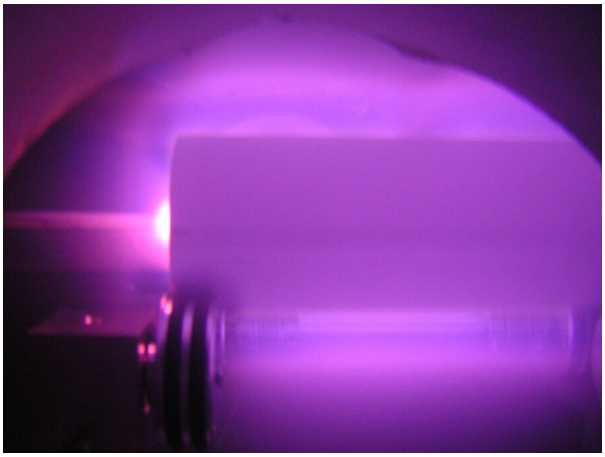

(a) Argon

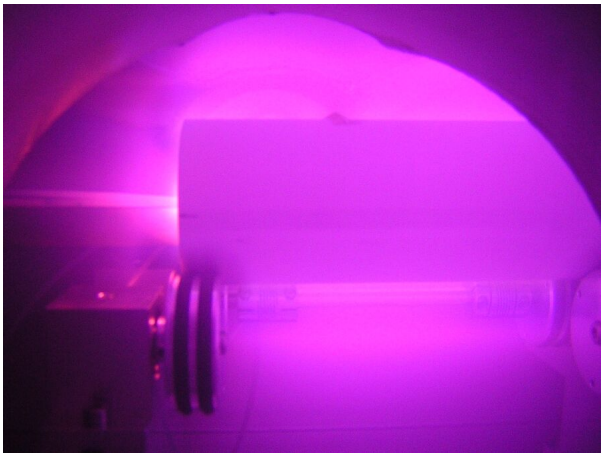

(b) Nitrogen

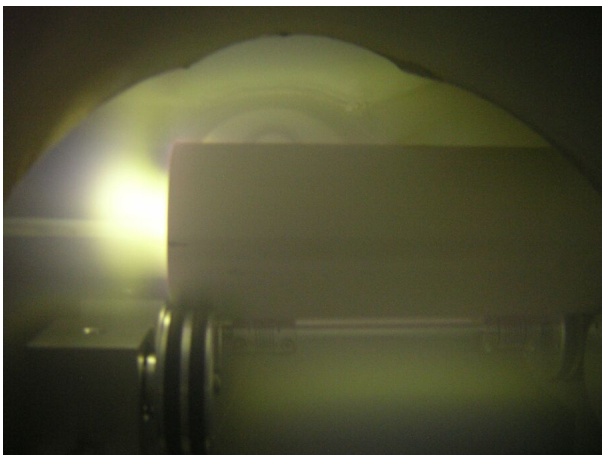

(c) Oxygen

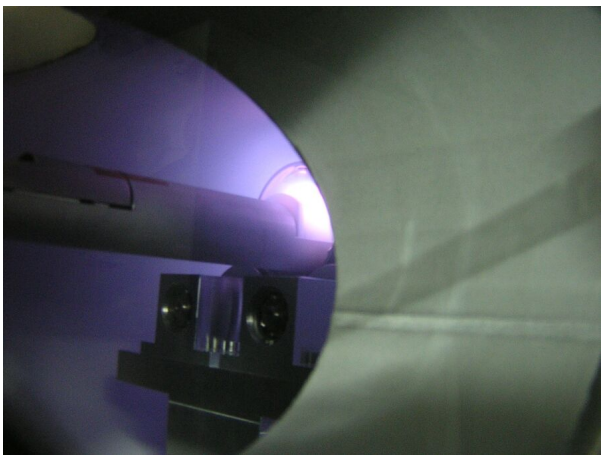

(d) Helium

Figure 3.22: Glow discharge cleaning with different gases.

current of 10 mA. Thus, the voltage between the GDC electrodes is of the order of 500 V, resulting in an averaged electric field strength of ∼50 kV/m. Again continuous cleaning was performed for about 2 hours. A significant improvement could be obtained as the lines close to the GDC electrode had nearly vanished.

The same test with nitrogen instead of argon showed about the same cleaning efficiency after about two hours. The cleaning current was 10-12 mA while the terminal voltage was 1000 V. The color of the glow discharge was slightly more reddish.

Significantly different values were obtained with oxygen. The terminal voltage was set to 1000 V and the resulting discharge current was of the order 8-10 mA. The color of the glow discharge was light yellow. After about 2 hours of continuous cleaning the lines were completely gone on an area significantly larger compared to the one which showed a cleaning effect during the previous tests. However, the oxygen glow discharge was slightly more unstable than the argon and the nitrogen glow discharge. Increasing the terminal voltage to 1100 V solved the problem.

Additional tests were performed with helium. No significant cleaning effect could be obtained, leading to the conclusion that the energy transfer of the helium ions on collisions with the substrate surface is not large enough to do sputtering of surface contaminations.

As oxygen showed the best cleaning performance it was subsequently used for all the samples where oxidization is not a problem, as stainless steel or any kind of glass. For oxidization-sensitive

substrates GDC with argon was used. The standard GDC process was chosen as continuous cleaning at 10-12 Pa with 1100 V terminal voltage in substrate translation steps of 5 cm with one hour cleaning per step. The tube-shaped substrate holder was rotated during the complete cleaning time.

3.4.3 Test samples produced with the tube-shaped substrate holder

The test samples described in Section 3.4.1 were produced by using only a small part of the ablation plume. The angles of emitted particles were small with respect to the surface normal, i.e. their kinetic energy is expected to be maximized. Coatings with thickness of the order of 50-150 nm were produced, being a factor 2-4 too thin for use as UCN wall coating. In order to achieve the goal thickness of ∼300 nm, either the deposition time has to be prolongated or a larger solid angle, i.e. a larger fraction of the plume, has to be used. As the first possibility is disadvantageous due to relatively small deposition rates of PLD compared to other deposition techniques as e.g. vacuum arc deposition, the second option was chosen. The angular selection of the ablated species was subsequently done by the target mask described above.

In order to determine the area which is coated with the new angle selection, a thin glass plate was mounted instead of the mask of the fixed substrate holder. A strip of Kapton® tape was stuck onto the glass plate in order to create a sharp step of the coating where its thickness can be measured with a profilometer. The resulting coating, produced with 12'000 pulses with ∼150 mJ/pulse, showed spontaneous delamination for major parts of the coated area, which had elliptical shape. The maximum coating thickness could not be measured due to spontaneous delamination but the color gradient of the coating indicates a maximum thickness of ≥100 nm. In order to investigate the problem of insufficient adhesion, various series of test samples were produced with the tube-shaped substrate holder. Table 3.4 gives an overview of various test samples produced with the tube-shaped substrate holder. For most of the samples with metallic substrate surface, the thickness was estimated by the color of the coating. The color changes from light yellow (∼20 nm) to yellow (∼40 nm), violet (∼55 nm), blue (∼70 nm) and finally to gray (∼100 nm and above).

All samples mounted in the tube-shaped substrate holder were first cleaned in an ultrasonic bath with solvents such as methanol, acetone or isopropanol (IPA) for ∼10 minutes with a few exceptions. After the substrate holder was installed in the Tube PLD setup, the deposition chamber was evacuated to $\sim 10^{-3}$ Pa. Subsequently the standard GDC process, as described in the previous section, was performed. When the GDC process had terminated, the deposition chamber was pumped down until a pressure below 10^{-4} Pa was reached; usually this was achieved by overnight pumping.

A few samples on different substrates, i.e. stainless steel, silicon and aluminum, were characterized with XPS. The sp^3 fractions obtained were of the order of 35-45% and therefore significantly lower compared to those of the previous test samples produced with the fixed substrate holder. Considering the deposition model described above, the drop in the sp^3 fraction can be explained by the larger fraction of low-energetic species in the outer parts of the ablation plume leading to a film growth on the surface (sp^2-like) instead of the sub-implantation growth as for particles with higher kinetic energies.

Adhesion was tested for different substrates, like stainless steel, aluminum and different types of glass including the glass substrates with thin metallic layers deposited by magnetron sputtering, and sand-blasted glass. The adhesion of the films was tested by the tape test, i.e. by using sticky tape and seeing how much of the coating adhered to the tape after removing it. Three groups of samples were found in terms of adhesion:

1. samples which showed no spontaneous delamination after deposition and which passed the tape test,

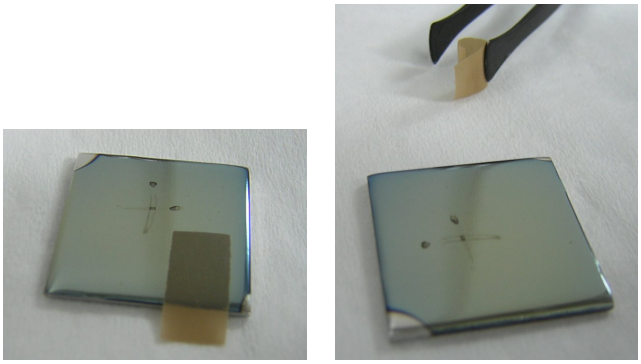

(a) Group 1 - before and after the tape test

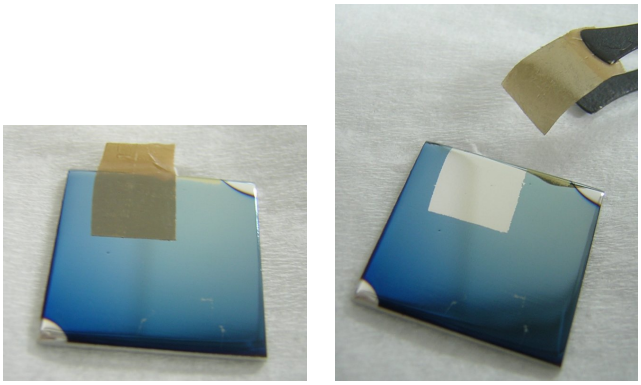

(b) Group 2 - before and after the tape test

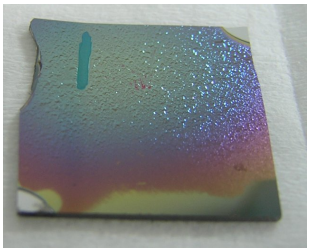

(c) Group 3

Figure 3.23: Test samples which belong to different groups in terms of adhesion (see text for the group definition).

2. samples which showed no spontaneous delamination after deposition but failed the tape test and

3. samples which showed spontaneous delamination immediately or after some minutes of exposure to air.

The second group was found to be very sensitive to humidity while the first group showed no such sensitivity. Table 3.4 shows the affiliation to the three groups for various samples. Figure 3.23 shows examples of all three groups. All the test samples on smooth glass substrates, including those with the thin metallic layer, showed the same behavior in terms of adhesion. Coatings up to a thickness of ∼40 nm belong to group 1, those with a thickness of up to 70-100 nm to group 2 and that with thicknesses above 100 nm belong to the third group. Similar limiting thicknesses were found for stainless steel.

In order to understand what causes the delamination, samples of group 3 were investigated with a microscope. A very characteristic surface structure, which is shown in Figure 3.24, was

Figure 3.24: Microscope image of the surface structure of a group 3 sample. The image shows a section of 280×210 μm^2 size.

found. Surface structures of that kind are known to originate from compressive stress within the DLC film [124] which limits the maximum thickness of adhesive films. The stress, Young's modulus and hardness, which is correlated with the sp^3 fraction, tend to be proportional to each other [41]. Common strategies for maximizing the thickness of films with sufficient adhesion are [41]:

1. surface cleaning by Ar ion bombardment before deposition,
2. using high ion energies for the first stage of deposition,
3. using a carbide-forming adhesion layer such as Si, Cr or W,
4. performing the deposition in multi-layer mode, i.e. depositing many thin DLC layers instead of one thick layer and
5. using softer intermediate layers of e.g. Al, Cu, Ti or stainless steel.

All five strategies were tested for the Tube PLD setup:

1. Most substrates were glow discharge cleaned with argon or oxygen, as described in Section 3.4.2 and shown in Table 3.4.
2. Tests with bias voltage were performed in order to increase the kinetic energy of the carbon ions and hence to increase the penetration depth of the carbon ions. Samples with the bias voltage applied during the entire deposition process as well as samples with bias voltage applied only in a first stage of the deposition were produced. Coatings with a thickness of 60-80 nm deposited on stainless steel substrates with different bias voltages failed the tape test. No improvement compared to samples deposited without bias voltage could be achieved for the glass samples with metallic layers using a constant bias voltage during deposition. Films with aluminum admixture, gradually decreasing bias voltage and a thickness of 70 nm were deposited on stainless steel substrates and passed the tape test. Similar films without the bias voltage failed the test. Films with ∼100 nm thickness which passed the tape test could be deposited on stainless steel substrates. Coatings of similar thickness without bias voltage failed the tape test. However, the maximum bias voltage possible was of the order of 220 V when using the graphite target in order to avoid electric breakdowns.
3. Two different materials were tested as intermediate layer between substrate and DLC film: Al and Cr. Coatings with a thickness of 70 nm and an aluminum interlayer deposited onto stainless steel failed the tape test. Only in combination with a bias voltage, an improvement could be obtained, see previous item. Chromium was used as interlayer material on chromium

coated glass and on stainless steel. While the coatings on the glass substrates were too thin to determine if the adhesion was improved, the coatings on stainless steel reached thicknesses of 80-100 nm and passed the tape test, indicating an improvement of about the same order of magnitude as for the bias voltage. However, whether the two effects are cumulative or not could not be determined as the necessary thicknesses were not reached during tests. The material of the intermediate layer was provided as secondary target, as shown in Figure 3.15. Silicon could not be used as its index of refraction at 193 nm wavelength is well below 1 and hence total reflection occurs at an angle of incidence of 45°.

4. When using the translation of the tube-shaped substrate holder, only films up to ∼30 nm thickness could be deposited as a single layer. For thicker films, the deposition was performed in multi-layer mode, i.e. one layer is deposited while moving the substrate trolley with the smallest velocity possible, the deposition is stopped and the substrate trolley is moved back to its initial position, subsequently performing the deposition for the next layer. No further partitioning of the deposition was made, i.e. no systematic investigation of the adhesion as a function of the number of layers was performed.

5. Aluminum, chromium and stainless steel were admixed each at a time to the first layers of DLC films produced in multi-layer mode. The admixture was done by regularly steering single laser pulses onto the second target. The metal concentration was reduced from layer to layer by using different ratios for the number of laser pulses on the graphite and on the metallic target. Typically one pure metallic layer, three mixed layers and subsequent pure DLC layers formed a multi-layer DLC film. Films with thickness of 60-70 nm and stainless steel admixture deposited on stainless steel substrates failed the tape test. The admixture of chromium, together with a chromium interlayer, as described above, allowed the deposition of a well adherent film with ∼100 nm thickness on a stainless steel substrate. The admixture of aluminum did not improve adhesion as a 70 nm thick AlC layer deposited on stainless steel failed the tape test.

An additional strategy, the deposition of a graphite-like intermediate layer, in order to reduce the stress within the coating, was not of success either, as a coating of 40 nm thickness failed the tape test.

The tests performed up to this point showed that adhesion is worse on smooth substrates. Thus, sand-blasted glass was used as substrate and the resulting films were compared to similar ones deposited on smooth glass. It was possible to grow a DLC film on the sand-blasted glass which passed the tape test and for which a film thickness of 175 nm was obtained by the profilometer. However, the roughness of the sand-blasted glass (see Table 3.3) is too high for using the material as UCN guide (see Chapter 4).

Deposition with about the same parameters as for the sand-blasted glass, as e.g. number of pulses, on microscope slides resulted in a ∼20 nm thick film, giving a significantly lower deposition rate. A possible explanation is an increased re-sputtering fraction. The probability of deposited material to be re-sputtered by subsequent pulses may be higher for smoother substrates due to a lower sputtering threshold caused by a lower averaged binding energy. The maximum deposition rate during the test sample production with the tube-shaped substrate holder was found to be ∼3 pm/pulse on a surface area of about 10 cm^2.

Table 3.4: Samples produced with the tube-shaped substrate holder. All coatings were produced at a pressure level of 10^{-4} Pa or below. The following abbreviations are used: US=ultrasonic bath, Meth=methanol, Ace=acetone, IPA=isopropanol, SSC=stainless steel-carbon, AlC=aluminum-carbon, CrC=chromium-carbon, GLC=graphite-like carbon (i.e. a-C with only few sp^3 bonds). Voltages in brackets denote bias voltage settings during the deposition of a certain layer, ratios denote the number of laser pulses which hit the main and the secondary target, respectively.

Smpl. no.	Subst. type	Cleaning	Laser parameters Rep. rate	Energy/ pulse	no. of pulses	coating description	coating thickness	adh. group
080	A,B,D	US/Meth	10 Hz	110 mJ	23200	2 DLC layers	100 nm	2
090A	E	US/Ace+GDC O_2	10 Hz	120 mJ	24870	2 DLC layers	60 nm	2
090B	E	US/Ace+GDC O_2	10 Hz	130 mJ	24870	DLC(+26V)/DLC	70 nm	2
090C	E	US/Ace+GDC O_2	10 Hz	130 mJ	24870	DLC(-26V)/DLC	80 nm	2
090D	E	US/Ace+GDC O_2	10 Hz	120 mJ	24870	DLC(+50V)/DLC	70 nm	2
090E	E	US/Ace+GDC O_2	10 Hz	130 mJ	24870	DLC(+75V)/DLC	60 nm	2
090F	E	US/Ace+GDC O_2	10 Hz	130 mJ	24870	DLC(+100V)/DLC	60 nm	2
091A	E	US/Ace+GDC O_2	10 Hz	100 mJ	24870	2 DLC layers	50 nm	2
091B	E	US/Ace+GDC O_2	15 Hz	100 mJ	24870	2 DLC layers	50 nm	2
091C	E	US/Ace+GDC O_2	30 Hz	95 mJ	24870	2 DLC layers	50 nm	2
091D	E	US/Ace+GDC O_2	30 Hz	90 mJ	24870	3 DLC layers	60 nm	2
091E	E	US/Ace+GDC O_2	20 Hz	100 mJ	24880	2 DLC layers	70 nm	2
091F	E	US/Ace+GDC O_2	45 Hz	80 mJ	24885	2 DLC layers	70 nm	2
093A	E	US/Ace+GDC O_2	10 Hz	80 mJ	16580	1 DLC layer	40 nm	1
093B	E	US/Ace+GDC O_2	10 Hz	90 mJ	16580	1 DLC layer	40 nm	2
093E	E	US/Ace+GDC O_2	10/30 Hz	85 mJ	56265	SSC(1:1)/SSC(1:10)/ SSC(1:20)/DLC	70 nm	2
093F	E	US/Ace+GDC O_2	10/30 Hz	85 mJ	106005	SSC(1:1)/SSC(1:10)/ SSC(1:20)/2×DLC	60 nm	2
095A	E	US/Ace+GDC O_2	10 Hz	75 mJ	50540	6×Al(750V,200V,150V, 100V,50V,0V)/2×DLC (750V,200V)/2×DLC	100 nm	1
095C	E	US/Ace+GDC O_2	10 Hz	70 mJ	50540	6×Al(600V,200V,150V, 100V,50V,0V)/2×DLC (330V,200V)/2×DLC	70 nm	1
095D	E	US/Ace+GDC O_2	10/20 Hz	65 mJ	75010	Al/AlC(1:1)/AlC(1:10)/ AlC(1:20)/2×DLC	70 nm	2
095F	E	US/Ace+GDC O_2	10 Hz	110 mJ	16580	AlC(1:10)	70 nm	2
096A	B	US/Ace+GDC Ar	10 Hz	95 mJ	41850	4×DLC(300-220V, 150V,100V,50V)/ 2×DLC	70 nm	1
096B	B	US/Ace+GDC Ar	10 Hz	95 mJ	41850	4×DLC(220V,150V,100V, 50V)/2×DLC	60 nm	1
096C	B	US/Ace+GDC Ar	10 Hz	85 mJ	35333	Al(200V/2×DLC	50 nm	1
098A	E	US/Ace+GDC O_2	10/20 Hz	110 mJ	77183	2×Cr/CrC(1:1)/CrC(1:10)/ CrC(1:20)/2×DLC	100 nm	1
098B	E	US/Ace+GDC O_2	10/20 Hz	110 mJ	75010	Cr/CrC(1:1)/CrC(1:10)/CrC (1:20)/2×DLC,+100V	80 nm	1
098D	E	US/Ace+GDC O_2	20 Hz	110 mJ	33160	CrC(1:1),0V CrC(1:20)/2×DLC,0V	40 nm	2
100A	H	GDC Ar	20 Hz	70 mJ	66320	2 DLC layers (100V)	70 nm	2
100B	H	GDC Ar	20 Hz	65 mJ	99480	3 DLC layers (0V)	70 nm	2
100D	J	GDC Ar	20 Hz	50 mJ	99480	3 DLC layers (100V)	40 nm	1
100E	J	GDC Ar	20 Hz	55 mJ	99480	3 DLC layers (0V)	40 nm	1
100F	J	GDC Ar	10/20 Hz	60 mJ	77183	Cr/CrC(1:1)/CrC(1:10)/ CrC(1:20)/2×DLC,0V	20 nm	1
101B	F	US/IPA+GDC Ar	10 Hz	50 mJ	85073	Cr(100V)/3×DLC(0V)	20 nm	1
101C	F	US/IPA+GDC Ar	10 Hz	45 mJ	68493	Cr(100V)/Cr(0V)/DLC (100V)/2×DLC	20 nm	1
102A	J	US/IPA+GDC Ar	10 Hz	50 mJ	66320	DLC(100V)/3×DLC	25 nm	1
102B	J	US/IPA+GDC Ar	10 Hz	50 mJ	82900	DLC(100V)/4×DLC	60 nm	2
102C	J	US/IPA+GDC Ar	10 Hz	50 mJ	99480	DLC(100V)/5×DLC	100 nm	3
103A	G	US/IPA+GDC Ar	10 Hz	50 mJ	82900	DLC(150V)/DLC(20V)/DLC	175 nm	1
103B	G	US/IPA+GDC Ar	10 Hz	45 mJ	66320	DLC(150V)/DLC(20V)/2×DLC	100 nm	1
103C	G	US/IPA+GDC Ar	10 Hz	60 mJ	66320	DLC(150V)/3×DLC	60 nm	1
104A	I	US/IPA+GDC Ar	10 Hz	60 mJ	116060	GLC/6×DLC	20 nm	1
104D	I	US/IPA+GDC Ar	10 Hz	60 mJ	132640	GLC/7×DLC	40 nm	2

3.5 Limits and Constraints

A variety of coatings was produced under conditions similar to those of the production of neutron guides. It was found that the sp^3 fraction did not exceed 45% when the substrate was moved during deposition. Low-energetic ablated carbon species are considered responsible for the low sp^3 fraction, which can be understood with the subplantation model, as it is described at the beginning of this chapter. This is consistent with the finding that for fixed substrates at ideally aligned positions the sp^3 fraction was found to be up to 70%. However, from various publications it is known that PLD at 193 nm wave-length should be able to produce DLC coatings with a sp^3 fraction of up to 85%. Limiting factors for the Tube PLD setup may be (1) an average kinetic energy of the carbon species in the ablation plume well below 100 eV and (2) a flat energy distribution, including kinetic energies too low for the growth of a sp^3 rich film.

An influence which belongs to category (1) may be the low transmission of the laser beam along the optical path. Most of the transmission losses, about 25%, are caused by the fast steering mirror, which is smaller than the cross section of the laser beam, and by the reflection at the entrance window system of at least 20%. Additional smaller loss factors, as from e.g. the fixed mirrors, further reduce the maximum energy which reaches the graphite target to less than half of the energy at the output of the laser. The coatings of the mirrors and the lens are close to their limits in terms of durability as the high power laser beam causes minor damages within the coatings.

An additional reduction of the kinetic energies of the ablated carbon species is caused by the use of a lens with large focal length, up to 2 m. This leads to a relatively large target area which is illuminated by the laser beam. The situation gets worse by the tilt angle of the target of 35°, which leads to an increase of the illuminated area by a factor $\cos(35°)=1.74$ compared to normal incident light. Thus, the energy density per pulse on the target may be marginal. Applying a bias voltage between target and substrate affects only the small fraction, ∼15% [123], of ionized particles in the ablation plume. It is therefore not surprising that an applied bias voltage does not positively affect the sp^3 fraction.

Detailed information of the energy distribution is not available as the Tube PLD setup lacks of any plume investigation equipment. Implementing such an equipment is not trivial as the space inside the substrate tube is strongly limited. However, the diffraction pattern in the laser beam, as described in Section 3.3.1, certainly has a non-positive effect on the kinetic energy distribution of the ablated carbon species, being the main influence of category (2). Using a rotating target and a fixed laser beam would allow for using a beam mask in order to block the low-density parts of the laser beam. Alternatively, the two-inch version of the fast steering mirror would allow for the elimination of the two fixed mirrors as the only reflection could be done in the horizontal plane. This would significantly (by up to 50%) increase the energy which reaches the target.

The determination of the energy density on the target is found not to be very reliable if done by monitoring the energy fraction transmitted by the first fixed mirror. As a consequence, the thickness of the coatings is rather un-reproducible. A more stable and reliable method to ensure homogeneous ablation rates by a constant energy density on the target is to monitor the resulting plume by e.g. an ion probe.

While the relatively low sp^3 fraction may be troublesome, the really serious problem is the insufficient adhesion of DLC films with a thickness above 100 nm. As described in the previous section, applying a bias voltage or using an intermediate layer made of chromium improved the adhesion slightly, although it could not be determined whether the two effects are cumulative or not. An improvement was found only for relatively rough substrates. Using common strategies for adhesion problems, no improvement of the adhesion could be achieved for smooth substrates.

Furthermore, deposition rates of 3 pm/pulse or lower for an area of ∼10 cm^2 were found. A rough estimation of the number of pulses needed for coating a tube with 1 m length and 7 cm inner diameter with a 200 nm thick DLC film, assuming the growth rate to be constant and the

adhesion problems to be resolved, yields

$$\text{no. of pulses} = \frac{\text{film thickness} \cdot \text{surface area}}{\text{deposition rate}} = \frac{200\,\text{nm} \cdot 2200\,\text{cm}^2}{3\,\text{pm/pulse} \cdot 10\,\text{cm}^2} = 1.47 \cdot 10^7. \tag{3.2}$$

This number of pulses could be achieved with about 9 days of continuous deposition at 20 Hz repetition rate or about 17 days at 10 Hz. A very reliable laser system is required for such long deposition times. However, the laser used in the Tube PLD setup was manufactured in 1990 and required already during the test measurements described here two major maintenance occasions involving a specialist from an external company (Radiant Dyes). An additional problem in the high voltage system of the laser lead to additional pulses. Such artificial pulses are characterized by non-homogeneous discharges inside the laser cavity which lead to the sputtering of the discharge electrode material (nickel). The sputtered nickel covers the output coupler on the area of the beam cross section, leading to a rapidly decreasing energy per pulse. If the additional pulses appear in rapid succession, the laser is switched off by an interlock. Such a situation abruptly finished the production phase of the test samples described in Section 3.4.3.

Thus, the present Tube PLD setup is not able to produce long UCN guides with large inner diameter. However, the coating of shorter parts which require substantially less pulses may be possible.

A significant improvement could be achieved by replacing the laser with a newer, more reliable model, equipped with unstable resonator optics which do not produce a diffraction pattern as the one observed with the present laser. With a more reliable system, more systematic investigations could solve the adhesion problem. Replacing the one inch fast mirror system by the two inch version now available would allow for a more simple optical path which consists only of the lens, the fast steering mirror and the entrance window of the deposition chamber. The benefits would be a higher power density on the target due to decreased losses and a longer deposition time between two gas fillings of the excimer laser, respectively.

Alternatively, a different deposition technique such as vacuum arc deposition or ion sputtering could be used. The production of the carbon plume would be realized outside the present deposition chamber which would allow for a filtering by magnetic fields. The resulting beam would be ionized by close to 100%. The kinetic energy of the ions could be tuned by electric fields which would allow for a close to ideal deposition process that could be sustained for up to days.

Chapter 4

The Double Plate Experiment

While the previous chapters deal with the production and characterization of a specific UCN wall coating material, DLC, this chapter focuses on the determination of the UCN reflectivity of surfaces as they are used for UCN guides. As mentioned in the introduction, it is not only the UCN loss probability per bounce which determines whether an UCN guide has a high transmission or not, but also how the UCN are reflected inside the guide. In addition to the two requirements for a high-quality UCN wall coating material, the high Fermi potential and the low loss probability per bounce, a third criterion exists especially for UCN guides: the reflections of the UCN from the walls of the guide have to be highly specular.

A detailed treatment of reflection by surfaces is given in Section 4.1. In order to investigate the UCN reflection properties of surfaces from various materials, a dedicated experiment was set up at the beamlines PF2-TST and PF2-DIFF at the PF2 instrument of the Institut Laue-Langevin (ILL) in Grenoble. The setup is described in Section 4.5 following an overview of the UCN source at ILL in Section 4.4. A description of the samples tested is given in Section 4.6. Details about the performance of the measurements are given in section 4.7. The experiment was simulated using Monte Carlo (MC) techniques, as described in Section 4.8. Detailed analysis of the measured data was done by a comparison to the MC model, as shown in Section 4.9.

4.1 Reflection by rough surfaces

Real surfaces, as smooth as they may be, are never totally flat on the microscopic level. In many cases, the length scale of the surface roughness is comparable to the wavelength of different kinds of radiation and therefore affects the reflection behavior. Reflections are generally separated in two types:

- **specular reflection**, where the angle of reflection is equal to the angle of incidence and
- **non-specular or diffuse reflection**, where the angular distribution of the reflected radiation is described by a characteristic distribution.

There are many different fields and applications where the two phenomena can be observed, e.g. the "sea clutter" observed in radar images of ships or the specular reflection of sunlight from a wavy water surface under glancing angle of incidence, as shown in Figure 4.1. There is a large body of literature about reflection of electromagnetic waves by rough surfaces, which is summarized e.g. in Ref. [125].

Categorizing a surface as rough or smooth can be done in different ways. A possible categorization is the *Rayleigh criterion*, which considers a surface to be rough if

$$H > \frac{\lambda}{8 \sin \beta}, \tag{4.1}$$

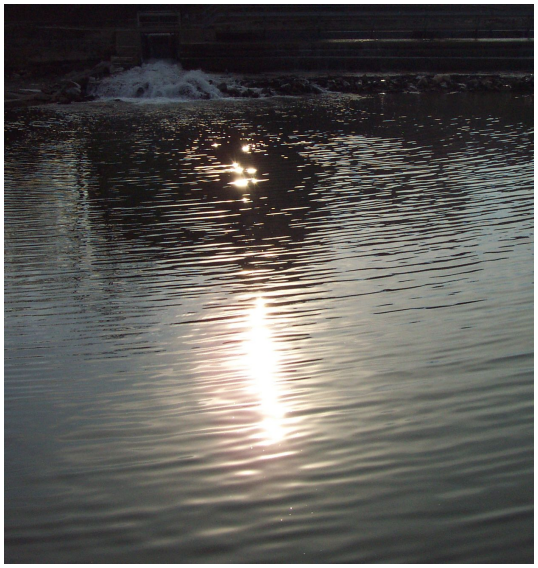

Figure 4.1: Reflection of sunlight from the wavy surface of the river Reuss close to Windisch.

where H is the height of the irregularities of the (step-like) surface, λ the wavelength of the incident radiation and β the angle of incidence.

Many models exist which describe the reflection of electromagnetic radiation from rough surfaces. They follow two different approaches to optics: i) wave optics and ii) geometrical optics. The first group of models are based on solving the Maxwell equations and can also take polarization into account, as e.g. the Beckmann-Spizzichino model [125]: typical assumptions are a Gaussian height distribution of the surface and the radius of curvature of surface irregularities to be large compared to the wavelength of the incident light (Kirchhoff's assumption). The second group of models uses the approximation for short wavelengths of light, i.e. geometrical optics. Lambert [126] was the first to investigate the mechanisms underlying diffuse reflection, resulting in Lambert's law for diffusely reflecting surfaces. For Lambertian surfaces the intensity scattered into a solid angle $d\Omega$ in direction θ (polar angle), I_{Lambert} is found to be independent of the incident angle,

$$dI_{\text{Lambert}} = I_0 \cos\theta \, d\Omega, \tag{4.2}$$

where I_0 is the incident intensity. A surface which satisfies this law appears equally bright from all directions, as e.g. a sheet of paper. There are two mechanisms that can produce Lambertian reflection:

multiple reflections of the light rays by surface undulations before they are scattered into space, as shown in Figure 4.2(a) and

internal scattering of light rays which penetrate the surface and encounter microscopic inhomogeneities in the surface medium, leading to repeated reflection and refraction at boundaries between regions with different refractive indices, as shown in Figure 4.2(b).

Real surfaces can be considered to be partially Lambertian, i.e. a fraction d of the incident intensity is scattered accordingly to Lambert's law. Another fraction s, with $s + d = 1$, is considered to be reflected specularly. Assuming the surface slope α to be normally distributed with standard deviation σ_α, the intensity of specular reflection is found as

$$dI_{\text{spec}} = \frac{I_0 \, d\Omega}{\cos\theta_{\text{spec}}} e^{-\frac{\alpha^2}{2\sigma_\alpha^2}}, \tag{4.3}$$

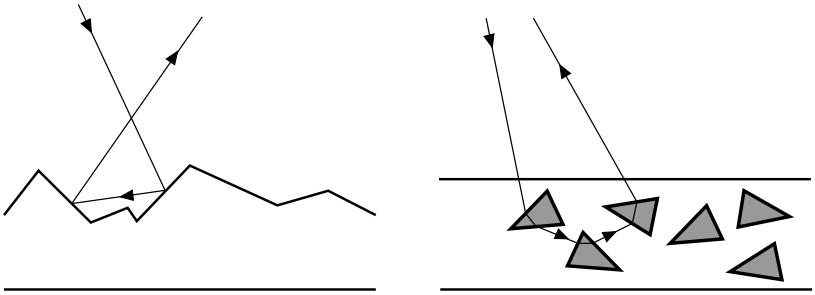

(a) multiple reflections (b) internal scattering

Figure 4.2: Scattering mechanisms leading to Lambertian reflection.

where θ_{spec} is the angle of incidence. This model is known as Torrance-Sparrow model [127]. It assumes that the surface consists of planar micro-facets the dimensions of which have to be much larger than the wave-length of the incident light.

Many publications exist about the reflection of x-rays and neutrons from rough surfaces, e.g. the work of Nevot and Croce [128–130] and their co-workers, which extends over almost two decades. Among other results, their theory relates the specular reflection coefficient of a surface with Gaussian roughness (see below) to the coefficient of an ideal surface. Sinha *et al.* [131] used Born approximation and a form of the distorted-wave Born approximation (DWBA) to a calculation of the specular and diffuse scattering of neutrons from statistically rough surfaces. The DWBA is based on solving the Schrödinger equation for a neutron interacting with a rough surface which involves a Hamiltonian $H = H_0 + V_1(\vec{r}) + V_2(\vec{r})$, where H_0 is the Hamiltonian of the free neutron, V_1 represents the interaction of the neutron with a reflecting medium with a smooth surface and V_2 is the perturbation due to surface roughness.

Model calculations relevant to UCN have been made by Steyerl [132], Ignatovich and Luschikov [133] and Ignatovich [134]. They are valid for surfaces with an RMS roughness below about 5 nm and are quite similar with the exception that Steyerl's model is the only model valid also for neutron energies above the Fermi potential. Therefore in the following, the model denoted as microroughness model refers to Steyerl's work [132]. The microroughness model, using the perturbation method based on distorted Green's function, is found to be equivalent to the DWBA approach [135, 136] and is described in Section 4.3.

Since the formulation of the reflection law for UCN more than 30 years ago, only few experimental studies of the reflection of UCN were performed. Such studies involved either guide tube transmission measurements or the reflectivity from flat samples. Guide transmission generally involves many different angles of incidence and a large surface area, the characterization of which is challenging. Thus, the use of transmission experiments such as in [132, 137, 138] for testing different reflection models is limited. Kügler et al. [139] measured the angular distribution of a beam of very cold neutrons (VCN, 8 m/s$\leq v \leq$ 40 m/s) after passage through a curved guide system with rectangular cross-section. A strong preference for the microroughness model as compared to the Lambert model was found by the analysis. However, the roughness parameters of the surfaces used were on the limit of applicability of the microroughness model (cf. Section 4.3) and no independent measurements of these parameter were available. Hence, this experiment cannot be considered as a satisfactory test.

Steyerl et al. [140] have obtained a specular reflectivity R_s of 0.99 for Ni Replika and glass mirrors as well as $R_s \approx$0.98-0.985 for Ni coatings on glass. The principle of the double plate experiment, as described in Section 4.5.1, was first developed in the search for neutron quantum states in gravity [141] and involves flat samples and better defined angles of incidence. This principle was also applied to measurements of the UCN reflectivity of polished sapphire [142]

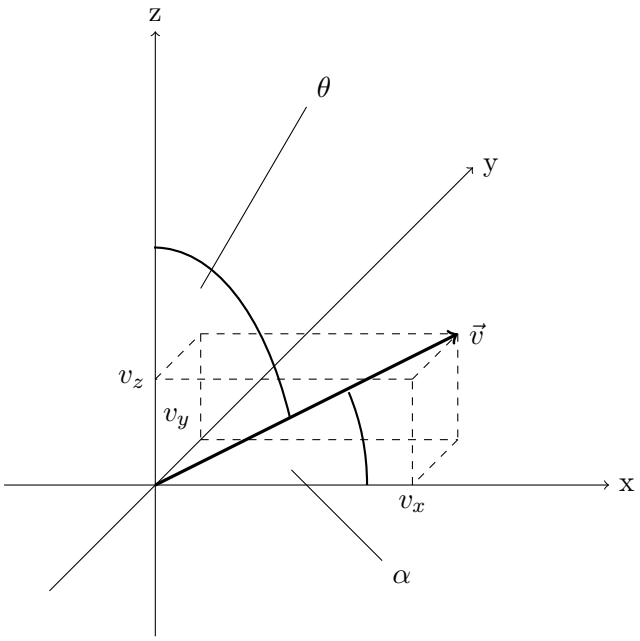

Figure 4.3: Coordinate system used for the double plate experiment and the corresponding considerations.

and of silica, carbon, sapphire and copper surfaces with very small roughness [143]. Specular reflectivities of $0.984 \leq R_s \leq 0.9995$ were measured. The differences in R_s were assigned to the difference of the RMS roughness b, 0.05 nm $\leq b \leq$ 1.5 nm or to a hypothetical inhomogeneity of the coating density. As the experiment excludes diffusely reflected neutrons to a large extent, it does not allow for testing the angular distribution of non-specularly reflected UCN. An earlier, more simple version of the double plate experiment by Plonka et al. [144] used a similar concept but recorded also an unknown fraction of diffusely reflected neutrons for the characterization of nickel coatings prepared by Replika technique[1].

4.2 Reflection angle in a cylindrical neutron guide

As shown in the introduction, the probability of UCN losses due to slits is minimized for cylindrical neutron guides. An experiment as the one described in the following, which tests different qualities of surfaces for their UCN reflectivity, has either to take all possible angles of incidence into account or a selected range in which most reflections occur. Practically, only the second option can be realized. A reasonable angular selection should therefore include the angle of incidence in a cylindrical neutron guide for which a maximum number of reflections occur.

For the considerations to follow, a coordinate system is defined as shown in Figure 4.3. The cylinder axis of the neutron guide defines the x-axis. The z-axis is defined by the vertical direction. As the coordinate system shall be right-handed, the y-axis is chosen accordingly. A vector $\vec{v}$ can be described with its Cartesian coordinates (v_x, v_y, v_z).

For the description of the angular distribution of the neutrons inside the guide, spherical coordinates are defined with α being the polar angle measured between $\vec{v}$ and the x-axis. The corresponding azimuthal angle β, starting on the y-axis into the direction of the z-axis, is omitted in Figure 4.3 for better visibility.

[1]For a description of this method see also Ref. [144]

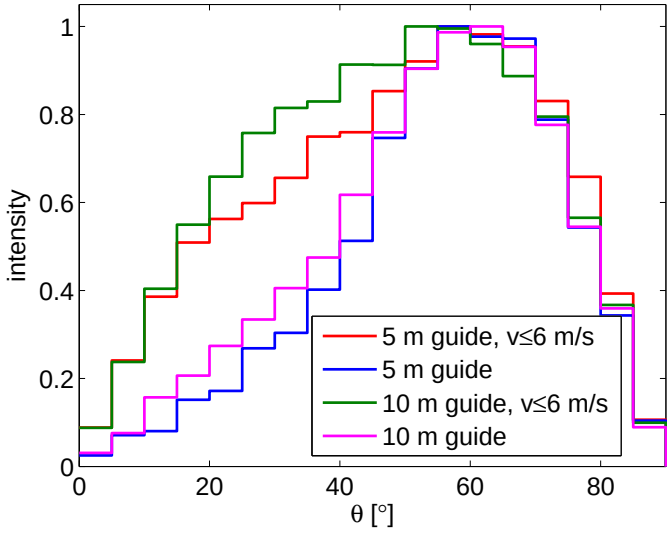

Figure 4.4: Simulated number of UCN reflections which occur in a cylindrical guide from stainless steel ($v_C = 6$ m/s) as a function of the angle of reflection [145].

For the description of the reflection from a surface element it is convenient to use the corresponding polar angle θ, measured between $\vec{v}$ and the z-axis, which is the angle of incidence. The corresponding azimuthal angle ϕ, starting on the x-axis into the direction of the y-axis, is also omitted in Figure 4.3.

For simplicity, the Lambert model is used, which assumes a cosine-distribution

$$\frac{\mathrm{d}I}{\mathrm{d}\cos\theta} = 2\cos\theta, \tag{4.4}$$

for the diffusely reflected intensities. With Equation 4.4, the probability as a function of the polar angle,

$$\frac{\mathrm{d}I}{\mathrm{d}\theta} = \sin(2\theta), \tag{4.5}$$

is found. This function has a maximum at 45°. For a completely diffusely reflecting guide surface, the most probable angle of reflection would therefore be 45°. The reflection frequency is higher for UCN with smaller θ and minimal for neutrons moving in the direction of the guide axis. Thus, the loss probability is higher for neutrons with smaller θ, leading to a more forward peaked UCN distribution and a slight shift of the most probable angle of incidence/reflection to larger values, as shown in Figure 4.4. In the double plate experiment, an angle of θ=50°was selected.

4.3 The microroughness model

In the following the procedure is described which was pioneered by Steyerl and Ignatovich and their co-workers. The expressions derived by Ignatovich and his co-workers, which can be found in e.g. Ref. [26, p. 34] are only valid for $v \leq v_C$. As this condition is not satisfied for part of the neutron velocity spectrum used in the double plate experiment, Steyerl's expressions for the microroughness model, which also extend to VCN, are used.

The topology of a guide surface can be characterized by the autocorrelation function,

$$f(\vec{\delta}) = \lim_{A\to\infty} \frac{1}{A} \int \xi(\vec{\rho})\xi(\vec{\rho}+\vec{\delta})\mathrm{d}^2\rho, \tag{4.6}$$

where $\xi(\vec{\rho})$ is the surface elevation at point $(\vec{\rho}, 0) = (x, y, 0)$ on the surface area A above its average, z=0. The root mean square amplitude of the surface structures,

$$b = \sqrt{\overline{\xi^2}} = \sqrt{f(0)}, \tag{4.7}$$

is usually referred to as the RMS roughness. For most cases of solid surfaces it is convenient to assume an isotropic short-range correlation of Gaussian form,

$$f(\vec{\delta}) = f(\delta) = b^2 \exp[-\delta^2/(2w^2)], \tag{4.8}$$

where w is called the correlation length. The Fourier transform of the autocorrelation function is

$$F(\vec{\kappa}) = \frac{1}{(2\pi)^2} \int_A f(\vec{\delta}) e^{-i\vec{\kappa}\cdot\vec{\delta}} \mathrm{d}^2\delta \tag{4.9}$$

and will be used later on. For the surfaces in question, the RMS roughness is at least one order of magnitude smaller than the typical wavelength of UCN ($\gtrsim$60 nm). Thus, no variation of the direction of the angle of reflection due to tilted surface facets with a length scale $\lesssim$60 nm is to be expected. Considering the Rayleigh distance

$$R = \frac{d^2}{\lambda}, \tag{4.10}$$

where d is the characteristic size of the diffracting structure and λ the wavelength (of the UCN), it is rather wave (Fraunhofer) diffraction which is important due to $R \ll L$, where L is a typical distance from the surface at which the UCN is observed. For an appropriate description of the problem the surface is considered to be ideally flat with small deviations $\xi(\vec{\rho})$, where $\overline{\xi(\vec{\rho})} = 0$.

The behavior of the neutron wave at the interface between medium 1 (usually vacuum) and medium 2 (the wall material) can be described by the wave equation

$$\nabla^2\psi(\vec{r}) + K^2(\vec{r})\psi(\vec{r}) = 0, \tag{4.11}$$

where $K(\vec{r})$ is the neutron wave number equaling k in medium 1 and equaling $k' = nk = \sqrt{k^2 - k_l^2}$ in medium 2, k_l being the limiting wave number from $V_F = \frac{(\hbar k_l)^2}{2m_n}$ as shown in Figure 4.3. The material volume is divided into two regions V_0 and V_1, where V_0 is bounded by an ideally smooth surface and V_1 is a thin surface layer of partly positive and negative 'thickness' $\xi(\vec{\rho})$. The problem can be solved with different methods of perturbation theory, e.g. the DWBA [135, 136] where the scattering amplitude is given as

$$f(\theta) = -(m_n/2\pi\hbar^2)\langle f|V_1|i\rangle \tag{4.12}$$

with initial and final states $|i\rangle$ and $\langle f|$, respectively. Steyerl [132] used a perturbation method based on distorted Green's function to solve the problem. The method was adapted from the

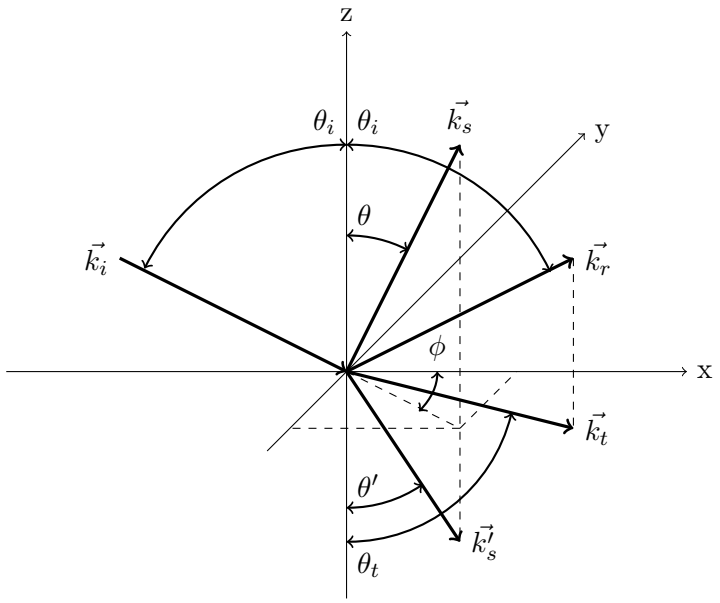

Figure 4.5: Specular and non-specular reflection from and transmission of neutrons through a slightly rough surface (z=0). Wave vectors: ($\vec{k_i}$) incident, ($\vec{k_r}$) specularly reflected, ($\vec{k_t}$) refracted, ($\vec{k_s}$) non-specularly reflected from the wall, ($\vec{k'_s}$) non-specularly scattered into the wall.

analogous treatment of acoustic wave scattering on rough surfaces by Morse and Ingard [146]. The diffusely scattered wave field is given as

$$\psi_s(\vec{\rho}) = -k_l^2/(4\pi) \int_{V_1} G(\vec{r}|\vec{r'})\psi_0(\vec{r'})\mathrm{d}^3r', \tag{4.13}$$

where $\psi_0(\vec{r'})$ is the unperturbed wave field determined by the incident plane wave, i.e. the space representation of $|i\rangle$. The Green's function $G(\vec{r}|\vec{r'})$ corresponds to the spherical wave of free space but is distorted by refraction into the medium. Their approximation for large distances from the wall includes the final state $\langle f|$ which shows the exact equivalence of the Green's function method and the DWBA (see also Refs. [135, 136]).

The amplitude of the non-specularly reflected and the transmitted wave relative to the amplitude of the incident wave are given by

$$R(\theta_i) = \frac{\cos\theta_i - \sqrt{\cos^2\theta_i - k_l^2/k^2}}{\cos\theta_i + \sqrt{\cos^2\theta_i - k_l^2/k^2}} \tag{4.14}$$

and

$$S(\theta_i) = 1 + R(\theta_i) = \frac{2\cos\theta_i}{\cos\theta_i + \sqrt{\cos^2\theta_i - k_l^2/k^2}}. \tag{4.15}$$

The amplitude of the reversely transmitted wave from medium 2 to medium 1 is

$$S'(\theta') = \frac{2\cos\theta'}{\cos\theta' + \sqrt{\cos^2\theta' + k_l^2/k'^2}}, \tag{4.16}$$

where θ' is the polar angle inside medium 2.

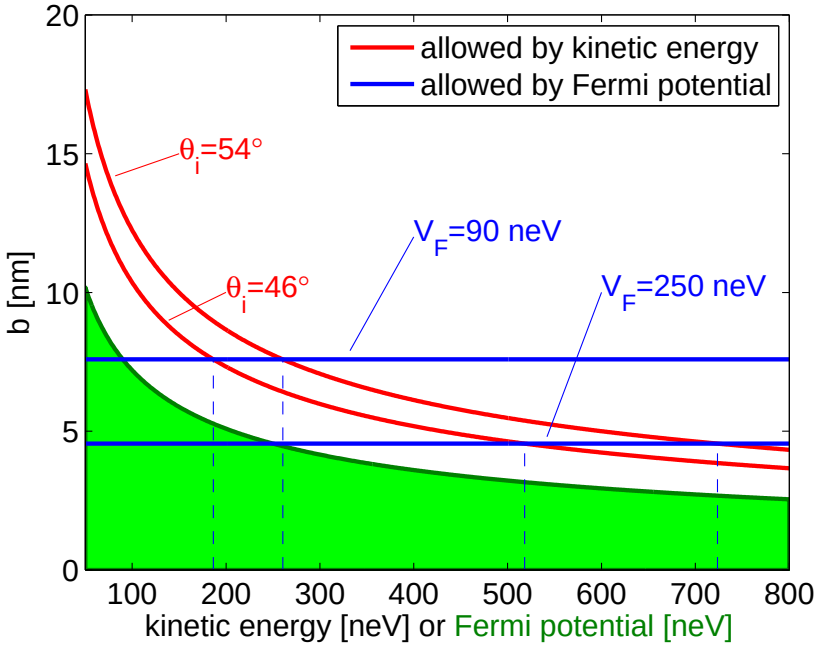

Figure 4.6: Allowed RMS roughness (b) as a function of the kinetic energy of the neutron and of the Fermi potential, shown for typical parameters of the double plate experiment. The two red lines indicate the limiting roughness for condition $2bk\cos\theta_i \lesssim 1$ of the angular range selected with the 30×50 mm^2 aperture S1, i.e. from θ_i=54° (top) to θ_i=46° (bottom). The horizontal blue lines correspond to the maximum allowed roughness for a Fermi potential of 90 neV and 250 neV, respectively (condition $2bk_l \lesssim 1$). The vertical dashed blue lines indicate the maximum kinetic energy for which UCN are reflected. The green area represents the allowed roughness values as a function of the Fermi potential (condition $2bk_l \lesssim 1$).

In the following, the term *microroughness* refers to sufficiently small surface irregularities such that there is constructive interference of scattering from different depths of the surface layer. This is the case, if the conditions

$$2bk\cos\theta_i \lesssim 1, \tag{4.17}$$
$$2bk_l \lesssim 1\,(\text{for } k_l^2 > 0), \tag{4.18}$$
$$2bk\cos\theta_r \lesssim 1, \tag{4.19}$$
$$2bk'\cos\theta' \lesssim 1 \tag{4.20}$$

are satisfied. Figure 4.6 shows the allowed RMS roughness as a function of the kinetic energy of the neutron for which the first two conditions are satisfied. The upper red line indicate the maximum RMS roughness allowed for θ_i=54° (largest angle for S1=30 mm×50 mm) while the lower red line corresponds to the limit for θ_i=46°(smallest angle). The two horizontal blue lines correspond to the maximum roughness allowed by the condition $2bk_l \lesssim 1\,(\text{for } k_l^2 > 0)$ for a Fermi potential of 90 neV and 250 neV, respectively. The vertical dashed blue lines correspond to the maximum kinetic energy for which UCN are reflected from the surface of the plates, taking the different angles of incidence into account. Thus, the maximum RMS roughness allowed for the double plate experiment by the microroughness model is determined by the Fermi potential. The green area in Figure 4.6 represents the allowed RMS roughness values as a function of the Fermi potential.

Using the Gaussian approach for a short-range correlation, Eq. (4.8), the Fourier transform of

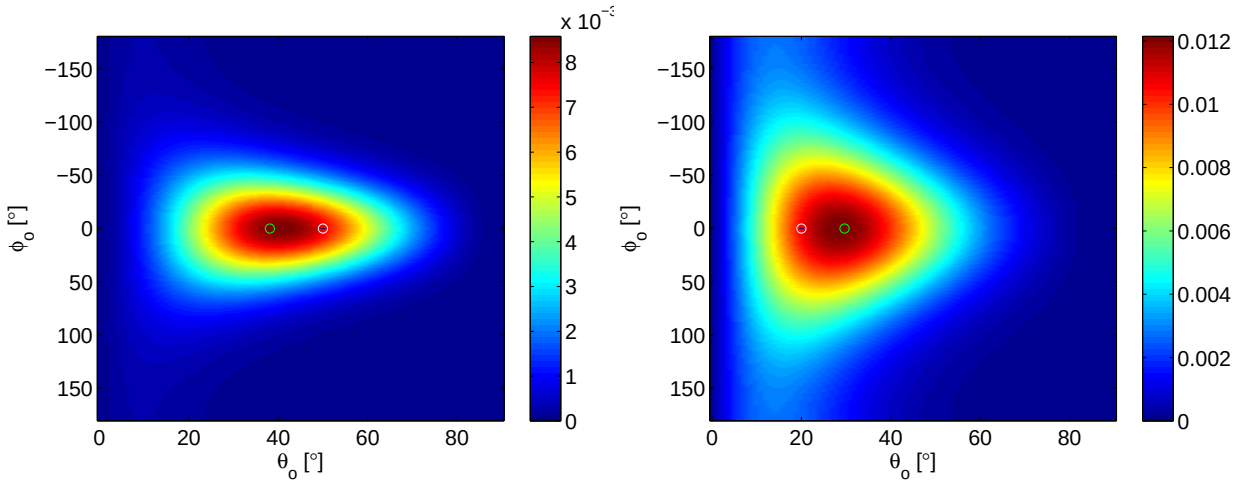

(a) θ_i=50° (b) θ_i=20°

Figure 4.7: Probability of (non-specular) surface reflection into unit solid angle, $I_+(\theta_o, \phi_o)$, described by the microroughness model using V_F=220 neV, $E_{\rm UCN}$=200 neV, b=1 nm and w=25 nm. The white circle indicates the angle of incidence while the green circle denotes the center of mass of I_+.

the correlation function, Eq. (4.9), becomes

$$F(\vec{\mu}) = F(\mu) = \frac{b^2 w^2}{2\pi} \exp(-\mu^2 w^2/2), \tag{4.21}$$

where the square of the component of the momentum transfer parallel to the surface, $\vec{\mu}$, is

$$\begin{aligned} \vec{\mu}^2 = \mu^2 &= k^2(\sin^2\theta_i + \sin^2\theta - 2\sin\theta_i \sin\theta\cos\phi) \\ &= k^2 \sin^2\theta_i + k'^2 \sin^2\theta' - 2kk' \sin\theta_i \sin\theta' \cos\phi', \end{aligned} \tag{4.22}$$

with the primed variables denoting the values inside the material.

The total probability of surface scattering away from the wall into unit solid angle at (θ,ϕ) is obtained by normalization of the outgoing intensity, $\sim r^2|\psi_s(r,\theta,\phi)|^2$, to the incident intensity, $\sim \cos\theta_i$, which leads to

$$I_+(\theta,\phi) = \frac{k_l^4}{4\cos\theta_i} |S(\theta_i)|^2 |S(\theta)|^2 F(\vec{\mu}). \tag{4.23}$$

Similarly, the probability of surface scattering into unit solid angle at (θ',ϕ') within the wall is found to be

$$I_-(\theta',\phi') = \begin{cases} \frac{k_l^4}{4\cos\theta_i} \frac{k'}{k} |S(\theta_i)|^2 |S'(\theta')|^2 F(\vec{\mu}) & \text{for } \cos^2\theta' > -k_l^2/k'^2 \\ 0 & \text{for } \cos^2\theta' < -k_l^2/k'^2 \end{cases} \tag{4.24}$$

Figure 4.7 shows $I_+(\theta_o, \phi_o)$ for V_F=220 neV, $E_{\rm UCN}$=200 neV (the kinetic energy of the UCN), (a) θ_i=50°/ (b) 20°, b=1 nm and w=25 nm, which is a typical case of the surface of a high-quality UCN guide. The angle of incidence is indicated by a white circle. A green circle denotes the center of mass of I_+, i.e. the averaged direction of diffuse reflection. The polar angle of this direction, $\overline{\theta_o}$, is smaller than the angle of incidence for $\theta_i \gtrsim 33.6°$. For smaller θ_i, i.e. for a direction of incidence closer to the surface normal, e.g. 20°, $\overline{\theta_o}$ is larger than the angle of incidence. Normal incidence is the only case for which the diffusely reflected neutrons are distributed uniformly with the azimuthal angle, i.e. where the probability distribution is not concentrated into the reflection plane.

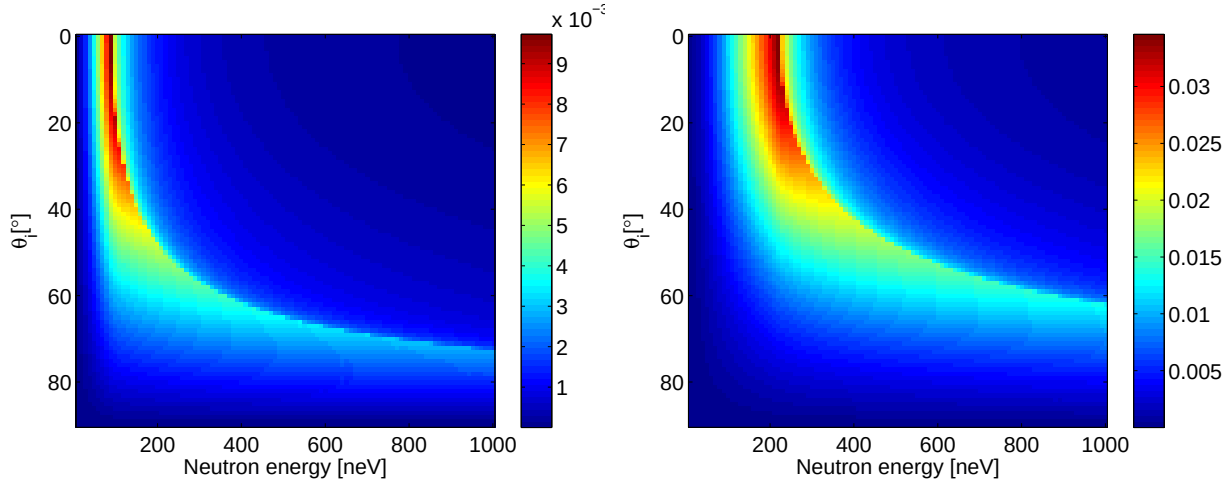

(a) V_F=90 neV (b) V_F=220 neV

Figure 4.8: Integral probability of (non-specular) reflection from a rough surface, R_{ns}, described by the microroughness model using V_F=220 neV, b=1 nm and w=25 nm. Please note the difference in the intensity scale for the two cases.

Following Eq. 4.23, the probability distribution and also the total probability for non-specular reflection,

$$R_{ns}(\theta_i, E_n) = \int I_+(\theta_i, E_n, \theta_o, \phi_o)\mathrm{d}\Omega_o = \int I_+(\theta_i, E_n, \theta_o, \phi_o)\sin\theta_o \mathrm{d}\theta_o \mathrm{d}\phi_o, \tag{4.25}$$

depend on the angle of incidence, neutron energy and Fermi potential. Figure 4.8, which shows R_{ns} as a function of θ_i and E_{UCN} for (a) V_F=90 neV and (b) V_F=220 neV, b=1 nm and w=25 nm, confirms this. The distinct ridge in R_{ns} denotes the threshold condition $E_{\mathrm{UCN}}/\cos^2\theta_i \geq V_F$, where (specular and diffuse) transmission begins and the reflectivity drops rapidly. The largest probability of diffuse reflection is found for normal incident neutrons with kinetic energy slightly below the Fermi potential. Its amount strongly depends on the kinetic energy of the neutron, due to the factor $k^4 \sim E_n^2$ which is found in I_+ by evaluation of $|S(\theta_i)|^2|S(\theta)|^2$. Figure 4.9 shows R_{ns} as a function of the neutron energy with a fixed angle of incidence of 50° for V_F = 90 neV and V_F = 200 neV with b=1 nm and w=25 nm. It is found that the maximum probability for diffuse reflection is about three times larger for materials with high Fermi potential (of the order of 220 neV), such as Ni-V or DLC, compared to glass (V_F ≈90 neV). As mentioned at the beginning of this section, there is another version of the microroughness model, developed by Ignatovich and his co-workers, which is only valid for $v \leq v_C$. Figure 4.10 compares the intensity of non-specular reflection for the two versions; the solid black line corresponds to I_+ of Steyerl's work and the dashed red line is I_{ns} from Ignatovich's model. While the two version agree for incident angles above a critical angle θ_C, which is determined by $v_\perp = v_C$, Steyerl's version show significantly lower values below θ_C and hence a slope which is similar to that of the specular case. Ignatovich's version is therefore thought to give too high probabilities for the non-specular reflection of neutrons with normal velocity component above the critical velocity of the reflecting material.

Surface roughness not only gives a non-specular contribution to the reflectivity but also enhances the loss probability per wall collision μ, see Eq. (1.19. It is found [133, 134] that the loss probability per wall collision for rough surfaces is

$$\mu_r = \mu\sqrt{1 + \frac{2b^2k_l^2}{1 + 0.85k_l w + 2k_l^2 w^2}}. \tag{4.26}$$

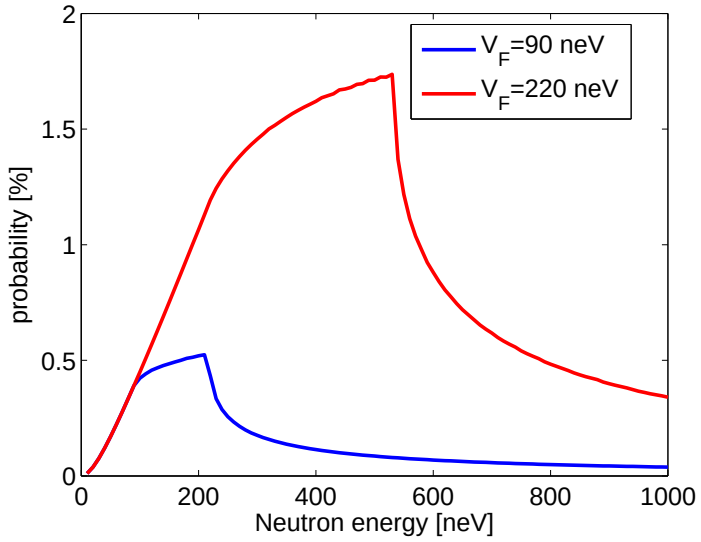

Figure 4.9: Integral probability of (non-specular) surface scattering away from the wall, R_{ns} as a function of the neutron energy for θ_i=50°, b=1 nm, w=25 nm and two different values of the Fermi potential.

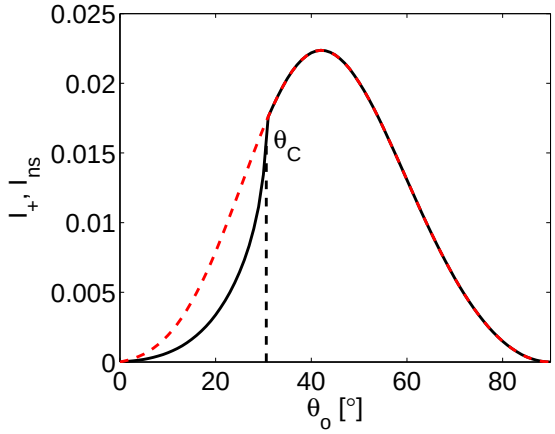

Figure 4.10: Comparison of the non-specular reflectivity obtained by Steyerl's (black solid line) and Ignatovich's (red dashed line) version of the microroughness model. The following parameters were used: $\theta_i = 50°$, $\phi_i = \phi_o = 0°$, $b = 1$ nm, $w = 25$ nm, $v_C = 6.8$ m/s and $v_n = 7.9$ m/s. The critical angle θ_C, for which $v_\perp = v_C$, is found as 30.6°.

For most cases the enhancement of μ is small; the above used example of b=1 nm, w=25 nm and V_F=200 neV, μ is enhanced by a factor of 1.0013. A larger enhancement is found for short correlation length and high roughness; a factor of 1.046 is found for b=3 nm, w=10 nm and V_F=200 neV. Technical information about the implementation of the micro roughness model into the GEANT4UCN [147] code can be found in appendix B.

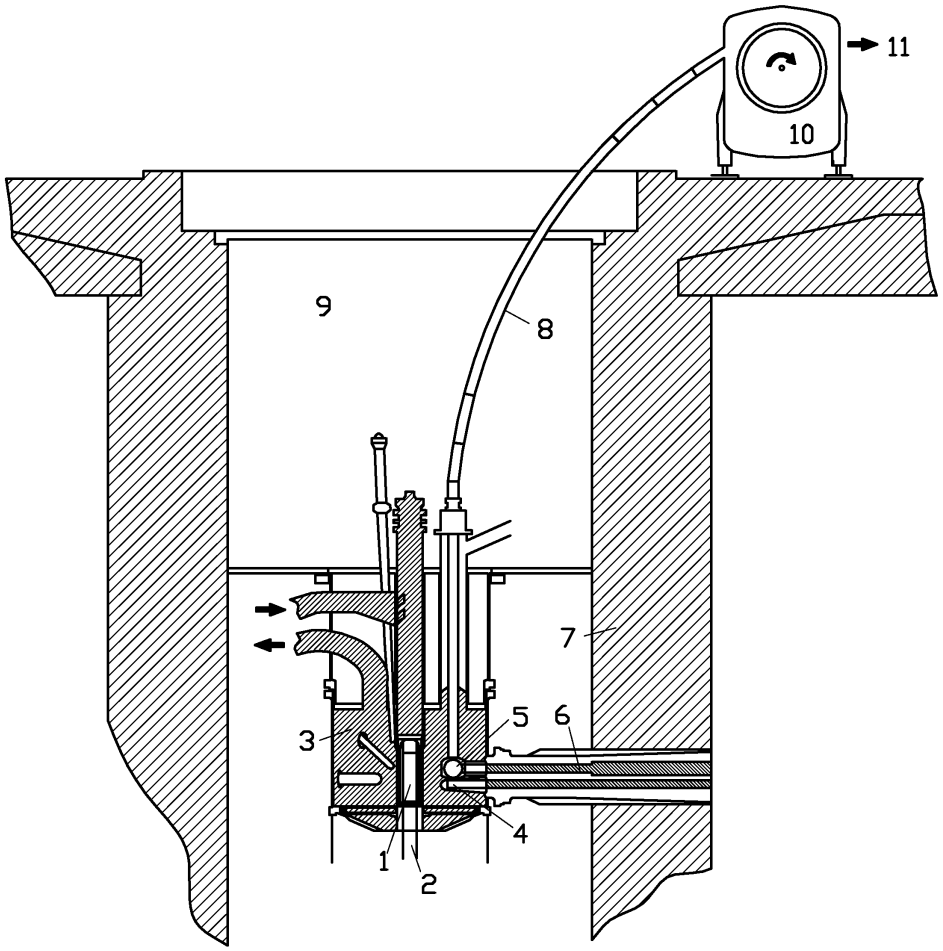

Figure 4.11: Cross section through the ultra-cold neutron source at the Institut Laue-Langevin in Grenoble: [1] fuel element, [2] control rod, [3] heavy water, [4] horizontal cold source, [5] vertical cold source, [6] neutron guides, [7] concrete, [8] bent neutron guide, [9] light water, [10] neutron turbine, [11] neutron guides to experiments.

4.4 The UCN source at ILL

At ILL, neutrons are produced by a research reactor which was operated at an averaged power of 53.50±0.11 MW during the double plate experiment. A cold source [148] is used for the production of cold neutrons. These are further decelerated in a neutron turbine [140] to produce UCN. A schematic cross section through the ILL UCN source is shown in Figure 4.11.

A single fuel element is placed in the middle of the reactor. A control rod from below controls the neutron production. The fast neutrons are moderated in a heavy water (D_2O) tank surrounding the fuel element. Two cold sources are placed inside the heavy water tank. For the production of UCN, the vertical cold source is used. It enhances the neutron flux above 3 Å and consists of an aluminum sphere of 38 cm diameter containing 20 liters of liquid deuterium at 25 K. A straight vertical neutron guide dips into the deuterium of the vertical cold source and extracts very cold neutrons. It is continued by a curved neutron guide of 12.8 m length with a curvature radius of 13 m. The inner walls of both guides consist of Ni coated glass plates. Due to the vertical

extraction, the neutrons are decelerated by gravity. The curvature of the upper guide part leads to the removal of fast neutrons which are not totally reflected by the guide walls.

Neutrons passing the vertical neutron guides are Doppler-shifted to the ultracold neutron range by the turbine. It consists of 690 cylindrically shaped blades mounted on a wheel with 1700 mm diameter. A 'receding' speed of about 25 m/s of these blades with high quality Nickel surfaces transforms neutrons into the low velocity range of 0 to 15 m/s. Four beamlines are connected to the turbine. One of them (the "TST" beamline) has a continuous beam, whereas a beam distributor guides the beam to one of the other three beamlines ("MAM", "DIFF" and "EDM") at a time. The energy spectra appear to be similar to a Maxwellian spectrum with a maximum at approximatively 10-15 m/s and are characteristic for each beamline. A lower energy cut-off is given by the limiting velocity of 100 μm thick aluminum safety windows, 3.2 m/s, which are mounted at the turbine exits.

4.5 Setup of the double plate experiment

The experiment was located at the "TST" beamline during the 15 days long test run and at the "DIFF" beamline during the 25 days long production run.

4.5.1 Experiment principle

The double plate experiment described in the following is a significantly improved version of the experiment of Plonka et al. [144]. Its aim is to correlate the specular and diffuse UCN reflectivity with the roughness parameters of the surface the UCN are reflected from. It records specularly and diffusely reflected neutrons in a way which allows for a significant test of different UCN reflection models. The experiment is based on the measurement of the transmission of a collimated UCN beam which is reflected k-times between two plates with known surface roughness. The variation of the gap size g between parallel plates allows for the adjustment of k. This leads to a gap-size-dependent transmission, which is

$$T(k) = T(k(g)) = (1-\mu)^{k(g)} = R_s^{k(g)} \tag{4.27}$$

for totally specularly reflected UCN. As the number of reflections k is of the order 70 to 140, diffuse reflection is likely to happen at least once during transmission through the plates. This and the possibility of non-parallel plate configurations which allow for the separation of diffusely and specularly reflected UCN make a simple analysis by evaluation of Equation 4.27 for different gap sizes impossible. Thus, the analysis is performed best by MC simulations. More detailed information about the different measurement configurations can be found in Section 4.7, after the description of the double plate setup.

4.5.2 Setup used during the test run

The experiment was mounted on the existing common platform of the "TST" and the "EDM" beamlines. The controls including electronics and the data acquisition (DAQ) system were located close to the experiment on the same platform. A schematic view of the setup at the "TST" beamline is shown in Figure 4.12a. The vertical position of the neutron guide between the turbine and the experiment (item 1 in Figure 4.12a) was 1.8 m above the platform. Nickel coated stainless steel guides with 70 mm diameter were used. A beamline shutter (item 2) was installed in front of the experiment. A vertical neutron guide to the monitor detector (item 6) was connected to the horizontal guide by using a T-piece (item 3) with a circular opening of 16 mm diameter. The entrance windows of both detectors (items 6 and 7) were approximately 1.1 m below the central axis of the horizontal neutron guide. This ensures that the kinetic energy of the UCN arriving at

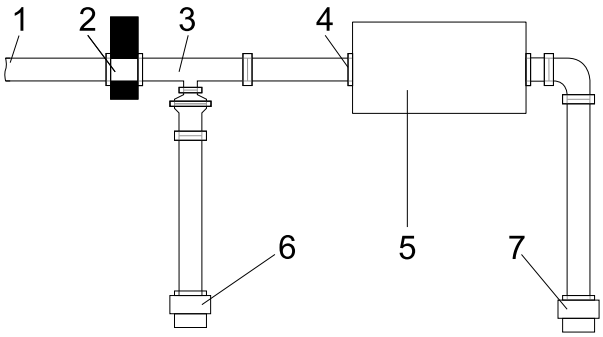

(a) setup at the "TST" beamline

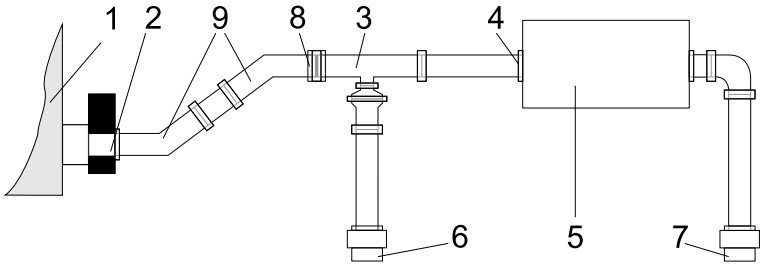

(b) setup at the "DIFF" beamline

Figure 4.12: The setup of the guide surface investigation experiment (not to scale). [1] Guide to UCN turbine (a), UCN turbine (b), [2] beamline shutter, [3] T-piece for connection to the monitor detector, [4] entrance main chamber, [5] main chamber, [6] monitor detector D1, [7] detector D2, [8] aluminum vacuum separation foil, [9] 30° bends of the neutron guide.

the detectors is well above 54 neV necessary for the transmission through the aluminum entrance windows of the detectors. The distance between the T-piece opening and the entrance into the main chamber (item 4) was 85 cm. A detailed description of the main chamber (item 5) and the elements therein is given in section 4.5.4.

The neutron guide between turbine and experiment, including the vertical guide to the monitor detector and the front part of the main chamber, was pumped using a turbomolecular pump with an oil-free roughing pump. A further pre vacuum pump and a turbomolecular pump was used for the central part of the main chamber. The rear part and the vertical neutron guide to the detector D2 were evacuated by a small pumping station. Pressure gauges were placed close to the beamline exit and directly onto the main chamber. The beamline vacuum was in the high 10^{-6} mbar range, the vacuum inside the main chamber around $5 \cdot 10^{-5}$ mbar.

4.5.3 Setup used during the production run

The experiment was mounted directly onto the frame of the existing platform for the "DIFF" beamline. The controls, i.e. electronics and data acquisition, were located below the platform. A schematic view of the setup at the "DIFF" beamline is shown in Figure 4.12b.

The "DIFF" beamline exits the UCN turbine (item 1 in Figure 4.12b) 43.5 cm above the platform through a beamline shutter (item 2). As the minimum necessary position of the neutron guide entrance of the main chamber (item 5) is significantly higher, two 30° bends (items 9) and a straight guide segment in between were used to raise the level of the neutron guide to a height of 102 cm above the platform. After the second bend, a 100 μm thick aluminum foil was mounted

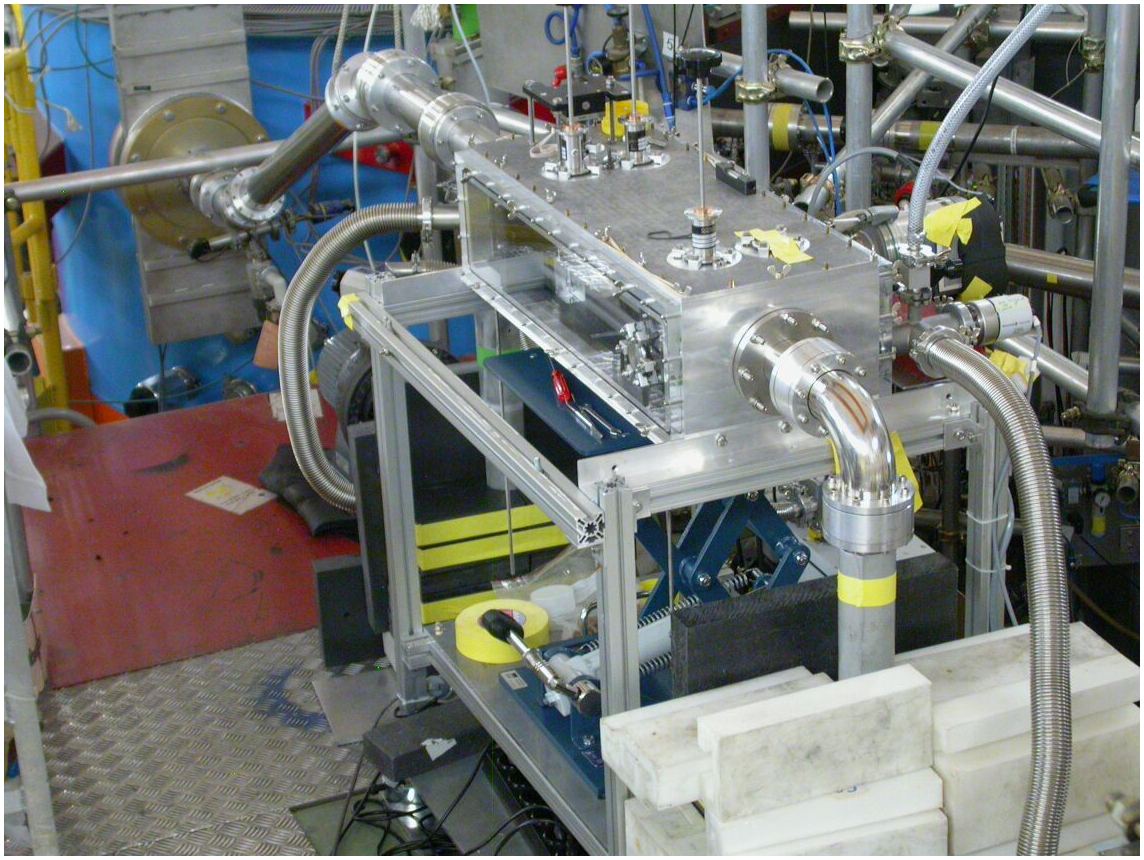

Figure 4.13: The setup at the "DIFF" beamline during the production run of the double plate experiment.

to separate the turbine vacuum from the experiment vacuum. Again, a T-piece (item 3) was used for the connection of the vertical neutron guide to the monitor detector but with a reduced circular opening of 3 mm diameter in order to compensate for the higher UCN rate of the "DIFF" beamline compared to the "TST" beamline. The entrance windows of the detectors were about 60 cm below the horizontal neutron guide. The distance between the T-piece opening and the entrance into the main chamber (item 4) was 83 cm. The main chamber and the elements therein are described below. The inner diameter of the neutron guide elements was 80 mm between the turbine exit and the aluminum foil. Behind the foil a reduced inner diameter of 70 mm was used.

The vacuum system was identical to the one used during the test run with the exception that the front pumping setup was not located directly at the beamline but at the monitor detector. Pressure gauges were placed directly below the T-piece and at the main chamber. The pressure measured below the T-piece was in the low 10^{-5} mbar range and in the high 10^{-5} mbar range in the main chamber. Figure 4.13 shows a photograph of the experimental setup at the "DIFF" beamline.

4.5.4 The main chamber

The main chamber (item 4 in Figure 4.12) consists mainly of a solid aluminum frame with two large aluminum plates mounted to the frame on top and at the bottom. Two smaller aluminum plates including the entrance and the exit neutron guide are mounted to the frame at the front and the rear side. At the two remaining sides of the frame, Plexiglas plates are mounted. The following description of the elements inside the main chamber refers to the items visualized in Figure 4.14.

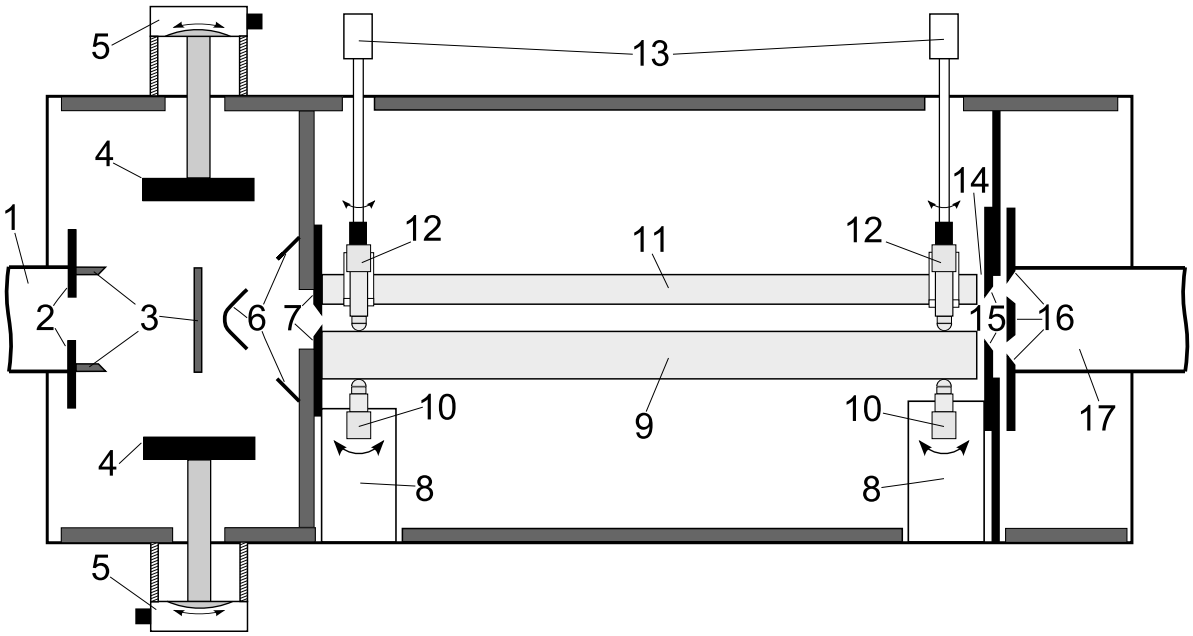

Figure 4.14: The main chamber of the double plate experiment (not to scale). [1] Neutron guide from the turbine, [2] aperture S1, [3] PE-collimator, [4] Ni-coated glass (UCN mirrors), [5] swivel stage for mirror adjustment, [6] wedge shaped beam collimator, [7] entrance aperture S2, [8] aluminum sockets for plate support system, [9] lower plate, [10] lower micrometer screws, [11] upper plate, [12] upper micrometer screws in upper plate brackets, [13] motion feedthrough with VITON™ caps, [14] gap between end of plates and exit aperture, [15] exit aperture S3, [16] double slit aperture S4, [17] exit neutron guide. The dark shaded bars along the inner walls of the main chamber and in front of the entrance aperture S2 represent PE plates.

The neutrons enter the main chamber through the entrance neutron guide (item 1). Part of the neutron beam passes the aperture S1, which is a 1 mm thick circular plate made out of a boron-aluminum mixture (4% boron) with rectangular cutout. Neutrons moving in the horizontal plane are blocked by an absorber (item 3) made of polyethylene (PE). The PE-absorber and the aperture S1 are directly mounted onto the end of the entrance neutron guide. Neutrons moving within the acceptance of the absorber can be reflected from two Nickel coated glass plates, i.e. neutron mirrors (items 4), at the top and at the bottom. Each mirror is mounted on a support which is connected to a swivel stage (items 5) outside vacuum, which allows tilting the mirror by up to a few degrees around a rotation axis on the mirror surface. The distance between each swivel stage and the corresponding aluminum support plate on top and at the bottom of the main chamber defines the vertical position of the mirror inside the chamber and can by adjusted by thread rods. Adjustability and vacuum leak tightness require the use of bellows for both mirror supports. A wedge shaped beam collimator made of titanium with rectangular cutouts (item 6) minimalizes the probability that randomingly scattered neutrons outside the acceptance of the PE-collimator and the mirrors pass the entrance aperture S2 (item 7). The chamfered and 1 mm thick entrance aperture S2 is made of titanium and is covered with double layer, made of gadolinium and titanium. The Gd layer ensures a negligible UCN transmission (Gd has one of the highest neutron absorption cross-sections, $\sigma = 49'700$ barn [85]) at regions of small thickness while the Ti layer avoids dispersal of gadolinium by abrasion. The horizontal midplane of the aperture S2 defines the zero coordinate of the vertical z axis. The opening of S2 has a width of 55 mm and a height of 2.5 mm.

Behind the aperture S2, the central part of the main chamber with the two sample plates is located. It is based on two aluminum sockets (items 8) of which the one close to S2 is equipped

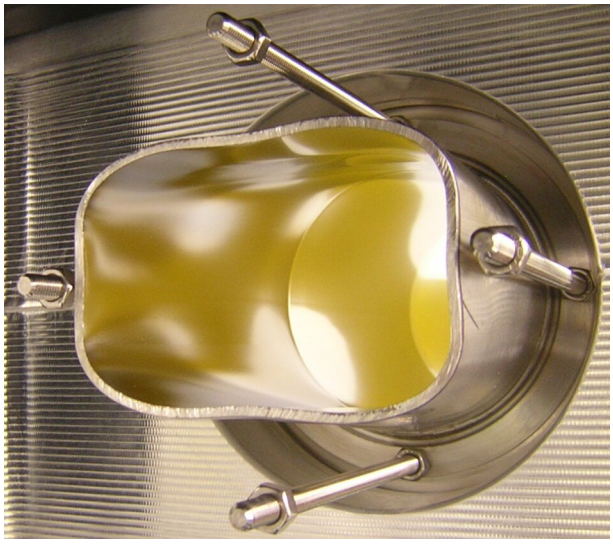

Figure 4.15: The deformed neutron exit guide.

with two and the other one with one micrometer screw (items 10). The lower plate (item 9) with a base area of 500×116 mm^2 lies on the spherical tips of the three micrometer screws. For plates with widths smaller than 116 mm, a dedicated plate adapter is used. It consists of an aluminum plate with a cut-out for the sample plate. Additional three micrometer screws in the plate adapter allow for the alignment of the sample plate relative to the plate adapter. Two brackets, one of them with two (the one close to S2) and the other one with only one micrometer screw (items 12), clasp the upper plate (item 11) with a base area of 500×70 mm^2 from above, fixed by two polyamide screws each. The tips of the micrometer screws of the upper plate are directly placed onto the surface of the lower plate. The upper micrometer screws can be manipulated from outside the main chamber without breaking vacuum by three motion feedthroughs (items 13) which are equipped with a piece of VITON^{TM} at the end. This allows the rotation of the upper micrometer screws by frictional transmission.

Not all sample plates are exactly 500 mm long. This results in a gap (item 14) between the end of the plates and the exit aperture S3 (item 15) made from boron-aluminum. In order to select mostly specular reflected UCN (with unchanged reflection angles; see also Section 4.7.2), a double slit aperture S4, made of titanium, is put at a distance of about 11.4 mm from S3. The slits of S4 have a height of 12 mm and are vertically separated by a bar with 12 mm height, located asymmetrically on the z axis, i.e. from z=-4 mm to z=+8 mm. Aperture S4 is directly mounted onto the exit neutron guide (item 17) and can be replaced by a single asymmetric bar representing the middle part of S4. The exit guide of 70 mm diameter is deformed at its front end in order to adapt its cross-section to the two slits of aperture S4 and is shown in Figure 4.15.

All elements inside the main chamber are mounted onto the lower aluminum plate, except the already mentioned elements mounted onto the entrance and exit neutron guide respectively, as well as the upper mirror and its support system which is mounted onto the upper aluminum plate. Opening of the chamber and changing settings thereafter can be done by controlled lowering of the lower aluminum plate with a lifting platform. As indicated in Figure 4.14, the inner aluminum walls of the main chamber were mostly covered by PE plates.

Most elements including the Nickel mirrors were pre-mounted at PSI. Their positions and distances relative to each others were measured on a 3D measurement machine. Scale settings were documented by photograph. Then the setup was transported to ILL where the settings were verified according to the photographs.

4.5.5 Electronics and Data Acquisition

The following description refers to the setup at the production run. During the test run an almost identical system was used.

Most controls of the experiment, namely the high voltage power supplies for the detectors, the detector readout electronics, the turbine communication, data acquisition (DAQ), data storage and online analysis, were located below the experiment platform. Pressure readout and low voltage power supply were located on the experiment platform.

Turbine control

The UCN turbine at ILL is operated as an user instrument. The neutron beam is shared between the three main beamlines. A stepper motor controlled neutron guide connects one of the three beamlines to the turbine wheel. The setting is controlled by a communication interface which consists of three signals of active-low type:

- Turbine request: A signal provided by the user informs the turbine to move the internal guide to the beamline, where the request comes from. No movement is performed if a veto signal from the currently active beamline is present.
- Turbine veto: A signal provided by the user of the currently active beamline in order to avoid a change of the active beamline.
- Turbine OK: A signal which indicates if a distinct beamline is currently active or not. It is produced by a mechanical contact switch and corresponds directly to the position of the guide inside the turbine.

For the experiment, the three signals were sent and received via an USB-6008 input/output box from National Instruments [149] connected to a personal computer subsequently referred to as control PC. During the production run, the "DIFF" beamline was kept active for 200 s by setting a veto signal. During the following 30 s the veto was not set. Afterwards the veto signal was set again in the case the "DIFF" beamline was still active or a request signal was set in the other case. This "interval mode" was controlled by the control program, which was written in LabVIEW™.

Detectors and readout electronics

Both UCN detectors used in the experiment were gas-filled proportional counters of type Dunia-10 made by A.V. Strelkov. Such detectors consist mainly of a gilt tungsten thread in a volume of 18 mbar ^{3}He, 12 mbar CO_2 and 1070 mbar Ar. Neutrons enter the gas volume through a $\sim$100 μm thick aluminum window. The neutron is absorbed in the reaction $\mathrm{n} + {}^3\mathrm{He} \rightarrow {}^3\mathrm{H} + \mathrm{p} + 764$ keV. The charge carriers produced by the triton and the proton are detected by the gilt tungsten thread which is set to a voltage of roughly 1 kV. The resulting signal is preamplified by the detector electronics. The analog detector output signal is a negative pulse with an amplitude up to 100 mV, a rise time of 300 ns and a length of 2 μs. In addition of the 1 kV high voltage, low voltage of $\pm$12 V is needed for the detector electronics.

Figure 4.16 shows the electronics which provides an amplified detector signal for digitization and a corresponding gate signal for one detector. The ^{3}He-detector (item 1 in Figure 4.16) is supplied with +12 V and -12 V by a low voltage DC power supply (item 2) and with 1200 V (for detector D1, reduced voltage of 1000 V for detector D2) by a high voltage power supply (item 3). The negative analog output signal of the detector electronics is fed into the "normal" input of an ORTEC 450 research amplifier (item 4). There it is inverted, amplified and shaped by a combination of integral and differential settings. The modified signal, taken from the unipolar output of the research amplifier, has a pulse height up to +10 V. It is fed directly into the signal

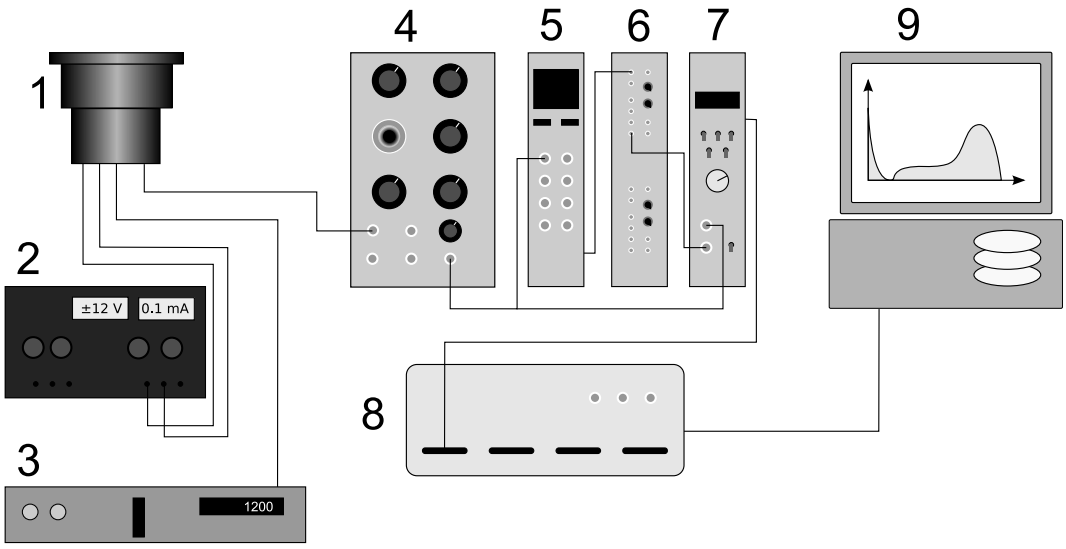

Figure 4.16: Detector, readout electronics for one detector and data acquisition. [1] ^{3}He detector, [2] low voltage power supply, [3] high voltage power supply, [4] ORTEC 450 research amplifier, [5] ORTEC 850 quad single channel analyzer, [6] SIN D102 delayed trigger, [7] FAST 7070 analog-to-digital-converter, [8] FAST MPA-3 data acquisition, [9] Computer for data acquisition and storage.

input of an analog-to-digital-converter (ADC, item 7) and in addition into an input of an ORTEC 850 quad single-channel analyzer (SCA, item 5). For each SCA an acceptance range with a lower level (LLD) and an upper level (ULD) can be set. The settings during the production run were LLD=0.20 V and ULD=9.90 V for both detectors. The output of the quad SCA is connected to the input of a SIN D102 delayed trigger (item 6). No delay is used but the width of the rectangular signal is extended to 3 μs. This signal is then used as a gate signal of the ADC. In order to have identical readout chains for both detectors, items 1, 3, 4 and 7 were present twice.

Data acquisition and storage

The data acquisition used for the experiment is of the type MPA-3 from FAST ComTec [150]. It consists of an electronic box which is shown as item 8 in Figure 4.16, a PCI plug-in module for a personal computer (item 9, subsequently referred to as DAQ PC) and the corresponding software. The system allows the simultaneous readout of both UCN detectors. The software starts and stops the data acquisition and stores the accumulated spectrum in binary format. Additionally each detector event is stored individually in a list file. The list file format is event-based and can be found in Ref. [151]. A digital on/off signal can be obtained at a special output of the MPA-3 system. This signal is read out by the control program written in LabVIEW™. Any changes in the DAQ on/off signal are written into a log file with a run-dependent name. Also included in the log file are changes of the turbine status. The same run number is used to create local copies of both the binary spectrum file and the list file after finishing an acquisition sequence. The list file is converted into a text file which can be read easily. Another text file is written which includes only events that are obtained during the time the turbine is online. The conversion programs are written in C. All data was regularly backed up to a RAID hard disk drive.

Table 4.1: Samples investigated with the double plate experiment. Each sample consists of two plates, denoted as *upper* and *lower*. The terms *normal growth* and *slow growth* refer to a standard process used for Ni coatings at PSI.

Sample no. (upper/lower)	substrate	coating	size (upper/lower) [mm × mm]
Ni 8/9	floatglass	Ni (400 nm) slow growth	70×500 / 116×500
Ni 5/10	floatglass	Ni (1000 nm) normal growth	70×500 / 116×500
NiMo 10/20	floatglass	NiMo (1000 nm) slow growth	70×500 / 116×500
2a/2b	Replika	Ni	70×500 / 70×500
11/11	floatglass	NiV (3 μm)	54×500 / 54×500
DLC Dresden	floatglass	DLC (300 nm)	70×500 / 70×500
SS 2/3	stainless steel	-	66.3×500 / 66.3×500
Optico 3/3	mirror finished glass	-	70×500 / 116×500
Optico 4/4	sand-blasted glass	-	70×500 / 116×500
Optico 5/5	sand-blasted glass	-	70×500 / 116×500
FG 7/15	floatglass	-	70×500 / 116×500
FG-HF 1/12	floatglass	HF etched	70×500 / 116×500

4.6 Samples

As mentioned in the introduction, surfaces of UCN guides have to have a high Fermi potential, a low loss probability per wall collision and a highly specular behavior for UCN reflections. There are several materials which satisfy all three conditions if machined the optimal way, which also includes coating a wall material on smooth substrates as floatglass. The influence of surface roughness to the specularity of UCN reflections can be investigated best with variations of the surface quality of the substrate material. Thus, the surface of floatglass was treated in different ways. Table 4.1 shows a list of the samples investigated with the double plate experiment.

4.6.1 Sample production and sample treatment

The sample plates made from precision-machined stainless steel (material no. 1.4435, AISI/SAE no. 316L) were glossy finished and subsequently electro-polished by Stalder AG, resulting in low roughness with minimized incorporation of polishing agent into the surface. This steel consists of 17-19% Cr, 12.5-15.0% Ni, 2.5-3.5% Mo and minor concentrations of C, Si, Mn, P and S. The resulting Fermi potential is calculated as 186 neV.

The Replika plates were those used in Ref. [144] and were produced by S-DH GmbH. A relatively thin (∼100 nm) Nickel layer is deposited onto a floatglass surface by rf magnetron sputtering. The thickness of the layer is enhanced by galvanic deposition to a few micrometers. Then, the Ni layer is detached from the glass and glued to a substrate (e.g. aluminum) in such a way that the smooth surface which was on the glass is now on the outside. The same company also performed the coating of the NiV plates (7% V) using rf magnetron sputtering directly on the glass plates. The same deposition method was used by PSI for the production of the Ni and the NiMo (7% Mo) coatings.

The DLC coatings were produced by the Fraunhofer Institut für Werkstoff- und Strahltechnik using ion beam assisted deposition (see section 1.5.2) with an IonSys 1600 [152].

Figure 4.17: One of the photographs of a micrometer screw, taken in order to document the proper setting for each screw and sample plate.

The uncoated floatglass samples were either left untreated (FG), etched with hydrofluoric acid (FG-HF; 30 min in a 2% HF bath followed by passivation in 7% HNO_3) or mirror finished by Optico Industrieoptik AG (Optico). Part of the latter samples were additionally sand-blasted on small scale by WÜLSAG in order to produce glass surfaces with different roughnesses.

The sample plates were either cleaned in an ultrasonic bath with isopropanol or wiped clean with a lint-free cloth soaked with isopropanol. Shortly before measuring the plates with the double plate experiment, they were cleaned with distilled water in order to remove any remains from the previous cleaning. The cleaning was done by dowsing the plates with demineralized water and subsequent wiping dry with a lint-free cloth.

4.6.2 Sample alignment

The samples consist of two plates each. Most of the plate pairs were pre-mounted and pre-adjusted at PSI. The position and orientation of the surfaces under investigation were measured with a 3D measurement machine. The settings of the micrometer screws was individually documented by photograph, as can be seen in Figure 4.17. The reproducibility of the settings was better than 5 μm. As cross-check and checkable criterion at the experiment location at ILL, the distances between the upper surface of the lower plate and the top of the aluminum sockets and the clamps of the upper plate and the lower plate were measured with a caliper. Upper and lower plates were selected in such a way that the individual curvatures of the plates canceled each other optimally. Badly matched curvatures may lead to unwanted changes of the reflection angle and thus to additional systematic uncertainties. The curvature of nearly all plates was a single bending with amplitude $\leq$200 μm. Only floatglass plates with small curvature amplitude, i.e. below 70 μm, were selected as samples.

At ILL, the micrometer screws were adjusted for each plate pair by one person accordingly to the photographs taken at PSI. A different person then cross-checked the settings. Subsequently the caliper measurements were repeated.

In many cases another method of adjusting the plates was used. All micrometer screws were adjusted as described above. Then the following procedure was repeated for each of the upper

Table 4.2: Summary of the roughness parameters obtained by AFM measurements: averaged RMS roughness (b_{avg}), averaged correlation length (w_{avg}), minimum RMS roughness (b_{min}) and the correlation length corresponding to the minimum RMS roughness ($w(b_{\mathrm{min}})$).

Sample	b_{avg} [nm]	w_{avg} [nm]	b_{min} [nm]	$w(b_{\mathrm{min}})$ [nm]
Ni 8/9	1.64±0.16	31.6±3.4	1.20	26.2±4.6
NiMo 10/20	1.51±0.13	22.5±1.0	1.09	24.8±5.4
Replika 2a/2b	1.51±0.04	39.2±2.0	0.65	21.4±5.4
NiV 11/11	0.63±0.08	22.8±3.6	0.41	13.3±6.7
DLC Dresden	0.30±0.05	36.9±4.8	0.13	37.9±19.3
SS 2/3	2.54±0.55	37.1±5.1	0.89	13.2
FG 7/15	1.00±0.15	36.5±5.6	0.13	28.5±6.2
FG-HF 1/12	1.36±0.23	41.0±5.3	1.03	28.8±7.3

micrometer screws. The screw was set to a position which resulted in a gap between the two plates that was slightly larger than the diameter of a rod with a precisely known diameter (±4 μm). The upper plate was softly set onto the spacer by unscrewing the micrometer screw. The micrometer screw was screwed in again up to the point where an increased resistance could be felt, indicating the spherical tip of the micrometer screw touched the surface of the lower plate. With this procedure, the uncertainty of the plate distance is the same for all three micrometer screw positions and determined by the uncertainty of the rod diameter.

4.6.3 Characterization of the sample surfaces

The surface structure of the sample plates was investigated by atomic force microscopy (AFM) at PSI. Two-dimensional scans of 1 μm× 1μm size were recorded for several points uniformly distributed over the central 150 mm of the plate surface. Each scan consists of 512×512 data points which results in a resolution of roughly 2 nm/point. This resolution allows for a reliable determination of the correlation length, which is expected to be of the order 10-100 nm (i.e. of the order of typical UCN wavelengths). The RMS roughness b and the correlation length w (cf. Section 4.3) were determined by a program written in MATLAB® [153]. The autocorrelation function is calculated with circular co-ordinates. It is assumed to have a Gaussian shape in radial direction, as supposed by the microroughness model (see Section 4.3). The correlation length is determined in all directions by calculating the $1/e$ contour line w.r.t. the maximum of the correlation function. The resulting values are averaged and are shown in Table 4.2 together with the averaged values of the RMS roughness. For each sample measured by AFM, the minimum RMS roughness, b_{min}, obtained in a single measurement and the corresponding correlation length, $w(b_{\mathrm{min}})$, are also displayed in Table 4.2. It gives a lower limit for the intrinsic roughness of the sample without additional roughness from surface contaminations, e.g. from dust particles.

Additional AFM measurements were performed at larger scan sizes such as 10 μm×10 μm and 100 μm×100 μm. For scan sizes up to 10 μm×10 μm, results for b and w were found which are consistent with those in Table 4.2 but have larger uncertainties. For 100 μm×100 μm, significantly different results were obtained which can be understood with the corresponding lateral resolution of ∼200 nm.

The stainless steel plates show grooves which make the determination of the correlation length in parallel direction impossible ($w \to \infty$). The value given for the correlation length of stainless steel therefore represents the direction perpendicular to the grooves. The HF-etching not only

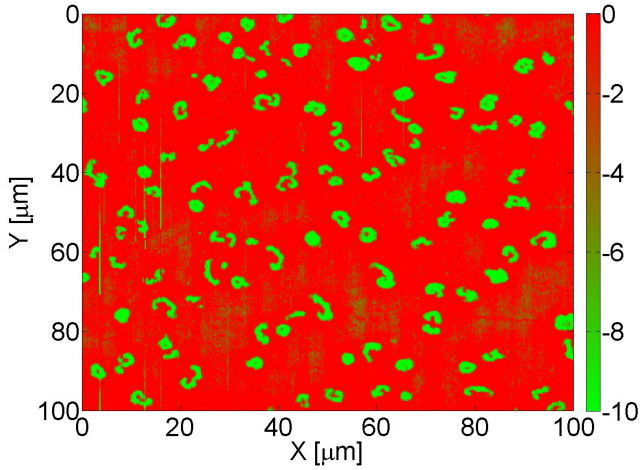

Figure 4.18: AFM picture of the FG-HF plate surface showing the pit-like structures produced by etching. Part of the z-scale is shown as color gradient (see text).

Table 4.3: Summary of the values for the SLD, obtained by cold neutron reflectometry, and the corresponding Fermi potential. The uncertainties correspond to the error of mean (statistical uncertainties). Values without uncertainties indicate single measurements, for which an accuracy of ± 10 neV is assumed.

Sample	SLD [Å^{-1}]	Fermi potential [neV]
Ni on FG	$(9.2 \pm 0.3) \cdot 10^{-6}$	239 ± 8
NiMo on FG	$9.4 \cdot 10^{-6}$	235
NiV on FG	$(8.4 \pm 0.1) \cdot 10^{-6}$	220 ± 2
DLC on FG	$(8.4 \pm 0.1) \cdot 10^{-6}$	220 ± 2
FG	$3.2 \cdot 10^{-6}$	84

increases the surface roughness but also leads to pit-like structures which are not visible on AFM pictures of 1 μm $\times$ 1 μmsize as their diameters are on a micrometer scale. Figure 4.18 shows an AFM picture of 100 μm $\times$ 100 μm size of the FG-HF plate surface. The vertical scale is represented by the color gradient. In order to improve the visibility of the pit-like structures, all points with $z > 0$ are shown with the same color (red). The lower limit of the color scale is set to -10 nm.

The Fermi potential of part of the sample plates was measured by cold neutron reflectometry with the NARZISS instrument [154] at the SINQ spallation source at PSI. The measuring technique is slightly different from the one described in Chapter 2 while the accuracy of the results is about the same. The sample plate was mounted vertically and is rotated by an angle θ while the detector is rotated by $2 \cdot \theta$. Table 4.3 shows the values for the scattering length density (SLD) obtained by fitting the intensity as a function of the rotation angle measured, as described in Chapter 2. No detailed evaluation of the χ^2-distribution as in Chapter 2 was performed. The obtained values were used as starting values for the simulations described in Section 4.8.

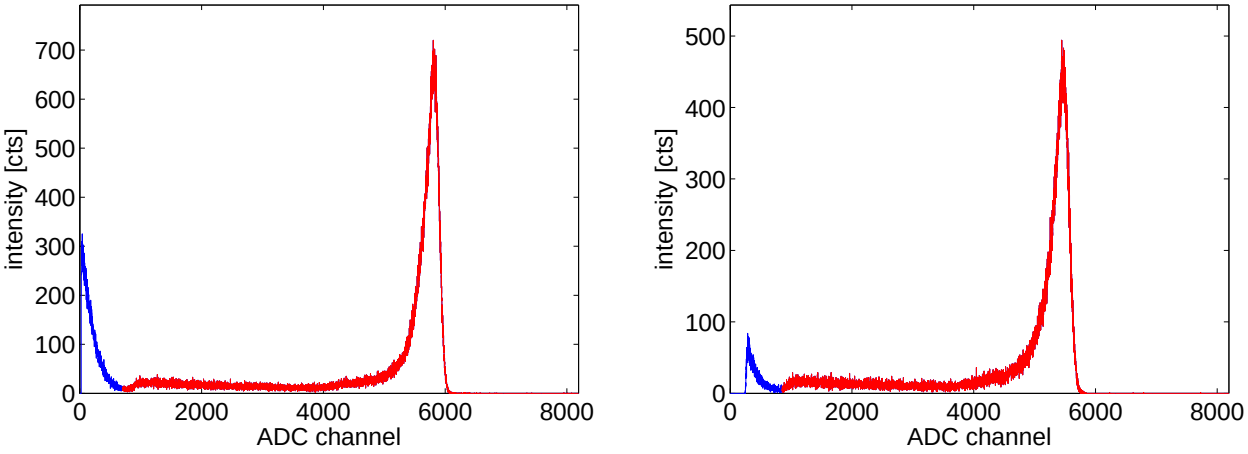

(a) Monitor detector D1

(b) Sample detector D2

Figure 4.19: Digitized pulse height distribution of ^{3}He-detector events.

4.7 Measurements

This section describes the basics of the measurements (Section 4.7.1) and the measuring procedure (Section 4.7.2). Section 4.7.3 describes the measurement of the longitudinal velocity component using a time-of-flight method.

The results of the standard measurements and a description of additional measurements performed for checking systematic uncertainties including the corresponding results are given in Section 4.9.

4.7.1 Detector counts and normalized rates

The pulse height distribution of the amplified pulses of a ^{3}He-detector has a characteristic shape, which is shown in Figure 4.19. Four main features are visible: a) an exponentially decreasing peak at low channel numbers, b) a slightly asymmetric peak of about Gaussian shape at high channel numbers and two plateaus with steps at channel numbers c) 4000 and d)1000. Feature a) is mainly due to electronic noise. Feature b) consists of detector signals which represent the avalanche of charged gas particles produced by both decay products, the proton and the triton. For part of the events only the proton (with a kinetic energy of 573 keV) is detected which corresponds to feature c). Detection of only the triton (with a kinetic energy of 191 keV) leads to feature d). Features c) and d) are plateaus instead of single peaks due to so-called "wall-effects", which means that protons and triton can leave the gas volume before they lost their complete energy, leading to a partial ionization. Features a) and d) are ideally separated by a gap with very few counts. This gap allows for the separation of the signal and electronic noise events in the lower channels. This is done by setting a lower limit for the channel number of accepted detector events (by software). The range above that threshold is usually referred to as region of interest (ROI). Events not related to the UCN beam also occur in the ROI, resulting in a background. This background was recorded in dedicated runs, usually while changing settings of the setup and preparing new measurements. The background rates calculated from the number of counts inside the ROI and the live-time of the ADC were found to be constant during the beamtime, as can be seen from Figure 4.20. The measured rates were fitted with a constant function. The values for minimum χ^2/DOF of the two fits are 3.48 and 1.06. The errors of the measured rates were subsequently multiplied by $\sqrt{\chi^2_{\min}}$

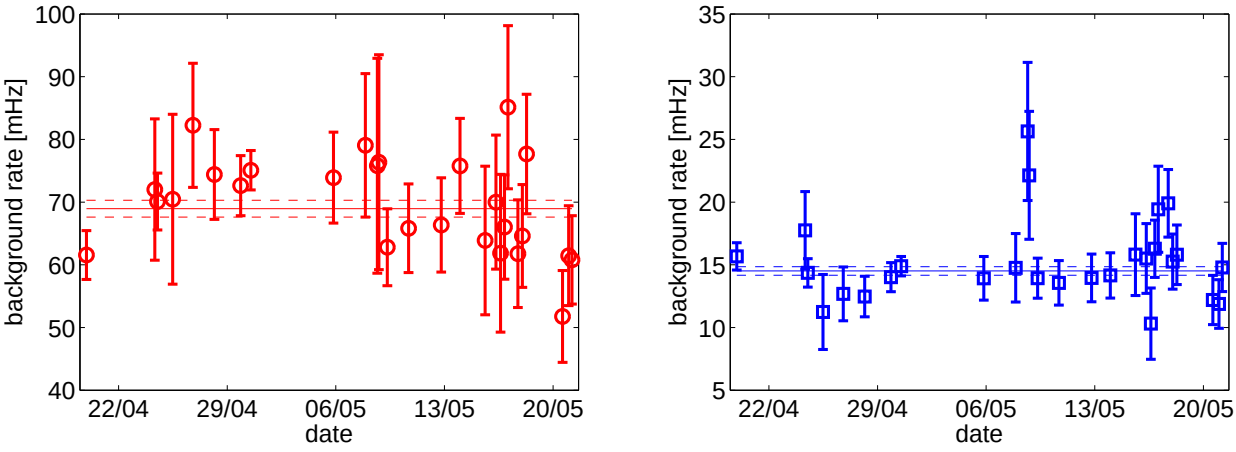

(a) Monitor detector D1

(b) Sample detector D2

Figure 4.20: Background rates measured during the beam time of the double plate experiment. The horizontal solid lines represent the averaged rates with their uncertainties (dashed lines). The uncertainties represent the values for which χ^2_{min}/DOF=1.

leading to the final result for the background rates,

$$n_{D1} = 68.96 \pm 1.34 \text{ mHz} \quad \text{and} \quad n_{D2} = 14.51 \pm 0.34 \text{ mHz}. \tag{4.28}$$

Each measurement consists of the number of detected UCN for the monitor detector D1, $N_{D1,ROI}$, and the sample detector D2, $N_{D2,ROI}$, within the ROIs as well as of the corresponding live-times of the two detectors and their electronics, t_{D1} and t_{D2}, respectively. The background was subtracted from the number of detected counts,

$$N_{D1} = N_{D1,ROI} - n_{D1} \cdot t_{D1} \quad \text{and} \quad N_{D2} = N_{D2,ROI} - n_{D2} \cdot t_{D2}. \tag{4.29}$$

The four values N_{D1}, N_{D2}, t_{D1} and t_{D2} are obtained by the DAQ system described in Section 4.5.5. The ratio N, which is subsequently referred to as the normalized rate, is calculated as

$$N_R = \frac{N_{D2}}{t_{D2}} : \frac{N_{D1}}{t_{D1}}. \tag{4.30}$$

It is independent of fluctuations in the incoming neutron flux, which is proportional to the reactor power. The fluctuations of the reactor power were on the level of 2‰, which is the RMS value of the data shown in Figure 4.21, which shows the reactor power as function of the beam time. The number of counts, N_{Di} with i=1,2, are taken from run files which include only events recorded while the turbine was online.

4.7.2 Standard measurement procedure for the sample plates

For each sample, the goal is to disentangle the contributions of specular and of diffuse reflection. Therefore, different kinds of measurements were performed. They are visualized in Figure 4.22 and are described in the following. The different configurations have in common that UCN undergo an angular selection by the apertures S1 and S2 and the two mirrors located in the region between the two apertures. Fine-tuning of the angle of reflection can be done by adjusting the vertical position of the two mirrors. The angle of incidence (polar angle) on the plates was selected to be θ_i=50°(cf. Section 4.2). In the following, the terms *non-specular* and *diffuse* refer to the situation where the angle of reflection is not identical to the angle of incidence. The *polar angle* used corresponds to θ defined in Section 4.2.

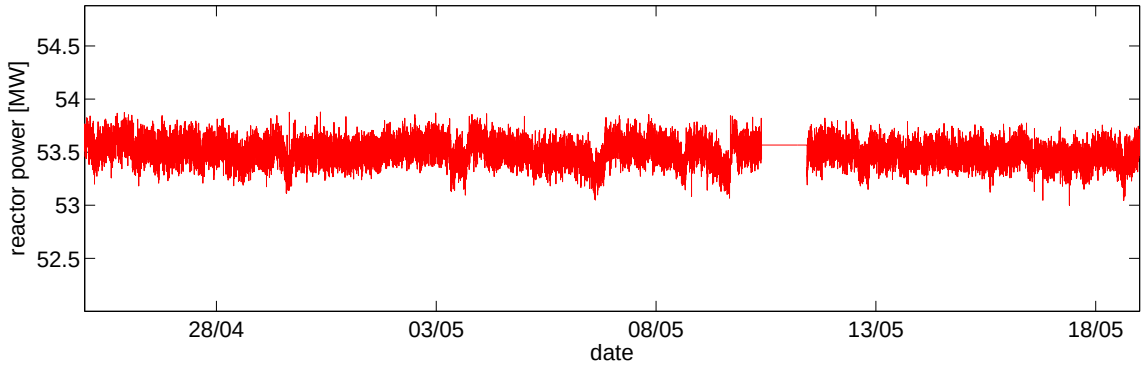

Figure 4.21: Reactor power at ILL from 25.04.2007 to 19.05.2007. The straight horizontal line indicates malfunctioning of the monitoring system, provided for the scientific users, while the reactor still runs.

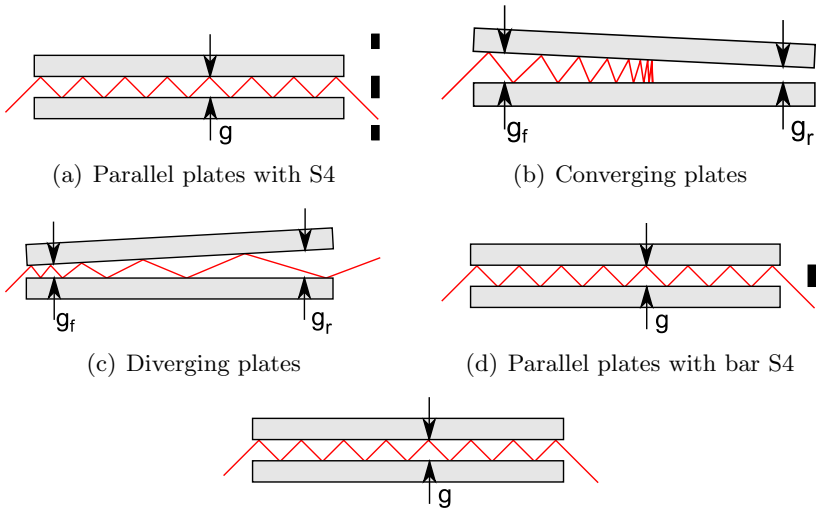

(a) Parallel plates with S4

(b) Converging plates

(c) Diverging plates

(d) Parallel plates with bar S4

(e) Parallel plates without S4

Figure 4.22: Different types of measurements which can be performed with the double plate experiment (not to scale). See text for a description of the methods.

a) **Parallel plates (Figure 4.22a):** The simplest configuration for the two plates is the parallel case, where a well adjustable (see Section 4.6.2) gap in between the plates together with the entrance angle determines the number of reflections performed by UCN until they reach the end of the plates. Only the upper plate was adjusted to change the gap size. For a calculation of the number of reflections between two plates of 500 mm length the UCN are assumed to be reflected only specularly and to have no significant velocity component in y-direction. Values found for θ_i=50° range from 71 reflections for a gap of 6 mm to 141 reflections for 3 mm gap. Neutrons reflected non-specularly can still be detected if they remain within the acceptance defined by apertures S3 and S4 at the end of the plates or if they undergo at least one further non-specular reflection which brings them back into acceptance. All other neutrons, especially those which are scattered into y-direction, are lost. Thus, purely specularly reflected UCN and a small fraction of diffusely reflected neutrons can be detected with parallel configurations. However, for samples with a low fraction of specular reflections a low normalized rate N is to be expected for parallel configurations. The smallest gap for which a measurement is possible

is determined by the entrance aperture S2 and the sharpness of the edges of the plates. It has to be made sure that UCN, which passed S2, make their first reflection on the plates at a position where the surface is flat and is not part of the edge of the plate. This is the case if the radius of the edge is smaller than the vertical space between the edge of aperture S2 and the plate surface. For plates with very sharp edges, measurements with 3 mm gap are possible for the used aperture S2 (height 2.5 mm). The largest gap for which measurements are possible is determined by the aperture S3. Neutrons which pass the plate gap must not be affected by the horizontal edges of S3 in order not to falsify the angle condition of S3-S4. The settings of parallel plate configurations are subsequently denoted by g/g, where g is the gap in between the plates in millimeters at the (front/back) micrometer screws.

b) **Converging plates (Figure 4.22b):** Several possibilities exist for converging configurations; they can be divided into two groups: configurations with only one plate tilted by an angle ζ_1 and configurations with both plates tilted by angles ζ_{2u} (upper plate) and ζ_{2l} (lower plate). For the double plate experiment only configurations of the first group were used. The upper plate was tilted by an angle ζ by lowering the micrometer screw at the rear end of the upper plate. For the calculation of the tilt angle ζ it has to be taken into account that the supporting points of the upper micrometer screws are at a distance of 26 mm from the ends of the upper plate. For measurements with converging plates, the plate gap at the front end of the plates was set to 5 mm. The smallest gap used at the rear end of the plates was 2 mm. Neutrons which are reflected from the lower plate behave the same way as for parallel plates whereas the trajectories of UCN reflected from the upper (tilted) plate are affected by ζ. The angle of incidence of such an UCN is $\theta_i + \zeta$. In the case of specular reflection, the angle of reflection is $\theta_i+\zeta$ w.r.t. the upper plate and $\theta_i+2\cdot\zeta$ w.r.t. the horizontal plane of the experiment, i.e. relative to the surface of the lower plate. Thus, each reflection of an UCN from the upper plate leads to a transformation of the polar angle $\theta \rightarrow \theta + 2 \cdot \zeta$. Repeated reflections from the upper plate transform the initial angle θ_i to $\theta_i + 2 \cdot k \cdot \zeta$, where k is the number of reflections from the upper plate. For k and ζ high enough this leads to normal incidence of the UCN on one of the two plates in the course of the passage through the plates and subsequent change of direction back to the front end of the plates. The smallest tilt angle of the upper plate, for which the purely specularly reflected UCN can be rejected (see Section 4.8.2 for the angular distribution of UCN entering the gap between the plates), is found as ζ=0.24°by calculation. This corresponds to gap settings of g_f=5 mm at the front end and g_r=3 mm at the rear end of the plates. The settings of converging plate configurations are subsequently denoted by g_f/g_r with g_f and g_r in millimeters. Part of the diffusely reflected UCN, which are scattered into larger polar angles and reach the end of the plates with angles that satisfies the S3-S4 angle condition, can still be detected. Converging configurations with tilt angles are the measurements which are most sensitive to diffuse reflection, as shown in Section 4.8.4.

c) **Diverging plates (Figure 4.22c):** Similar to the converging case, diverging plates can be used for the transformation of the angles of reflection. If ζ is the tilt angle of a plate, UCN reflection from this plate leads to $\theta_i \rightarrow \theta_i - 2 \cdot \zeta$. Repeated reflection from diverging plates lead to a reduction of the angle until the end of the plates is reached or until $\theta_i < \zeta$. Practically, relatively large tilt angles are necessary to produce a significant reduction of θ_i. This requires a large gap at the end of the plates. However, this distance is limited by aperture S3, as described above. Thus, configurations with diverging plates were not systematically used for the double plate experiment.

d) **Parallel plates with bar S4 or without S4 (Figure 4.22d and e):** For case a), the parallel configuration, the apertures S3 and S4 define a condition for the exit angle of the UCN at the end of the plates. Purely specularly reflected UCN always satisfy the condition in vertical direction and also part of the diffusely reflected neutrons are accepted. The double slit aperture

Table 4.4: Measured configurations for the various samples investigated with the double plate experiment.

Sample	measured configurations
FG 7/15	3.5/3.5, 4/4, 5/5, 6/6, 5/3, 5/2, 4/4/S and 4/4/O
Optico 3/3	3/3, 3.5/3.5, 4/4, 5/5, 6/6, 7/7, 5/4, 5/3, 5/2, 4/4/S and 4/4/O
FG-HF	4/4, 5/5, 6/6, 5/3, 5/2, 4/4/S and 4/4/O
Ni PSI 8/9	4/4, 5/5, 6/6, 5/3, 5/2, 4/4/S and 4/4/O
Ni PSI 5/10	4/4, 5/5, 6/6, 4/4/S and 4/4/O
NiMo PSI 10/20	4/4, 5/5, 6/6, 5/3, 5/2, 4/4/S and 4/4/O
NiV 11/11	4/4, 5/5, 6/6, 5/3, 5/2, 4/4/S and 4/4/O
DLC 30×50	3.5/3.5, 4/4, 4.5/4.5, 5/5, 5.5/5.5, 6/6, 5/5.5, 5/5.25, 5/4.75, 5/4.5, 5/4.25, 5/4, 5/3.5, 5/3, 5/2.5, 5/2, 4/4/S and 4/4/O
DLC 5×60	3.5/3.5, 4/4, 5/5 and 6/6
Replika 30×50	3/3, 4/4, 5/5 and 6/6
Replika 40×50	5/5, 5/4, 5/3, 5/2.45, 5/5/S and 5/5/O
Replika 10×60	3/3, 4/4, 5/5, 6/6, 6/6/S and 6/6/O
SS 2a/2b	3.5/3.5, 5/5, 6/6, 5/3, 5/2, 6/6/S and 6/6/O

S4 blocks UCN with $\theta \lesssim 30°$, and especially such with $\theta \gtrsim 70°$. As described in Section 4.5.4, the aperture S4 can be replaced by a bar which still blocks UCN with very large polar angles but allows for the transmission of neutrons with smaller polar angles as long as they enter the exit neutron guide of the setup. Removing the aperture S4 allows for the transmission of all neutrons which are within the acceptance defined by the plate exit (S3) and the opening of the exit guide. Configurations with the horizontal bar instead of S4 are subsequently denoted by g/g/S and those without S4 by g/g/O.

By default, three to four different parallel configurations, e.g. 3/3, 4/4, 5/5 and 6/6 for plates with sharp edges, two converging configurations, 5/3 and 5/2, and configurations with bar S4 and without S4 for one gap size, e.g. 4/4/S and 4/4/O, were measured for each pair of sample plates. For plates of special interest, e.g. DLC Dresden, additional configurations were measured. For samples with very low transmission, part of the configurations listed above were skipped due to limited beam time. Table 4.4 shows the measured configurations for the various samples.

4.7.3 Measurements of the longitudinal velocity component in the UCN guide

An adequate MC simulation of the experiment requires information about the energy spectrum and the angular distribution of the neutron beam. Part of this information can be obtained by measuring the distribution of the longitudinal velocity component.

The most convenient way to determine the distribution of the longitudinal velocity component, v_x, of UCN traveling through a guide is the measurement by the time-of-flight (TOF) method, as described e.g. in Ref. [155]. The measurement of v_x at the UCN beam line at ILL was performed directly after the production run of the double plate experiment. The setup used for the TOF measurement is shown in Figure 4.23. An UCN chopper (cf. Ref. [155]; item 6 in Figure 4.23) is mounted right after the T-piece (item 2) used during the double plate experiment. The guide configuration between the UCN turbine and the T-piece was exactly the same as used for the

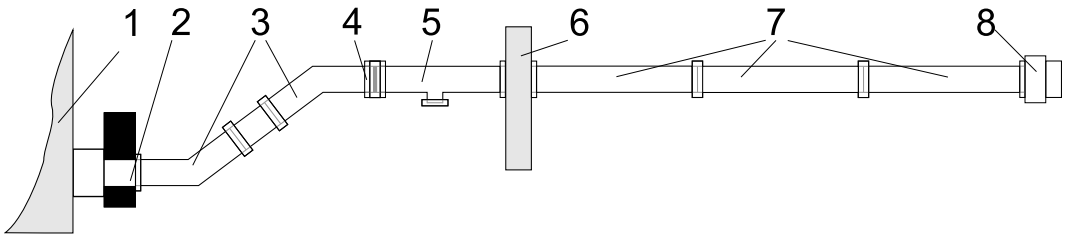

Figure 4.23: The TOF setup at the UCN beam line at ILL: [1] UCN turbine, [2] beamline shutter, [3] 30° bends of the neutron guide, [4] aluminum vacuum separation foil, [5] T-piece for connection to the monitor detector (blanked off), [6] UCN chopper, [7] guide tubes for flight path, [8] detector.

double plate experiment. The UCN detector (item 8), i.e. one of the ^{3}He proportional counters used during the double plate experiment, was connected to the chopper exit by a guide of length L, which was varied (by combining guide tubes of one meter length) between 1 m and 3 m. The chopper was run at a frequency of 0.8 Hz. Once per rotation a start signal is generated. This signal is used as trigger for the data acquisition which records each detector event for 1.25 s as a function of time, t_{obs}, elapsed since the receipt of the trigger signal.

The time t_{obs} recorded by the DAQ may have an offset δt which is the time difference between the trigger signal from the chopper and its real opening time. It is $t_{obs} = t_{real}+\delta t = s/v_{max}+\delta t$ with the true time-of-flight, t_{real}, for a guide length s between chopper and detector. The longitudinal velocity component for which a maximum number of neutrons is detected, is subsequently referred to as v_{max}. Fitting a linear function with slope $1/v_{max}$ and offset δt to the times corresponding to the maxima of the three TOF spectra (shown in Figures 4.24a-c) for s=1,2,3 m results in δt=0.0258 s. The measured TOF spectra could be well fitted by a function consisting of four Gaussians; $\chi^2_{\min}$ is 11.58 for the 1 m data, 2.77 for 2 m and 6.67 for 3 m while the degrees of freedom are 992 for all three lengths. The fits of the spectra are indicated by red lines in Figures 4.24a-c.

The chopper resolution was measured using a very slow rotation (<30 mHz) and with the detector at only 1 m distance from the chopper; it is shown in Figure 4.24d. The recording time of the DAQ was set to 36 s. The chopper resolution function derived from the corresponding spectrum was centered in time, i.e. the halftime of the chopper opening is set to 0. The fitted TOF spectra were corrected for δt. Next, the spectra were de-convoluted using the matrix method. The de-convoluted spectra were found as

$$f_i = \sum_j R_{ij}^{-1} \cdot F_j, \tag{4.31}$$

where $R_{ij} = R(t_i - t_j)$ is the matrix form of the chopper resolution function and $F_j = F(t_j)$ and $f_i = f(t_i)$ are the TOF spectra before and after de-convolution, respectively. For the resulting spectra Four-Gaussian fits were performed; the fitted spectra are shown in Figure 4.25(a). The TOF spectrum for 1 m flight path was not used for further evaluation due to its relatively large uncertainties after de-convolution of the chopper resolution. The data represent the neutron event distribution dN/dt. The velocity distribution in longitudinal direction, dN/dv_x, can be obtained by multiplication of the data with the derivative $|dt/dv_x| = t^2/L$ with the flight path L. The resulting spectra for the longitudinal velocity component, v_x, are shown in Figure 4.25(b). The excellent agreement between both curves is taken as evidence for the reliability and robustness of the measurements and its analysis.

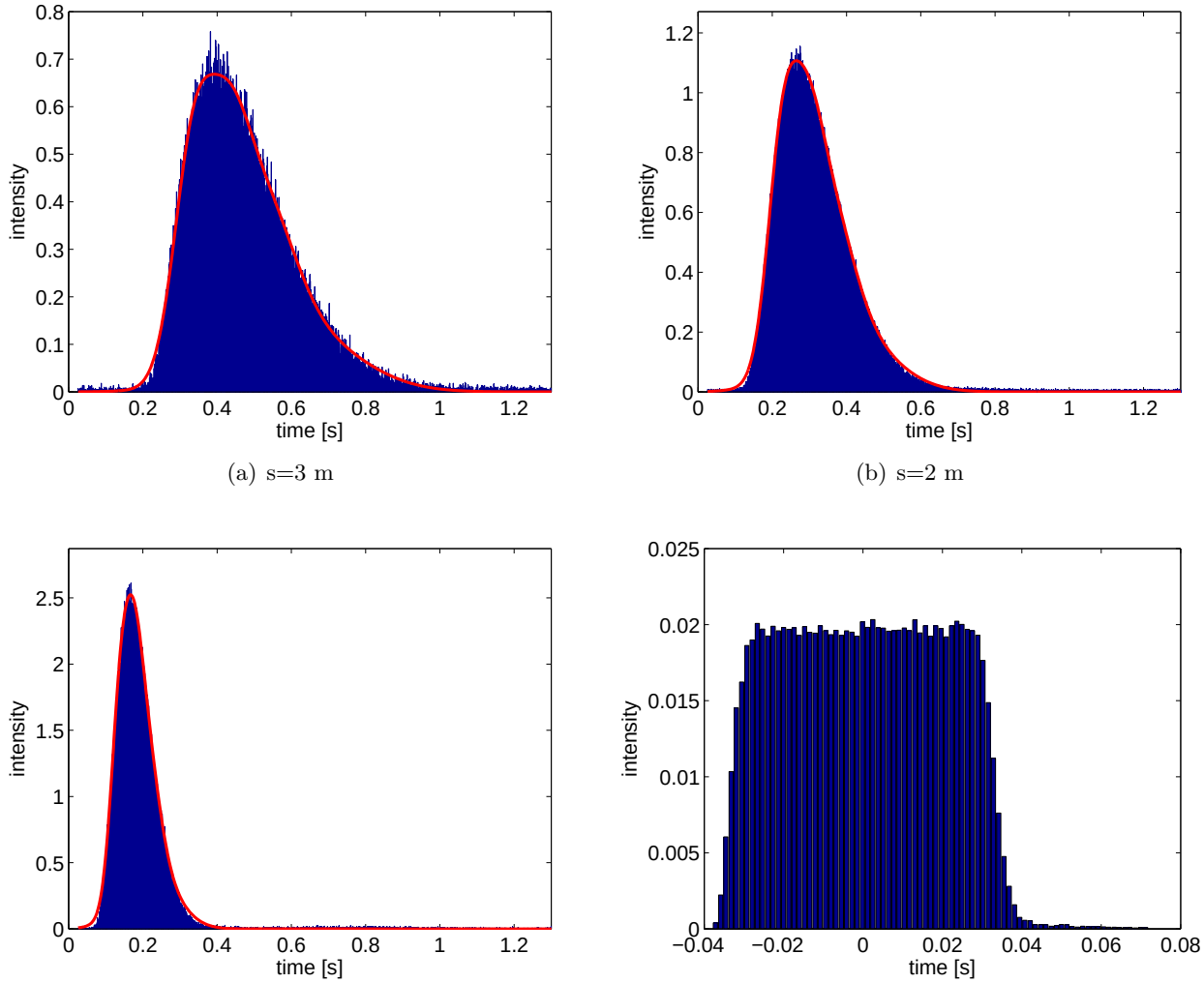

(a) s=3 m

(b) s=2 m

(c) s=1 m

(d) chopper resolution

Figure 4.24: Time-of-flight spectra for different guide lengths (a-c) and the chopper resolution spectrum (d). The TOF spectra are normalized to the number of chopper rotations; the area of the chopper resolution spectrum is normalized to 1.

4.7.4 Reflection from aperture S1

The first aperture, S1, was changed several times during the beam time in order to test for effects connected to the angular acceptance. Different materials with different openings were used, see Table 4.5. It was found that different openings lead to different count rates for the monitor detector D1, also listed in Table 4.5. The count rates were taken from the various measurements performed during the production run. An averaged count rate was calculated for each type of S1, assuming the incoming neutron flux to be constant over the beam time. This is the case, as is shown in Figure 4.21. The change in the D1 rate for different S1 dimensions is caused by the difference in the reflectivity between the S1 types. The reflectivity of S1 is a function of the calculated cross-sectional area blocked by S1 and of the S1 material. Figure 4.26 shows the situation of the neutron guide between the T-piece and the aperture S1. A part k_D of the incoming neutron flux from the UCN source, I_0, is directly transmitted through the opening leading to the monitor detector D1, contributing to the detected intensity I_{D1}. Another part of I_0, k_B, is reflected at the aperture S1. A part of the reflected intensity, $k_R \cdot k_B \cdot I_0$, is transmitted through the opening and

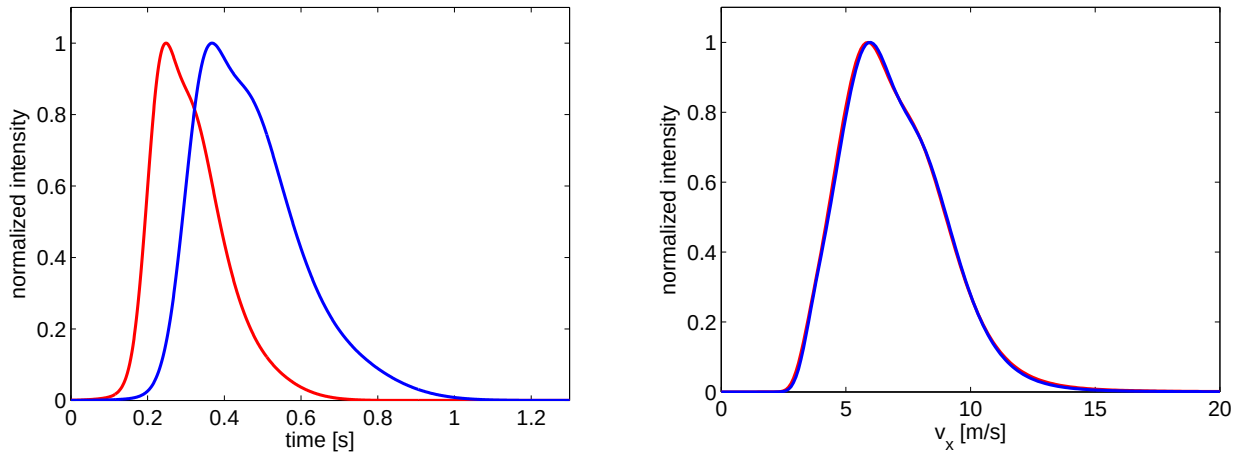

(a) TOF spectra

(b) velocity spectra

Figure 4.25: De-convoluted TOF spectra and distribution of the longitudinal velocity component for the TOF measurements with 2 m (red) and 3 m (blue) guide length. Intensities are normalized to unity.

Table 4.5: Averaged D1 count rates, number of measurements and normalization factors for different types of aperture S1.

S1 material	opening dimensions S1	averaged D1 count rates	no. of measurements	normalization factor
Boral	40 mm × 50 mm	16.827 ± 0.018 Hz	47	1.147 ± 0.002
Boral	30 mm × 50 mm	19.297 ± 0.025 Hz	163	1
Boral	20 mm × 50 mm	21.478 ± 0.092 Hz	3	0.898 ± 0.004
Boral	10 mm × 60 mm	23.873 ± 0.017 Hz	13	0.808 ± 0.002
Titanium	5 mm × 60 mm	15.287 ± 0.020 Hz	4	1.262 ± 0.002

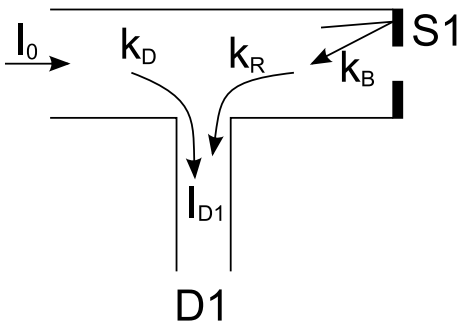

Figure 4.26: Schematic overview of the neutron guide between T-piece and aperture S1 (not to scale).

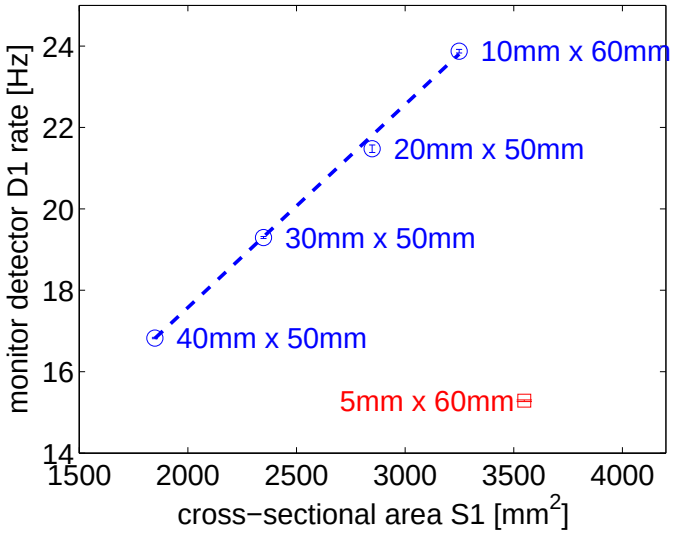

Figure 4.27: Monitor detector D1 rate as a function of the cross-sectional area blocked by aperture S1 for Boral (blue circles) and Ti (red squares).

also contributes to I_{D1}. Thus, the detected rate is found as

$$I_{D1} = (k_D + k_R \cdot k_B)I_0 \doteq I_D + k_B \cdot I_R, \tag{4.32}$$

with $I_D = k_D \cdot I_0$ and $I_R = k_R \cdot I_0$. The factor k_B is the cross-sectional area blocked by S1, i.e. a purely geometrical factor. Equation 4.32 describes the detected intensity at the monitor detector as a linear function of the cross-sectional area of S1 with slope I_R and offset I_D. This model was applied to the different S1 apertures made from the same material, e.g. Boral. Figure 4.27 shows the monitor detector rate as a function of the cross-sectional area of S1 and the corresponding linear function following Equation 4.32. Only statistical errors of the D1 rates are used. Although the χ^2/DOF=8 is relatively large, the quality of the fit is considered to be good as it describes 3 of 4 data points well. The only exception is the point for S1=20 mm $\times$ 50 mm. The poor statistics of this point gives the major contribution to χ^2.

In order to correctly compare measurements with different types of S1, the D1 rates have to be normalized to a single type of S1. As most measurements were taken with S1=30 mm $\times$ 50 mm, this type of S1 was used for the D1 rate normalization, i.e. the D1 rates for all other types were multiplied with the corresponding factor given in the last column of Table 4.5.

4.8 Monte Carlo Simulations

Information on particle trajectories is not easily accessible by UCN detection with proportional counters as used for the double plate experiment. Thus, a model description of the trajectories is needed. Early approaches used analytical models which include kinetic gas theory or diffusion. Such models are inadequate for extensive experimental geometries. With randomized numerical models, e.g. Monte Carlo (MC) simulations, such information can be more easily obtained. Information about earlier MC simulations for UCN applications can be found in Refs. [26, p. 99], [156, p. 95] and [28, 157]. Especially the analysis of the double plate experiment requires the usage of MC simulations as the direction of flight of non-specularly reflected UCN is randomized within a characteristic distribution.

The MC simulation of the double plate experiment was split into three parts:

1. simulation of the UCN trajectory parameters from the turbine to the entrance of the double plate experiment (aperture S1), delivering position, energy- and angular distributions at S1,

2. simulation of the angle selection by the two apertures S1 and S2, including the Ni mirrors, and

3. simulation of the UCN transmission through the double plates, including apertures S3 and S4 and the stainless steel bend at the exit of the main chamber.

The three parts are described in Sections 4.8.1, 4.8.2 and 4.8.3. Part 1 was performed using the MCUCN code [158] (see acknowledgment). A standard code from the particle physics field, GEANT4 [159, 160], and the corresponding extension to UCN physics, GEANT4UCN [147], were used for the simulation of parts 2 and 3. This simulation toolkit has been successfully used for other UCN experiments [20,37]. The code version used as a basis for the simulation is GEANT4.8.2.p01. By default, reflection of UCN by rough surfaces can be modeled with GEANT4UCN by using a constant fraction of non-specular reflection distributed accordingly to Lambert's law. For specularly reflected UCN, only the solution of θ_i=θ_o, where θ_i is the angle of incidence and θ_o is the angle of reflection, is considered. The code was extended with the microroughness model, described in section 4.3, which was only used for the sample plates. For the stainless steel guides, the Lambert model with 1% probability of diffuse reflection was used. This is an adequate description of the guides as no position information is required within the guides and the angular distribution of reflected UCN is of minor importance. The correct implementation of the microroughness model was tested by calculating sample configurations with GEANT4UCN and MCUCN (see Ref. [158]) with subsequent comparison. A visualization of the geometric model is shown in Figure 4.28.

4.8.1 Trajectories passing aperture S1

Stainless steel tubes (V_F=186 neV, cf. Section 4.6.1) with a fraction of diffuse UCN reflection (Lambert model) are assumed. The measured spectrum of the longitudinal velocity component (see Section 4.7.3), v_x, was incorporated. The fraction of diffuse reflection was varied as well as the angular distribution of the input spectrum at the turbine in order to test the output of the guide simulation for systematic effects. Only differences within statistical uncertainties, which were kept below 1%, were found. The present version is calculated using a cosine distribution as input of the guide simulation, a fraction of non-specular reflection of 1% and a loss probability of 10^{-3} per wall collision.

The angular distribution of the guide output spectrum is found to be energy- and slightly radius-dependent. Subsequent descriptions refer to the polar angle α defined in Section 4.2. The azimuthal angle, measured from the y-axis, is referred to as β. The simulated UCN which pass S1 are characterized according to their $v_x = v \cdot \cos\alpha$. An interval of Δv_x=0.5 m/s is used for each group. Different simulation was performed corresponding to the individual openings of aperture

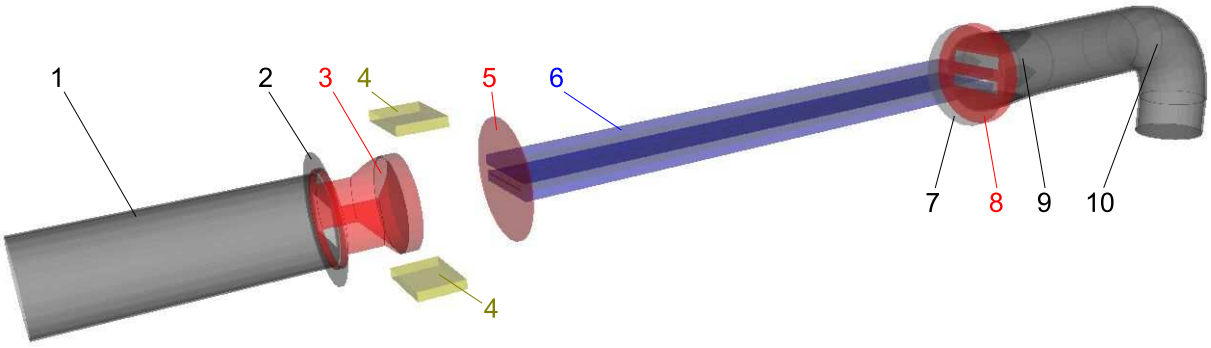

Figure 4.28: Overview of the GEANT4 simulation model of the double plate experiment: [1] UCN entrance guide, [2] aperture S1, [3] PE-absorber, [4] Ni coated mirrors, [5] aperture S2 in front of the plates, [6] sample plates, [7] aperture S3 at the end of the plates, [8] double slit aperture S4, [9] deformed UCN exit guide, [10] stainless steel bend.

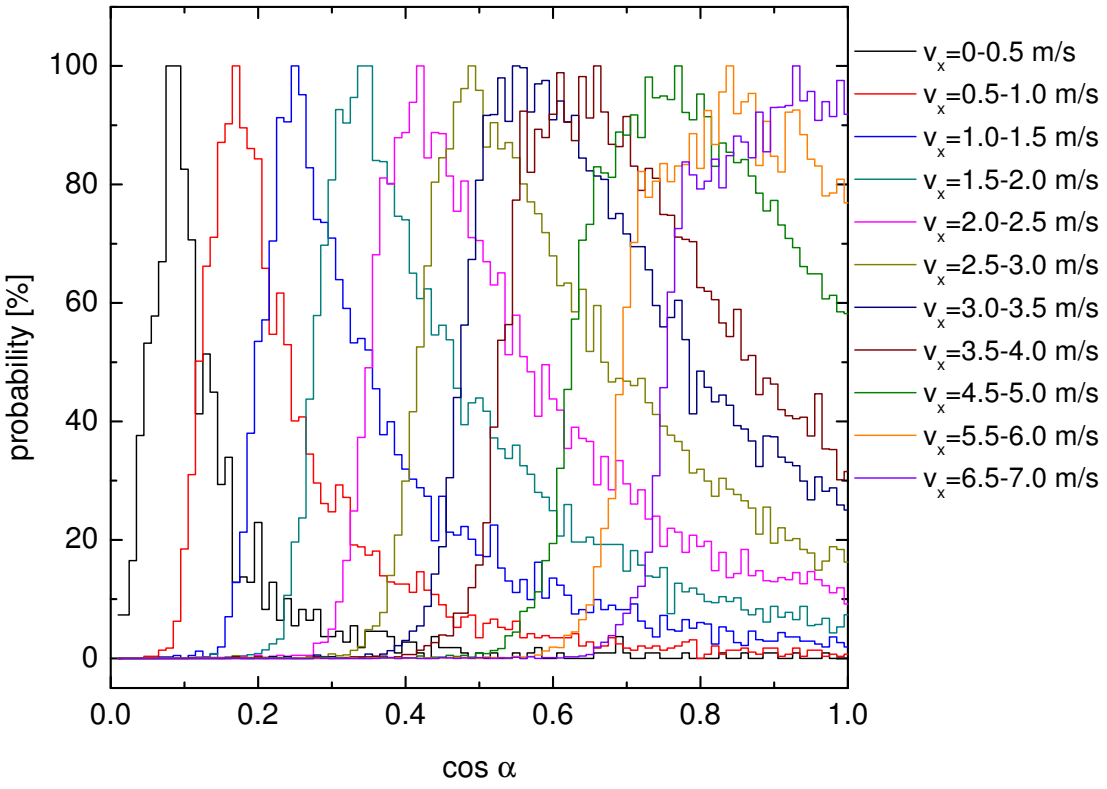

Figure 4.29: The $\cos\alpha$-distribution for different longitudinal velocities v_x for an S1 opening of 30 mm×50 mm. Every second interval above v_x=4 m/s and the intervals above v_x=7 m/s are omitted for better visibility.

S1. Figure 4.29 shows the $\cos\alpha$-distributions for an opening of 30 mm×50 mm. It shows that for higher longitudinal velocities, the trajectories of the UCN are preferentially directed more forward while for lower longitudinal velocities, a broader distribution at lower values of $\cos\alpha$ is found.

The distribution of the azimuthal angle β is found to be constant within statistics. Close to constant is also the UCN density in the guide. However, a small radial dependence is found, as shown in Figure 4.30. This dependence can be understood with the following considerations which

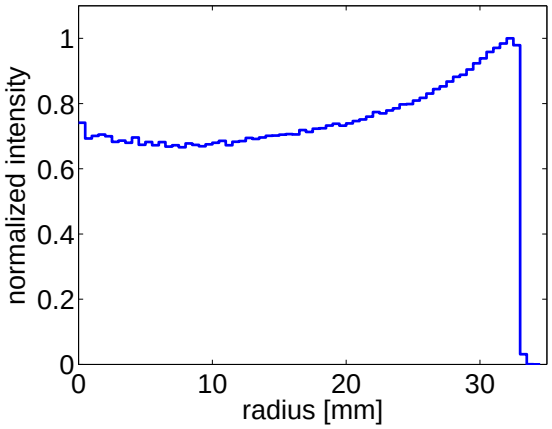

Figure 4.30: Radial dependence of the UCN density within the guide. The maximum intensity is normalized to unity. The maximum radius is r=33 mm.

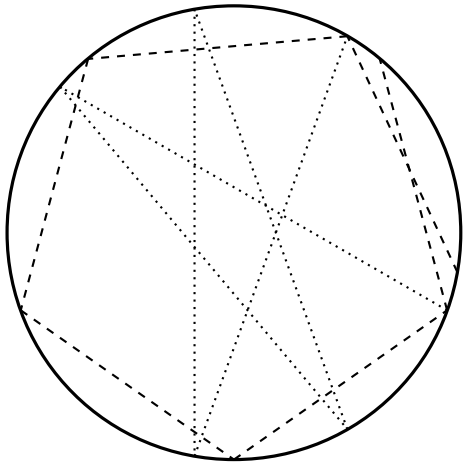

Figure 4.31: Transversal and peripheral neutron trajectories in a guide. See text for explanation.

refer to Figure 4.31. It is sufficient to have a look at the projection of each possible trajectory within the guide onto the yz-plane. The trajectories can then be split into two groups: a) trajectories which cross the guide close to its central axis, as indicated by the dotted lines in Figure 4.31 and b) trajectories which result from glancing incidence on the guide wall, as indicated by the dashed lines in Figure 4.31. Some of the neutrons from group a) have kinetic energies above the Fermi potential of the guide material, i.e. VCN, and can be transmitted through the guide wall depending on the longitudinal velocity component v_x. Neutrons with the same kinetic energy, but from group b) are most probably not lost as their angle of incidence, θ_i, is larger. The consequence is that less neutrons populate the central section of a neutron guide compared to the outer section. Thus, less neutrons are to be expected for small radii. In the outermost section, close to the guide wall, only few neutrons with trajectories of group b) can be found due to the very large angle of incidence necessary. Such angles are suppressed by the angular distribution of the beam, as e.g. shown in Figure 4.4.

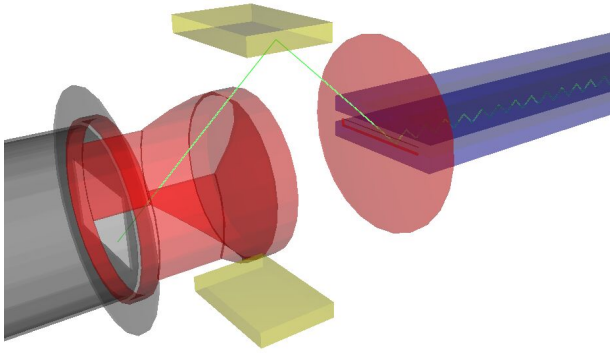

Figure 4.32: Image of the simulation model for the section between apertures S1 and S2. The green line represents the trajectory of an UCN which satisfies the angle condition defined by S1, the Ni mirror and S2.

4.8.2 Angular and energetic distribution of UCN entering the plate gap

In the second part of the MC simulation, neutrons are generated at positions ($x = x_{S1}/y/z$), where x_{S1} is the x-position of aperture S1. The y- and z-position is determined by a random generator, taking the dimensions of the S1 opening and the radial distribution into account. The direction of motion and the kinetic energy of the UCN are determined in three steps: 1) v_x is determined according to the measured spectrum of the longitudinal velocity component; 2) $\cos\alpha$ is determined by evaluation of the $\cos\alpha$-distribution corresponding to v_x; 3) a uniformly distributed β is generated.

The Ni coated mirrors are assumed to have a Fermi potential of 252 neV and are assumed to be perfectly specular. Introducing diffuse reflection for the Ni mirrors is not necessary as the increase in accepted angles is marginal, due to the limited reflecting area of the mirrors (the reflection angle of diffusely reflected neutrons would be anyway close to the specular case) and the fact that only a single reflection occurs. Apertures S1 and S2 as well as the absorber mounted behind S1 are considered to be perfectly black, i.e. the tracking for each UCN reaching a surface of one of these items is immediately stopped. This is a good approximation of the real case in which the few reflected (not absorbed) UCN are diffusely scattered, most of them into angles outside the acceptance of the experiment. Immediate stop also happens for neutrons which reach z-positions above the upper mirror surface or below the lower mirror surface, i.e. which missed both mirrors. The tracking of "successful" UCN, i.e. neutrons which are reflected by one of the two mirrors and subsequently pass the opening of the aperture S2, as shown in Figure 4.32, is stopped when the UCN touches the surface of a sample plate. In this case, their kinetic energy, momentum direction and position information is written into a file.

The momentum direction of "successful" UCN, together with the surface of the sample plate it is reflected from, defines the angle of incidence θ_i, i.e. the polar angle of the momentum direction relative to the surface normal of the sample plate. The horizontal divergence of the selected beam, is found to be smaller than $\pm 22°$ with small variation for different widths of the opening of aperture S1.

As mentioned in Section 4.5.4, the PE-absorber is used to block the direct path between apertures S1 and S2. During first series of simulations a simplified absorber, i.e. a disk which blocks the direct path, was used. Subsequent simulation series were performed with a complete model of the absorber, as shown in Figure 4.32, in order to check for accidental cutting of the UCN beam by the absorber. A comparison of the two cases, simplified and full absorber model, shows no difference in the distribution of the angle of incidence θ, which indicates that no systematic effect is induced by the PE absorber. The θ-distribution is shown in Figure 4.33. The mean value of the

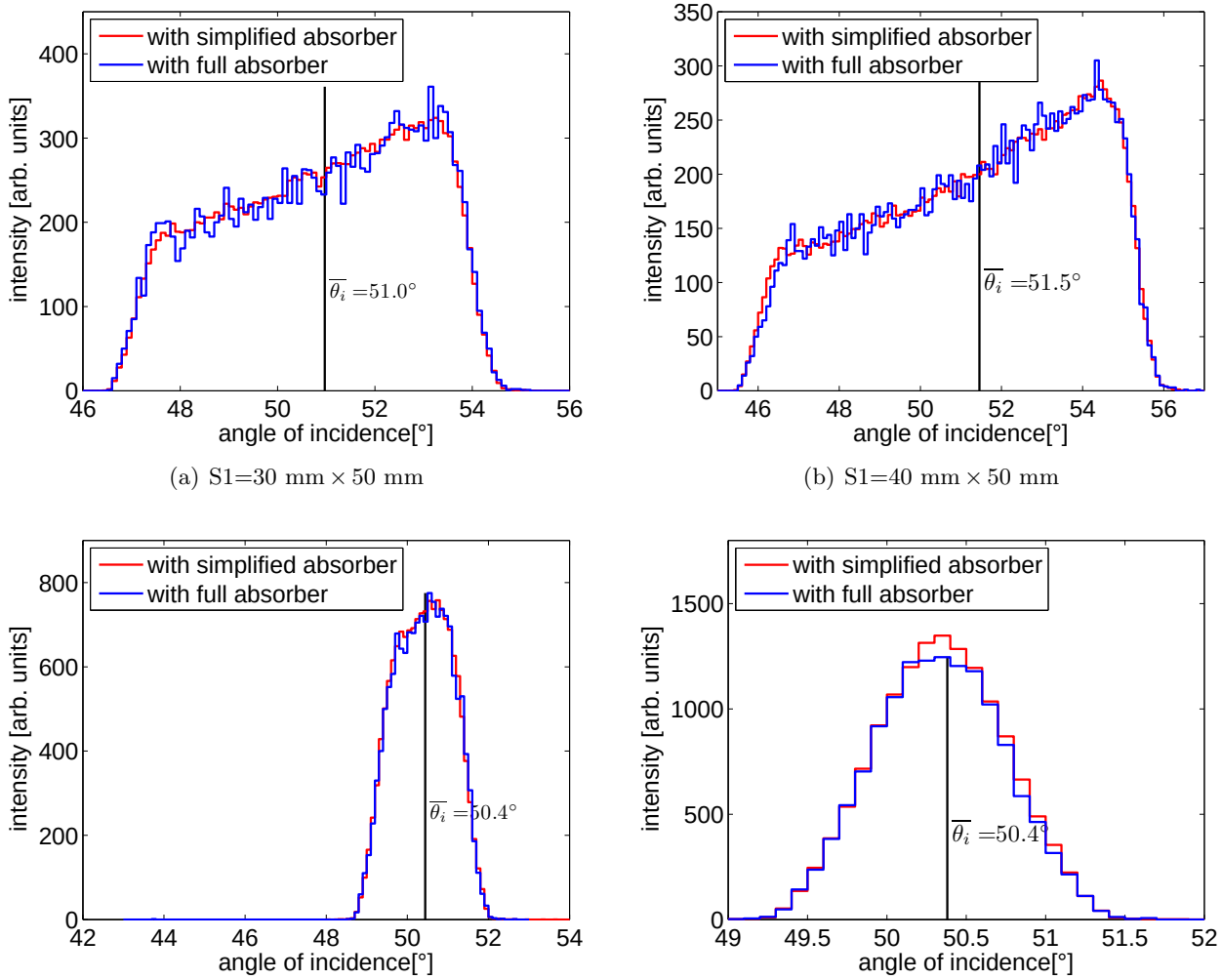

(a) S1=30 mm × 50 mm

(b) S1=40 mm × 50 mm

(c) S1=10 mm × 60 mm

(d) S1=5 mm × 60 mm

Figure 4.33: Distribution of the polar angle θ (angle of incidence) for four different openings of aperture S1. The vertical solid line represents the mean angle of incidence, $\overline{\theta_i}$.

angle of incidence, $\overline{\theta_i}$, can be obtained from the angular distributions and is shown as a vertical solid line in Figure 4.33. The distribution of the velocity is found to be the same for the different openings of aperture S1; an example is given in Figure 4.34. It shows the total velocity v, the longitudinal component v_x and the vertical component $v_z = v \cdot \sin\alpha \sin\beta$ for S1=30 mm × 50 mm. The oscillations in the falling edge of v_x are an artifact of the particle generator. It calculates a new v_x each time a previously generated UCN is rejected due to other constraints such as the $\cos\alpha$-distribution, which is only available in discrete steps of v_x. This leads to a mapping of this discrete structure onto v_x. However, v_z is the crucial velocity component for the reflection of the UCN from the plates. As the falling edge of the v_z distribution is mainly determined by the Fermi potential of the entrance neutron guide, v_z does not show any oscillation effect. The v-distribution and therefore also the energy distribution is not affected either. Hence, the effect was neglected.

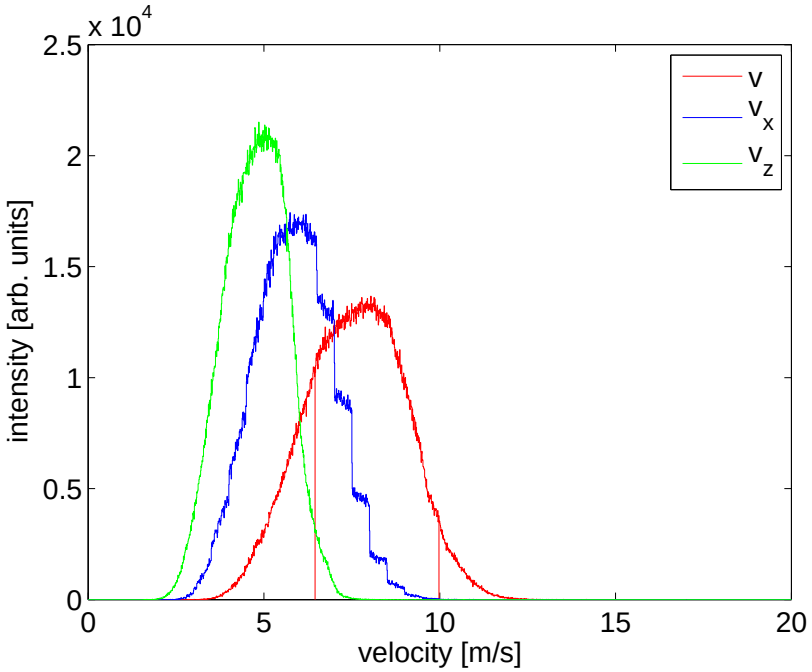

Figure 4.34: Distribution of the velocity at the first reflection from the sample plates for S1=30 mm × 50 mm: total velocity (v), longitudinal velocity component (v_x) and the vertical velocity component (v_z); the distributions for other dimensions of S1 are almost identical. The vertical red lines correspond to the critical velocities of glass and of DLC where an angle of incidence of 50° was taken into account.

4.8.3 Plate geometry and number of reflections in the plate gap

The third part of the MC simulation is separated from the second part because the rigid angle selection in the latter causes the number of transmitted UCN to be 2-3 orders of magnitude lower than the initial intensity at the beginning of the second part, i.e. the output of the guide simulation.

Each simulated UCN trajectory starts with the first reflection from the sample plates, i.e. with the output of the simulations described in Section 4.8.2. For each contact with the sample plates, the probability of non-specular reflection is evaluated and the calculation of the angle of reflection is performed accordingly, as described in Appendix B. Some of the UCN exit the plates by the rear end (x=500 mm) but outside the acceptance of apertures S3 and S4. Their trajectories are stopped on collision with one of the apertures. The remaining UCN, which pass the plates within the acceptance defined by apertures S3 and S4, enter the deformed exit neutron guide. The shape of the deformed part is approximated by different facets of curved and flat shape. The exit guide is followed by a stainless steel 90° bend. It eliminates those UCN which have a transversal velocity component larger than the critical velocity of stainless steel, 6.1 m/s. Figure 4.35 compares the velocity spectrum of UCN transmitted by a perfectly specularly reflecting surface with $V_F = 215$ neV at S4 with the corresponding spectrum after the exit guide and the stainless steel bend. While the spectra are identical up to ∼7 m/s, a significant reduction due to the bend is observed for higher velocities. For a Fermi potential significantly lower than V_F of stainless steel, e.g. of glass, the reduction due the bend is negligible. After the bend, the remaining UCN are detected, i.e. information about the trajectory is written to a file.

The sample plates can be tilted in x-direction (converging configurations) and in y-direction for systematic investigations. In the general case, the two plates are flat. For special cases, a wavy-like curvature can be used. The following items refer to the case of parallel plates.

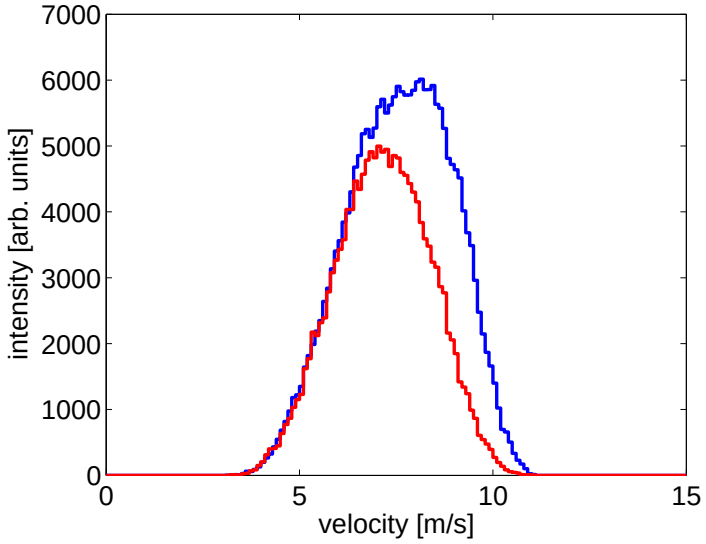

Figure 4.35: Velocity spectrum at aperture S4 (blue) and after the stainless steel bend (red) for perfectly specularly reflecting plate surfaces with $V_F = 215$ neV.

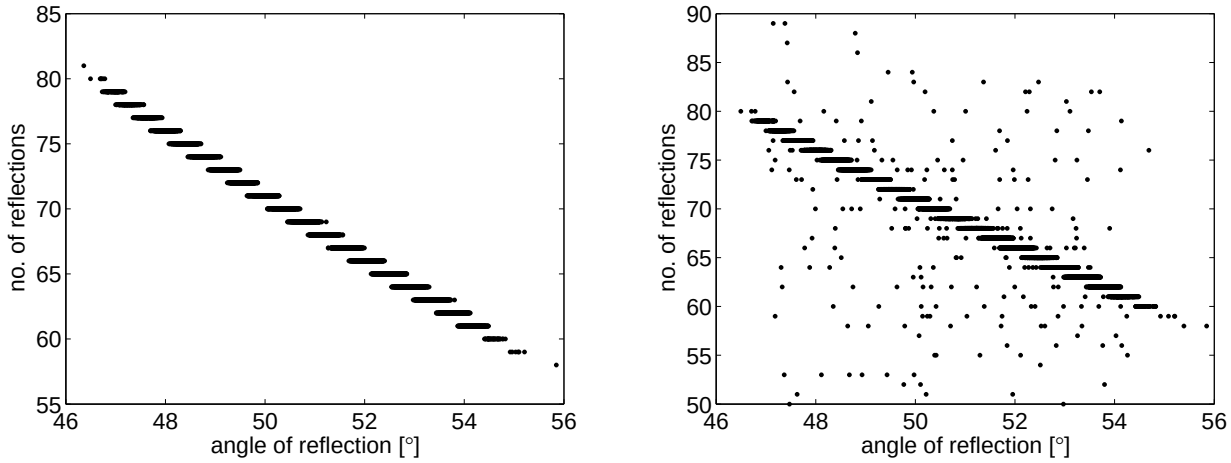

(a) purely specular case

(b) specular and diffuse case (1%, Lambert model)

Figure 4.36: Number of reflections in the plate gap as a function of the angle of reflection (g=6 mm).

The number of specular reflections in the plate gap, k, can be estimated by

$$k = \frac{L}{g \cdot \tan(\overline{\theta})}, \tag{4.33}$$

where L is the plate length, $\overline{\theta}$ the averaged angle of reflection and g the plate gap. As shown in Figure 4.33, the angle of incidence has a distribution which is characteristic for the angle condition determined by apertures S1 and S2. This angular distribution leads to a distribution of k. An example is shown in Figure 4.36, where the number of reflections is plotted vs. the angle of reflection. For the specular case, only a narrow band is allowed for k while in case of an additional diffuse reflectivity (e.g. 1%, Lambert model) there are also random k values possible.

In Figure 4.37, the angle of reflection is plotted vs. the kinetic energy of simulated UCN using the energy distribution derived in Section 4.8.2. The plot shows a continuous distribution of the

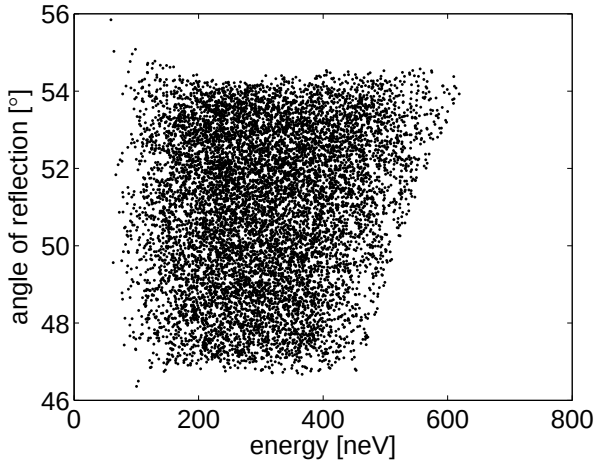

Figure 4.37: Angle of reflection vs. kinetic energy of simulated UCN for DLC coated floatglass plates. The kinetic energy is limited at the upper end by the Fermi potential of the sample plates.

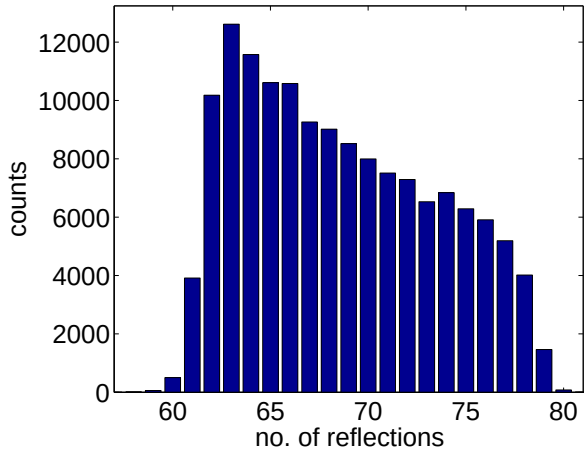

Figure 4.38: Number of reflections between two NiV coated floatglass plates with 6 mm gap for the case of totally specular reflection.

simulated UCN within the allowed range of kinetic energy and angle of reflection. The upper limit for the kinetic energy, determined by the Fermi potential of the sample plates, depends on θ, as it is visible from Figure 4.37. Only UCN with $|v_z|$, the velocity component perpendicular to the plate surface, smaller than the critical velocity of the plate material, v_C, are reflected from the plate. In the other case, the UCN are transmitted and are lost.

As larger θ allow for the reflection of UCN with higher kinetic energy, a higher population is to be expected for larger angles of incidence because the energy-distribution peaks at a value above the Fermi potential. A larger angle of incidence leads to a lower number of reflections. As a consequence, the histogrammed number of reflection shows a slight asymmetry, as can be seen in Figure 4.38. Here, the histogram is shown for NiV coated floatglass plates with a gap of 6 mm (fully specular case).

For converging plates, as discussed in Section 4.7.2, a limiting tilt angle of the upper plate should be observable above which no totally specular reflected UCN pass the plates, see Figure 4.39, which shows the convergence curve, i.e. the simulated number of UCN that pass the plates as function of the tilt angle. For the specular case, no UCN pass the plates for a tilt angle above a critical angle ζ_C close to 0.2°. This angle is smaller as that obtained by the calculation mentioned

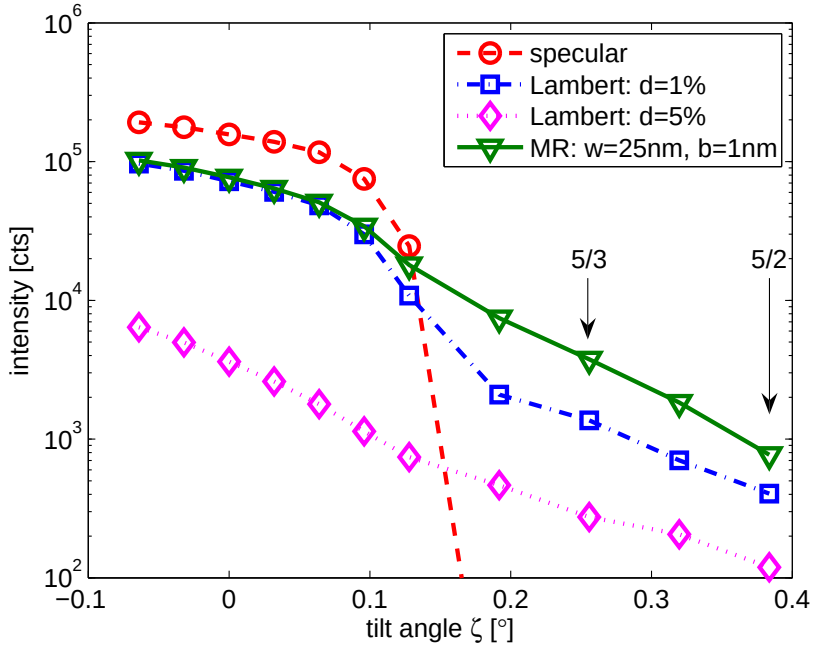

Figure 4.39: Number of UCN, which pass the DLC coated floatglass plates as a function of the tilt angle of the upper plate. Simulations were started with 10^6 UCN. Purely specular reflection is compared with partially diffuse reflection using the Lambert model, fractions 1% and 5%, and the microroughness (MR) model with a correlation length of 25 nm and a RMS roughness of 1 nm. The lines between the simulated points are to guide the eye. The "standard" converging configurations 5/3 and 5/2, used for many samples, are annotated.

in Section 4.7.2. The difference is caused by two facts: a) the MC simulation considers the wall losses which become more important due to the increased number of reflections and b) the motion of the UCN in y-direction becomes dominant compared to the motion in x-direction which leads to more trajectories outside the acceptance of the experiment. The corresponding curve for a Lambert model 1% diffuse calculation is about half as high as the one for the specular case. For a diffuse fraction of 5%, the obtained values are more than an order of magnitude lower than for the 1% case. A significant transmission is observed for tilt angles above ζ_C. The number of neutrons which pass the plates in parallel configuration is 46.0% (2.3%) for a Lambertian fraction of 1% (5%) compared to the specular case. A fourth convergence curve is shown for the microroughness model with parameters b=1 nm and w=25 nm. While its curvature is comparable to the 1% Lambert case for $\zeta < \zeta_C$, it shows a behavior which resembles qualitatively that of the 5% Lambert case. However, the number of counts for tilt angles above ζ_C is much larger in the microroughness model case than in the Lambert model case. Hence, converging configurations are sensitive not only to diffuse reflection in general but also to the angular distribution of diffusely reflected neutrons.

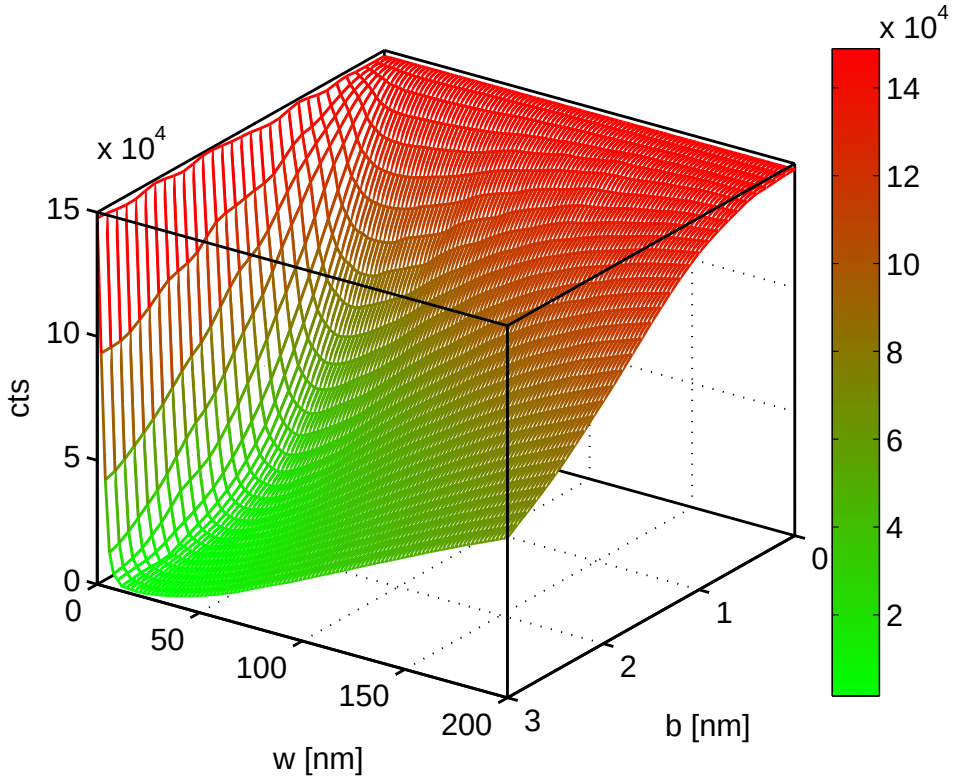

Figure 4.40: Transmission vs. (b, w) obtained by GEANT4UCN simulations of the parameter space of the microroughness model for the parallel configuration 4/4 of the NiV 11/11 sample plates. The mesh is a curvature interpolation, done by MATLAB®, of the simulated points, which are not shown for better visibility.

4.8.4 Simulation of the microroughness-parameter space

In order to determine the values of the two parameters b (RMS roughness) and w (correlation length) of the microroughness model which correspond to the sample plates (see Section 4.9), a limited part of the parameter space was simulated for different configurations. For most sample plates this part is defined by $b = [0, 3]$ nm and $w = [0, 200]$ nm. For some sample plates, e.g. the Ni coated floatglass plates from PSI, the b-range was extended to 4 nm. Higher values were not used in order not to violate the validity conditions of the microroughness model.

A grid of points in the b-w-parameter space was simulated for each configuration used during the corresponding measurements of the sample plates. Figures 4.40 and 4.41 show the simulated grids for selected configurations of the NiV-coated floatglass plates (NiV 11/11). Parameters $b = 0$ and/or $w = 0$ represent the specular case of the microroughness model. Thus, a single simulation run using only specular reflection was used for these points instead of individual simulations for each (w,0) and (0,b). Qualitatively, two different curvatures are observed, one for parallel configurations, including variations of S4, and one for converging configurations.

The number of UCN trajectories simulated for each configuration was 10^6, which is a compromise between statistical accuracy and computation time. A typical point in the b-w-parameter space, which consists of 8 different configurations, needs 6-9 hours of computation time on an Intel® Core™2 CPU with 2.0 GHz. The grids were computed on the Merlin3 Linux cluster at PSI and on the grid computing farm at the Physics Institute of the University of Zurich.

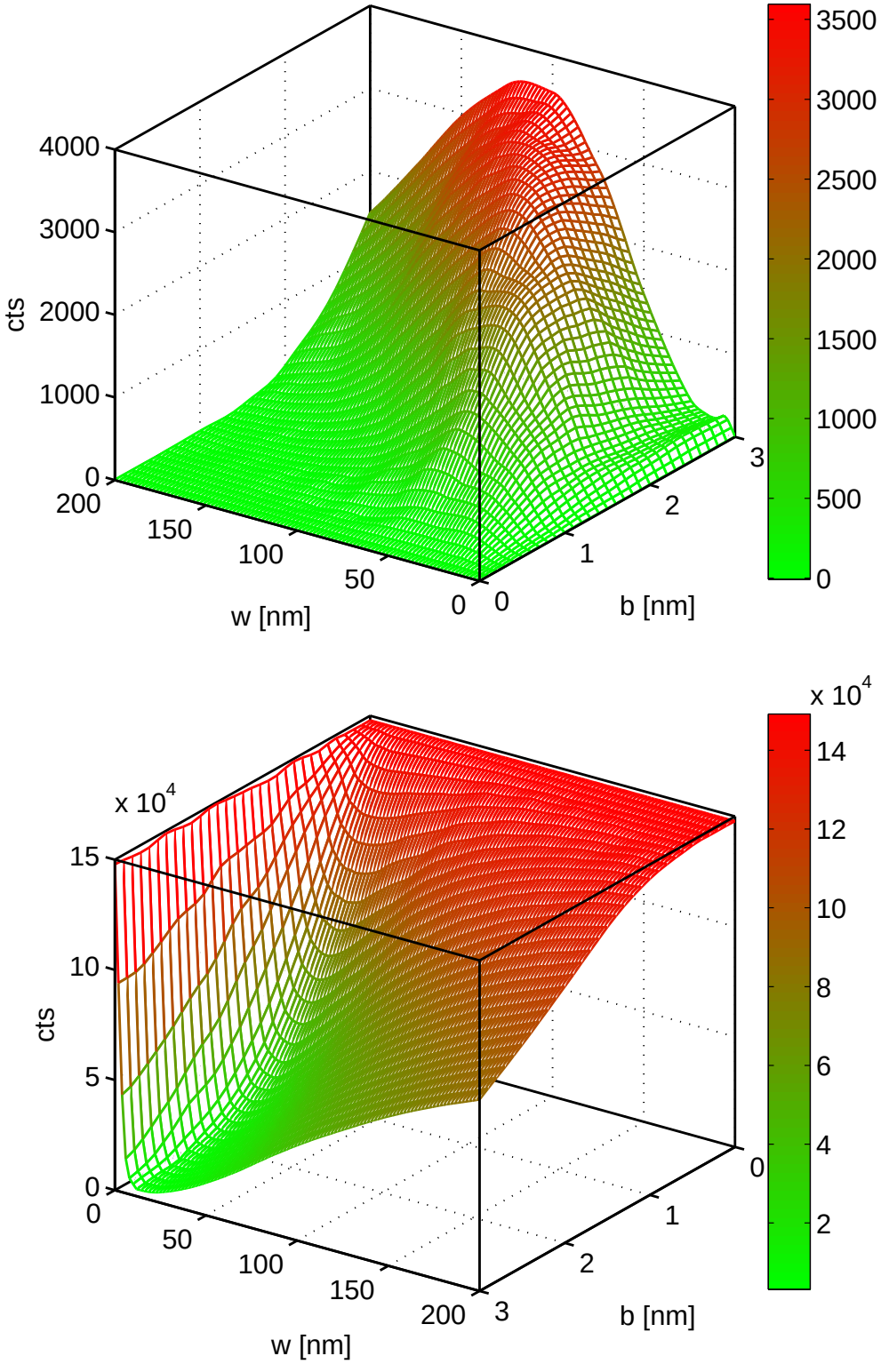

Figure 4.41: Transmission vs. (b, w) obtained by GEANT4UCN simulations of the parameter space of the microroughness model for the converging configuration 5/2 (top) and the configuration without S4 (bottom) of the NiV 11/11 sample plates. The mesh is a curvature interpolation, done by MATLAB®, of the simulated points, which are not shown for better visibility.

4.8.5 Simulation with the Lambert model

Similar grids were calculated for the Lambert model, which has only one parameter, the fraction of diffuse reflection d. Figure 4.42 shows the simulated grids for a parallel configuration and a converging configuration of the NiV-coated floatglass plates (NiV 11/11). As in the previous case of the microroughness model, 10^6 trajectories were simulated for each configuration. Due to the simpler calculations for the evaluation of the angle of reflection of a diffusely reflected neutron, the computation time is about half of the time needed for the same statistic with the microroughness model. The geometrical model is identical to the one described in Section 4.8.4. A close to exponential dependency of the number of transmitted neutrons on the fraction of diffuse reflection is found for the parallel configurations. The converging configurations show a maximum transmission in the range of 1% for the diffuse fraction.

4.9 Fitting simulated data to the measurements

It is one of the goals of the double plate experiment to extract the surface roughness parameters b and w from the measured transmission through the double plates. This can be achieved by fitting simulated data (cf. Section 4.8) to the measurements (cf. Section 4.7).

Sections 4.9.1 and 4.9.2 describe the fit procedures used for the microroughness and the Lambert model, respectively. Section 4.9.3 shows and discusses the results which are obtained by fitting the two reflection models with only statistical uncertainties to the measured data. The final results, which include also systematic uncertainties, are given in Section 4.11.

4.9.1 Fit procedure for the microroughness model

A theoretical function $f(c)$, where c stands for the different configurations measured for a sample (e.g. 4/4, 5/5, 6/6, 5/3,...), is fitted to the measured data using a non-linear least square fitting procedure in MATLAB®. The theoretical function,

$$f(c) = N \cdot h(c), \tag{4.34}$$

consists of the simulated transmission of the different configurations, $h(c)$, and a normalization factor, N. The latter is necessary due to the difference in the normalization of the measured

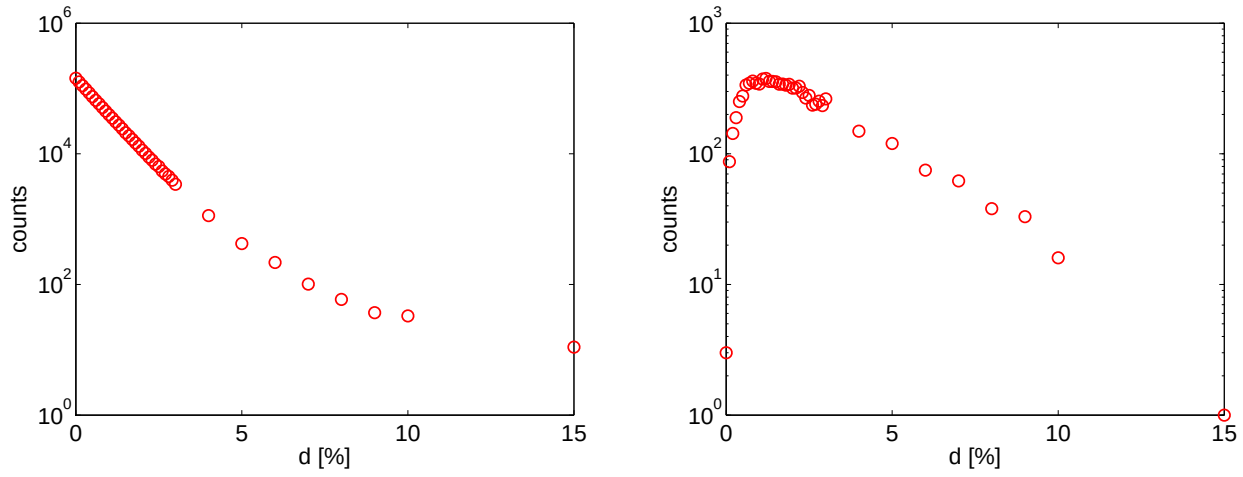

(a) parallel configuration (3/3)

(b) converging configuration (5/2)

Figure 4.42: GEANT4UCN simulations of the d-parameter space of the Lambert model for different configurations of the NiV 11/11 sample plates.

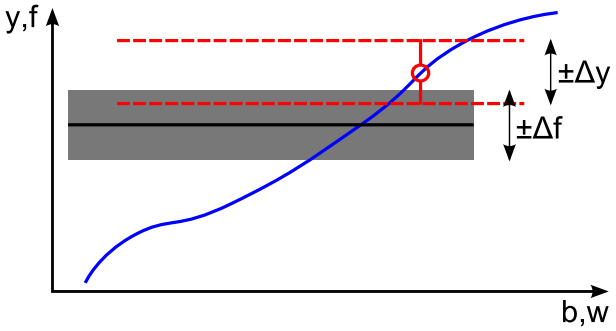

Figure 4.43: Visualization of $\sigma_c = |\Delta y_c + \Delta f|$; see text for explanation.

data (normalized to the rate of the monitor detector) and of the simulated data (normalized to 10^6 UCN satisfying the angle condition S1-S2 and hitting the sample plates). The two types of normalization must depend linearly on each other as both of them depend linearly on the incoming neutron flux in the UCN guide, I_0. The normalization factor has the same value for all samples if the MC simulation perfectly describes the experiment and should be independent of the reflection model used. For $h(c)$, the transmitted number of neutrons for 10^6 starting UCN in part 3 of the MC simulation (cf. Section 4.8) was used.

As can be seen from Eq. 4.34, N and h are statistically independent. Thus, the uncertainty of f is calculated as

$$\Delta f = \sqrt{(\Delta N \cdot h)^2 + (N \cdot \Delta h)^2}, \tag{4.35}$$

where ΔN and Δh are the uncertainties of N and h, respectively. The values of Δh are obtained by cubic spline interpolation of the statistical uncertainties of the grid point values, i.e. the same way as the values of h. As $h(c) \gtrsim 50$ for all configurations at each grid point, the uncertainties of h are assumed to be normally distributed and $\Delta h = \sqrt{h}$ was used. The most probable values of the three parameters N, b and w, found by χ^2-fit, are subsequently referred to as N_0, b_0 and w_0. These values are determined by searching the minimum of

$$\chi^2 = \sum_c \frac{y_c - f(c)}{\sigma_c}, \tag{4.36}$$

where y_c is the measured value (normalized rate) for a configuration c and σ_c is the total uncertainty. The latter is calculated in the most conservative way by $\sigma_c = |\Delta y_c + \Delta f|$ in order to include non-trivial co-variances between the different variables. Such co-variances occur if the measured data and the theoretical function are not independent of each other which is the case for step 3 in the fit procedure described below. The total uncertainty, σ_c, can be understood as the overlap of two contour bands in the b-w-parameter space, as shown in Figure 4.43: A simulated and normalized value $f(c)$ shall be considered to agree with the corresponding measured values if the sum of their uncertainties is larger than or equal to their deviation.

The fit procedure consists of the following steps:

1. **3-parameter fit:** The simulated data is fitted to the measured data, using the theoretical function $f(c)$ with fit parameters N, b and w. As N is a fit parameter, $\Delta N = 0$. The number of degrees of freedom (DOF) is the number of configurations used minus the number of fit parameters, i.e. DOF = #(c)-3.

2. **calculation of ΔN:** The uncertainties of N are determined by evaluation of the χ^2 distribution in N, using $\chi^2(N_0 \pm \Delta N) = \chi^2_{\text{min}} + 1$ with $\chi^2_{\text{min}} = \chi^2(N_0)$. As N is statistically independent of the other two parameters, its χ^2-distribution is a parabola. This can be seen

from Figure 4.44(a), which shows the χ^2-distribution in N for NiV coated floatglass (NiV 11/11).

3. **2-parameter fit:** The simulated data is fitted to the measured data, using the theoretical function $f(c)$ with fit parameters b and w. The normalization factor N is fixed as $N_0 \pm \Delta N$. The number of DOF is the number of configurations used minus the number of fit parameters and the number of boundary conditions, which leads to DOF = #(c)-3, as in step 1. Using ΔN in the fit leads to an increase of the total uncertainty used in the χ^2-function. Thus, the $\chi^2_{\min}$ of the 2-parameter fit is slightly lower than $\chi^2_{\min}$ in step 1. The values found for b and w are subsequently denoted as b_0 and w_0.

4. **error determination:** The χ^2-distribution is plotted as a function of b and w, as can be seen e.g. in Figure 4.44(b). The 1σ-, 2σ- and 3σ-contours, corresponding to χ^2 values of $\chi^2_{\min}+1$, $\chi^2_{\min}+4$ and $\chi^2_{\min}+9$ are evaluated using the appropriate MATLAB® function. The maximum extensions of the 1-σ contour line and their differences to the coordinates of the fitted point (b_0,w_0), respectively, determine the uncertainties in b and w. They are subsequently denoted as Δb_0 and Δw_0. For most samples the contour lines deviate from the elliptical shape, indicating a non-linear correlation between the parameters b and w.

It has to be pointed out that the normalization factors cannot directly be compared with each other if they are obtained for different sizes of S1. This has two reasons: a) The different reflection behavior of aperture S1, as discussed in Section 4.7.4 and b) different values for the transmission through the part of the experiment between aperture S1 and the sample plates, i.e. the second step of the MC simulations. For the "standard" size of aperture S1, 30 mm × 50 mm, it is

$$N_R(c) = f(c) = N \cdot h(c), \tag{4.37}$$

where N_R is the normalized rate (cf. Eq. 4.30). If a different size of aperture S1 is used, denoted by index "x", the relation extends to

$$N_R/k_{\mathrm{D1}} = N \cdot h(c) \frac{A_x}{A_{30\times50}} \cdot \frac{T_x}{T_{30\times50}} \doteq N \cdot h(c)/k_{\mathrm{D2}}, \tag{4.38}$$

where k_{D1} is the measured correction factor for the rate of detector 1 (cf. Table 4.5, point a) above), A_x the area of the S1 opening used, $A_{30\times50} = 1500$ mm^2 the area of the opening of the "standard" aperture S1 and $T_x/T_{30\times50}$ the relative transmission between S1 and the sample plates for the aperture size used compared to the "standard" opening (point b) above). Equation 4.38 can be brought to the same form as Eq. 4.37 by the substitution $\tilde{N} = N \cdot k_{\mathrm{D1}}/k_{\mathrm{D2}}$. In this term, $\tilde{N}$ is the factor obtained directly by the fit. Thus, the "standard" normalization factor, i.e. the normalization factor which would apply to the "standard" size of S1 and which can be compared for the different sizes of S1, is

$$N = \tilde{N} \cdot \frac{k_{\mathrm{D2}}}{k_{\mathrm{D1}}}. \tag{4.39}$$

The relative transmission $T_x/T_{30\times50}$ was determined by the MC simulation for each size of S1. Table 4.6 shows a summary of the correction factors k_{D1} and k_{D2}.

The values found by fitting the measured data with the microroughness model, for the RMS roughness and the correlation length, b_0 and w_0, can be used for the calculation of an averaged fraction of non-specular reflection, $d_{\mathrm{MR}}(b_0, w_0)$. Although this number does not allow for a direct comparison of the microroughness model with the Lambert model, it is nevertheless useful to get a rough idea of the "diffusity" of a sample. It depends on the energy- and the angle-distribution of the probing UCN, $f(E_n, \theta_i)$, and the integral probability of non-specular reflection, $R_{ns}(\theta_i, E_n)$, which is shown in Eq. 4.25:

$$d_{\mathrm{MR}}(b_0, w_0) = \int f(E_n, \theta_i) \cdot R_{ns}(\theta_i, E_n) \mathrm{d}E_n \, \mathrm{d}\theta_i. \tag{4.40}$$

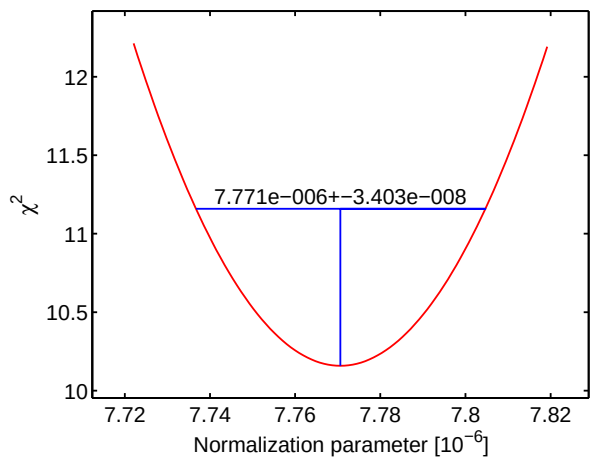

(a) χ^2-distribution in N

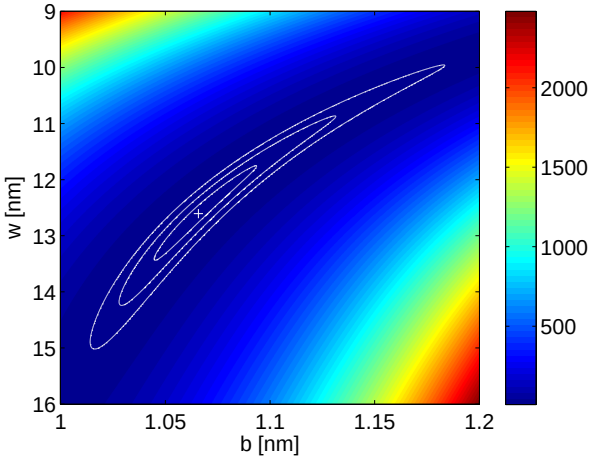

(b) χ^2-distribution in b and w (microroughness model)

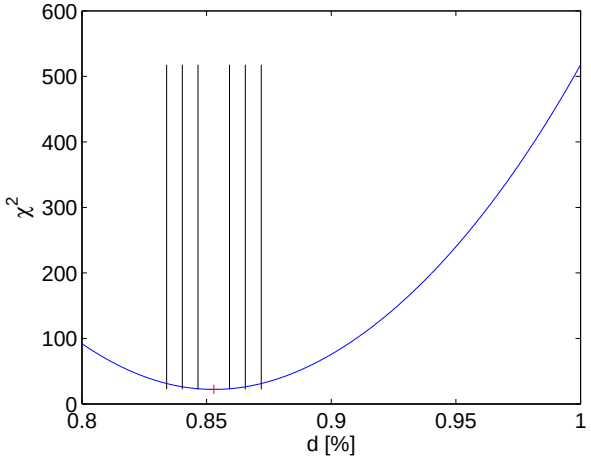

(c) χ^2-distribution in d (Lambert model)

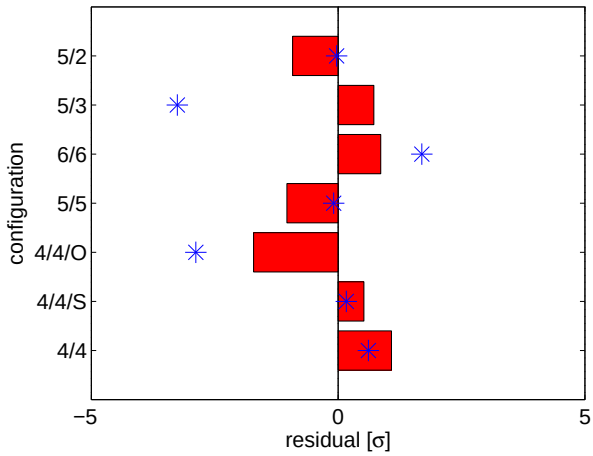

(d) Residual plots for the microroughness model fits (red bars) and the Lambert model fits (blue asterisks)

Figure 4.44: χ^2-distributions and residual plots for the fits of NiV coated floatglass. The fits are performed with $\eta = 0$, using only statistical uncertainties.

Table 4.6: Correction factors used for sizes of aperture S1 openings different from the "standard" case 30 mm × 50 mm.

S1 size	k_{D1}	k_{D2}
40 mm × 50 mm	1.147 ± 0.002	0.721 ± 0.008
10 mm × 60 mm	0.808 ± 0.002	2.80 ± 0.03
5 mm × 60 mm	1.262 ± 0.002	6.32 ± 0.07

The energy- and angle-distributions were obtained at the plate exit using a dedicated MC simulation with purely specular reflection behavior of the sample plates. This allows for a selection of the neutrons within the acceptance of the experiment without a falsification of the incident angle distribution by diffuse reflection.

4.9.2 Fit procedure for the Lambert model

In contrast to the microroughness model, the Lambert model contains only one fit parameter, the probability of diffuse reflection d. The fit procedure for the Lambert model is conceptually the same as for the microroughness model. The theoretical function $f_L(c)$ is fitted to the measured data using the same procedure in MATLAB® as used for the microroughness model fit. It is

$$f_L(c) = N \cdot h_L(c) \tag{4.41}$$

and consists, analogously to the previous case, of the simulated transmission of the different configurations, $h_L(c)$, and a normalization factor, N. For $h_L(c)$, the transmitted number of neutrons for 10^6 starting UCN in part 3 of the MC simulation (using the Lambert model for the sample plates) was used. The expression for the χ^2 function becomes

$$\chi^2 = \sum_c \frac{y_c - f_L(c)}{\sigma_c}, \tag{4.42}$$

with $\sigma_c = |\Delta y_c + \Delta f_L|$, using the most conservative calculation of the total uncertainty for the same reasons as described above. The fit procedure for the Lambert model consists of the following steps:

1. **2-parameter fit:** The simulated data is fitted to the measured data, using the theoretical function $f_L(c)$ with fit parameters N and d. As N is a fit parameter, $\Delta N = 0$. The number of DOF is the number of configurations used minus the number of fit parameters, i.e. DOF = #(c)-2.

2. **calculation of ΔN:** The uncertainties of N are determined by evaluation of the χ^2 distribution in N, using $\chi^2(N_0 \pm \Delta N) = \chi^2_{\min} + 1$ with $\chi^2_{\min} = \chi^2(N_0)$. As in the microroughness case, N is statistically independent of the other parameter and therefore its χ^2-distribution is a parabola.

3. **1-parameter fit:** The simulated data is fitted to the measured data, using the theoretical function $f_L(c)$ with the single fit parameter d. The normalization factor N is fixed as $N_0 \pm \Delta N$. The number of DOF is #(c)-2, as in step 1. Again, the $\chi^2_{\min}$ value is slightly smaller than in step 1 due to $\Delta N \neq 0$.

4. **error determination:** The χ^2-distribution is plotted as a function of d, as can be seen e.g. in Figure 4.44(c). The uncertainty of d is determined by evaluation of the d-values for which $\chi^2 = \chi^2_{\min} + 1$.

The same restrictions for the comparability of the normalization factor (concerning the opening size of S1) as for the microroughness model also apply to the Lambert model.

Table 4.7: Summary of the fit results obtained with only statistical uncertainties from measurement and simulation of the microroughness model. The simulations were performed with $\eta = 0$.

Sample	b_0 [nm]	w_0 [nm]	$\tilde{N}_0$ [10^{-6}]	χ^2_{min}/DOF	$d_{\mathrm{MR}}(b_0, w_0)$ [%]
FG 7/15	1.23±0.03	42.2±5.1	10.13±0.05	19.4/4	0.99±0.12
Optico 3/3	1.21±0.01	77.9±2.3	9.97±0.04	46.5/8	1.34±0.18
FG-HF	$2.03^{+0.02}_{-0.01}$	$52.3^{+3.1}_{-3.0}$	10.57±0.11	2.5/4	3.02±0.37
NiV 11/11	$1.07^{+0.03}_{-0.02}$	$12.6^{+0.8}_{-0.9}$	7.77±0.03	7.6/4	1.00±0.24
Ni PSI 8/9	$2.97^{+0.03}_{-0.02}$	24.9±0.1	11.70±0.16	9.66/4	13.09±3.47
Ni PSI 5/10	2.96±0.03	25.3±0.4	6.86±0.12	1.64/2	13.11±3.49
NiMo PSI 10/20	2.72±0.04	10.9±0.3	10.91±0.11	20.6/4	6.10±1.68
DLC 30×50	0.942±0.003	36.5±0.6	7.32±0.02	164/15	1.44±0.36
DLC 5×60	$1.41^{+0.48}_{-0.44}$	$14.3^{+56.7}_{-53.2}$	0.987±0.01	0.917/1	4.64±1.42
Replika 30×50	$0.98^{+0.07}_{-0.03}$	$36.1^{+12.4}_{-7.6}$	6.97±0.04	11.5/1	1.66±0.47
Replika 40×50	0.94±0.04	$70.6^{+4.7}_{-4.2}$	6.88±0.05	4.9/3	1.94±0.65
Replika 10×60	$1.14^{+0.08}_{-0.05}$	$45.5^{+9.2}_{-6.8}$	1.98±0.01	4.08/3	2.56±0.77
SS 2a/2b	$2.59^{+0.02}_{-0.01}$	19.6±1.0	14.80±0.17	46.4/4	6.64±1.27

4.9.3 Results using only statistical uncertainties and $\eta = 0$

In a first step, the samples listed in Table 4.1 were analyzed using the fit procedures described above. The corresponding simulations were performed using $\eta = 0$, as the material-dependent losses described by η are small compared to the geometry-dependent losses in the double plate experiment. Some of the results from these fits are needed for the determination of systematic uncertainties (see Section 4.10) and are hence given in the following.

A summary of the results from fitting the measured data with the procedure described above is shown in Table 4.7 for the microroughness model and in Table 4.8 for the Lambert model.

The first table includes the RMS roughness, b, the correlation length, w, the (uncorrected) normalization factor, $\tilde{N}$, the corresponding χ^2_{min} for the microroughness model with the DOF and the fraction of diffuse reflection, d_{MR}. For the Lambert model, the fraction of diffuse reflection, d, the (uncorrected) normalization factor, $\tilde{N}$, and the corresponding χ^2_{min} with the DOF is shown.

Three samples are found to be limited by statistics within the microroughness model: FG-HF, Ni 5/10 and DLC 5×60. The latter is found to be limited by statistics also within the Lambert model. The Lambert model fits for the Ni coatings and for the "40×50" data set of the Replika sample are considered to be unreasonable due to the significantly larger normalization factor compared to all other samples/fits.

As the results shown here are intermediate results, they are not further discussed in the following. A discussion of the final results obtained for a single normalization factor and including statistical and systematic uncertainties can be found in Section 4.11.

Table 4.8: Summary of the fit results obtained with only statistical uncertainties from measurement and simulation of the Lambert model. The simulations were performed with $\eta = 0$.

Sample	d [%]	$\tilde{N}$ [10^{-6}]	$\chi^2_{\min}$/DOF
FG 7/15	0.797±0.007	12.00±0.06	274/6
Optico 3/3	0.649±0.005	10.79±0.04	927/9
FG-HF	$1.310^{+0.001}_{-0.002}$	8.70±0.09	360/5
NiV 11/11	0.853±0.006	7.99±0.04	22.2/5
Ni PSI 8/9	$13.14^{+0.23}_{-0.27}$	446.5±23.8	60.4/5
Ni PSI 5/10	$12.35^{+0.24}_{-0.25}$	192.5±9.8	50.3/3
NiMo PSI 10/20	2.584±0.014	4.12±0.03	171/5
DLC 30×50	1.031±0.003	9.48±0.02	2390/15
DLC 5×60	0.466±0.008	10.39±0.01	0.98/2
Replika 30×50	0.778±0.007	6.43±0.03	11.3/2
Replika 40×50	$3.487^{+0.022}_{-0.023}$	65.73±0.74	127/4
Replika 10×60	0.919±0.007	1.86±0.01	38.9/4
SS 2a/2b	$3.016^{+0.021}_{-0.020}$	5.94±0.05	735/5

4.10 Consistency checks and systematics

This section deals with systematic uncertainties of the results described in Section 4.9.3. Such uncertainties may be caused by inaccuracies in the energy- and angle-distributions used for the MC simulation, by an inaccurate alignment of the plates or by insufficient knowledge of material-dependent quantities such as the Fermi potential or the UCN loss coefficient. Consistency checks of the distributions used in the MC simulation are described in Sections 4.10.1 and 4.10.2. Influences from surface cleaning to the measured data are discussed in Section 4.10.3. Systematic uncertainties caused by the uncertainties of the Fermi potential and the loss probability and by the curvature of the sample plates are discussed in Sections 4.10.4, 4.10.5 and 4.10.6.

4.10.1 Polyethylene foil measurements

For the MC simulation of the transmission through the double plates, an energy spectrum was used which was determined by the measurement of the longitudinal velocity component of the neutrons in the guide (cf. Section 4.7.3) and by another MC simulation (cf. Section 4.8) which gives the angular distribution of the neutrons within the guide. In order to check if this simulated energy spectrum is an adequate description of the real energy spectrum (at least for those angles used for the measurements), dedicated measurements were performed. For these measurements, the DLC coated floatglass plates with a gap of 6 mm were used. Layers of PE foil with ∼0.01 mm thickness (standard household foil, "M-Budget") were mounted with Kapton® tape onto the wedge-shaped beam collimator (item 6 in Figure 4.14). The number of layers was changed from measurement to measurement. For each setting, the normalized rate was determined and divided by the normalized rate measured without PE foils,

$$I(x) = N_R(x)/N_R(0) = \int_0^\infty e^{x \cdot d/s_0} f(v) \mathrm{d}v, \tag{4.43}$$

where x is the number of PE foil layers, d the thickness of a single PE foil layer, s_0 the mean free path length of the incident neutrons within the PE and $f(v)$ the (simulated) velocity distribution.

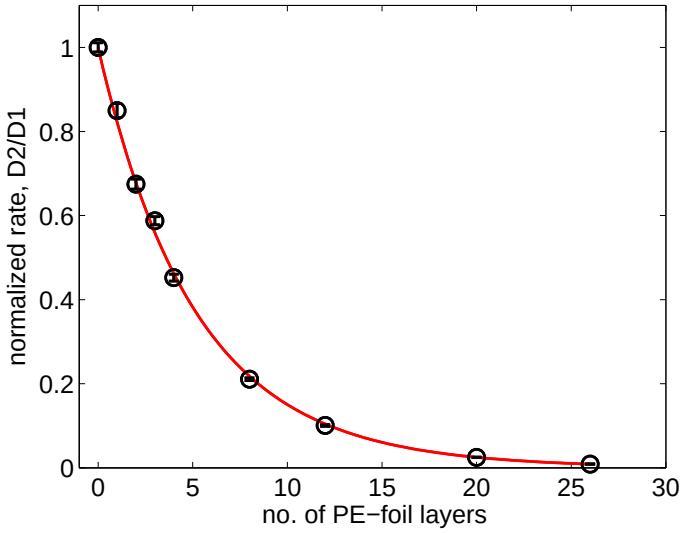

Figure 4.45: Relative transmission measured for different numbers of PE foil layers at the plate entrance and corresponding fit.

The mean free path length can be written as

$$s_0 = \frac{1}{\sigma \cdot N_{\mathrm{PE}}} \underbrace{=}_{\sigma \sim 1/v \Rightarrow \sigma = \tilde{k}/v} \frac{v}{\tilde{k} \cdot N_{\mathrm{PE}}}, \tag{4.44}$$

using the fact that the absorption cross-section for UCN in a material is proportional to $1/v$. Using $k \doteq \tilde{k} \cdot d \cdot N_{\mathrm{PE}}$, Eq. 4.43 becomes

$$I(x) = \int_0^\infty e^{x \cdot k/v} f(v)\, \mathrm{d}v. \tag{4.45}$$

For a given energy or velocity distribution, the measured data can be compared to Eq. 4.45 by a fit with only one parameter, k. The measured data for $I(x)$ and the resulting curve from the fit are shown in Figure 4.45. No uncertainty was taken into account for x. For the fit, $\chi^2_{\mathrm{min}}/\mathrm{DOF} = 19.6/8 = 2.45$ was found. The corresponding residuals are plotted in Figure 4.46 as blue squares. The fit was repeated using an uncertainty for x, Δx (red stars in Figure 4.46). In order to get $\chi^2_{\mathrm{min}}/\mathrm{DOF}=1$, $\Delta x = \pm 3\%$ is required. This uncertainty can be well understood as a foil thickness change caused by streching the foil or by wrinkles. Hence, the velocity/energy spectrum used is found to be an adequate description of the real spectrum.

4.10.2 Influence of laterally tilted plates

During standard measurements the plates were aligned in such a way that they were equally spaced along the y-direction. A gap difference, caused by an inaccurate setting of a micrometer screw, may lead to systematically different results as it alters the reflection in a similar way as a converging configuration. An idealized UCN trajectory within the central vertical plane, $y = 0$, is bent to one side of the plates and misses the exit apertures S3 and S4, as indicated in Figure 4.47 (right). For an expanded UCN beam restricted by the angle condition defined by apertures S1 and S2, laterally, i.e. in y-direction, tilted plates select a different, less intense, part of the beam. Systematic test were performed using the DLC coated floatglass plates. Figure 4.48 shows the measured normalized rate obtained for a 4 mm plate gap (parallel configuration) where the upper plate was tilted around an axis parallel to the x-axis by variation of the setting of a single micrometer screw (front left in

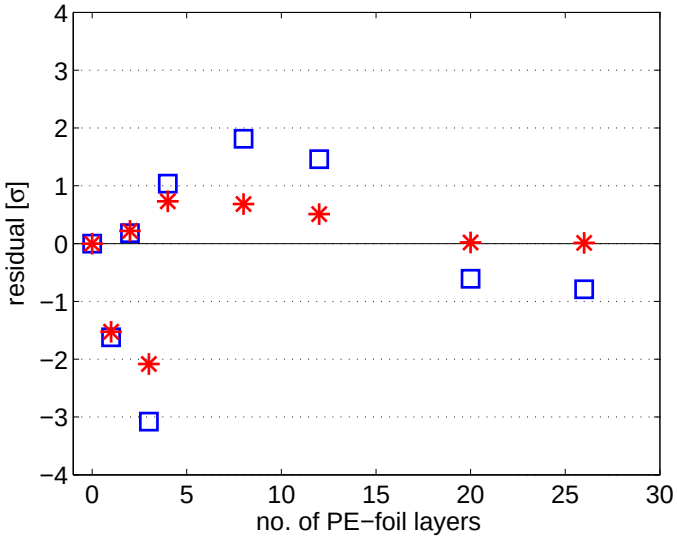

Figure 4.46: Residuals for the fit of the PE foil measurements shown in Figure 4.45. The fits are performed without uncertainty in the number of layers (blue squares) and with an uncertainty of 3% in the number of layers (red stars).

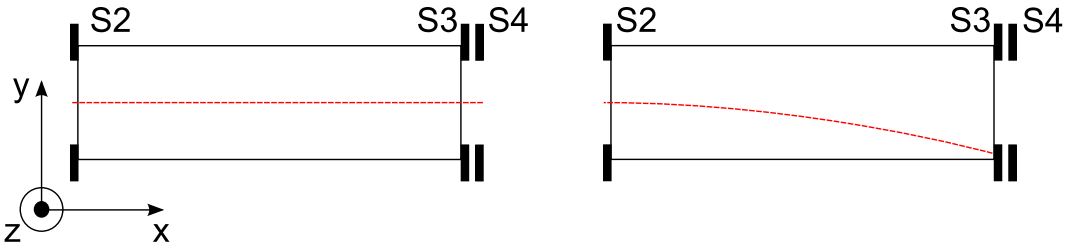

Figure 4.47: Effect of laterally tilted plates (views from top) on a single UCN trajectory: perfectly aligned plates (left) and plates tilted around an axis parallel to the x-axis (right). The dashed red line denotes the trajectory of an UCN which enters the plate gap with $v_y = 0$.

beam direction, denoted as B0). It also shows the transmission determined by the GEANT4UCN simulation. The simulated data was normalized to the measured values at a height difference B_0=0. Both curves have two relatively steep slopes and a flat top of ∼0.2 mm width. The flat top represents the range for which the exit aperture S3 is fully illuminated by the UCN beam. The size of this range is expected to decrease with decreasing plate gap (due to the increasing number of reflections) and vice versa. A flat top indicates a homogeneous density distribution of the UCN beam in y-direction. The simulated data is systematically higher than the measured values which indicates that the simulated angular distribution is wider than in reality. As the value of 4 mm represents a relatively small plate gap, no systematic uncertainties have to be expected, since the uncertainty of the parallelism of the plates (±8 μm, cf. Section 4.6.2) is much smaller than the flat top width of 0.2 mm.

4.10.3 Influence of surface treatment

As described in Section 4.6.1, the sample plates were cleaned in two stages. In the first stage, they were cleaned with isopropanol and in the second stage, shortly before measurement, with distilled water. As different qualities of distilled water were used, the systematic uncertainties caused by the cleaning of the plates were investigated.

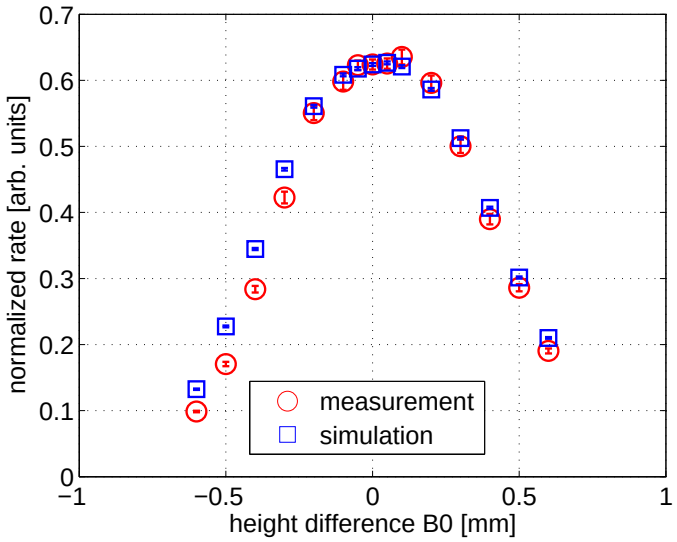

Figure 4.48: Normalized rate for laterally tilted upper plate, realized by the variation of the setting of micrometer screw B0 (front left in beam direction). The abscissa shows the deviation of B0 from the nominal plate gap of 4 mm.

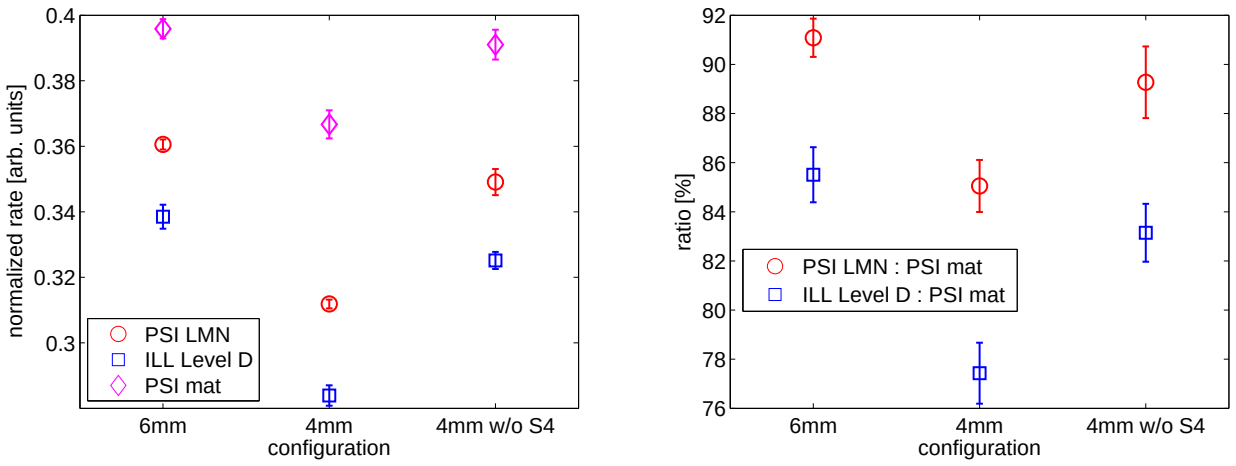

(a) Normalized rates

(b) Ratio

Figure 4.49: Measured normalized rates and corresponding ratios for different configurations after cleaning with three different qualities of distilled water.

For this purpose, a sample with very smooth surface, Optico 3/3, was used. It was subsequently cleaned with the three qualities of distilled water available (in chronological order):

- PSI LMN; distilled water obtained from laboratory for micro- and nano-technology at PSI.
- ILL Level D; distilled water obtained directly at ILL on level D of the reactor building.
- PSI mat; distilled water obtained from the materials group at PSI.

After each cleaning procedure, three different configurations were measured: 6/6, 4/4 and 4/4/O. The resulting normalized rates are shown in Figure 4.49(a). It is found that they are substantially different for the three qualities of distilled water. The highest rates are found for

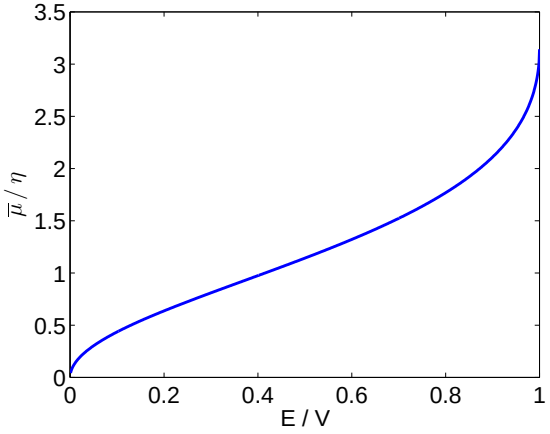

Figure 4.50: Energy-dependent coefficient of the loss probability averaged over the angle of incidence as a function of E/V.

"PSI mat"; the lowest rates are found for "ILL Level D". When comparing the two qualities with lower rates to the best one, a relative decrease of up to 22% is found, as shown in Figure 4.49(b). As the decrease is different for the two different gap sizes, it clearly depends on the number of reflections. A rough estimation can be done assuming purely specular reflection and that the decrease is caused by additional losses per reflection. The averaged number of reflections for the three configurations, obtained from MC simulations, are 66.5±6.6 (6/6), 98.5±10.9 (4/4) and 97.1±13.7 (4/4/O). It is $n_1/n_2 = (1-\overline{\mu_{12}})^{k_1-k_2}$ with the normalized rates n_i, the additional loss probability $\overline{\mu_{12}}$ and the averaged number of reflection k_i from above. This leads to $\overline{\mu_{\text{add}}} = 2.0\cdot10^{-3}$ for "PSI LMN" compared to "PSI mat" and to $\overline{\mu_{\text{add}}} = 2.8\cdot10^{-3}$ for "ILL Level D" compared to "PSI mat". In the following, $\eta = 0$ is assumed for the latter. For an estimation of the increase in η, Eq. 1.19 can be averaged over the angle of incidence [26],

$$\overline{\mu}(E) = 2\int_0^1 \mu(E,\theta_i)\cos\theta_i \mathrm{d}(\cos\theta_i) = 2\eta[\frac{V}{E}\sin^{-1}\left(\frac{E}{V}\right)^{1/2} - \left(\frac{V}{E}-1\right)^{1/2}]. \tag{4.46}$$

Figure 4.50 shows $\overline{\mu}(E)/\eta$ as a function of E/V. For the relevant interval of E/V, i.e. the interval which most of the neutrons used for probing the sample plates belong to, numbers between 1 and 3 are found for $\overline{\mu}(E)/\eta$. Thus, the increment in η is expected to be of the order of up to $\sim 1\cdot10^{-3}$.

The difference of the normalized rates between the configurations 4/4 and 4/4/O is caused by the difference of the angular acceptance. The corresponding ratio can be roughly reproduced by MC simulations with different values for η, as shown in Table 4.9.

4.10.4 Influence of the Fermi potential

The Fermi potential of a material can be calculated with Eq. 1.14. Measurements of the Fermi potential, e.g. by cold neutron reflectometry, usually find slightly lower values due to decreased density close to the material surface (cf. Section 2.2.5). Thus, it is adequate to assume the uncertainties to be roughly proportional to the height of the Fermi potential, i.e. larger for materials with $V_F \geq 200$ neV compared to e.g. glass. In the following, an uncertainty of $\Delta V_F = \pm5$ neV is assumed for the uncoated glass plates and $\Delta V_F = \pm10$ neV for the other samples.

The microroughness model has three fit parameters, b, w and N. All of them may be affected by a change in the Fermi potential. In order to determine which parameters are affected, the sample FG 7/15 was used. The relatively low Fermi potential which probes the steep gradient of the neutron velocity distribution (see Figure 4.34) makes the sample very sensitive to changes

Table 4.9: Ratio of the configurations 4/4/O and 4/4 calculated with measured data for different qualities of distilled water (top) and with MC simulations for different values of η (bottom).

Measurement	PSI LMN	ILL Level D	PSI mat
4/4/O : 4/4	1.119±0.014	1.145±0.016	1.066±0.018

MC simulation	$\eta = 0$	$\eta = 10.5 \cdot 10^{-4}$	$\eta = 2 \cdot 10^{-3}$
4/4/O : 4/4	1.097±0.008	1.103±0.010	1.114±0.011

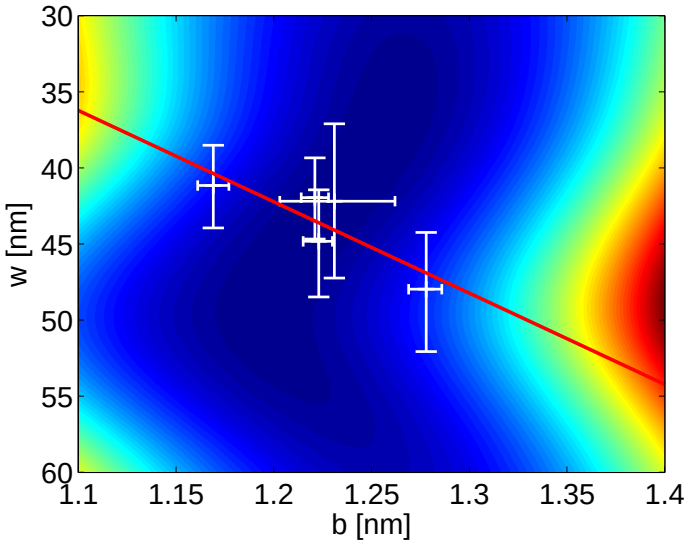

Figure 4.51: Values for b and w (white crosses) found by fitting simulated grids with different Fermi potentials, $V_F \in \{80, 85, 88, 90, 95\}$ neV (from lower right to upper left), to the data of sample FG 7/15. The red line corresponds to a linear fit of the (b,w) pairs. The χ^2-distribution of the microroughness model fit with $V_F = 88$ neV is shown on the color scale, where the lowest values are blue.

in the Fermi potential. Grids with different Fermi potentials, $V_F \in \{80, 85, 88, 90, 95\}$ neV, and $\eta = 0$ were simulated. Values for the three parameters of the microroughness model were obtained with the fit procedure described in Section 4.9.1. The resulting (b,w) pairs including statistical uncertainties are plotted in Figure 4.51 as white crosses. The color scale in the background of the figure represents the χ^2-distribution of the microroughness model fit for the grid with $V_F = 88$ neV. The (b,w) pairs show a systematic drift with V_F. Thus, a linear function is fitted to the (b,w) pairs (χ^2 of this fit is 0.51), visible as red line. It represents the drift direction, which is found to be roughly parallel to the gradient of the χ^2-distribution. Thus, in the following, the problem is considered to be one-dimensional. In this picture, the fit model is thought to have only two parameters, N and (b,w). This is the situation as it is shown in Figure 4.52. A change in (b,w) leads to a different transmission through the plates and therefore requires a change in N in order to obtain a simulated rate which still corresponds to the measured normalized rate. The example

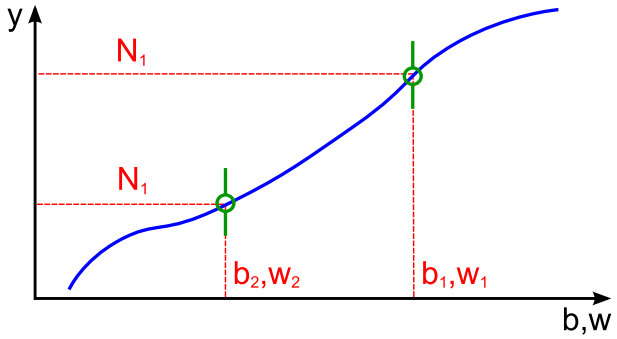

Figure 4.52: Schematic overview of the change in N as a consequence of a change in (b, w). See text for explanation.

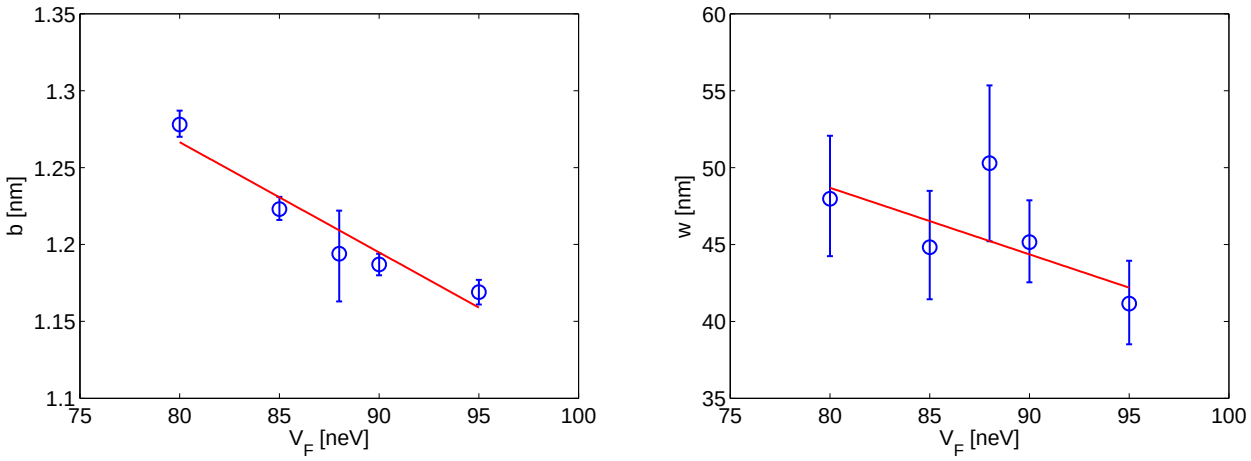

(a) RMS roughness

(b) Correlation length

Figure 4.53: Systematic variation of the RMS roughness and the correlation length for FG 7/15 as a function of the Fermi potential used in the MC simulation.

in Figure 4.52 corresponds to the situation where a change $(w(1), b(1)) \rightarrow (w(2), b(2))$ leads to a change $N(1) \rightarrow N(2)$. In this picture, $b(1)$, $w(1)$ and $N(1)$ correspond to a higher (simulated) value of the Fermi potential and $b(2)$, $w(2)$ and $N(2)$ to a lower value. Inversely, a change in N requires a change in (b, w). Defining a systematic uncertainty in N can hence be used for the determination of the uncertainty in (b, w). On a more mathematical level, the additional uncertainty flattens the χ^2-distribution and allows for the inclusion of the desired (b, w) pairs into the error contour. Within this approximation, it is only necessary to perform simulations at the point (b_0, w_0), i.e. with the values of b and w obtained by the fit with statistical uncertainties.

Figure 4.53 shows the values of b and w obtained by the microroughness model fit as a function of the Fermi potential. Linear fits are performed for both quantities; b_g=1.21±0.04 nm and w_g=45.2±2.2 nm are found by evaluation of the fit function for $V_F = 88 \pm 5$ neV. For the evaluation of the normalization factor, a quadratic function is used and $N_g = (10.18 + 2.08 - 1.38) \cdot 10^{-6}$ is found.

The point (b_g, w_g) was then evaluated for different values of the Fermi potential. A single parameter, N_l, is needed for a comparison of the various simulations of this point with the measured data. Figure 4.54 shows the χ^2-distribution of the fit of N_l (top) and the corresponding values of N_l (bottom). As the microroughness model is also sensitive to the Fermi potential, optimal values can be found with an iterative procedure of MC simulation and fitting the resulting data to the

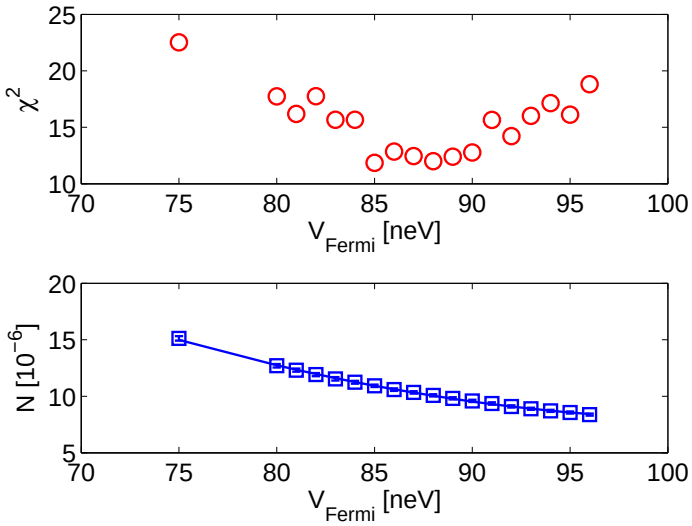

Figure 4.54: Top: χ^2-distribution obtained for the N_l-fit of the point (b_g, w_g) to the measured data; bottom: corresponding values for the fit parameter N_l.

measured data, as seen on top in Figure 4.54. A quadratic function is used for the interpolation of $N_l(V_F)$. A normalization factor of $N_l = (10.05 + 1.56 - 1.14) \cdot 10^{-6}$ is found for $V_F = 88 \pm 5$ neV. Using N_l in step 3 of the microroughness model fit procedure (cf. Section 4.9.1) leads to $b_l = 1.21 + 0.10 - 0.11$ nm and $w_l = 42.4 + 11.3 - 8.3$ nm. A comparison of (b_g, w_g) with (b_l, w_l) and N_g with N_l shows that the approximative method delivers uncertainties of the same size or larger as the full evaluation with individual grids. The approximation is therefore considered to be adequate.

The systematic uncertainties caused by the uncertainty of the Fermi potential are determined for all samples by using the approximative method as described above, but with a non-trivial loss coefficient $\eta = 10.5 \cdot 10^{-4}$ (cf. Section 4.10.5 below). A summary of the obtained uncertainties is given in Table 4.10.

For the Lambert model, the systematic uncertainties caused by the uncertainty of the Fermi potential are determined by the corresponding approximation method which is identical to the method described above with (b, w) replaced by d. A summary of the obtained uncertainties is given in Table 4.11. As some of the samples could not be fitted by the Lambert model in a reasonable way (cf. Section 4.11), the systematic uncertainties of these samples were not determined.

4.10.5 Influence of the loss coefficient

The loss coefficient of materials used for UCN applications is usually of the order of a few times 10^{-4} (see e.g. Ref. [156, p. 351]). An additional loss probability can be introduced by the surface treatment, e.g. by cleaning with insufficiently pure distilled water, as described in Section 4.10.3. As a conservative estimation of the range of the loss coefficient, η, its lower limit was set to $1 \cdot 10^{-4}$ and its upper limit to $2 \cdot 10^{-3}$. Thus, the evaluation of the uncertainties caused by the uncertainty of η is performed within $\eta = (10.5 \pm 9.5) \cdot 10^{-4}$.

A similar approximative method as the one described in Section 4.10.4 is tested for the evaluation of the uncertainties caused by the uncertainty of the loss coefficient. Values for the N, b and w, i.e. the parameters of the microroughness model, were obtained with the fit procedure described in Section 4.9.1 for sample NiV. The resulting (b, w) pairs including statistical uncertainties are plotted in Figure 4.55 as white crosses.

The values of (b, w) obtained for the different values of η are found to be roughly consistent

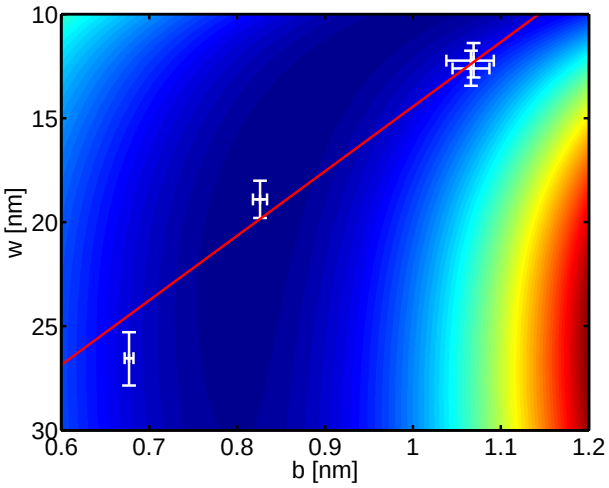

Figure 4.55: Values for b and w (white crosses) found by fitting simulated data for different values of the loss coefficient, $\eta \in \{0,\ 1.25 \cdot 10^{-4},\ 1 \cdot 10^{-3},\ 2 \cdot 10^{-3}\}$ (from upper right to lower left), to the sample NiV. The red line corresponds to a linear fit of the (b,w) pairs. The χ^2-distribution for $\eta = 3 \cdot 10^{-3}$ neV is shown on the color scale, where the lowest values are blue.

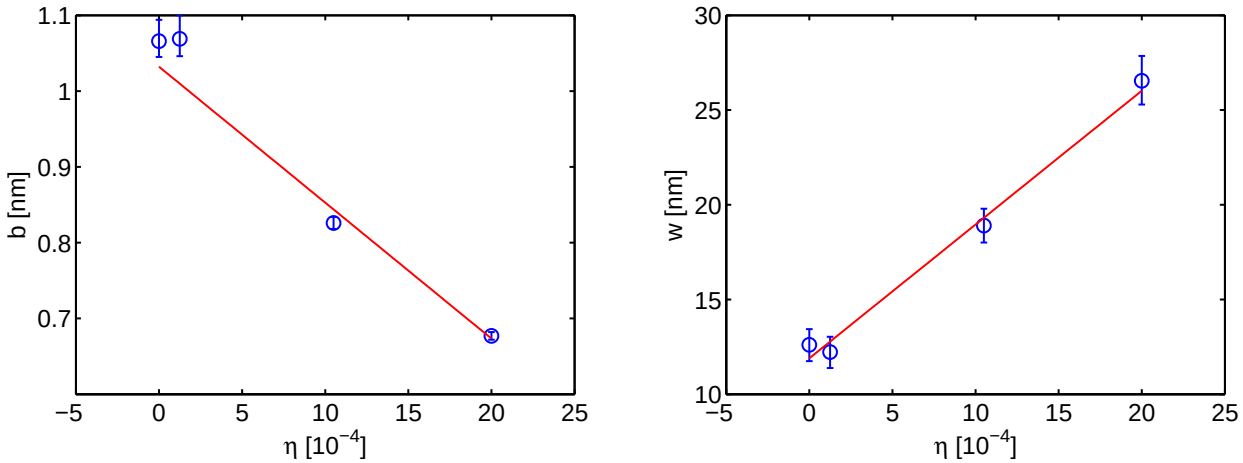

(a) RMS roughness

(b) Correlation length

Figure 4.56: Systematic variation of the RMS roughness and the correlation length as a function of the loss coefficient used in the MC simulation.

with a linear function, as can be seen in Figure 4.55, where the red line corresponds to this linear function. In the following, the performance of the approximative method described in the previous section (with η instead of V_F) is compared to the complete evaluation of the uncertainties of the parameters b, w and N.

In a first step, the values for b and w obtained by the fits of the four grids corresponding to $\eta = 0,\ 1.25 \cdot 10^{-4},\ 1 \cdot 10^{-3},\ 2 \cdot 10^{-3}$ are plotted against the loss coefficient, as can be seen in Figure 4.56. Both quantities are interpolated with linear functions. With these functions, $b_g = 0.84 \pm 0.17$ nm and $w_g = 19.3 \pm 6.7$ nm are found for $1 \cdot 10^{-4} \leq \eta \leq 2 \cdot 10^{-3}$. The corresponding range of the normalization factor is found to scatter within the range $N_g = (7.81 \pm 0.08) \cdot 10^{-6}$. Next, simulations for different values of η are performed for (b_g, w_g) and are fitted to the measured data using a single parameter N_l. The values of $N_l(\eta)$ can be well interpolated by a quadratic

function which allows for the determination of N_l corresponding to $1 \cdot 10^{-4} \leq \eta \leq 2 \cdot 10^{-3}$; $N_l = (7.77 \pm 1.33) \cdot 10^{-6}$ is found. Using this value for the normalization factor in step 3 of the microroughness model fit procedure (cf. Section 4.9.1) leads to $b_l = 0.82 \pm 0.08$ nm and $w_l = 20.1 \pm 3.5$ nm.

A comparison of the parameter values obtained by the two different methods shows that for $N \pm \Delta N$ the approximative method is able to determine a conservative estimation and can alternatively be used. However, for the uncertainties of b and w, the approximative method finds values which are about a factor of 2 smaller than required. An additional uncertainty, which is independent of N has therefore to be found for the correlation length and the RMS roughness.

A simple, but rather conservative method to find these uncertainties is their estimation by the deviation of the (b, w)-pair obtained by the fit of the "$\eta = 0$"-grid to the measured data from the corresponding value of the "$\eta = 10.5 \cdot 10^{-4}$"-grid. Assuming that the probability of the real value of η is equally distributed within $1 \cdot 10^{-4} \leq \eta \leq 2 \cdot 10^{-3}$, the standard deviations of b and w are found to be

$$\Delta b = \frac{|b_0 - b_1|}{\sqrt{3}} \qquad \text{and} \qquad \Delta w = \frac{|w_0 - w_1|}{\sqrt{3}}, \tag{4.47}$$

using $\sigma^2 =$ width of interval/12 [161]. A summary of these standard deviations for all measured samples and of the uncertainties in N obtained with the approximative method is given in Table 4.10.

Analogous evaluations were performed for the Lambert model; the resulting uncertainties in N are summarized in Table 4.11.

4.10.6 Systematic uncertainties from the curvature of the plates

Measurements of the plate surfaces with the 3D measurement machine (cf. Section 4.6.2) showed curvatures for all samples. In most cases the curvature has the shape of a single bend in x-direction making the plate slightly convex (where the surface in the central region is higher up compared to the end regions) or slightly concave. By selection of appropriate plates, the spread of the bend, Δs, i.e. the height difference of the highest and the lowest point on the surface, was kept below 70 μm for floatglass plates (including coated samples). For stainless steel, 112 μm (concave) and 54 μm (convex) were found; for the Replika plates 55 μm and 129 μm (both concave). Such a bend introduces artificial angle transformation on reflections. This effect can be suppressed by combining a concave plate with a convex one. If the two plates have exactly the same curvature, an angle change induced by the reflection from one plate is fully compensated with the subsequent reflection from the other plate.

A full compensation is practically not possible due to the different curvatures. Systematic uncertainties are therefore introduced which depend on the curvature difference of the upper and the lower plate. The uncertainties in N are estimated by the simulation of a plate pair of which the lower plate has a curvature of bend-like shape. The upper plate is assumed to be flat. Values of +200 μm, +100 μm, 0 μm (flat), -100 μm and -200 μm were used for the spread of the lower plate, where "+" refers to plates which have their central section at the largest z-coordinate, i.e. to convex plates. The normalization factor for spread values between the simulated numbers are interpolated using a quadratic function for $N(\Delta s)$. The maximum spread used for the evaluation of the uncertainty of N is ± 50 μm for coated and uncoated floatglass plates, ± 100 μm for the stainless steel plates and ± 200 μm for the Replika plates.

These simulations were performed for both reflection models. The uncertainties in N for the microroughness model and the Lambert model are summarized in Tables 4.10 and 4.11, respectively.

Table 4.10: Systematic uncertainties in N for the microroughness model caused by the uncertainties of the Fermi potential, $\Delta N(\Delta V_F)$, of the loss coefficient, $\Delta N(\Delta\eta)$, and by the curvature of the sample plates, $\Delta N(\Delta s)$. The total systematic uncertainties of N, $\Delta N_{\text{tot}}^{\text{syst}}$, are obtained by quadratic addition of the individual uncertainties. Additional uncertainties in b and w caused by $\Delta\eta$ are estimated by the shift of the point (b_0, w_0), i.e. the fit result for the simulated grid with $\eta = 0$, to the point (b_1, w_1), which is the fit result for the grid simulated at $\eta = 10.5 \cdot 10^{-4}$.

Sample	$\Delta N(\Delta V_F)$ $[10^{-6}]$	$\Delta N(\Delta\eta)$ $[10^{-6}]$	$\Delta b(\Delta\eta)$ [nm]	$\Delta w(\Delta\eta)$ [nm]	$\Delta N(\Delta s)$ $[10^{-6}]$	$\Delta N_{\text{tot}}^{\text{syst}}$ $[10^{-6}]$
FG 7/15	2.300	4.467	0.14	33.9	0.362	5.037
Optico 3/3	2.116	4.012	0.12	30.1	0.323	4.547
FG-HF	1.862	3.322	0.11	6.1	0.365	3.826
Ni 8/9	0.314	1.061	0.01	0.1	0.391	1.174
Ni 5/10	0.189	0.586	0.02	0.1	0.213	0.651
NiMo 10/20	0.358	1.762	0.20	0.01	0.539	1.877
NiV 11/11	0.034	1.332	0.14	3.6	0.097	1.336
DLC 30×50	0.084	1.353	0.04	12.8	0.084	1.358
DLC 5×60	0.019	0.193	0.29	7.4	0.009	0.194
Replika 30×50	0.028	1.119	0.03	9.9	0.384	1.183
Replika 40×50	0.039	1.202	0.02	4.1	0.300	1.240
Replika 10×60	0.013	0.329	0.03	8.1	0.134	0.356
SS 2a/2b	0.591	1.651	0.02	0.7	0.639	1.866

4.10.7 Summary of the systematic effects

The systematic uncertainties determined in Sections 4.10.4, 4.10.5 and 4.10.6 are summarized in Table 4.10 for the microroughness model and in Table 4.11 for the Lambert model. The values of b, w and N to which these uncertainties apply to are given in Section 4.11. The total systematic uncertainties of N, $\Delta N_{\text{tot}}^{\text{syst}}$, are obtained by quadratic addition of the individual uncertainties, i.e. by

$$\Delta N_{\text{tot}}^{\text{syst}} = \sqrt{(\Delta N(\Delta V_F))^2 + (\Delta N(\Delta\eta))^2 + (\Delta N(\Delta s))^2}. \tag{4.48}$$

For both models, the total uncertainty in N is dominated by the uncertainty caused by $\Delta\eta$. The following considerations apply to the microroughness model. It must be pointed out that the systematic uncertainties listed here refer to the *uncorrected* normalization factors $\tilde{N}$. The uncertainties found for the data sets which are limited by statistics, i.e. for FG-HF, Ni 5/10 and DLC 5×60, are found to be significantly lower than the corresponding values of similar data sets/samples. This is due to the decreased sensitivity to the systematic variation of the Fermi potential, the loss coefficient and the plate curvature.

The largest values for $\Delta N(\Delta V_F)$ are found for the uncoated glass plates, significantly above the corresponding values of the other samples. This can be understood with the large change in the transmission through the plates for even the smallest change in the Fermi potential of glass due to the characteristic distribution of the neutron kinetic energies (which peaks well above the Fermi potential of glass). Materials with a Fermi potential above that of stainless steel are found to have $\Delta N(\Delta V_F) \leq 0.4 \cdot 10^{-6}$ and are therefore relatively insensitive to changes of the Fermi potential.

Table 4.11: Systematic uncertainties in N for the Lambert model caused by the uncertainties of the Fermi potential, $\Delta N(\Delta V_F)$, of the loss coefficient, $\Delta N(\Delta\eta)$, and by the curvature of the sample plates, $\Delta N(\Delta s)$. The total systematic uncertainties of N, $\Delta N_{\mathrm{tot}}^{\mathrm{syst}}$, are obtained by quadratic addition of the individual uncertainties.

Sample	$\Delta N(\Delta V_F)$ $[10^{-6}]$	$\Delta N(\Delta\eta)$ $[10^{-6}]$	$\Delta N(\Delta s)$ $[10^{-6}]$	$\Delta N_{\mathrm{tot}}^{\mathrm{syst}}$ $[10^{-6}]$
FG 7/15	2.000	5.016	0.421	5.416
Optico 3/3	2.067	4.184	0.350	4.680
FG-HF	1.786	3.232	0.290	3.704
NiMo 10/20	0.048	0.581	0.088	0.589
NiV 11/11	0.138	1.816	0.133	1.826
DLC 30×50	0.156	1.830	0.142	1.842
DLC 5×60	0.017	0.206	0.009	0.206
Replika 30×50	0.055	1.095	0.319	1.142
Replika 10×60	0.021	0.433	0.125	0.451
SS 2a/2b	0.288	1.237	0.282	1.301

This can be understood by the energy spectrum used which is cut by the Fermi potential of stainless steel (used as guide material). Within the group of samples with $V_F \geq 200$ neV, differences in $\Delta N(\Delta V_F)$ of up to one order of magnitude are found. Higher values are found for samples which have a large fraction of diffuse scattering as Ni or NiMo, which means that these samples are more sensitive to changes in the Fermi potential compared to e.g. NiV, DLC or Replika. This can be understood by the fact that for the microroughness model, the averaged angle of reflection for UCN which are reflected diffusely is smaller than the angle of incidence if the latter is around 50° (cf. Section 4.3). This transformation of the angle to smaller values leads to an increased velocity component normal to the reflecting surface, $v_\perp$, and therefore to an increased sensitivity to the Fermi potential.

Also $\Delta N(\Delta\eta)$ is found to be significantly larger for low Fermi potentials which is not obvious as in the simulation η is defined as a quantity which is independent of the Fermi potential. More detailed considerations show that the (simulated) transmission through the plates, T, is proportional to the fraction of neutrons which is reflected at the Fermi potential barrier, p_E, and the probability of not being lost $(1-\mu)$ during the various reflections (k), i.e. $\sim (1-\mu)^k$. The normalization factor, N, correlates T with the measured normalized rate, x, i.e. $x = N \cdot T$. This leads to

$$N = \frac{x}{p_E(1-\mu)^k} \quad \text{and} \quad \frac{\mathrm{d}N}{\mathrm{d}\mu} = \frac{k \cdot x}{p_E(1-\mu)^{k+1}}, \tag{4.49}$$

from which can be seen that $\Delta N \sim 1/p_E\,\Delta\eta$. Consequently, the uncertainties must become larger for lower Fermi potentials as p_E is small in this case.

Nuances between the values of $\Delta N(\Delta\eta)$ are found within the group of samples with high Fermi potential. Larger values are found for samples with a small fraction of non-specular reflectivity. They can be understood with the larger sensitivity of such samples to additional loss channels as the losses caused by diffuse reflection and subsequent leaving of the acceptance are minimized by the large fraction of specular reflectivity. The value of NiMo seems to be contradictory. However, it has to be taken into account that for NiMo a very large value was found for $\tilde{N}$ compared to the other samples (cf. Table 4.12 below).

For $\Delta N(\Delta s)$, quite similar uncertainties are observed for most of the samples. Exceptions are the samples with high Fermi potential and very low surface roughness, NiV and DLC. These samples show a $\Delta N(\Delta s)$ which is significantly smaller compared to the rest of the samples. This can be understood if the reflections from these sample plates are considered to be purely specular. Such a reflection behavior allows for the compensation of any angle transformation by the plate curvature if the curvature is symmetric in x-direction, which is the case for the simulated bend-like curvature. Although FG 7/15 and Optico 3/3 were found to have a small fraction of diffuse reflectivity, they show about the same sensitivity to plate curvature as diffusely reflecting plates with high Fermi potential. This can be explained by the fact that the angle transformation caused by the curvature leads to changes in the size of $v_\perp$. Surfaces with a low Fermi potential show an increased sensitivity to such changes. Please note that for stainless steel and Replika, significantly larger values were used for Δs compared to the other samples, which explains the higher values of $\Delta N(\Delta s)$ for these samples.

For the Lambert model, $\Delta N(\Delta V_F)$, $\Delta N(\Delta \eta)$ and $\Delta N(\Delta s)$ are also found to be higher for low Fermi potential surfaces. Nuances within groups of samples with similar height of the Fermi potential as determined for the microroughness model could not be observed for the Lambert model due to the insufficient agreement of the simulated values with the measured data. The systematic uncertainties of samples, for which no reasonable fit results can be obtained using the Lambert model, such as the Ni coated floatglass plates or Replika 40×50, were not determined (cf. Table 4.13 below).

4.11 Results of the double plate experiment

The results of b_0 and w_0, using MC simulations with $\eta = 0$ and statistical uncertainties, which are summarized in Tables 4.7 and 4.8, are obtained with different normalization factors N_0 for the individual sample plates. The full analysis has to use a single normalization factor, N_m, and must include systematic uncertainties. As N_m is not determined directly from a dedicated measurement, it has to be derived from the values obtained for the different plates, i.e. by averaging.

In order to account for the systematic uncertainties obtained in the previous sections, the model fits have to be repeated at $\eta = 10.5 \cdot 10^{-4}$ instead of $\eta = 0$, still using only statistical uncertainties. Using the fit procedures described in Sections 4.9.1 and 4.9.2, this leads to the values b_1, w_1 and $\tilde{N}_1$ for the microroughness model, which are shown in Table 4.12, and to the values d_1 and $\tilde{N}_1$ for the Lambert model, which are shown in Table 4.13.

For all quantities, small shifts in b to partly lower and partly higher values are obtained compared to the results determined with the simulations at $\eta = 0$. The shifts in w are somewhat larger but tend to go to higher values. The same trend is found for the normalization factor and can be understood as a compensation of the additional losses caused by $\eta = 10.5 \cdot 10^{-4}$.

The total uncertainty in $\tilde{N}$, $\Delta\tilde{N}_{\mathrm{tot}}$, is calculated by taking the root-mean-square of the statistical uncertainty $\Delta\tilde{N}_1$ and the systematic uncertainty $\Delta N_{\mathrm{tot}}^{\mathrm{syst}}$. It is shown in Table 4.14 which also shows the values of N converted to the standard opening of S1, 30 mm × 50 mm. The fourth column in the table indicates which samples are included/excluded into/from the average value of N, subsequently referred to as $\overline{N}$. The samples FG-HF, Ni 5/10 and DLC 5×60 are excluded because they were previously found to be limited by statistics. The data set "Replika 40×50" was excluded from the average as the corresponding measurements were not performed in consecutive order which may result in (disregarded) additional systematic uncertainties due to limited reproducibility of the experimental settings. Averaging is performed using the weights $1/\Delta\tilde{N}_{\mathrm{tot}}^2$. The uncertainty of $\overline{N}$ is found as the error of mean, using the same weights. Both, systematic and statistical uncertainties, have to be included into the weights as they show different values for the various samples. For the standard size of the opening of aperture S1, 30 mm × 50 mm,

$$\overline{N} = (9.248 \pm 1.193) \cdot 10^{-6} \tag{4.50}$$

is found. The corresponding values for the other sizes of the S1 opening are $(14.716 \pm 1.904) \cdot 10^{-6}$ for 40 mm $\times$ 50 mm, $(2.672 \pm 0.346) \cdot 10^{-6}$ for 10 mm $\times$ 60 mm and $(1.846 \pm 0.239) \cdot 10^{-6}$ for 5 mm $\times$ 60 mm.

Calculation of a corresponding value for $\overline{N}$ with the values obtained using the Lambert model gives a significantly lower result: $\overline{N} = (6.317 \pm 1.666) \cdot 10^{-6}$. As the Lambert model turns out to be a significantly less precise description of the reflection behavior, this value is not used.

Additional information for the discussion of the fit results can be obtained directly from the measured data: Table 4.15 shows a summary of ratios of normalized rates from different configurations, such as 5/3 : 5/5, 5/2 : 5/5, x/x/S / x/x and x/x/O / x/x, where in most cases x=4(mm). It shows large differences between some of the sample plates.

4.11.1 Results from the model fits using averaged normalization

The following results are obtained using the fit procedures for the microroughness model, as described in Section 4.9.1, and for the Lambert model, as described in Section 4.9.2. In step 3 of these procedures, the averaged normalization factor $\overline{N}$ from above (obtained with the fits of the microroughness model) was used.

Table 4.16 summarizes the resulting values of this final fit; b_2 and w_2 are the resulting parameter values of the microroughness model fit and d_2 is the resulting parameter value of the Lambert model fit. The additional uncertainties for b and w caused by $\Delta\eta$ are included *after* fitting, using the root-mean-square of the contributions from the fit and from $\Delta b(\Delta N)$ and$\Delta b(\Delta N)$, respectively, and are therefore not included in the fit. For some samples, no fit of the Lambert model was performed as their underlying results in Table 4.14 are considered to be unreasonable, indicated by very large values of $\tilde{N}$. The data set "DLC 5×60" could not be fitted with the Lambert model at all.

In general, the values for χ^2_{min}/DOF are below 1 for the microroughness model fits. This is a clear indication for an overestimation of the systematic errors. However, there are a few exceptions. The samples FG 7/15 and Optico 3/3 show a normalized χ^2_{min} of 7.8 and 7.5, respectively. This can be explained by the fact that χ^2_{min} corresponds to the model fit which does not take the additional uncertainties $\Delta b(\Delta\eta)$ and $\Delta w(\Delta\eta)$ into account which are about three times larger for FG 7/15 and Optico 3/3 compared to the other samples. The two data sets "30×50" and "10×60" of the Replika plates show a very flat χ^2-distribution (caused by the lack of converging configurations) and therefore have large uncertainties in b and w.

By comparison, the values for χ^2_{min}/DOF are well above 1 and much larger for the Lambert model fits (see last column of Table 4.16) with two exceptions: The two data sets "30×50" and "10×60" of the Replika plates can be well fitted by the Lambert model. As indicated above, these two data sets are significantly less sensitive to non-specular reflection.

Figure 4.57 shows the χ^2-distributions of the microroughness model fits for the samples FG 7/15, Optico 3/3, Ni 8/9, NiV, DLC 30×50 and SS. The 1σ-, 2σ- and 3σ-contours are visible as white lines around the white cross which denotes (b_2, w_2). The red squares around the red cross correspond to once and twice the uncertainties in b_{avg} and w_{avg} obtained by the AFM measurements, see Table 4.2. The corresponding residual plots for the microroughness and the Lambert model fits are shown in Figure 4.58. The residual plots show that especially for converging configurations, the Lambert model fits the data much worse compared to the microroughness model.

The error contours of all samples are significantly larger compared to those of the fits obtained with only statistical uncertainties in Section 4.9.3. The fit results are discussed in more details in the following. A comparison of the microroughness model fits to corresponding values obtained by AFM is performed in Section 4.11.2 while Section 4.12 discusses the consequences from the results.

Table 4.12: Results from fitting simulated data to measured data using statistical uncertainties and the microroughness model. The simulations correspond to $\eta = 10.5 \cdot 10^{-4}$.

Sample	b_1 [nm]	w_1 [nm]	$\tilde{N}_1$ [10^{-6}]	$\chi^2_{\min}$/DOF
FG 7/15	$1.00^{+0.03}_{-0.07}$	$101.0^{+6.7}_{-6.0}$	12.20±0.07	26.9/5
Optico 3/3	1.00±0.02	$130.0^{+4.8}_{-4.1}$	11.78±0.05	66.7/8
FG-HF	1.83±0.03	$62.9^{+3.6}_{-3.4}$	11.53±0.12	3.87/4
Ni 8/9	$2.99^{+0.03}_{-0.02}$	24.7±0.1	12.96±0.18	5.77/4
Ni 5/10	3.00±0.03	25.1±0.2	7.70±0.13	1.03/2
NiMo 10/20	$3.07^{+0.08}_{-0.11}$	$10.9^{+0.7}_{-0.5}$	19.16±0.23	24.6/4
NiV 11/11	0.83±0.01	18.9±0.9	7.73±0.03	7.77/4
DLC 30×50	0.87±0.01	$58.7^{+1.5}_{-1.4}$	7.26±0.02	99.1/15
DLC 5×60	$0.90^{+0.13}_{-0.43}$	$130.6^{+19.5}_{-115.3}$	1.01±0.01	0.721/1
Replika 30×50	$0.92^{+1.61}_{-0.05}$	$51.2^{+146.3}_{-8.2}$	6.83±0.04	11.3/1
Replika 40×50	0.90±0.03	$63.5^{+4.1}_{-3.7}$	8.17±0.06	5.45/3
Replika 10×60	$1.08^{+0.11}_{-0.07}$	$59.5^{+10.7}_{-8.9}$	2.36±0.01	3.91/3
SS 2a/2b	2.54±0.01	$20.7^{+0.7}_{-0.8}$	11.87±0.13	9.18/4

Table 4.13: Results from fitting simulated data to measured data using statistical uncertainties and the Lambert model. The simulations correspond to $\eta = 10.5 \cdot 10^{-4}$.

Sample	d_1 [%]	$\tilde{N}_1$ [10^{-6}]	$\chi^2_{\min}$/DOF
FG 7/15	0.36±0.01	12.76±0.07	363/6
Optico 3/3	0.17±0.01	11.13±0.04	938/9
FG-HF	0.86±0.01	9.16±0.09	379/5
Ni 8/9	$9.78^{+0.11}_{-0.09}$	195.7±7.3	88.7/5
Ni 5/10	$8.09^{+0.06}_{-0.05}$	89.23±3.73	291/3
NiMo 10/20	$2.54^{+0.01}_{-0.02}$	4.71±0.04	207/5
NiV 11/11	0.96±0.01	10.54±0.05	749/5
DLC 30×50	0.90±0.01	10.32±0.26	2930/16
DLC 5×60	0.23±0.01	1.04±0.01	0.908/2
Replika 30×50	0.58±0.01	2.36±0.01	37/2
Replika 40×50	2.90±0.01	50.63±0.54	166/4
Replika 10×60	0.75±0.01	6.50±0.03	10.7/4
SS 2a/2b	$3.16^{+0.03}_{-0.02}$	8.05±0.08	739/5

Table 4.14: Normalization factors for both reflection models including statistical and systematic uncertainties for the individual opening sizes of S1 ($\tilde{N}$) and converted to the standard size of the S1 opening (N).

Sample	Microroughness model			Lambert model	
	$\tilde{N}$ [10^{-6}]	N [10^{-6}]	included in average	$\tilde{N}$ [10^{-6}]	N [10^{-6}]
FG 7/15	12.20±5.04	12.20±5.04	yes	12.76±5.42	12.76±5.42
Optico 3/3	11.78±4.55	11.78±4.55	yes	11.13±4.68	11.13±4.68
FG-HF	11.53±3.83	11.53±3.83	no	9.16±3.71	9.16±3.71
Ni 8/9	12.96±1.19	12.96±1.19	yes	195.7±7.3	195.7±7.3
Ni 5/10	7.70±0.66	7.70±0.66	no	89.23±3.73	89.23±3.73
NiMo 10/20	19.16±1.89	19.16±1.89	yes	4.71±0.59	4.71±0.59
NiV 11/11	7.73±1.34	7.73±1.34	yes	10.54±1.83	10.54±1.83
DLC 30×50	7.26±1.36	7.26±1.36	yes	10.32±1.86	10.32±1.86
DLC 5×60	1.01±0.19	5.05±0.98	no	1.04±0.21	5.21±1.04
Replika 30×50	6.83±1.18	6.83±1.18	yes	2.36±1.14	2.36±1.14
Replika 40×50	8.17±1.24	5.13±0.78	no	50.63±8.46	31.82±5.33
Replika 10×60	2.36±0.36	8.17±1.24	yes	6.50±0.45	22.48±1.59
SS 2a/2b	11.87±1.87	7.46±1.18	yes	8.05±1.30	5.06±0.82

Table 4.15: Ratios of normalized rates of different configurations. The variation of S4 was performed at plate gap x.

Sample	5/3 : 5/5 [%]	5/2 : 5/5 [%]	x [mm]	x/x/S : x/x [%]	x/x/O : x/x [%]
FG 7/15	1.8±0.1	0.33±0.04	4	100.3±0.9	111.2±1.5
Optico 3/3	1.7±0.1	0.43±0.06	4	102.0±1.0	111.9±1.4
FG-HF	7.5±0.4	1.39±0.20	4	100.0±3.1	140.5±3.5
NiV 11/11	2.2±0.1	0.51±0.05	4	101.5±1.3	108.8±1.3
Ni PSI 8/9	24.1±1.0	9.95±0.58	4	99.6±2.3	248.8±4.6
Ni PSI 5/10	-	-	4	101.1±3.0	265.7±6.1
NiMo PSI 10/20	7.8±0.3	2.49±0.13	4	105.0±2.1	130.4±2.2
DLC 30×50	5.0±0.2	0.84±0.04	4	105.9±0.6	117.8±0.6
DLC 5×60	-	-	-	-	-
Replika 30×50	-	-	-	-	-
Replika 40×50	6.6±0.2	-	5	106.3±1.9	122.2±3.0
Replika 10×60	-	-	6	101.9±2.1	118.0±2.2
SS 2a/2b	16.1±0.6	5.09±0.23	6	105.5±2.2	157.2±3.3

Table 4.16: Final results using the fits of the microroughness model and of the Lambert model for the various samples. The fits were performed using an averaged normalization factor $\overline{N} = (9.248 \pm 1.193) \cdot 10^{-6}$. The values for $\chi^2_{\mathrm{DOF}} = \chi^2_{\mathrm{min}}/\mathrm{DOF}$ correspond to the fits only and do not take $\Delta b(\Delta N)$ and $\Delta b(\Delta N)$ into account.

Sample	Microroughness model (MR)				Lambert model (L)		
	b_2 [nm]	w_2 [nm]	χ^2_{DOF}	d_{MR2} [%]	d_2 [%]	χ^2_{DOF}	$\frac{\chi^2_{\mathrm{DOF}}(\mathrm{L})}{\chi^2_{\mathrm{DOF}}(\mathrm{MR})}$
FG 7/15	0.91±0.15	$95.9^{+35.1}_{-35.5}$	39.0/5	0.81±0.12	$0.31^{+0.03}_{-0.02}$	287/6	6.1
Optico 3/3	0.96±0.13	$125.9^{+30.6}_{-30.5}$	60.2/8	0.99±0.15	0.11±0.03	355/9	5.2
FG-HF	$1.78^{+0.59}_{-0.20}$	$92.3^{+64.1}_{-21.3}$	0.597/4	3.04±0.42	0.87±0.05	249/5	333.7
Ni 8/9	$2.70^{+0.06}_{-0.05}$	$24.8^{+0.9}_{-0.7}$	1.17/4	10.79±2.86	-	-	-
Ni 5/10	$3.13^{+0.12}_{-0.10}$	$25.1^{+0.5}_{-0.4}$	0.39/2	14.60±3.87	-	-	-
NiMo 10/20	$2.38^{+0.27}_{-0.22}$	11.8±1.4	1.63/4	5.00±1.34	$3.31^{+0.08}_{-0.09}$	11.7/5	5.7
NiV 11/11	$1.01^{+0.16}_{-0.15}$	$15.0^{+4.4}_{-4.5}$	1.28/4	1.02±0.23	0.99±0.01	496/5	310.0
DLC 30×50	0.94±0.05	$34.0^{+13.1}_{-13.0}$	6.64/15	1.39±0.34	0.71±0.01	639/16	90.2
Repl. 30×50	$1.89^{+1.11}_{-0.92}$	$105.2^{+84.9}_{-102.8}$	0.364/1	8.41±2.80	0.94±0.07	1.72/2	2.4
Repl. 40×50	1.12±0.06	$21.7^{+4.7}_{-4.5}$	4.46/3	1.71±0.45	-	-	-
Repl. 10×60	$1.55^{+1.45}_{-0.48}$	$69.3^{+93.0}_{-66.5}$	1.20/3	5.36±1.72	$1.09^{+0.06}_{-0.07}$	2.77/4	1.7
SS 2a/2b	$2.61^{+0.07}_{-0.06}$	$20.3^{+2.3}_{-2.2}$	0.719/4	6.89±1.33	$3.35^{+0.11}_{-0.13}$	113/5	125.7

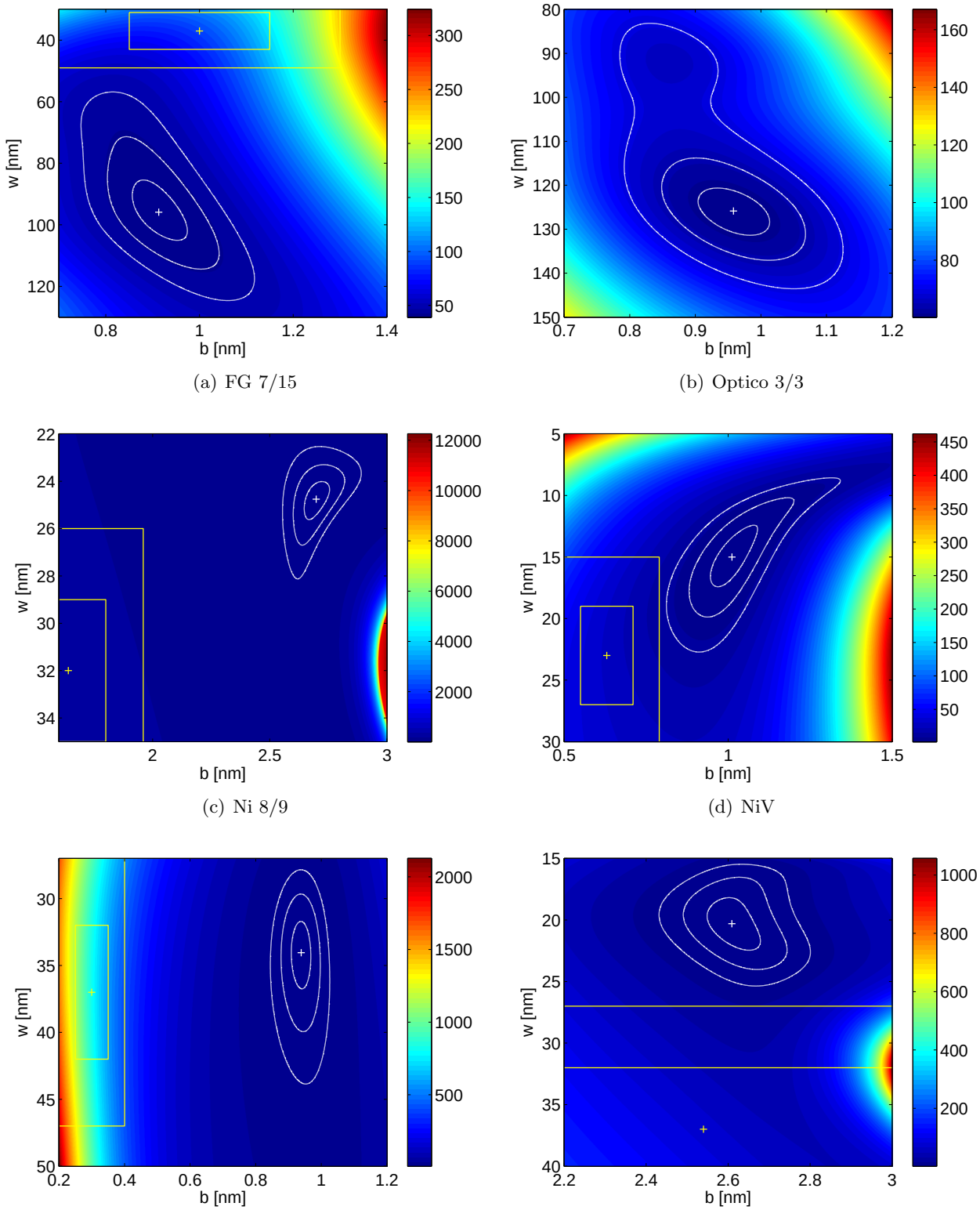

Figure 4.57: χ^2-distributions of the microroughness model fits for various samples including statistical and systematic uncertainties (excluding $\Delta b(\Delta\eta)$ and $\Delta w(\Delta\eta)$). The fits were performed using an averaged normalization factor $\overline{N}$. The 1σ-, 2σ- and 3σ-contours of the fit result are drawn as white lines while the yellow lines correspond to 1σ and 2σ of the AFM measurements.

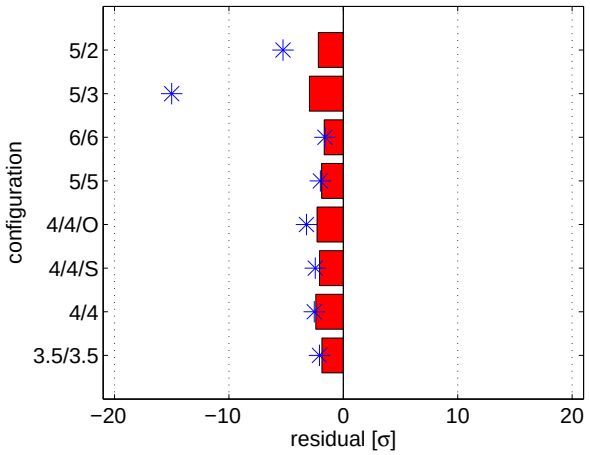

(a) FG 7/15

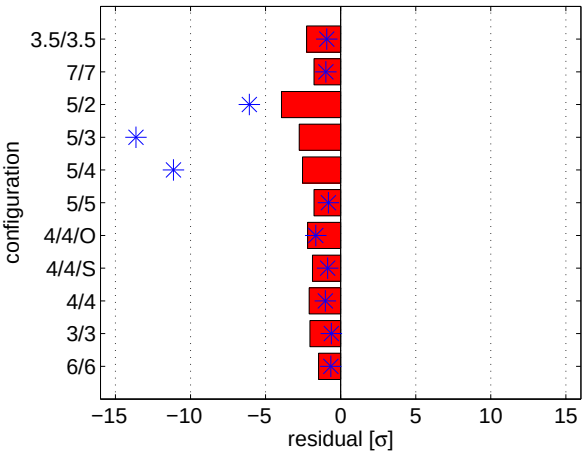

(b) Optico 3/3 (w/o AFM data)

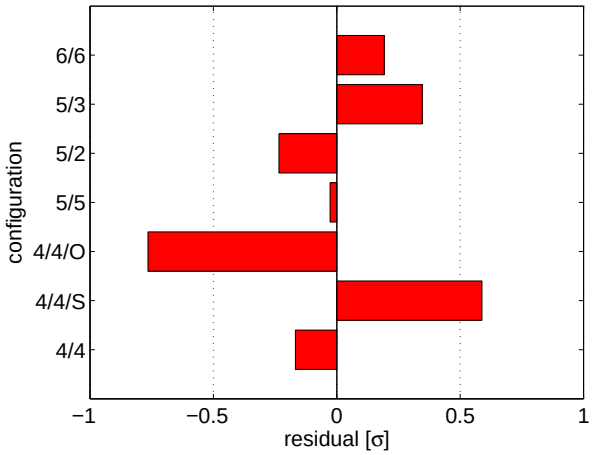

(c) Ni 8/9

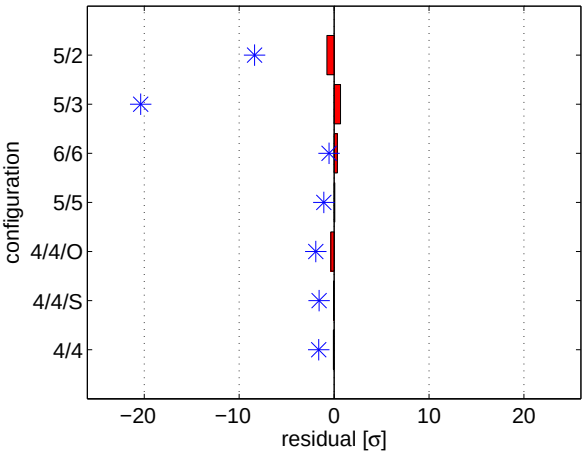

(d) NiV

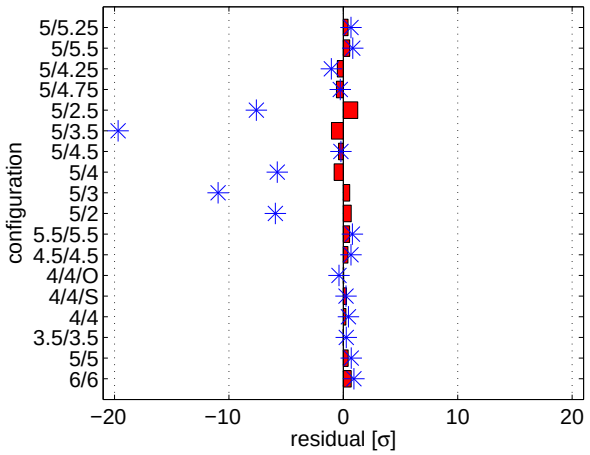

(e) DLC 30×50

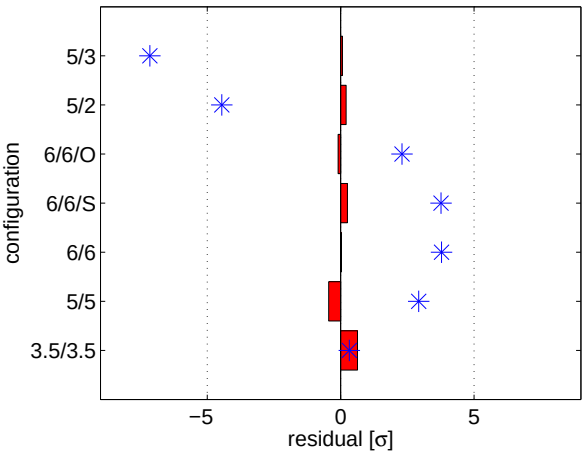

(f) stainless steel

Figure 4.58: χ^2-distributions of the microroughness model fits for various samples including statistical and systematic uncertainties. The fits were performed using an averaged normalization factor $\overline{N}$.

Uncoated glass plates

The samples Optico 3/3 and FG 7/15 show very similar values of the RMS roughness, slightly below 1 nm. This is within the expectations for the roughness of glass, which is of the order of 1 nm. Large values are found in both cases for w. Although the correlation lengths of the two samples are identical within uncertainties, the fit value found for Optico 3/3 is slightly larger than for standard floatglass. Mirror finishing, as used for the Optico plates, is expected to eliminate short-scale roughness and to produce longer-scale waviness. Such a surface consequently has a larger correlation length.

With the systematic variation of the Fermi potential, as described in Section 4.10.4, the best values for the Fermi potential of the three samples are found to be consistent with each other (uncertainties: ± 5 neV for all three samples): 87 neV (FG-HF), 88 neV (FG 7/15) and 89 neV (Optico 3/3).

The Lambert model fits of FG 7/15 and Optico 3/3 show very low fractions of diffuse reflection, well below 1%. The corresponding fraction of FG-HF is significantly larger but still below 1%.

Floatglass with Ni and NiX coatings

Floatglass plates have a small intrinsic roughness, typically $\lesssim$1 nm, as found above, which leads to a low probability of diffuse reflection accordingly to the microroughness model. A serious disadvantage of glass is the low Fermi potential of 90 neV or less. Coating the glass surface with a layer of a material with high Fermi potential combines the advantage of small surface roughness with a larger number of reflected neutrons due to the higher Fermi potential. However, the deposition of the reflecting material layer increases the surface roughness by an amount which depends on the material and on the deposition technique used. A possible material with high Fermi potential, which can be deposited onto glass, is nickel.

The microroughness model fits show about the same values of b and w for the two nickel coated floatglass plates. The RMS roughness of Ni 5/10 is the highest obtained for all samples under investigation. The correlation length of about 25 nm is also very disadvantageous as the transmission for parallel configurations has a minimum around that value for rougher plates, as can be seen e.g. in Figure 4.40. The corresponding transmission for converging configurations is high. For Ni 8/9 and Ni 5/10, the highest values of all investigated plates were found (cf. Table 4.15).

For NiMo 10/20, a slightly lower value is obtained for the RMS roughness. The correlation length is found to be significantly smaller than for the Ni coated plates. Thus, it is not in the region of minimum transmission for parallel configurations. For converging configurations and the configuration without S4, the transmission is found to be significantly lower than for Ni coated floatglass plates.

For NiV on floatglass, b is significantly smaller and close to that usually observed for uncoated glass substrates. This leads to a very low transmission for converging configurations and S4 variations.

Lambert model fits were performed only for NiMo 10/20 and NiV. A quite large value is found for d of NiMo 10/20 which can be understood with the large transmission of converging configurations. Within the Lambert model it requires many diffuse reflections due to the lack of a dedicated direction of the non-specularly reflected neutrons. For NiV, a value of $\sim$1% is obtained for d, which is significantly higher as that of uncoated floatglass and even comparable to that of FG-HF.

Floatglass with DLC coating

As a main focus of the recent UCN wall coating research and development at PSI was put on DLC, it was planned for the double plate experiment to investigate DLC coatings from different origins, one of them produced by the TubePLD setup described in chapter 3. As discussed in

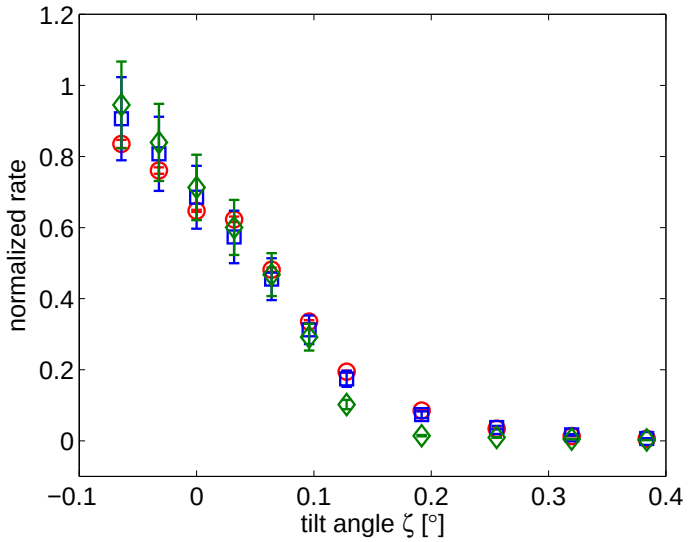

Figure 4.59: Normalized rates for DLC on floatglass as a function of the converging angle: measured data (red circles), microroughness model fit (blue squares) and Lambert model fit (green diamonds).

Section 3.5, the present version of the TubePLD setup cannot produce large area coatings. This is why only one sample, which consists of two DLC coated floatglass plates, was available for the double plate experiment. Nevertheless, a major interest is put into the DLC coating and its performance. Hence, extensive measurements were performed. Model fits were performed only for the data set "DLC, S1=30 mm × 50 mm", as the data set "DLC, S1=5 mm × 60 mm" was found to be limited by statistics for both reflection models and as it consists only of configurations which are relatively insensitive to non-specular reflections.

Figure 4.59 shows the measured normalized rates for the DLC sample plates as a function of the converging angle (red circles) and the corresponding fits of the microroughness model (blue squares) and the Lambert model (green diamonds). The measured curve shows a convex behavior for small tilt angles and a distinct tail at large tilt angles. Such a behavior was found in Section 4.8.3 for a convergence curve produced by MC simulation using the microroughness model and is significantly better described by the microroughness model fit compared to the Lambert model fit (see also Figure 4.58(e)).

The large number of configurations used for the microroughness model fit results in very small statistical uncertainties for b_1, w_1 and $\tilde{N}_1$. While the total uncertainty (including the systematic uncertainties) is still small for b_2, the uncertainty of w_2 is dominated by the relatively large uncertainty $\Delta w(\Delta\eta)$. A value slightly below 1 nm is found for the RMS roughness which shows that the deposition technique used for the DLC layer, i.e. ion beam sputtering, increases the surface roughness only marginally and is therefore well suitable for DLC films used as UCN wall coatings.

Ni Replika plates

As mentioned above, the Replika plates were used in a previous version of the double plate experiment [144], where a total reflectivity of (99.99±0.01)% was determined based on a purely specular model (cf. Eq. 4.27).

Microroughness model fits were performed for all three data sets. Large differences are found between the resulting b and w of the data set "S1=40 mm×50 mm" compared to the other two data sets, although the values are consistent with each other due to the large uncertainties for

the data sets "S1=30 mm × 50 mm" and "S1=10 mm × 60 mm". Although it has a $\chi^2_{\min}$/DOF slightly above 1, the data set "S1=40 mm × 50 mm" is considered to be the best description of the Replika plates. It has an RMS roughness of the order of 1 nm, which is much smaller than the roughness values obtained for the Ni coatings on floatglass, although the initial deposition process (magnetron sputtering, but with different facilities and operating parameter) was the same for both sample types. The major difference between the two samples types is which surface is on the outside. The outside of a grown layer (as in the case of Ni on floatglass) can be expected to be rougher than the interface between the layer and the smooth glass substrate. Such an interface is the outside of the Replika samples.

With the Lambert model fits, d is found to be roughly of the same order for the data sets "S1=30 mm × 50 mm" and "S1=10 mm × 60 mm" while for the third data set no reasonable fit could be performed.

Stainless steel plates

Coatings from materials with high Fermi potential on glass substrates allow for a good transmission of UCN in a guide due to minimized losses caused by $v_\perp > v_C$ and low surface roughness. However, there is a major drawback of glass substrates for the usage in or close to an UCN source: their insufficient radiation hardness. A possible replacement is stainless steel, however not as coating on glass, but e.g. as solid-walled tube. The way the surface of the stainless steel sample plates was treated, is expected to result in the lowest surface roughness possible without incorporation of significant amount of polishing agents. Application of a similar treatment to the inner wall of tubes is expected to result in a slightly higher roughness value.

The evaluated RMS roughness of the stainless steel plates is of about the same size as for NiMo while the correlation length is larger. For converging configurations and S4 variations, ratios were found which are slightly smaller than for NiMo.

With the Lambert model, the fraction of diffuse reflection, d, is found to be very similar to NiMo.

4.11.2 Roughness parameters

The two parameters of the microroughness model, the RMS roughness, b, and the correlation length, w, were determined by fitting measured data of the double plate experiment (cf. Table 4.16), leading to $(b, w)_{\mathrm{DP}}$, and with atomic force microscopy (AFM, cf. Table 4.2), leading to $(b, w)_{\mathrm{AFM}}$. This section discusses the agreement of the two methods for the different samples. The second column of Table 4.17 summarizes the deviation of $(b, w)_{\mathrm{DP}}$ and $(b, w)_{\mathrm{AFM}}$ for the different samples. The values are obtained graphically by iterative evaluation of the error contours for different multiples of the uncertainties of both measurements, e.g. for FG 7/15, the error contours which correspond to 1.8 times the total uncertainties do not overlap while 1.9σ do. The accuracy is therefore limited to $\pm 0.1\sigma$. The error contours for the double plate measurements are obtained by determination of the level curve for which $\chi^2 = \chi^2_{\min} + m^2$ where m is the multiple. The uncertainties $\Delta b(\Delta\eta)$ and $\Delta w(\Delta\eta)$ are taken into account by shifting one of the error contours with respect to the other.

For FG 7/15 and NiV, the agreement is good as it is within 95% C.L. (2σ). A moderate agreement (2-5σ) is found for the samples/data sets FG-HF, Replika 10×60, Replika 30×50 and stainless steel. The samples Ni 8/9, NiMo 10/20, DLC 30×50 and Replika 40×50 require more than 5σ to agree.

As the AFM values can be altered by local defects, dust particles and coating artifacts (such as e.g. over-coated particulates, cf. Chapter 3), it is advantageous to extract a lower limit for the RMS roughness by selecting the AFM measurement with the lowest value measured. This is done for all samples characterized by AFM; the selection is shown in Figure 4.60. As they are plotted

Table 4.17: Deviation in multiples of sigma between the microroughness parameters measured with the double plate experiment and with AFM (second column) and individual differences $b_2 - b_{\text{avg}}$, $b_2 - b_{\text{min}}$ and $w_2 - w_{\text{avg}}$ (columns 2-5, cf. Table 4.2).

Sample	deviation in σ	$b_2 - b_{\text{avg}}$ [nm]	$b_2 - b_{\text{min}}$ [nm]	$w_2 - w_{\text{min}}$ [nm]
FG 7/15	1.9	-0.09±0.21	0.79	59.4±36.0
Optico 3/3	-	no AFM data (plates too thick for AFM)		
FG-HF	3.2	0.42±0.63	0.75	51.3±64.3
Ni 8/9	5.9	1.06±0.17	1.50	-6.8±3.5
Ni 5/10	-	no AFM data		
NiMo 10/20	6.4	0.87±0.30	1.29	-10.7±1.7
NiV 11/11	1.9	0.38±0.18	0.61	-7.8±5.7
DLC 30×50	10.0	0.64±0.07	0.81	-2.9±13.9
Replika 30×50	4.0	0.38±1.11	1.24	66.0±102.8
Replika 40×50	6.0	-0.39±0.07	0.47	-17.5±5.1
Replika 10×60	2.5	0.04±1.45	0.90	30.1±93.1
SS 2a/2b	2.6	0.07±0.55	1.72	16.8±5.6
Average		0.34	1.01	14.4

on exactly the same z-scale, the roughness of the different samples can be directly compared. The differences between smooth samples such as FG 7/15 or DLC and rougher samples such as Ni or NiMo are distinct.

The differences between the final RMS roughness values (Table 4.16) obtained by the double plate experiment and by AFM (Table 4.2) are shown in Table 4.17, columns 3-5. For 50% of the samples, the difference between the averaged RMS roughness obtained by AFM and b from the double plate experiment is consistent with 0.

Compared with the minimum RMS roughness obtained for each sample, the values from the double plate experiment are systematically higher. The difference ranges from 0.5 nm up to 1.72 nm. In average, the additional roughness obtained with the double plate experiment is 1 nm. Scratches and small cracks in a coating can be an additional source of roughness. While all samples show this to some extent, the samples Replika and DLC show such defects on a higher level: scratches are distributed over the entire surface of the Replika plates, and are therefore expected to be measured with both methods, small cracks are visible on the surface of one DLC coated floatglass plate, most probably caused by internal stress of the coating. They are located on a part of the surface which is not accessible by the AFM device and are hence expected to increase only the value obtained by the double plate experiment. This may explain the 10σ deviation for (b, w) of the DLC plates which is mainly caused by the large difference in the RMS roughness while the correlation lengths obtained by the double plate experiment and by AFM are similar.

The differences between the correlation length values obtained by the double plate experiment and by AFM are shown in the last column of Table 4.17. For most of the samples, the values from the two methods are consistent within 2σ. However, an averaged overestimation of 14.4 nm by the double plate experiment is observed. It is dominated by the Replika data sets "S1=30 mm × 50 mm" and "S1=10 mm × 60 mm" (which are relatively insensitive to non-specular reflections) and by the glass samples. Excluding the former reduces the averaged overestimation to 6.6 nm.

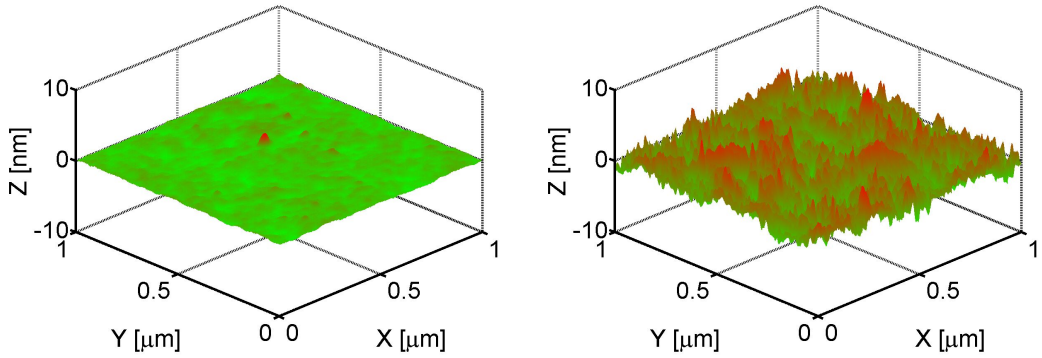

(a) FG 7/15

(b) FG-HF

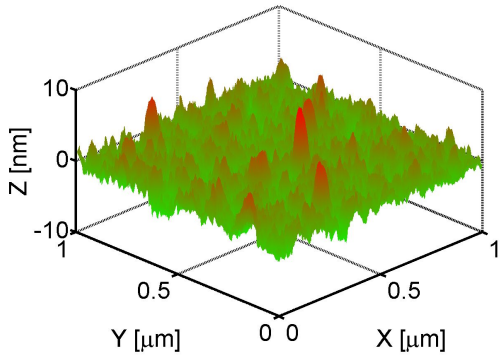

(c) Ni 8/9

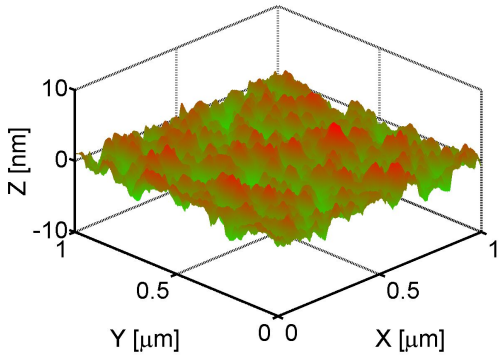

(d) NiMo 10/20

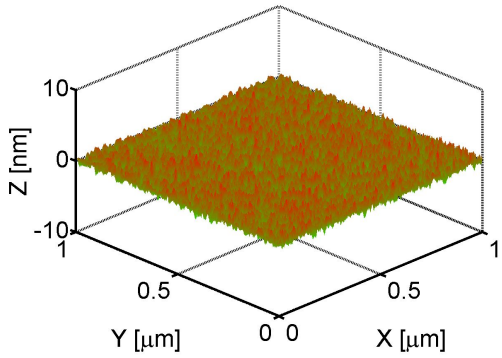

(e) NiV

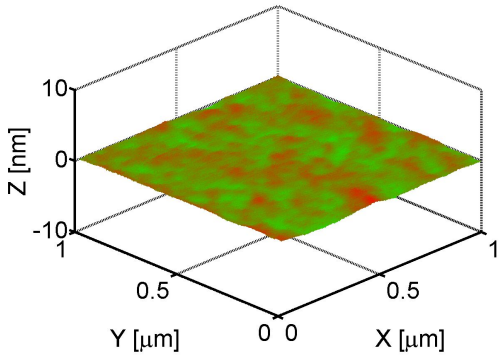

(f) DLC

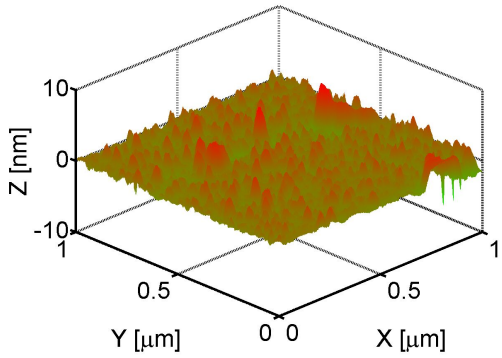

(g) Replika

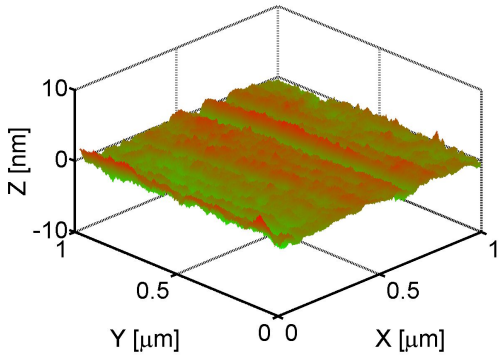

(h) stainless steel

Figure 4.60: Two-dimensional roughness profiles of various samples obtained with AFM. The profiles represent the measurements with minimum RMS roughness.

The stainless steel plates show an aligned surface structure, i.e. grooves, as can be seen in Figure 4.60(h). This is thought to be caused by the polishing. The grooves make a proper determination of the correlation length extremely difficult, as it is close to infinity (compared to the scan length of 1 μm) in direction of the grooves. However, the values for the RMS roughness obtained with the two methods are in good agreement for the sample SS.

The deviations found above raise the question how good the agreement of the results from the two methods can be expected to be. They use fundamentally different mechanisms, actually different interactions, in order to determine the surface structure. While the strong interaction is used with the double plate experiment, AFM uses mechanical contact forces which are based on the electromagnetic interaction. Thus, the results of the two methods do not necessarily have to agree.

Systematic effects do not only exist for the double plate experiment but also for AFM. In general, surfaces investigated with AFM are not required to be conductive. However, for very dry surfaces, local surface charges can lead to artifacts [162]. The size of the AFM tip is also known to have an influence on the quality of the surface spectra [163]. Especially an increase in the tip size, caused by long-term abrasion, leads to a decrease of the obtained RMS roughness for small lateral scan sizes [164] such as the size used here.

Different sources of systematic uncertainties in the double plate experiment were discussed in Section 4.10, but the list might be incomplete. On the microscopic scale, structures of a size similar to UCN wavelengths may cause additional (elastic) scattering. In ferromagnetic materials such as Nickel, magnetic domains can exist which are of that scale. This then leads to elastic scattering of the neutrons at these domains, as was investigated in e.g. Ref. [165]. Such a kind of scattering may appear as additional surface roughness and/or change of the correlation length for the microroughness model. The addition of 7% molybdenum or vanadium to the nickel suppresses the presence of magnetic domains at least partially [166, 167]. As the same deposition facility was used for the Ni and the NiMo coatings, they may have the same RMS roughness, around 2.7 nm. In this case, the additional $\sim$0.3 nm of the Ni coatings would be caused by the magnetic effects.

Another possibility of scattering centers may be density fluctuations within the reflecting material. Scattering at them is found to be similar to small angle scattering with cold neutrons [168].

4.12 Discussion

Two main classes of information can be derived from the results of the double plate experiment: 1) general information about UCN reflectivity, especially about the angular distribution of non-specularly reflected neutrons, and 2) the surface parameters of different materials, which allow for a material selection for UCN guides. The following two sections deal with these two classes of information.

4.12.1 Comparison of the reflection models

The values for $\chi^2_{\min}$/DOF in Table 4.16 are significantly smaller for the fits with the microroughness model compared to those with the Lambert model. In many cases the difference is about two order of magnitudes.

This can also be seen in the residual plots, shown in Figure 4.58. While the residuals of the parallel configurations are slightly larger for the Lambert model, the deviation from those of the microroughness model is tremendous for some converging configurations. Thus, diffuse reflection of UCN is well described by the microroughness model and cannot be described by the Lambert model.

Table 4.16 shows the average fraction of diffuse reflection, d_{MR2}, calculated from b_2 and w_2 using Eq. 4.40. The lowest values of d_{MR2} are found for FG 7/15 and Optico 3/3. From all samples with high Fermi potential, NiV shows the lowest value, closely followed by DLC. On the other end, the highest values are found for Ni, NiMo and SS. A large fraction of non-specular reflection does not necessarily mean a low transmission if such surfaces are used in an UCN guide. Especially surfaces for which a large correlation length is found show a large fraction of diffuse reflection, for which the angular distribution of the reflected neutron trajectories is well concentrated around the specular direction. For the practical use, this kind of diffuse reflection can hardly be distinguished from purely specular reflection behavior. Wide angular distributions of the diffusely reflected neutrons are observed for small correlation lengths. Although they may show a smaller total fraction of diffuse reflection, a lower transmission through an UCN guide can result, caused by storage effects due to e.g. backward reflected neutrons. Thus, d_{MR2} should not be used for the classification of an UCN guide surface. Furthermore, while d is representative for any neutrons reflected from a surface, d_{MR2} only describes the diffuse reflectivity for the energy- and angle-distributions used in the double plate experiment. A direct comparison of the two models on the level of their fractions of non-specular reflection is therefore not possible.

On a conceptual level, the success of the microroughness model and the failure of the Lambert model can be explained by the different angular distributions. While the Lambert model gives a homogeneous distribution in the azimuthal angle, i.e. it does not account for the direction of incidence, the microroughness includes it explicitly. Such an incorporation of the incident direction is not unique for the microroughness model but can be found in other reflection models as e.g. the Torrance-Sparrow model described in Section 4.1. Such a model is valid for faceted surfaces with facet sizes larger than the wavelength of the incident radiation, i.e. in the case of UCN larger than ~ 60 nm. Indeed, tests with a model similar to the Torrance-Sparrow model applied on the data of the double plate experiment point in this direction [169].

In Figure 4.2, possible mechanisms leading to the cosine-distribution of the Lambert model are given. They are based on multiple reflections at the surface or on multiple refraction within the material. Such multiple scattering mechanisms hence are less important for UCN reflected from rough surfaces. Rather a single reflection perturbed by the surface roughness is the more correct description. For any UCN applications where the exact knowledge of the trajectories is important, only the microroughness model should be used in MC simulations. However, for the simulation of UCN storage, especially in "bottles" with very rough wall surfaces, the Lambert model might be an adequate approximation if the exact knowledge of the individual UCN trajectories is of minor

importance.

4.12.2 Surface parameters and UCN guide transmission

High quality UCN guides are characterized by high transmission. Purely specular reflectivity leads to forward peaking of the UCN beam within a guide, see e.g. Refs. [170, 171]. This increases the longitudinal velocity and reduces the number of reflections from the guide walls. The wall loss probability is also decreased due to a decrease of the normal velocities. The combination of these effects leads to high transmission. It is therefore advantageous to use wall (coating) materials for which a close to specular reflection behavior is observed.

Within the microroughness model, such a reflection behavior is observed for very smooth surfaces such as of floatglass. The lowest values of the RMS roughness, b, are found for uncoated floatglass, for DLC on floatglass and for NiV on floatglass. These surfaces are therefore expected to be ideal as UCN wall materials. However, due to the much higher Fermi potential, the transmission of DLC on floatglass and of NiV on floatglass must be significantly higher.

Not only the RMS roughness is important for the reflection behavior but also the correlation length, w. While purely specular reflectivity is only observed for $b \to 0$, two limits of w exist for which totally specular reflection is observed: $w \to 0$ and $w \to \infty$. This can also be seen in Figure 4.40 which shows the simulated transmission through the double plates as a function of b and w. Very short and very long correlation lengths lead hence to a high transmission while a correlation length around 25 nm was found to result in a minimum transmission if combined with a higher value of the RMS roughness, as for the Ni coatings. Although the samples NiMo and NiV show a trend to a short correlation length, the good performance of NiV and the difference in transmission between NiMo and Ni coatings cannot be explained by their correlation lengths. Much smaller values for w, of the order of 5 nm, are required for a significant improvement of the transmission. Such a surface would consist of needle-like structures which are arbitrary distributed.

On a more mathematical level, these findings can be seen in Eq. 4.21, where the correlation length acts as inverse width of the Gaussian. There, the distribution of the non-specular reflection probability is narrowly distributed for large correlation lengths. The resulting trajectories are close to the direction of specular reflections. For short correlation lengths, a wide distribution is to be expected. However, another factor of w^2 precedes the Gaussian and reduces $F(\vec{\mu})$ significantly for small values of w. For $w \approx 25$ nm, a maximum is found for $F(\vec{\mu})$ and large b which leads to the minimum in the transmission shown in Figure 4.40.

In order to determine the transmission of a typical UCN guide with one of the tested surfaces from above, a MC simulation using GEANT4UCN was performed. A 5 m long cylindrical guide with 66 mm inner diameter was investigated. The diameter is a standard size, used commonly at e.g. the UCN source at ILL. The length corresponds to a typical distance between an UCN source and an experiment. The direction in which the guide is oriented is denoted as x, as for the double plate experiment. The guide is extended into negative x-direction and closed with a perfectly reflecting end cap ($V_F = \infty$) at $x = -1$ m. This extension is an approximation for e.g. the storage tank of the PSI UCN source. The loss coefficient is chosen as $10.5 \cdot 10^{-4}$ for all materials. The microroughness model is used for the description of the UCN reflection behavior.

All simulations are performed by starting 10^6 UCN trajectories with $v_x > 0$. The vertices are equally distributed within the guide at $x = 0$. The same energy spectrum and angular distribution as for the standard size of S1 in the double plate experiment are used. The energy spectrum therefore includes a significant fraction of VCN. The number of reflections and the time of flight is recorded for each UCN the trajectory of which is "successfully ended" at $x = 5$ m. From this information, an averaged reflection frequency is calculated. The transmission, T, as a function of time is calculated as

$$T(t) = \int_0^{t'} I(t')\,\mathrm{d}t', \tag{4.51}$$

Table 4.18: Results from the MC simulation of a 5 m long cylindrical guide with 66 mm inner diameter: maximum transmission $T_{\max}$, averaged reflection frequency $\overline{f_{\text{refl}}}$ and rise time of the transmission t_{rise}.

Sample surface	$T_{\max}$ [%]	$\overline{f_{\text{refl}}}$ [Hz]	t_{rise} [s]
FG 7/15	48.68±0.07	40.23±0.03	0.56±0.01
Optico 3/3	47.36±0.07	39.93±0.03	0.56±0.01
FG-HF	35.80±0.06	36.37±0.03	0.54±0.01
Ni 8/9	31.92±0.06	45.43±0.05	2.72±0.01
NiMo 10/20	45.74±0.07	50.02±0.04	1.35±0.01
NiV 11/11	75.83±0.09	55.07±0.03	0.64±0.01
DLC (30×50)	70.62±0.08	52.18±0.03	0.61±0.01
Replika (40×50)	69.78±0.08	53.94±0.03	0.68±0.01
SS 2a/2b	35.19±0.06	43.63±0.04	0.88±0.01

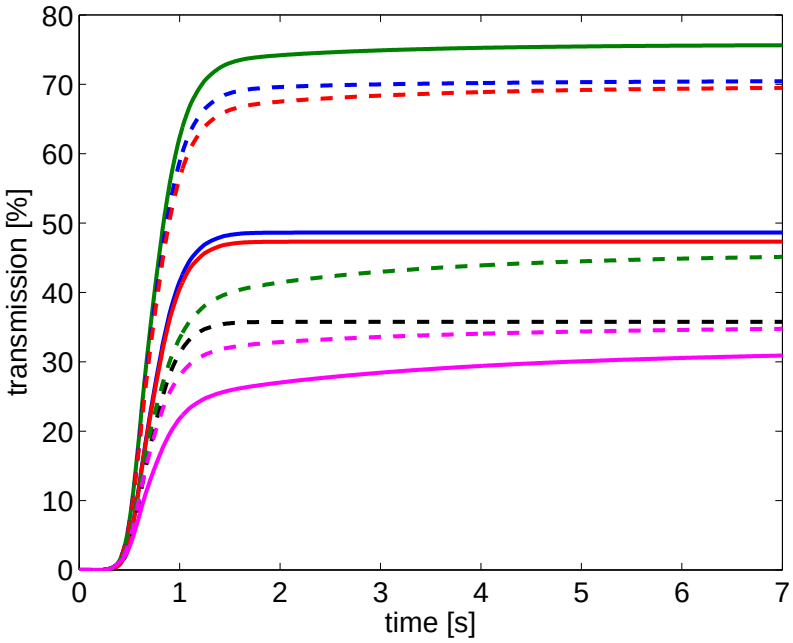

Figure 4.61: Transmission as a function of time observed by the MC simulation of a 5 m long cylindrical guide with 66 mm inner diameter for the sample surfaces NiV 11/11 (solid green), DLC (dashed blue), Replika (dashed red), FG 7/15 (solid blue), Optico 3/3 (solid red), NiMo 10/20 (dashed green), FG-HF (dashed black), SS (dashed magenta) and Ni 8/9 (solid magenta).

where $I(t')$ is the number of UCN which arrive at time t' within the interval $\mathrm{d}t'$ at the end of the guide relative to the number of UCN (10^6) started at $t = 0$. The maximum transmission $T_{\max}$, the averaged reflection frequency $\overline{f_{\text{refl}}}$ and the rise time of the transmission t_{rise} (from 10% to 90% of the maximum value) are shown in Table 4.18; $T(t)$ is shown in Figure 4.61.

The highest transmission is observed for NiV on floatglass, which is therefore a preferred material for UCN guides. However, as the admixture of 7% vanadium may not completely suppress local magnetization, it might depolarize a beam of polarized UCN. For polarized UCN, DLC on

floatglass would hence be the material of choice as its transmission is only marginally lower than that of NiV while it has no magnetic centers. In radiative environment such as the area close to an UCN source, glass substrates cannot be used. The best choice of a guide surface for such an environment would be a radiation hard substrate such as aluminum with a nickel layer produced by the Replika technique. Stainless steel, which was investigated with respect to its use in a radiation environment, should only be used if no alternative is available as it has a relatively low transmission. Another guide simulation with (b, w) from stainless steel and $V_F = 220$ neV leads to $T_{\max}$=34.86±0.06%. Thus, coating the stainless steel with a material with higher Fermi potential does not improve the transmission. The additional losses caused by the higher fraction of diffuse reflection (which depends on the Fermi potential within the microroughness model) overcompensates the gain due to the higher Fermi potential. However, one exception exists: If the coating changes the correlation length to much smaller values, the surface might show a less diffuse reflection behavior.

Uncoated glass also shows a relatively low transmission. This is caused by the losses due to the low Fermi potential of ≤90 neV. The same loss channel is also partially responsible for the suboptimal performance of stainless steel ($V_F = 186$ neV) due to the significant fraction of VCN and UCN with high kinetic energy, i.e. ≥186 neV. The Ni coating on glass is found to be at the lower end of the transmission range obtained with the guide simulation. Its poor transmission is caused by large roughness.

The reflection frequency is found to be higher for higher Fermi potential. This can be understood with the larger fraction of neutrons with a larger velocity components in radial direction (i.e. perpendicular to the x-axis) which are transported by the guide. For materials with low Fermi potential only neutrons with small radial velocity component, i.e. under glancing incidence, are transported. Such forward peaked neutron trajectories result in a lower reflection frequency and also in a slightly shorter rise time, as can be seen in Table 4.18.

A short rise time is important for pulsed UCN sources as it determines the maximum UCN density which can be reached at the end of the guide, i.e. in the experiment. Significantly higher rise times are observed for NiMo and Ni while for SS only a moderate increase is obtained. These increases are a consequence of the wide distribution of the (large) non-specular reflection probability, caused by relatively short correlation lengths and large RMS roughness. However, they are not short enough to substantially decrease $F(\vec{\mu})$. Within this wide distribution, a significant fraction of the trajectories are altered in such a way that their direction becomes more radial within the guide. Diffuse reflection may even lead to a direction with negative x-component, i.e. to UCN which travel back through the guide. This backflow is not a problem per se as another non-specular reflection can bring the neutrons back into the right direction. Thus, they still can pass the guide but are delayed. However, the number of reflections is increased with a twofold direction change and hence the total loss probability too. For a more dedicated simulation of a particular guide, neutron-related parts of the UCN source have to be included in more details as the backflow and the corresponding fraction of neutron which pass the guide again can strongly depend on the reflection behavior of these parts.

It has to be pointed out that the results of the guide simulation are strongly determined by the selected values for the loss coefficient, the guide geometry as well as by the energy distribution of the neutrons. Guides with larger inner diameters such as those planned for the PSI UCN source (inner guide diameter 180 mm) are less sensitive to the differences between the various surface qualities as the smaller reflection frequency leads to a lower number of reflections. On the other hand, the surface parameters used for the guide simulation correspond to values which are representative for flat plates. For the inner walls of tubes, a higher roughness is usually observed. The energy distribution used in the guide simulation contains many neutrons which are rather VCN than UCN, i.e. which have kinetic energies above ∼300 neV. Such neutrons are affected by losses due to $v > v_C$. Such losses may be of minor importance if the experiment at the end of the

UCN guide is based on an UCN storage measurement.

In general, surfaces with small roughness from materials with high Fermi potential are found to be the best choice as UCN guide walls. Such surfaces lead to a close to specular reflection behavior of the UCN. Thus, the findings in e.g. Refs. [170, 171] are confirmed by the double plate experiment and the MC guide simulation.

4.13 Possible improvements for the double plate experiment

The performance of the double plate experiment and the subsequent analysis of the measured data has shown that there is still some room for improvements.

For some plates, especially for those with very low transmission, beam-time was saved by reducing the number of measured configurations. In particular, omitting converging configurations save large amounts of beam time. However, it is counterproductive for a proper determination of the reflection behavior. An improved strategy should include the measurement of various converging configuration, as it was done for the DLC on floatglass sample plates. A reduction could be done for the parallel configurations, i.e. for the ones least sensitive to diffuse reflection.

Parallel configurations should not be fully omitted but performed at plate spacings which differ very strongly. In particular, parallel configurations with even larger plate gaps than those used for the present data are expected to improve the consistency of the normalization factors, N, as the number of reflections is small. Thus, the transmitted UCN rate gets closer to the incident rate which allows for a better determination of the latter. Alternatively, diverging configurations could be used for a reduction of the number of reflections, although this may have a large impact on the design of the rear part of the experiment as the exit gap of the plates would be significantly larger compared to parallel configurations.

For the improvement of the double plate experiment, a main focus should be put on the reduction of the systematic uncertainties. For a proper consideration of the curvature of the plates the data is already available, as all plates were measured with a 3D measurement machine. However, correct implementation of measured surface curvatures with irregularities of the order of up to $\sim$100 μm is a task for future, more UCN related, MC codes (cf. below). A moderate improvement for the systematic uncertainties caused by the uncertainty in the Fermi potential can be achieved by more detailed measurements with neutron reflectometry and a more elaborate analysis subsequently. However, an uncertainty below 1 neV is a challenge with the present devices using cold neutrons. Highly monochromatic cold neutron beams produced by transformation of the UCN phase space to higher energies may improve the accuracy of such measurements. A phase spacer transformer is projected for the UCN source at PSI [172].

By far the largest systematic uncertainties within the double plate experiment are caused by the inaccurate knowledge of the loss coefficient, η, of the material under investigation. Measurements of the loss coefficient exist for various materials, see e.g. [156, p. 351]. They are obtained under many different conditions, leading to fundamentally different results to some extend. Only a dedicated measurement including exactly the same plate surface as used for the double plate experiment can deliver a reliable result for η. This result can be obtained best by a storage measurement, where one or both plates is part of an UCN "bottle".

The individual measurement of the loss coefficient for each sample also has the advantage of including eventual losses from non-ideal surface treatment, in particular from cleaning. Although the cleaning procedure used for the samples of the double plate experiment is considered to be good in terms of UCN losses, a systematic investigation of surface cleaning effects with the double plate experiment would be advantageous.

For the analysis of the experiment, MC simulations performed with the GEANT4UCN code were used. As it is based on a code which is widely used in particle physics (GEANT4) and therefore well accepted, its adjustment to UCN physics is limited. Its step-wise tracking algorithms

are valuable for the computation of UCN trajectories in e.g. inhomogeneous magnetic fields. The double plate experiment is an experiment where the interaction of UCN is limited to the reflection from surfaces. For this purpose, a less sophisticated (but well adjusted for UCN) code as MCUCN, which calculates intersection points of UCN trajectories with material surfaces instead of splitting the trajectories into steps, may deliver the same results in shorter computation time. For future versions of the double plate experiment or similar experiments, the usage of such a code should be strongly considered.

The first part of the MC simulation, the simulation of the entrance guide, was performed using the Lambert model. In Section 4.10.2, it was found that the real angular distribution is more forward peaked than described by the simulation. An improved description of the angular distribution may be achieved by using the microroughness model for the MC simulation of the entrance guide, as the averaged direction of non-specularly reflected UCN is much closer to the direction of specular reflection compared to the Lambert model. A more forward peaked distribution would also lead to a decrease of the neutron velocities obtained for UCN within the angular range of interest. The consequence would be a larger fraction of neutrons transmitted through the double plates for a low Fermi potential such as of floatglass. This might decrease the differences in the normalization factor between the uncoated glass samples and the samples with higher Fermi potential.

Another possibility for testing the reflection behavior of UCN would be the detection of neutrons which originate from a well collimated beam and which are reflected only once from a plate. Such an experiment requires high statistics which is most conveniently achieved by using a segmented (pixels) large area UCN detector (covering a solid angle of 2π). If the intensity of the incoming beam could be determined quantitatively, e.g. by separately performed measurements of the beam intensity and the usage of a monitor detector during the reflection measurements, the loss coefficient might be determined simultaneously.

Chapter 5

Conclusions

A facility for coating the inner wall of UCN guides with DLC (TubePLD setup) was built and test coatings were produced. A standard procedure for the structural characterization of DLC coating was developed. An experiment for testing the reflectivity of UCN using surfaces with roughness (double plate experiment) was performed. The main conclusions from this work are:

- Well adherent large area DLC coatings could not be produced with the present TubePLD setup. The major bottleneck of the Tube PLD system are the low deposition rates of PLD in general, combined with the deficiencies of the used laser system. Exchanging the laser and the optical components with e.g. a vacuum-arc system may improve the situation, see e.g. Ref. [123]. If equipped with a magnetic filtering system, the ablated carbon particles would consist only of ions. Electric fields would allow for tuning the kinetic energies of the ablated particles. The system would hence benefit from larger deposition rates and kinetic energies of the ablated particles which are close to the ideal case. Together with an in-situ monitoring device for the kinetic energies of the carbon particles, a deposition process much closer to the ideal case as the current one could be achieved.

- The standard procedure for the structural characterization of DLC coatings developed here consists of three stages. The first stage (Raman spectroscopy) allows for crude selection of high-quality DLC coatings. The second stage (X-ray photoelectron spectroscopy) determines the sp^3 fraction of the DLC surface layer (and hence the film density close to the surface) with an accuracy of $\sim$10%. With the third stage (cold neutron reflectometry), the Fermi potential can be determined independently with $\leq$2% accuracy (with present instruments), from which the density obtained in stage 2 can be cross-checked. The third stage requires mirror-like surfaces and a neutron source while the first two stages get by with table-top equipment and rough and/or wavy surfaces.

- The double plate experiment described represents the first systematic study of UCN reflection as a function of the surface morphology (RMS roughness and correlation length), of the material Fermi potential, of the UCN energy and of the angle of incidence. It allows to disentangle the specular from the non-specular component of UCN reflections. This is achieved by the use of various configurations with different sensitivity to specular and non-specular reflectivity. In particular, the utilization of converging plate configurations is a significant improvement compared to earlier versions of the experiment and allows to test directly the diffuse reflection contribution.

- Standard UCN reflectors from high Fermi potential-materials such as Ni, NiMo, NiV and DLC coated floatglass plates as well as Ni coated plates produced with Replika technique and stainless steel were investigated and compared to uncoated floatglass plates (Fermi potential $\simeq$90 neV). Monte Carlo simulations of the experiment were performed using GEANT4UCN

for the b-w-parameter space of the microroughness model and for the d-parameter space of the Lambert model. These simulations were used for fitting measured data. The data of all samples could be well fitted with the microroughness model while the fits with the Lambert model describe the measured data much worse. Thus, for UCN reflectors with low roughness ($b \leq 5$ nm), the microroughness model by Steyerl from 1972 yields a description of the non-specular reflection consistent with experimental findings. Diffuse UCN reflection is a wave-interference phenomena connected to the structure and Fermi potential of the surface, to the UCN energy and to the angle of incidence.

- Uncoated floatglass as well as the DLC and the NiV coated floatglass plates showed the lowest fractions of diffuse reflection within the microroughness model. Due to the significantly higher Fermi potential of the coated samples, they are the most suitable materials for UCN guides. Both surface show remarkably small roughness, around 1 nm which leads to high transmission.

- For the first time, the values of the RMS roughness and the correlation length obtained with UCN were compared to the corresponding values measured with AFM for the same samples. Moderate agreement was found. The values of the RMS roughness found with the double plate experiment range from 0.91±0.06 nm for uncoated floatglass to 3.13±0.12 nm for Ni coated floatglass. The correlation lengths were found to be between 11.8±1.4 nm (NiMo on floatglass) and 125.9±5.5 nm (Optico 3/3).

Appendix A

The Tube PLD software

This appendix provides additional information about the Tube PLD software described in section 3.3.2. It is completely written in LabVIEW™ (Version 7.1) [121].

A.1 The slow control system

The slow control system monitors the pressure inside the deposition chamber, the temperatures of the laser cavity, the cooling water, the cryo pump, etc., the status of the pumping station, the laser energy meter and, if selected by the user, the status and position of the substrate trolley. As these values usually change on a time scale of minutes or hours, it is sufficient to read them out every ten seconds.

Most of the corresponding subsystems have a separate controller which is read out via serial link; this is the case for the temperature monitor of the cryo pump (Scientific Instruments Cryo-Temp Monitor), the pressure gauges (Pfeiffer RVC-300 and Pfeiffer DualGauge), the PLC of the pumping station (Bollrath FPS-32) and the stepper motor controller of the substrate trolley (Phytron TMC-93-70 MINI). The energy meter is read out via universal serial bus (USB), the temperature sensors via analog inputs of the NI-interface card.

Temperature, pressure and the laser energy can be monitored on the graph tab of the Tube PLD software and stored in a log file.

A.2 The fast control system

The fast control system operates the laser trigger and the fast steering mirror where the variation of the analog control signals is triggered by the same clock signal which is used as external trigger of the excimer laser. The analog output signals for the two axes of the fast steering mirror system are varied in such a way that the reflected laser beam follows a wiggly line on the graphite target. The fast control system also monitors the laser-on signal which is generated by the excimer laser itself if it is running.

A.3 The macro system

A macro system is included in the Tube PLD software. It allows the automated control of almost all subsystems of the Tube PLD setup and reads the information from a simple text file. Each command consists of a starting time relative to the starting time of the macro, a keyword and appropriate options. A commented example of a short macro is given in the following.

0	`tmc send command;XP14S200`	defines the translation velocity of the substrate trolley
3	`set frequency;10`	sets the laser repetition rate
4	`dual area;off`	uses only the main target
4	`set area borders;1,20,35,5,2.1,-3.4,-2.4`	sets the borders of the fast steering mirror movement
5	`tmc drive;X975`	starts the translation of the substrate trolley
15	`fsm scan mode;on`	activates the scanning mode of the fast steering mirror
20	`trigger;on`	switches on the clock (trigger)
21	`tmc acquisition;on`	starts the position monitoring of the substrate trolley
1678	`trigger;off`	switches off the clock (trigger)
1679	`fsm scan mode;off`	deactivates the scanning mode of the fast steering mirror
1679	`tmc acquisition;off`	stops the position monitoring of the substrate trolley
1685	`send message;Coating finished!`	sends a short message to a mobile phone
1690	`end macro;`	terminates the macro

A.4 The warning system

Five different values can be watched by the Tube PLD software:

1. The status of the pumping station,
2. the status of the laser,
3. the pressure inside the deposition chamber,
4. the temperature of the cold head and
5. the status of the end switches of the substrate trolley system.

For items 3) and 4) threshold values can be specified. Excess of these values or, for items 1), 2) and 5), the loss of the ok-signal leads to the activation of an emergency routine which interrupts any running macro, switches off the laser and sends a short message to a mobile phone. Reaction times of the warning system are below one second; however e.g. a sudden increase of the pressure inside the deposition chamber may be handled up to 10 s later due to the slow control interval time.

Appendix B

Implementation of the microroughness model into GEANT4UCN

In this appendix, information about the implementation of the microroughness model, as described in Section 4.3, in the GEANT4/GEANT4UCN code is given. Subsequently, the term diffuse refers to non-specularity as defined by the microroughness model. It has two parameters, the RMS roughness b and the correlation length w, from which the probability of diffuse reflection into direction (θ_o,ϕ_o) with incident angle θ_i ($\phi_i = 0$) for a UCN with kinetic energy E_n can be calculated by Equation 4.23. For the primary decision of specular or diffuse reflection I_+ has to be integrated over all possible angles of reflection, leading to Equation 4.25. Test have shown that $\mathrm{d}\theta_o, \mathrm{d}\phi_o = 1°$ is the minimal value for which numerically stable results can be obtained for R_{ns}. This leads to a large computation load which cannot be performed for each reflection. Thus, a two-dimensional look-up table for R_{ns} is computed at initialization of the simulation for a single pair of parameters (b, w). The grid is computed for base values 0 neV$\leq E \leq$1000 neV with 10 neV resolution and $0° \leq \theta_i \leq 90°$ with 1° resolution. Not only R_{ns} was computed for each cell of the look-up table but also $\max I_+$, i.e. the probability of diffuse reflection for the most probable direction of reflection, (θ_o, ϕ_o). This value is needed by the accept-reject method used to determine the direction of diffuse reflection (see below). A corresponding look-up table is also calculated for the probability of diffuse transmission,

$$T_{ns}(\theta_i, E_n) = \int I_-(\theta_i, E_n, \theta_o, \phi_o)\mathrm{d}\Omega_o = \int I_-(\theta_i, E_n, \theta_o, \phi_o) \sin\theta_o \mathrm{d}\theta_o \mathrm{d}\phi_o, \tag{B.1}$$

i.e. the probability of UCN to be scattered into the wall material under angles different from that determined by Snell's law of refraction, and $\max(I_-)$.

The microroughness model was applied only to the two sample plates in the simulation. Information about the angular distribution of reflected UCN is not needed or can be obtained using a completely specular case, as e.g. for the reflection on one of the two mirrors between apertures S1 and S2, where using any diffuse reflection would lead to no other results for the angular distribution of "accepted" UCN due to the relatively small surface of the mirrors and hence rigorous angular condition.

For each reflection of a UCN on the surface of the sample plates, i.e. for passing from the material "vacuum" to the material "plate", it is first decided by the generation of a random number if the UCN is lost, reflected specularly, reflected diffusely or, if its normal velocity component exceeds the critival velocity of the material, transmitted diffusely or accordingly to Snell's law. If one of the two diffuse cases is selected, the angles of the reflected (transmitted) UCN are generated using the accept-reject method [173]. For each direction (θ_o, ϕ_o) its probability is computed

separately during run-time of the simulation.

For the loss probability per wall collision on the surfaces of the sample plates is enhanced by the microroughness, i.e. Equation 4.26 is used, while for all other surfaces, where the microroughness model is not applied, Equation 1.19 is used for the calculation of the loss probability.

Bibliography

[1] J. Chadwick, Proc. R. Soc. London A **136** (1932) 692.

[2] E. Rutherford, Nature **105** (1920) 500.

[3] E. Fermi, Ricerca Scientifica **7** (1936) 13.

[4] W.-M. Yao *et al.* (Particle Data Group), J. Phys. G 33 (2006) (URL: http://pdg.lbl.gov).

[5] E. Fermi, W.H. Zinn, Phys. Rev. **70** (1946) 103.

[6] E. Fermi, L. Marshall, Phys. Rev. **71** (1947) 666.

[7] Ya.B. Zeldovich, Sov. Phys. JETP-**9** (1959) 1389.

[8] V.I. Lushikov *et al.*, Sov. Phys. JETP Lett. **9** (1969) 23.

[9] A. Steyerl, Phys. Lett. **B29** (1969) 33.

[10] N. Cabibbo, Phys. Rev. Lett. **10** (1963) 531.

[11] M. Kobayashi, T. Maskawa, Prog. Theor. Phys. *4*9 (1973) 652.

[12] W.-M. Yao *et al.* (Particle Data Group), J. Phys. G **33**, 1 (2006) and 2007 partial update for edition 2008 (URL: http://pdg.lbl.gov)

[13] S. Arzumanov, L. Bondarenko, S. Chernyavsky, W. Drexel *et al.*, Phys. Lett. B **483** (2000) 15.

[14] A. Serebrov, V. Varlamov, A. Kharitonov, A. Fomin *et al.*, Phys. Lett. B **605** (2005) 72.

[15] H.J. Christenson, J.W. Chronin, V.L. Fitch, R. Turlay, Phys. Rev. Lett. **13** (1964) 138.

[16] C.A. Baker, D.D. Doyle, P. Geltenbort, K. Green *et al.*, Phys. Rev. Lett. **97** (2006) 131801.

[17] N.F. Ramsey, Molecular Beams, Oxford University Press, London.

[18] I.B. Khriplovich, S.K. Lamoreaux, *CP Violation without Strangeness*, Springer (1997), Berlin.

[19] A.Y. Voronin, H. Abele, S. Baessler, V.V. Nesvizhevsky *et al.*, Phys. Rev. **D73** (2006) 044029.

[20] G. Ban, K. Bodek, M. Daum, R. Henneck *et al.*, Phys. Rev. Lett. **99** (2007) 161603.

[21] R. Carr *et al.* (UCNA Collaboration), A proposal for an accurate measurement of the neutron spin-electron angular correlation in polarized neutron beta-decay with ultracold neutrons, 2000.

[22] Yu.V. Borisov *et al.*, Sov. Phys. Tech. Phys. **33** (1988) 574.

[23] F. Atchison, M. Baumann, B. Blau, K. Bodek *et al.*, Proc. ICANS-XVIII (2007).

[24] M. Wohlmuther, G. Heidenreich, Nucl. Instr. and Meth. A **564** (2006) 51.

[25] F. Atchison, *Calculated values for heating, particle fluxes and activation in components of the UCN source*, PSI technical manual TM-14-02-02 (2002).

[26] R. Golub, D. Richardson, S.K. Lamoreaux, *Ultra-Cold Neutrons*, Adam Hilger (1991), Bristol.

[27] A. Serebrov, V. Mityukhlyaev, A. Zakharov, A. Karitonov *et al.*, Nucl. Instr. and Meth. A **440** (2002) 658.

[28] C.L. Morris, J.M. Anaya, T.J. Bowles, B.W. Filippone *et al.*, Phys. REv. Lett. **89** (2002) 272501.

[29] A. Saunders, J.M. Anaya, T.J. Bowles, B.W. Filippone *et al.*, Phys. Lett. B **593** (2004) 55.

[30] F. Atchison, B. van den Brandt, T. Brys, M. Daum *et al.*, Phys. Rev. C **71** (2005) 054601.

[31] F. Atchsion, B. van den Brandt, T. Brys, M. Daum *et al.*, Phys. Rev. Lett. **95** (2005) 182502.

[32] K. Bodek, B. van den Brandt, T. Brys, M. Daum *et al.*, Nucl. Instr. and Meth. A **533** (2004) 491.

[33] V.F. Sears, *Neutron Optics*, Oxford University Press (1989), Oxford.

[34] T. Brys, M. Daum, P. Fierlinger, A. Fomin *et al.*, Nucl. Instr. and Meth. A **551** (2005) 429.

[35] F. Atchison, A. Bergmaier, M. Daum, M. Döbeli *et al.*, Nucl. Instr. and Meth. A **587** (2008) 82.

[36] F. Atchison, T. Bryś, M. Daum, P. Fierlinger *et al.*, Phys. Lett. B **625** (2005) 19.

[37] F. Atchison, T. Bryś, M. Daum, P. Fierlinger *et al.*, Phys. Rev. C **76** (2007) 044001.

[38] F. Atchison, B. Blau, M. Daum, P. Fierlinger *et al.*, Phys. Rev. C **74** (2006) 055501.

[39] F. Atchison, B. Blau, M. Daum, P. Fierlinger *et al.*, Phys. Lett. B **642** (2006) 24.

[40] J. Clayden, N. Greeves, S. Warren, P. Wothers, *Organic chemistry*, Oxford University Press (2006), Oxford.

[41] J. Robertson, Mater. Sci. Eng. R **37** (2002) 129.

[42] P. Koidl, C. Wagner, B. Dischler, J. Wagner *et al.*, Mater. Sci. Forum **52** (1990) 41.

[43] M.G.D. van der Grinten, J.M. Pendlebury, D. Shiers, C.A. Baker *et al.*, Nucl. Instr. and Meth. A **423** (1999) 421.

[44] S. Aisenberg, R. Chabot, J. Appl. Phys. **42** (1971) 2953.

[45] M. Weiler, S. Sattel, K. Jung, H. Ehrhardt *et al.*, Appl. Phys. Lett. **64** (1994) 2797.

[46] D.R. McKenzie, Rep. Prog. Phys. **59** (1996) 1611.

[47] H.-J. Scheibe, B. Schultrich, Thin Solid Films **246** (1994) 92.

[48] F. Atchison, T. Bryś, M. Daum, P. Fierlinger *et al.*, Diamond and Rel. Materials **16** (2007) 334.

[49] E.C. Samano, G. Soto, A. Olivas, L. Cota, Appl. Surf. Sci. **202** (2002) 1.

[50] J. Kulik, Y. Lifshitz, G. Lempert, J. Rabalais *et al.*, J. Appl. Phys. **76** (1994) 5063.

[51] P. Merel, M. Tabbal, M. Chaker, S. Moisa *et al.*, Appl. Surf. Sci. **136** (1998) 105.

[52] K. Kanda, Y. Shimizugawa, Y. Haruyama, I. Yamada *et al.*, Nucl. Instr. and Meth. B **206** (2003) 880.

[53] A.C. Ferrari, J. Robertson, Phys. Rev. B **61** (2000) 14095.

[54] D. Knight, W. White, J. Mater. Res. **4** (1989) 385.

[55] M. Guerino, M. Massi, H.S. Maciel, C. Otani *et al.*, Diamond and Rel. Materials **13** (2004) 316.

[56] M. Pandey, D. Bhatacharyya, D.S. Patil, K. Ramachandran *et al.*, Surface & Coating Tech. **182** (2004) 24.

[57] B. Petereit, P. Siemroth, H.-H. Schneider, H. Hilgers, Surface & Coating Tech. **174-175** (2003) 648.

[58] B. Schultrich, C.-F. Meyer, H.-J. Scheibe, T. Witke *et al.*, Materials Science Forum **287-288** (1998) 381.

[59] D. Schneider, P. Siemroth, T. Schülke, J. Berthold *et al.*, Surface & Coating Tech. **153** (2002) 252.

[60] A.C. Ferrari, A. Libassi, B.K. Tanner, V. Stolojan *et al.*, Phys. Rev. B **62** (2000) 11089.

[61] A.C. Ferrari, J. Robertson, Phys. Rev. B **64** (2001) 075414.

[62] S. Sails, D. Gardiner, M. Bowden, J. Savage *et al.*, Diamond and Rel. Materials **5** (1996) 589.

[63] J. Ager, S. Anders, A. Anders, I. Brown, Appl. Phys. Lett. **66** (1995) 3444.

[64] J. Schwan, S. Ulrich, V. Batori, H. Ehrhardt *et al.*, J. Appl. Phys. **80** (1996) 440.

[65] P.A. Temple, C.E. Hathaway, Phys. Rev. B **7** (1973) 3685.

[66] S. Prawer, K.W. Nugent, Y. Lifshitz, G.D. Lempert *et al.*, Diamond and Rel. Materials **5** (1996) 433.

[67] XPS Peak, written by R. Kwok, download at `http://www.phy.cuhk.edu.hk/~surface/XPSPEAK/`.

[68] D. Shirley, Phys. Rev. B **5** (1972) 4709.

[69] G. Wertheim, M. Butler, K. West, D. Buchanan, Rev Sci. Ins. **45** (1974) 1369.

[70] J.C. Lascovich, R. Giorgi, S. Scaglione, Appl. Surf. Sci. **47** (1991) 17.

[71] G. Comelli, J. Stöhr, W. Jark, Phys. Rev. B **37** (1988) 4383.

[72] T. Capehart, T. Perry, C. Beetz, D. Belton *et al.*, Appl. Phys. Lett. **55** (1989) 957.

[73] J. Stöhr, NEXAFS spectroscopy, Springer, 1992.

[74] C. Quitmann, U. Flechsig, L. Patthey, T. Schmidt *et al.*, Surface Science **480** (2001) 173.

[75] D. Schneider, H.-J. Scheibe, T. Schwarz, P. Hess, Diamond and Rel. Materials **2** (1993) 1396.

[76] D. Schneider, T. Schwarz, H.-J. Scheibe, M. Panzner, Thin Solid Films **295** (1997) 107.

[77] Y. Lifshitz, Diamond and Rel. Materials **8** (1999) 1659.

[78] D. Schneider, C.F. Meyer, H. Mai, B. Schöneich *et al.*, Diamond and Rel. Materials **7** (1998) 973.

[79] Fraunhofer Institut für Werkstoff- und Strahltechnik, Dresden`http://www.iws.fhg.de`.

[80] E. Findeisen, R. Feidenhans'l, M.E. Vigild, K.N. Clausen *et al.*, J. Appl. Phys. **76** (1994) 4636.

[81] D. Clemens, P. Gross, P. Keller, N. Schlumpf *et al.*, Physica B **276-278** (2002) 140.

[82] M. Gupta, T. Gutberlet, J. Stahn, P. Keller *et al.*, Pramana - J. Phys. **63** (2004) 57.

[83] L. Parratt, Phys. Rev. **95** (1954) 359.

[84] Parratt32, written at HMI Berlin, download at
`http://www.hmi.de/bensc/instrumentation/instrumente/v6/refl/parratt_en.htm`.

[85] V. Sears, Neutron News 3, No. **3** (1992) 29ff.

[86] J. Budai, Z. Toth, submitted to Physica Status Solidi C.

[87] J. Robertson, Diamond and Rel. Materials **2** (1993) 984.

[88] J. Robertson, Diamond and Rel. Materials **3** (1994) 361.

[89] J. Robertson, Diamond and Rel. Materials **14** (2005) 942.

[90] A.A. Voevodin, M.S. Donley, Surf. Coat. Technol. **82** (1996) 199.

[91] M. Makela, PhD thesis, advised by B. Vogelaar, virginia Polytechnic Institute and State University, 2005.

[92] K. Yamamoto, Y. Koga, S. Fujiwara, F. Kokai *et al.*, Applied Physics **A66** (1998) 115.

[93] D.B. Chrisey, G.K. Hubler, *Pulsed Laser Deposition of Thin Films*, John Wiley (1994), New York.

[94] J.F. Ready, Appl. Phys. Lett. **3** (1963) 11.

[95] R.M. White, J. Appl. Phys. **34** (1963) 3559.

[96] G.A. Askar'yan, A.M. Pokhorov, G.F. Chantutiya, G.P. Shipulo, Sov. Phys. JETP **17** (1963) 6.

[97] R.G. Meyerand, A.F. Haught, Phys. Rev. Lett. **9** (1963) 403.

[98] H.M. Smith, A.F. Turner, Appl. Opt. **4** (1965) 147.

[99] F.J. McClung, R.W. Hellwarth, J. Appl. Phys. **33** (1962) 828.

[100] D. Dijkkamp *et al.*, Appl. Phys. Lett. **51** (1987) 619.

[101] R. Kelly, A. Miotello, B. Braren, A. Gupta *et al.*, Nucl. Instr. and Meth. B **65** (1992) 187.

[102] R. Kelly, A. Miotello, Appl. Phys. **B57** (1993) 145.

[103] H. Opower, W. Press, Z. Nat. Forsch **21a** (1966) 344.

[104] W. Demtröder, W. Jantz, Plasma Phys. **12** (1970) 691.

[105] Y.A. Bykovskii, N.N. Degtyarenko, V.F. Elesin, V.E. Kondrashov *et al.*, Sov. Phys. Tech. Phys. **18** (1974) 1597.

[106] K.H. Song, X. Xu, Appl. Surf. Sci. **127-129** (1998) 111.

[107] J.F. Friichtenicht, REv. Sci. Instrum. **45** (1974) 51.

[108] R. Diamant, E. Jimenez, E. Haro-Poniatowski, L. Ponce *et al.*, Diamond and Rel. Materials **8** (1999) 1277.

[109] R.F. Bunshah, *Deposition Technologies for Films and Coatings*, Noyes (1982), Park Ridge NJ.

[110] Ch. Kittel, *Einführung in die Festkörperphysik*, Oldenbourg (1999), Mnchen.

[111] T. Brys, M. Daum, P. Fierlinger, A. Foelske *et al.*, Diamond and Rel. Materials **15** (2006) 928.

[112] P.R. Willmot, J.R. Huber, Reviews of Modern Physics **72** (2000) 315.

[113] A.M. Keszler, L. Nemes, Journal of Molecular Structure **695-696** (2004) 211.

[114] J.C. Orlianges, C. Champeaux, A. Catherinot, Th. Merle *et al.*, Thin Solid Films **453-454** (2004) 285.

[115] D. Basting, G. Marowsky, *Excimer Laser Technology*, Springer (2005), Berlin.

[116] Ch.A. Brau, *Rare Gas Halogen Excimers*, in: Ch.K. Rhodes, *Topics in Applied Physics, Vol. 30, Excimer Lasers*, Springer (1984), Berlin.

[117] OSLO EDU Edition, by Lambda Research Corporation, `http://www.lambdares.com`.

[118] `http://www.heraeus-quarzglas.com`

[119] R. Abraham, LambdaPhysik / Coherent Inc., personal communication.

[120] R.P. Govier, G.M. McCracken, J. Vac. Sci. and Techn. **7** (1970) 552.

[121] `http://www.labview.com`, `http://www.ni.com`

[122] S. Heule, F. Atchison, M. Daum, A. Foelske *et al.*, Appl. Surf. Sci. **253** (2007) 8245.

[123] T. Witke, T. Schuelke, J. Berthold, C.F. Meyer *et al.*, Surf. Coat. Technol. **116** (1999) 609.

[124] R.J. Narayan, *Diamond-Like Carbon: Medical and Mechanical Applications* in: R. Eason, *Pulsed Laser Deposition of Thin Films*, John Wiley (2007), New York.

[125] P. Beckmann, A. Spizzichino, *The Scattering of Electromagnetic Waves from Rough Surfaces*, Artech House (1987), Norwood MA, USA.

[126] J.H. Lambert, *Photometria sive de mensura de gratibus luminis, colorum et umbrae*, Eberhard Klett (1760), Augsburg, Germany.

[127] K. Torrance, E. Sparrow, J. opt. Soc. Am. **57** (1967) 1105.

[128] P. Croce, L. Prod'homme, Nouv. Rev. Opt. **7** (1976) 121.

[129] P. Croce, Nouv. Rev. Opt **8** (1977) 127.

[130] L. Nevot, P. Croce, Rev. Phys. Appl. **15** (1980) 761.

[131] S.K. Sinha, E.B. Sirota, S. Garoff, H.B. Stanley, Phys. Rev. B **38** (1988) 2297.

[132] A. Steyerl, Z. Physik **254** (1972) 196.

[133] V.K. Ignatovich, V.I. Luschikov, JINR, Dubna, Commun. **P3** (1975) 8795.

[134] V.K. Ignatovich, JINR, Dubna, Commun. **P4** (1973) 7055.

[135] R. Pynn, Phys. Rev. B **45** (1992) 602.

[136] A. Steyerl, S.S. Malik, L.R. Iyengar, Physica B **173** (1991) 47.

[137] A. Steyerl, *Transmissionsmessungen mit ultrakalten Neutronen*, PhD thesis, TU Munich, 1971.

[138] A. Steyerl, Nucl. Instr. Meth. **101** (1972) 295.

[139] K.J. Kügler, W. Paul, U. Trinks, Z. Physik B - Cond. Mat. **39** (1980) 361.

[140] A. Steyerl, H. Nagel, F.-X. Schreiber, R. Gähler *et al.*, Phys. Lett. A **116** (1986) 347.

[141] V.V. Nesvizhevsky, H.G. Borner, A.K. Petukhov, H. Abele *et al.*, Nature **415** (2002) 297.

[142] V.V. Nesvizhevsky, Nucl. Instr. Meth. A **557** (2006) 576.

[143] V.V. Nesvizhevsky, G. Pignol, K.V. Protasov, G. Quemener, Nucl. Instr. Meth. A **578** (2007) 435.

[144] C. Plonka, P. Geltenbort, T. Soldner, H. Häse, Nucl. Instr. and Meth. A **578** (2007) 450.

[145] G. Zsigmond, private communication.

[146] P.M. Morse, K. Ingard, *Theoretical acoustics*, Princeton University Press (1968), Princeton NJ, USA.

[147] F. Atchison, T. Bryś, M. Daum, P. Fierlinger *et al.*, Nucl. Instr. and Meth. A **552** (2005) 513.

[148] P. Ageron, Nucl. Instr. Meth. A **284** (1989) 197.

[149] National Instruments Corp., USB-6008,
`http://sine.ni.com/nips/cds/view/p/lang/en/nid/14604`

[150] `http://www.fastcomtec.com/products/product-lines/multiparameter-multichannel-analyzers/mpa-3.html`

[151] MPA-3 Multiparameter Data Acquisition System User Manual, FAST ComTec GmbH, Version 1.59, March 3, 2005.

[152] P. Gawlitza, S. Braun, S. Lipfert, *et al.*, Proceedings of SPIE **6317** (2006) 63170G.

[153] MATLAB®, The Mathworks Inc., `http://www.matlab.com`.

[154] `http://kur.web.psi.ch/narziss/`

[155] P. Fierlinger, A. Pichlmaier, H. Rauch, Nucl. Instr. and Meth. A **557** (2006) 572.

[156] V.K. Ignatovich, *The Physics of Ultracold Neutrons*, Clarendon Press (1990), Oxford, UK.

[157] G.F. Gareeva, A.Yu. Muzychka, Yu.N. Pokotilovski, Nucl. Instr. and Meth. A **369** (1996) 180.

[158] G. Zsigmond *et al.*, ICANS-XVII, LA-UR-06-3904 (2006) 168.

[159] S. Agostinelli, J. Allison, K. Amako, J. Apostolakis *et al.*, Nucl. Instr. and Meth. A **506** (2003) 250.

[160] J. Allison, K. Amako, J. Apostolakis, H. Araujo *et al.*, IEEE Trans. on Nucl. Sci. **53** (2006) 270.

[161] I.N. Bronstein, K.A. Semendjajew, G. Musiol, H. Mühlig, *Taschenbuch der Mathematik*, Verlag Harri Deutsch (1999), Frankfurt a.M., Germany.

[162] L. Emerson, G. Cox, Micron bf25 (1994) 267.

[163] K.L. Westra, D.J. Thomson, J. Vac. Sci. Technol. B **12** (1994) 3176.

[164] D.L. Sedin, K.L. Rowlen, Appl. Surf. Sci. **182** (2001) 40.

[165] R. Lermer, A. Steyerl, Phys. stat. sol. (a) **88** (1976) 531.

[166] A. Amamou, F. Gautier, B. Loegel, J. Phys. F: Metal Phys. **5** (1975) 1342.

[167] S. Gosh, N. Das, A. Mookerjee, arXiv:cond-mat/9809137v1 (1998).

[168] G. Engelmann, A. Steyerl, A. Heidemann, A. Kostorz *et al.*, Zeitschr. f. Physik B **35** (1979) 345.

[169] F. Atchison, private communication.

[170] I. Berceanu, V.K. Ignatovich, Vacuum **23** (1973) 441.

[171] M. Brown, R. Golub, J.M. Pendlebury, Vacuum **25** (1974) 61.

[172] S. Mayer, G. Zsigmond, P. Allenspach, Nucl. Instr. and Meth. A **586** (2008) 110.

[173] J. von Neumann, Nat. Bureau Standards **12** (1951) 36.

Danksagung

Obschon Dissertationen nur einen Autoren haben, ist doch meistens eine Fülle von Menschen an ihnen beteiligt. Dies ist bei der vorliegenden Arbeit nicht anders. Mein Dank geht daher an all jene, die zum Gelingen dieser Arbeit beigetragen haben.

Zunächst an Ulrich Straumann, meinen Doktorvater, der es mir sehr unbürokratisch ermöglichte, eine Arbeit am PSI durchzuführen und diese vom Anfang bis zum Ende aktiv unterstützte. Speziell bedanken möchte ich mich für das Vertrauen, das er in mich und meine Arbeit setzte und für das Verständnis und die Geduld, die er mir entgegen brachte als sich das Projekt verzögerte.

Natürlich an Reinhold Henneck, meinen Betreuer für seine wertvollen Denkanstösse, seine Ideen und die viele Zeit, die er in das Projekt investiert hat. Speziell erwähnen möchte ich an dieser Stelle, dass das Doppelplattenexperiment ohne seinen unermüdlichen Einsatz kaum Chancen auf Erfolg gehabt hätte.

An Manfred Daum, für die tatkräftige organisatorische Unterstützung des Projekts und für seine stete Hilfsbereitschaft. Dank ihm konnte ich mich stets auf die physikalischen und technischen Herausforderungen dieser Arbeit konzentrieren.

An Thomas Lippert, für seine Unterstützung bei den DLC-Beschichtungen und den Strukturuntersuchungen. Er hat mir viele wichtige Informationen und Denkanstösse geliefert und mir in sehr grosszügiger Weise die Gerätschaften seiner Gruppe zur Verfügung gestellt. Speziell bedanken möchte ich mich dafür, dass er mich offiziell zu seinem Forschungsteam gezählt hat. Ein Dankeschön geht auch an die Mitgliedern eben dieses Forschungsteams, der Materialiengruppe am PSI, speziell an Lukas Urech.

An die vielen Kollegen und Freunde in der UCN-Gruppe am PSI: An Peter Fierlinger, speziell für das Erstlesen dieser Arbeit; an Axel Pichlmaier, speziell für einen denkwürdigen München-Ausflug; an Klaus Kirch, speziell für unzählige wertvolle Hinweise; an Andreas Knecht, Malgorzata Kasprzak, Marcin Kuzniak; an Geza Zsigmond, speziell für die Simulation des Neutronenleiters am ILL, an Francis Atchison, Bernhard Lauss und Gerdt Petzold. Ein ganz spezieller Dank geht an Michael Meier, nicht nur für das gemeinsame Aufbauen der Beschichtungsanlage und die technische Unterstützung beim Doppelplattenexperiment, sondern auch für viele gemeinsame Unternehmungen ausserhalb des PSI. Besonders danken möchte ich auch Michael Wohlmuther, für die andauernde Freundschaft zur UCN-Gruppe und sein aktives Interesse am Projekt und speziell am Doppelplattenexperiment.

An Rüdiger Kötz und Annette Foelske für die Ausbildung an der XPS-Apparatur, die dazugehörige Benutzungserlaubnis und die wertvolle Unterstützung, die sie dem Projekt damit gaben.

An Thomas Brenner, Peter Geltenbort und Christian Plonka für ihre tatkräftige Unterstützung beim Doppelplatten-Experiment.

Ein Dank geht auch an die Mitarbeiter des PSI, speziell an die Werkstätten, die Vakuumgruppe sowie an Roland Scheidegger vom Transportdienst.

Zuletzt auf dieser Seite, aber nicht in der Wichtigkeit, möchte ich allen meinen Verwandten und Bekannten danken, die mich in den vergangenen vier Jahren motiviert haben, allen voran meinem Vater, der mir eine sehr wertvolle Stütze war.